

Advanced Structured Materials

Sergei M. Aizikovich ·
Holm Altenbach · Victor Eremeyev ·
Michael Vincent Swain ·
Alexander Galybin *Editors*



Modeling, Synthesis and Fracture of Advanced Materials for Industrial and Medical Applications

 Springer


Advanced Structured Materials

Volume 136

Series Editors

Andreas Öchsner, Faculty of Mechanical Engineering, Esslingen University of Applied Sciences, Esslingen, Germany

Lucas F. M. da Silva, Department of Mechanical Engineering, Faculty of Engineering, University of Porto, Porto, Portugal

Holm Altenbach , Faculty of Mechanical Engineering, Otto von Guericke University Magdeburg, Magdeburg, Sachsen-Anhalt, Germany

Common engineering materials reach in many applications their limits and new developments are required to fulfil increasing demands on engineering materials. The performance of materials can be increased by combining different materials to achieve better properties than a single constituent or by shaping the material or constituents in a specific structure. The interaction between material and structure may arise on different length scales, such as micro-, meso- or macroscale, and offers possible applications in quite diverse fields.

This book series addresses the fundamental relationship between materials and their structure on the overall properties (e.g. mechanical, thermal, chemical or magnetic etc.) and applications.

The topics of *Advanced Structured Materials* include but are not limited to

- classical fibre-reinforced composites (e.g. glass, carbon or Aramid reinforced plastics)
- metal matrix composites (MMCs)
- micro porous composites
- micro channel materials
- multilayered materials
- cellular materials (e.g., metallic or polymer foams, sponges, hollow sphere structures)
- porous materials
- truss structures
- nanocomposite materials
- biomaterials
- nanoporous metals
- concrete
- coated materials
- smart materials

Advanced Structured Materials is indexed in Google Scholar and Scopus.

More information about this series at <http://www.springer.com/series/8611>


Sergei M. Aizikovich · Holm Altenbach ·
Victor Eremeyev · Michael Vincent Swain ·
Alexander Galybin
Editors


Modeling, Synthesis and Fracture of Advanced Materials for Industrial and Medical Applications


 Springer

Editors

Sergei M. Aizikovich
Research and Educational Centre
Don State Technical University
Rostov-on-Don, Russia

Victor Eremeyev 
Faculty of Civil and Environmental
Engineering
Gdańsk University of Technology
Gdańsk, Poland

Alexander Galybin 
Schmidt Institute of Physics of the Earth
Moscow, Russia

Holm Altenbach 
Chair of Engineering Mechanics
Institute of Mechanics
Faculty of Mechanical Engineering
Otto von Guericke University Magdeburg
Magdeburg, Sachsen-Anhalt, Germany

Michael Vincent Swain
Biomechanical Department, AMME
University of Sydney
Sydney, NSW, Australia

ISSN 1869-8433

Advanced Structured Materials

ISBN 978-3-030-48160-5

<https://doi.org/10.1007/978-3-030-48161-2>

ISSN 1869-8441 (electronic)

ISBN 978-3-030-48161-2 (eBook)

© Springer Nature Switzerland AG 2020

This work is subject to copyright. All rights are reserved by the Publisher, whether the whole or part of the material is concerned, specifically the rights of translation, reprinting, reuse of illustrations, recitation, broadcasting, reproduction on microfilms or in any other physical way, and transmission or information storage and retrieval, electronic adaptation, computer software, or by similar or dissimilar methodology now known or hereafter developed.

The use of general descriptive names, registered names, trademarks, service marks, etc. in this publication does not imply, even in the absence of a specific statement, that such names are exempt from the relevant protective laws and regulations and therefore free for general use.

The publisher, the authors and the editors are safe to assume that the advice and information in this book are believed to be true and accurate at the date of publication. Neither the publisher nor the authors or the editors give a warranty, expressed or implied, with respect to the material contained herein or for any errors or omissions that may have been made. The publisher remains neutral with regard to jurisdictional claims in published maps and institutional affiliations.

This Springer imprint is published by the registered company Springer Nature Switzerland AG
The registered company address is: Gewerbestrasse 11, 6330 Cham, Switzerland

Preface

Recent technological development brings with it a wide class of novel advanced materials with properties which previously could not *a priori* have been designed. In addition, new techniques such as additive technologies (3D printing), along with various approaches to manufacture coatings (impulse laser deposition, magnetron sputtering deposition, etc.), have been developed. Obviously, such novel materials are finding applications in an ever expanding range of engineering fields, for example, as thermal barrier coatings as well as in electronic, photovoltaic and biomedical areas. Among such applications, we highlight those used in medicine related to the production of new types of implants, medical instruments and their components. Considering medical applications of these new materials, one has to take into account not only “standard” mandatory requirements for materials such as strength, durability, fatigue, failure and wear resistance, high fracture limit, but also a range of clinically specific issues. Firstly, biocompatibility of these new materials is the most important factor. To help achieve this outcome, various types of coatings have been proposed in the literature to improve this property. Secondly, high resistance and stability to the biological environment play an important role for ensuring survival when required for long-term applications. Last, but not the least, in this list of peculiarities for such applications is the requirement for a genuine understanding of the biomechanics of the wide variability of the material properties of biological tissues, which must be taken into the account for the development of implants and other medical devices.

This volume of the Advanced Structured Materials Series collects papers on theoretical and experimental studies of advanced materials. In addition, some papers that address the mechanical properties and resistance to environmental factors are presented. Kislyakov et al. analysed the influence of citric acid on mechanical properties of human enamel and dentine samples using nanoindentation techniques. Nanoindentation was also used by Nikolaev et al. in order to study the hardness and other properties of thin Microposit S1813 films deposited on a substrate. In order to improve the quality of implants, Mukhanova et al. performed tests to analyse the *in vitro* degradation of hydroxyapatite. Kudryakov et al. investigated the fatigue wear behaviour under liquid droplet impacts on various industrial alloys

and ion-plasma coatings. Orthopaedic applications of novel carbon porous bone implants are presented by Golubev et al., where both experimental and clinical studies were investigated. A number of papers addressed the analysis of mechanical properties of metals, alloys and powder-based materials. In particular, Bragov et al. studied the fracture of different titanium alloys under dynamic impact loading, where compression, tensile and shear tests were performed. These authors also proposed a corresponding mathematical analysis. Marathe et al. studied experimentally the friction properties of novel compacts made of aluminium and iron powder against various substrates and in different environments. In order to analyze the long-term strength of some metals and alloys, a novel damage mechanics model was proposed by Volkov et al. Finally, a series of papers are devoted to the mathematical modelling of complex structures. These include a mathematical model for mechanical response of a human eye following various surgical corrections to the cornea which is discussed by Bauer et al. Using the complex variable technique, Galybin investigated the identification and mechanics of interfacial cracks in layered media. Modelling of microstructured materials utilizing some well-known generalized continuum models has been discussed. In this volume, an exact solution for the behaviour of an elastic micropolar sphere is given by Zubov, where the key-point of the analysis was the role of distributed dislocations.

Rostov on Don, Russia
Magdeburg, Germany
Gdańsk, Poland/Rostov on Don, Russia
Sidney, Australia
Moscow, Russia
April, 2020

Sergei M. Aizikovich
Holm Altenbach
Victor Eremeyev
Michael Vincent Swain
Alexander Galybin

Contents

1	The Method of Elastotometry for Cornea Weakening in the Peripheral Annular Zone	1
	Svetlana M. Bauer, Liudmila A. Venatovskaya, and Larisa A. Avershina	
1.1	Introduction	2
1.2	Problem Statement	2
1.3	Results and Discussion	4
1.4	Conclusion	8
	References	9
2	Deformation and Fracture of Titanium Alloys Under Dynamic Loading	11
	Anatolii M. Bragov, Leonid A. Igumnov, Aleksandr Yu. Konstantinov, and Andrey K. Lomunov	
2.1	Introduction	12
2.2	Methods of Experimental Research	12
2.2.1	Tests of Samples Under Uniaxial Compression	13
2.2.2	Shear Experiments	14
2.2.3	Determination of the Dynamic Characteristics of Friction	15
2.2.4	Determining the Deformation Curves and Strength Characteristics Under High-Speed Tension	17
2.2.5	High-Temperature Experiments	18
2.2.6	Verification Experiments	18
2.3	Experimental Results	18
2.3.1	Deformation Curves	18
2.3.2	Ultimate Failure Characteristics	21
2.3.3	Results of the Study of Dynamic Friction	23

2.4	Modeling the Properties of the Materials	27
2.5	Verification of Mathematical Models	29
2.6	Conclusions	31
	References	32
3	Direct and Inverse Problems for Interface Crack Identification in Layered Media	35
	Alexander N. Galybin	
3.1	Introduction	35
3.2	Preliminaries	37
	3.2.1 Kolosov–Muskhelishvili Formulas	37
	3.2.2 Fourier Transforms	38
3.3	Problem Formulation	39
3.4	Direct Boundary Value Problems for an Elastic Strip	41
3.5	Solution of the Cauchy Problem for the Inhomogeneous Strip	45
3.6	Inverse Problem of Crack Detection	48
	3.6.1 An Interface Crack	48
	3.6.2 Example: Discussion of Possibility of Crack Detection	50
3.7	Conclusions	53
	References	54
4	Experimental and Clinical Investigation of Carbon Nanostructural Material for Orthopaedic Applications	57
	George Sh. Golubev, Valery N. Varavka, and Michael B. Rodin	
4.1	Introduction	57
4.2	Types of Carbon Materials and Implants for Orthopaedic Applications	58
4.3	Carbon Nanostructured Materials	60
4.4	Testing of Carbon Nanostructural Material’s Properties	61
4.5	Biomechanical Properties and Clinical Applications of Carbon Nanostructural Implants	66
4.6	Clinical Applications of Carbon Nanostructural Implants	68
	4.6.1 Long Bones Defects	68
	4.6.2 Bone Axial Disorders	70
4.7	Conclusion	71
	References	72

5	Nanoindentation Derived Mechanical Properties of Human Enamel and Dentine Subjected to Etching with Different Concentrations of Citric Acid	75
	Evgeniy A. Kislyakov, Roman V. Karotkiyan, Evgeniy V. Sadyrin, Boris I. Mitrin, Diana V. Yogina, Artur V. Kheygetyan, and Stanislav Yu. Maksyukov	
5.1	Introduction	76
5.2	Materials and Methods	76
	5.2.1 Sample Preparation	76
	5.2.2 Nanoindentation	77
5.3	Results	77
5.4	Discussion	81
5.5	Conclusion	82
	References	83
6	Experimental and Theoretical Solution of the Problem on the Generating of Fatigue Wear in Heterogeneous Materials and Coatings	85
	Oleg V. Kudryakov, Valery N. Varavka, Igor Yu. Zabiya, and Natalia I. Bronnikova	
6.1	Introduction	86
6.2	Conditions for Initiation of Destruction (Wear) Under Droplet-Impact Cyclic Effects	87
6.3	Theoretical Bases of Quantitative Estimates for the Stage of Microstructural Fracture Mechanics Under Droplet Impacts	89
6.4	Main Design Parameters for the Nucleation Stage of Destruction and Wear Under Drip-Impact Cyclic Loading	91
6.5	Application of Calculation Model	95
	6.5.1 Compact Materials (Metals and Alloys)	95
	6.5.2 Coatings	102
6.6	Conclusion	108
	References	109
7	Interface Frictional Behaviour of Aluminium and Iron Powder Compacts at Room Temperature	111
	Pragat P. Marathe, Kanhu C. Nayak, Prashant P. Date, and Sergei Alexandrov	
7.1	Introduction	111
7.2	Experimental Procedure	113
7.3	Results and Discussion	117
7.4	Conclusions	122
	References	122

8	In Vitro Degradation Test of Gd-, Si-Substituted Hydroxyapatite	125
	Elizaveta A. Mukhanova, Ekaterina S. Ivanyutina, Maxim Yu. Stupko, and Irina V. Rybal'chenko	
8.1	Introduction	126
8.2	Material and Method	127
	8.2.1 Synthesis	127
	8.2.2 Degradation Test	127
	8.2.3 Characterization	127
	8.2.4 Statistical Analysis	128
8.3	Results and Discussion	128
	8.3.1 XRD Analyses	128
	8.3.2 SEM Analyses	129
	8.3.3 In Vitro Degradation Study	132
8.4	Conclusion	133
	References	134
9	Mechanical Properties of Microposit S1813 Thin Layers	137
	Andrey L. Nikolaev, Boris I. Mitrin, Evgeniy V. Sadyrin, Vladimir B. Zelentsov, Adair R. Aguiar, and Sergei M. Aizikovich	
9.1	Introduction	138
9.2	Materials and Methods	139
	9.2.1 Sample Preparation	139
9.3	Results	140
	9.3.1 Thickness Measurements	140
	9.3.2 AFM	140
	9.3.3 Nanoindentation	141
9.4	Conclusion	145
	References	145
10	A Continual Model of Damage for Analyzing Long-Term Strength of Materials and Structural Elements	147
	Ivan A. Volkov, Leonid A. Igumnov, and Svetlana Yu. Lutvinchuk	
10.1	Introduction	148
10.2	Defining Relations of Mechanics of Damaged Media	151
10.3	Investigation Results	156
10.4	Conclusions	171
	References	173
11	Nonlinear Deformations of an Elastic Sphere with Couple Stresses and Distributed Dislocations	175
	Leonid M. Zubov	
11.1	Introduction	175
11.2	Basic Relations of Nonlinear Micropolar Continuum	176

11.3	Continuously Distributed Dislocations	177
11.4	Spherically Symmetric State	179
11.5	Physically Linear Material	182
11.6	Exact Solution of the Eigenstress Problem	183
11.7	Conclusion	186
	References	186

Contributors

Adair R. Aguiar University of Sao Paulo, Sao Paulo, Brazil

Sergei M. Aizikovich Don State Technical University, Rostov-on-Don, Russia

Sergei Alexandrov Ishlinsky Institute for Problems in Mechanics, Russian Academy of Sciences, Moscow, Russia

Larisa A. Avershina Cheboksary branch of S. Fyodorov Eye Microsurgery Federal State Institution of Russian Ministry of Health, Cheboksary, Russian Federation

Svetlana M. Bauer Saint Petersburg State University, St. Petersburg, Russian Federation;
Research and Education Center “Materials”, Don State Technical University, Rostov-on-Don, Russian Federation

Anatolii M. Bragov Research Institute for Mechanics, National Research Lobachevsky State University of Nizhny Novgorod, Nizhny Novgorod, Russia

Natalia I. Bronnikova Don State Technical University, Rostov-on-Don, Russian Federation

Prashant P. Date Department of Mechanical Engineering, Indian Institute of Technology Bombay, Mumbai, India

Alexander N. Galybin The Schmidt Institute of Physics of the Earth (IPE RAS), Moscow, Russia

George Sh. Golubev Department of Trauma and Orthopaedic Surgery, Rostov State Medical University, Rostov-on-Don, Russian Federation

Leonid A. Igumnov Research Institute for Mechanics, National Research Lobachevsky State University of Nizhny Novgorod, Nizhny Novgorod, Russia

Ekaterina S. Ivanyutina Chemistry Department, Southern Federal University, Rostov-on-Don, Russian Federation

Roman V. Karotkiyan Don State Technical University, Rostov-on-Don, Russia

Artur V. Kheygetyan Rostov State Medical University, Rostov-on-Don, Russia

Evgeniy A. Kislyakov Don State Technical University, Rostov-on-Don, Russia

Aleksandr Yu. Konstantinov Research Institute for Mechanics, National Research Lobachevsky State University of Nizhny Novgorod, Nizhny Novgorod, Russia

Oleg V. Kudryakov Don State Technical University, Rostov-on-Don, Russian Federation

Andrey K. Lomunov Research Institute for Mechanics, National Research Lobachevsky State University of Nizhny Novgorod, Nizhny Novgorod, Russia

Svetlana Yu. Lutvinchuk Research Institute for Mechanics, National Research Lobachevsky State University of Nizhny Novgorod, Nizhny Novgorod, Russian Federation

Stanislav Yu. Maksyukov Rostov State Medical University, Rostov-on-Don, Russia

Pragat P. Marathe Department of Mechanical Engineering, Indian Institute of Technology Bombay, Mumbai, India

Boris I. Mitrin Don State Technical University, Rostov-on-Don, Russia

Elizaveta A. Mukhanova Chemistry Department, Southern Federal University, Don State Technical University, Rostov-on-Don, Russian Federation

Kanhu C. Nayak Department of Mechanical Engineering, Indian Institute of Technology Bombay, Mumbai, India

Andrey L. Nikolaev Don State Technical University, Rostov-on-Don, Russia

Michael B. Rodin Department of Orthopaedic Surgery, Rostov City Center of Trauma and Orthopaedic Surgery, Rostov-on-Don, Russian Federation

Irina V. Rybal'chenko Chemistry Department, Southern Federal University, Rostov-on-Don, Russian Federation

Evgeniy V. Sadyrin Don State Technical University, Rostov-on-Don, Russia

Maxim Yu. Stupko Chemistry Department, Southern Federal University, Rostov-on-Don, Russian Federation

Valery N. Varavka Research and Education Centre "Materials", Don State Technical University, Rostov-on-Don, Russian Federation

Liudmila A. Venatovskaya Saint Petersburg State University, St. Petersburg, Russian Federation

Ivan A. Volkov Research Institute for Mechanics, National Research Lobachevsky State University of Nizhny Novgorod, Nizhny Novgorod, Russian Federation

Diana V. Yogina Rostov State Medical University, Rostov-on-Don, Russia

Igor Yu. Zabiya Don State Technical University, Rostov-on-Don, Russian Federation

Vladimir B. Zelentsov Don State Technical University, Rostov-on-Don, Russia

Leonid M. Zubov Southern Federal University, Rostov-on-Don, Russian Federation

Chapter 1

The Method of Elastotonometry for Cornea Weakening in the Peripheral Annular Zone



Svetlana M. Bauer, Liudmila A. Venatovskaya, and Larisa A. Avershina

Abstract The mechanical response of the eye to cornea loading by Maklakoff tonometers weighting 5; 7.5; 10; and 15 g is studied in the case of weakening of the cornea in the peripheral annular zone due to hyperopia surgical correction. Firstly sequential measurements of intraocular pressure are carried out, then the dependence curve of the tonometric intraocular pressure (IOP) versus tonometer weight is plotted and analyzed (so-called Maklakoff elastotonometry is used). The mathematical model of measuring the IOP by the Maklakoff tonometer is made in the engineering simulation software ANSYS Inc. The elastic system cornea–sclera is presented as two joint transversely isotropic spherical segments with different radii of curvature and biomechanical properties loaded with internal pressure. The results of elastotonometry for the preoperative stage and two different methods of vision correction LASIK and Femto LASIK are compared.

Keywords Joint spherical segments · Elastotonometry · LASIK · Femto LASIK · Hyperopia

S. M. Bauer (✉) · L. A. Venatovskaya
Saint Petersburg State University, Universitetskaya nab. 7/9, St. Petersburg 199034, Russian Federation
e-mail: s.bauer@spbu.ru

L. A. Venatovskaya
e-mail: l.venatovskaya@spbu.ru

S. M. Bauer
Research and Education Center “Materials”, Don State Technical University, pl. Gagarina 1, Rostov-on-Don 344000, Russian Federation

L. A. Avershina
Cheboksary branch of S. Fyodorov Eye Microsurgery Federal State Institution of Russian Ministry of Health, Traktorstroitelny Prospekt 10, 428028 Cheboksary, Russian Federation
e-mail: lar.fedotova@mail.ru

© Springer Nature Switzerland AG 2020

S. M. Aizikovich et al. (eds.), *Modeling, Synthesis and Fracture of Advanced Materials for Industrial and Medical Applications*, Advanced Structured Materials 136,
https://doi.org/10.1007/978-3-030-48161-2_1

1.1 Introduction

In recent studies, a change of the elastic properties of fibrous tunic of the eye in clinic and treatment of many eye diseases, including myopia and glaucoma, is widely discussed [2, 4, 5, 9]. It is known that its non-mechanical properties vary significantly in both myopia and glaucoma and these changes are multidirectional. In both cases, scleral stretching occurs but in myopia the strength properties of the sclera and rigidity decrease while in glaucoma these properties increase [5]. Ocular Response Analyzer (ORA) can only state the presence of biomechanical disorders of the fibrous tunic, fixing the same decrease in corneal hysteresis and increase in corneal resistance factor in myopia and glaucoma, and doesn't differentiate their different nature. In [4, 5], it is noted that at present there are practically no clinical methods for assessing the biomechanical properties of the fibrous tunic of the eye.

The results of current research have shown high sensitivity of the elastotonometry to the presence and type of biomechanical disorders of the fibrous tunic of the eye [2, 4, 5, 9]. This method was proposed by V.P. Filatov and S.F. Kalfa and was originally used only for the diagnostics of glaucoma. It is known that deviation of the elastocurve from the norms occurs in such corneal pathologies as glaucoma and marginal ectatic dystrophy, when the nonuniform cornea becomes particularly weak in the vicinity of the sclera. The surgical correction of hyperopia also leads to the weakening of the cornea at the periphery; nevertheless, the behavior of elastocurves has not been studied enough.

In the present paper, we consider the method of elastotonometry to assess changes in biomechanical properties of the cornea after LASIK and Femto LASIK correction of hyperopia.

1.2 Problem Statement

Elastotonometry is based on sequential measurements of intraocular pressure by Maklakoff tonometers weighting 5; 7.5; 10; and 15 g, then the dependence curve of the tonometric intraocular pressure (IOP) versus tonometer weight is plotted and analyzed.

In the Maklakoff method of measuring the IOP, the tonometer with a flat foundation is placed on the cornea, under this load cornea deforms and the diameter of the imprint created by the contact with instrument is measured. In the present finite element (FE) simulation, the IOP is defined as it used in applanation tonometry by relation $p_t = W/S$, where W is the weight of the tonometer, S is the contact area [9]. The corneoscleral eye shell is modeled as joint spherical segments with different radii and different elastic properties. It is assumed that before loading the composite shell is filled by incompressible liquid with true pressure p . Therefore, the problem of the stress-strain state of soft and close to soft shells under the load with a flat base (tonometer) is solved numerically by selecting such tonometric pressure p_t , at which

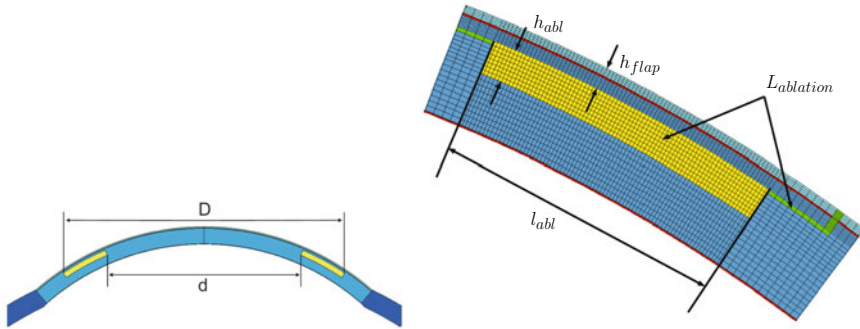


Fig. 1.1 Parameters of the annular layer ablated during LASIK and Femto LASIK correction

the application of the load does not change the internal volume before loading. In the simulation, the intraocular pressure increases due to cornea loading with tonometer, and it is assumed that internal volume remains constant $V = const$, by this means the true IOP is obtained. Nonlinear analysis is performed by means of the engineering simulation software ANSYS Inc. Axisymmetric large deformations are considered.

The FE models of applanation tonometry after refractive surgeries are described in detail in [6, 7]. According to clinical data [3], it is assumed that during LASIK correction an annular layer of the cornea tissue ($L_{ablation}$) is removed with laser beam. During Femto LASIK correction, an annular layer of the same width l_{abl} but with greater inner diameter is removed. The thickness of the corneal flap is taken as parameter h_{flap} , the depth of the removed annular layer as h_{abl} (see Fig. 1.1). The cut of the corneal flap is also simulated as layer $L_{ablation}$.

FE simulation presented in [6, 7] showed that after refractive surgery the bending stiffness of the cornea reduces, which, consequently, reduces the IOP readings obtained by applanation tonometers. It was found that the IOP readings depend on the inner and outer diameters of the annular layer, on the depth of the ablation zone and on the thickness of corneal flap. The changes in the IOP readings obtained by the Maklakoff tonometer were imperceptible. The advantage of refractive hyperopia correction surgeries made by the Femto LASIK method compared to the LASIK method is shown in paper [6, 7]. Because of the fact that during the LASIK surgery the annular layer with smaller inner and outer diameters is ablated and thicker corneal flap is cut, larger deformations and displacements in the thinning region of the cornea, as well as greater decrease of the flexural rigidity of the cornea, is observed.

Clinical data showed that the value of the postoperative IOP increases due to increase in corneal curvature when the initial (preoperative) cornea is flat 40D–42D (diopters) in keratometry, and practically does not change when keratometry before surgery 43D–45D. Therefore calculations in this study are made for eyes with an average radii of curvature 7.5 and 8.4 mm, which correspond to refractive power of the central cornea 40D and 45D.

1.3 Results and Discussion

For presented results the following parameters were taken: the inner diameter of the removed annular (the ablation zone) in LASIK surgery 6.0 mm, in Femto LASIK 6.5 mm; its width l_{abl} 1,375 mm, its depth h_{abl} 172 μ [3]; the thickness of the corneal flap h_{flap} in LASIK 160 μ , in Femto LASIK 110 μ . The thickness of the cornea is assumed to be equal to the average value 520 μ .

The thickness h and elastic moduli of the main layers of the cornea, sclera, and ablation layer are shown in Table 1.1. The elastic moduli of each layer of the cornea

Table 1.1 The thicknesses and elastic coefficients of the cornea, sclera, and ablation layer

Parameter	Epithelium	Bowman's membrane	Stroma	Descemet's membrane	Sclera	Ablation layer
h (mm)	0.04	0.012	0.5	0.01	0.6	0.017 \div 0.172
E (MPa)	0.06	0.6	0.3	0.9	15.0	0.001 \div 0.01

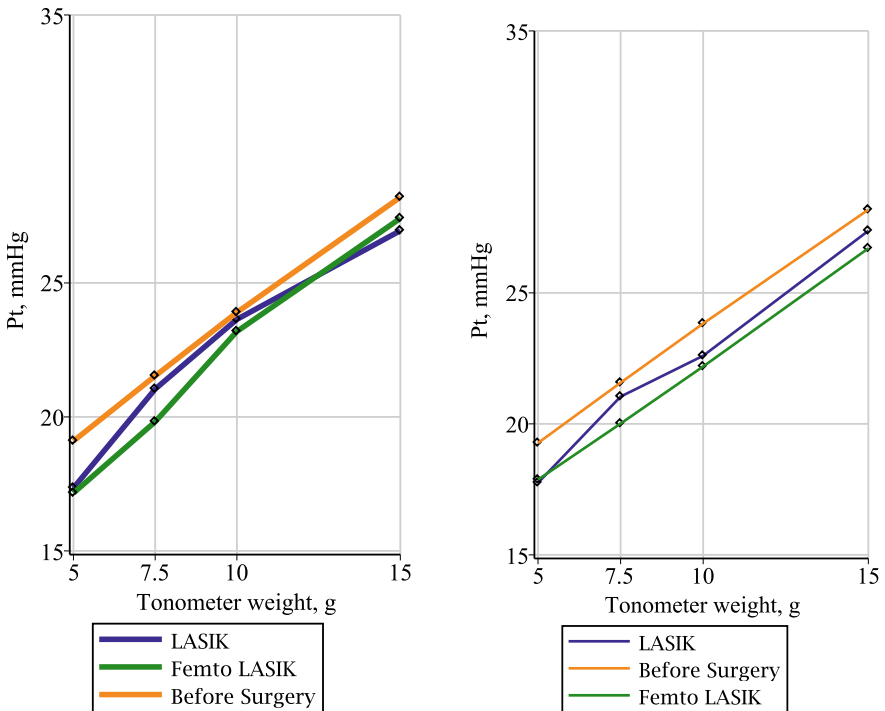


Fig. 1.2 Elastocurves for the eye before and after LASIK and Femto LASIK surgery for the true IOP 15 mmHg and refractive power of the central cornea 40D

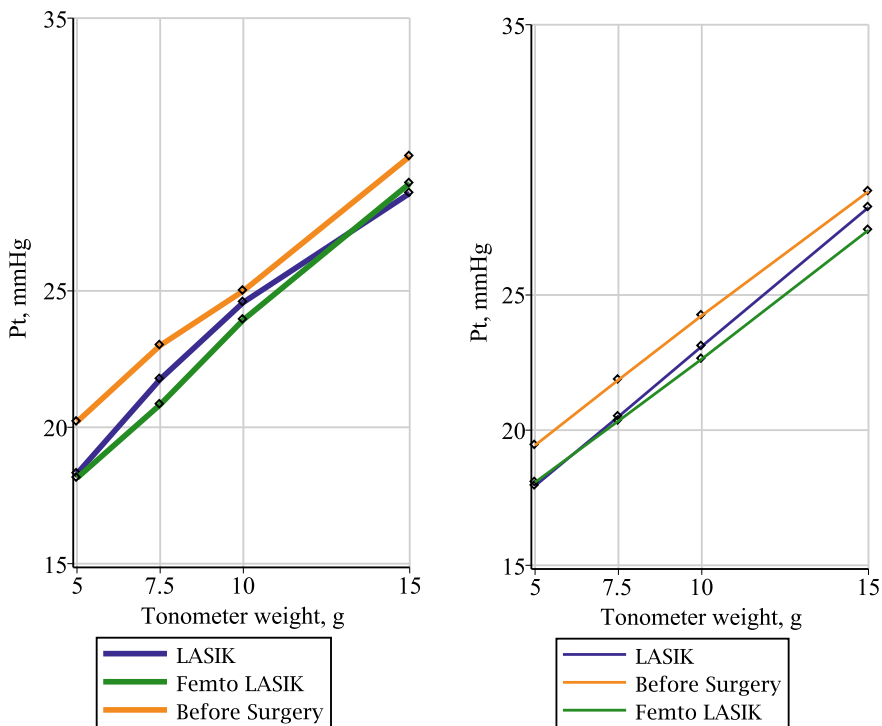


Fig. 1.3 Elastocurves for the eye before and after LASIK and Femto LASIK surgery for the true IOP 15 mmHg and refractive power of the central cornea 45D

in normal direction E' are taken 20 times less than in tangential direction E [8, 9]. Poisson's ratios of the cornea, sclera, and ablation layer at the surface of the isotropy are taken $\nu = 0.49$, in the thickness direction— $\nu' = 0.01$; shear coefficients are $G = E/2(1 + \nu)$ and $G' = G/2$.

The curves for which the IOP is determined from the ratio $p_t = W/S$ (on the left) and corresponds to the Maklakoff IOP and the curves for which the IOP is determined from the condition of constant volume $V = const$ (on the right) and corresponds to the true pressure in the eye, which elevates due to loading with tonometer, are shown in Figs. 1.2, 1.3, 1.4, and 1.5. Results are shown for eyes with average optic power 40D and 45D for the true IOP of 15 and 25 mmHg. Numerical values are presented in Tables 1.2, 1.3, 1.4, and 1.5, respectively.

When analyzing the curve its beginning, range, shape, and the rise of the curve Δ (the difference in readings of the tonometers of larger and smaller weights) are taken into account. The last indicator, according to S.F. Kalfa, can serve as a measure of the elasticity (rigidity) of the eye. In normal eyes the value of IOP at the beginning of the curve does not exceed 21 mmHg, its range is between 7 and 12 mmHg (the average value is 9.9 mmHg), the maximum value does not exceed 30 mmHg. The

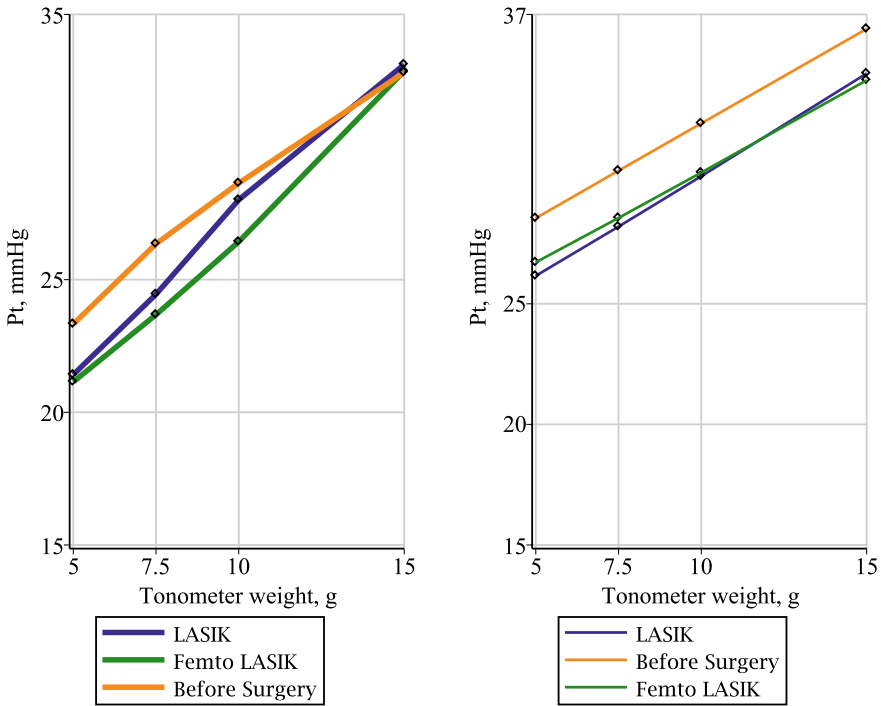


Fig. 1.4 Elastocurves for the eye before and after LASIK and Femto LASIK surgery for the true IOP 25 mmHg and refractive power of the central cornea 40D

form of the normal curve is close to a straight line [9]. The high value of the IOP at the beginning of the curve (above 21 mmHg) and the high brokenness of the curve indicate pathology of the eye.

The calculations show that for the eyes with the average values of the true intraocular pressure (≈ 15 mmHg) the IOP readings obtained by the Maklakoff tonometer are close to the true pressures during loading. For the true IOP greater than 20 mmHg estimations of the tonometric IOP obtained by the Maklakoff tonometer are significantly underestimated, which should be taken into account in clinical practice. In this case, the best approximation gives the results obtained by tonometers with weights 10 and 15 g.

Elastocurves based on tonometric pressure determined from the condition of constant volume $V = const$ show that after LASIK surgery the rise of the curve elevates considerably, while Maklakoff tonometry does not show this effect.

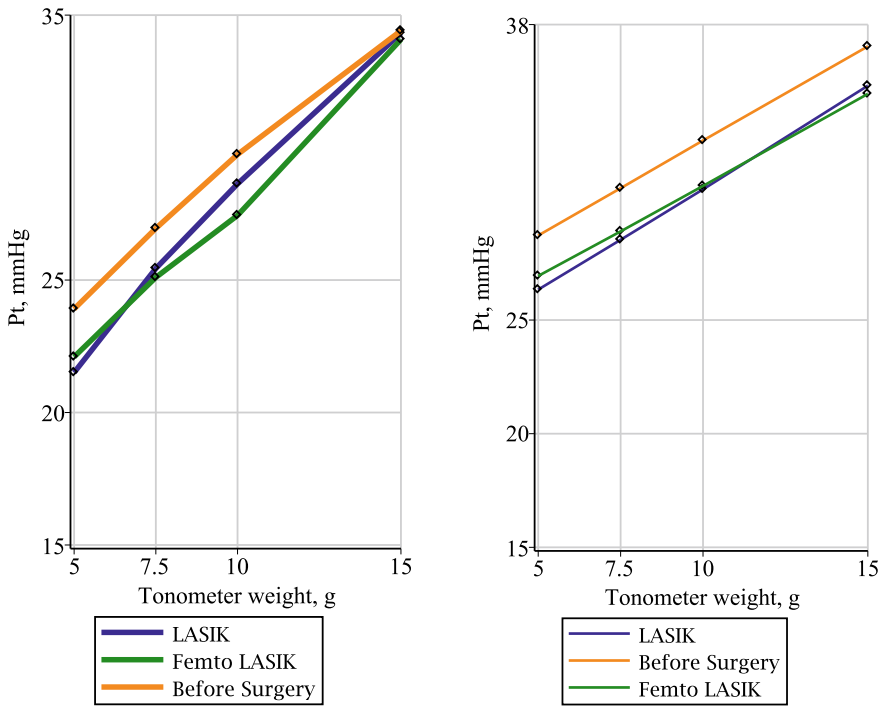


Fig. 1.5 Elastocurves for the eye before and after LASIK and Femto LASIK surgery for the true IOP 25 mmHg and refractive power of the central cornea 45D

Table 1.2 Maklakoff IOP obtained by elastotometry method for the true IOP 15 mmHg, refractive power of the central cornea 40D

Tonometer weight W (g)	Before surgery	LASIK	Femto LASIK
5	19.10	17.35	17.16
7.5	21.53	21.04	19.82
10	23.90	23.64	23.19
15	28.20	26.95	27.41
The rise of the curve Δ (mmHg)	9.10	9.60	10.25

Table 1.3 Maklakoff IOP obtained by elastotonometry method for the true IOP 15 mmHg, refractive power of the central cornea 45D

Tonometer weight W (g)	Before surgery	LASIK	Femto LASIK
5	20.20	18.30	18.14
7.5	23.00	21.76	20.83
10	25.00	24.58	23.94
15	29.93	28.58	28.94
The rise of the curve Δ (mmHg)	9.73	10.28	10.80

Table 1.4 Maklakoff IOP obtained by elastotonometry method for the true IOP 25 mmHg, refractive power of the central cornea 40D

Tonometer weight W (g)	Before surgery	LASIK	Femto LASIK
5	23.33	21.42	21.15
7.5	26.35	24.45	23.68
10	28.64	28.01	26.43
15	32.81	33.11	32.86
The rise of the curve Δ (mmHg)	9.48	11.69	11.71

Table 1.5 Maklakoff IOP obtained by elastotonometry method for the true IOP 25 mmHg, refractive power of the central cornea 45D

Tonometer weight W (g)	Before surgery	LASIK	Femto LASIK
5	23.91	21.51	22.10
7.5	26.95	25.44	25.10
10	29.74	28.63	27.44
15	34.41	34.32	34.08
The rise of the curve Δ (mmHg)	10.5	12.81	11.98

1.4 Conclusion

The results of the numerical simulation show that after surgical correction of hyperopia flexural rigidity of the cornea reduces therefore the rise of the elastocurve increases. For the elevated IOP, the stronger rise of the curve is observed. After LASIK surgery, the rise of the curve increases considerably due to elevation of the true IOP, while in the preoperative state and after Femto LASIK this change is not significant. For the last two cases, the dependencies of the IOP readings obtained by the

Maklakoff method on the tonometers weights almost linear. This may be explained in such a way: after LASIK surgery the larger deformations and displacements in the thinning region of the cornea are observed, which indicates the greater decrease in the flexural rigidity of the cornea [9].

When tonometer overlaps the ablation zone (after LASIK it occurs at a load of 10 g, after Femto LASIK at a load close to 15 g), the contact area begins to grow rapidly and the tonometric pressure starts to decrease, as a result the LASIK curve becomes broken. The last data obtained in the Cheboksary branch of S. Fyodorov Eye Microsurgery Federal State Institution (in Russian Federation) also confirm the smoother behavior of the elastocurves after Femto LASIK surgery. Brokenness of the curve can also occur since with a small load 5 and 7.5 g the sclera does not affect the measurements, but at a load of 10 g sclera starts to affect the IOP readings. At a load of less than 10 g, the IOP readings obtained after LASIK (due to large deformations in the thinning region of the cornea) are slightly higher than the IOP readings obtained after Femto LASIK. Estimations of the IOP readings obtained by the Maklakoff tonometer for the average values of the true intraocular pressure (≈ 15 mmHg) are close to the true pressure during loading. IOP estimations obtained for the true intraocular pressures greater than 20 mmHg are significantly underestimated and the best approximation for the IOP readings give tonometers with weights 10 and 15 g.

Acknowledgments This research was supported by the Government of Russia, grant No. 14.Z50.31.0046.

References

1. Iomdina, E.N., Bauer, S.M., Kotlyar, K.E.: Biomechanics of the human: theoretical aspects and clinical applications. Real Time, Moscow (2015)
2. Shevchenko M.V., Bratko O.V., Shugurova N.E.: Clinical evaluation of biochemical parameters of the fibrous capsule in patients with glaucoma and myopia. *Izvestiya of the Samara Russian Academy of Sciences Scientific Center. Social, Humanitarian, Medicobiological Sciences* **17**, 898–903 (2015)
3. Fedotova, L.A., Kulikova, I.A.: The advantage of the treatment of hyperopia using femtosecond laser. *Health Care Chuvashia* **2**, 47–50 (2009)
4. Avetisov, S.E., Bubnova, I.A., Antonov, A.A.: Variability in biomechanical properties of the fibrous tunic of the eye in a healthy population. *Vestnik oftal'mologii* **5**, 20–24 (2015)
5. Shevchenko, M.V., Bratko, O.V.: Evaluation of biomechanical peculiarities of fibrous eye layer in myopia and glaucoma. *Russ. Med. J.* **4**, 124 (2011)
6. Bauer, S.M., Venatovskaia, L.A.: Biomechanical analysis of the human eye after the surgical correction of hyperopia. In: Petrosyan, L.A., Zhabko, A.P. (eds.) 2015 International Conference on “Stability and Control Processes” in Memory of V.I. Zubov (SCP), pp. 513–515. IEEE Inc., New York (2015). Article number 7342200
7. Bauer, S.M., Venatovskaya, L.A.: Analysis of stress-strain state of a human eye by the method of elastotonometry after the surgical correction of hyperopia. In: Kustova, E.V., Leonov, G.A., Yushkov, M.P., Morosov, N.F., Mekhonoshina, M.A. (eds.) International Scientific Conference on Mechanics: 8th Polyakhov’s Reading. American Institute of Physics Inc., New York (2018). Article number 090001

8. E. Iomdina: Mechanical properties of the human eye tissues. In: Shtein A., Tsaturyan A. (eds) *Modern Problems of Biomechanics*, Iss. 11: *Biomechanics: Achievements and Prospects*, pp. 184–201. Moscow University Press, Moscow (2006)
9. Nesterov, A., Bunin, A., Katsnelson, L.: *Intraocular Pressure. Physiology and Pathology*. Nauka, Moscow (1974)

Chapter 2

Deformation and Fracture of Titanium Alloys Under Dynamic Loading



Anatolii M. Bragov, Leonid A. Igumnov, Aleksandr Yu. Konstantinov,
and Andrey K. Lomunov

Abstract The paper presents the results of dynamic tests of some titanium alloys. The tests for compression, tension, and shear were carried out using the Kolsky method and its modifications. In addition, a technique for determining the dynamic coefficient of friction, based on the Kolsky method, was implemented. As a result of the tests, dynamic, and static strain diagrams were plotted. Ultimate strength dependencies versus strain rate (yield stress σ_{02} , ultimate tensile strength σ^B , ultimate plasticity characteristics, axial strain δ and lateral strain ψ at fracture) were determined on the basis of the diagrams. The positive sensitivity of the strength characteristics to the strain rate was noted for the tested materials. At the strain rates more than $5 \times 10^2 \text{ s}^{-1}$ the intensive growth of the strength characteristics is observed. The ultimate plasticity characteristics weakly depend on the strain rate. For the titanium alloy, the value of the dynamic coefficient of friction was obtained, which turned out to be close to its static value. The parameters of the well-known Johnson-Cook model were calculated using the obtained data. Verification experiments were performed, the results of which were compared with the results of virtual (computational) experiments. Good qualitative and quantitative agreement between experimental and numerical results was noted.

Keywords Titanium alloys · Strain rate · Experimental investigation · Plastic deformation · Identification · Verification · Temperature softening · Material model · Tension · Compression · Ultimate strain · Dynamic friction

A. M. Bragov (✉) · L. A. Igumnov · A. Yu. Konstantinov · A. K. Lomunov
Research Institute for Mechanics, National Research Lobachevsky State University of Nizhny
Novgorod, Gagarin Ave. 23, 603950 Nizhny Novgorod, Russia
e-mail: bragov@mech.unn.ru

L. A. Igumnov
e-mail: igumnov@mech.unn.ru

A. Yu. Konstantinov
e-mail: konstantinov.al@yandex.ru

A. K. Lomunov
e-mail: lomunov@mech.unn.ru

2.1 Introduction

At present, the necessity of numerical modeling at the early stages of designing new technology objects is beyond doubt. In addition to reduce the design time, mathematical modeling allows one to significantly optimize the developing design. This is due to the possibility to analyze a larger number of configurations (geometry, materials, connection methods, etc.), as well as operating conditions relative to the traditional design. It should be noted that numerical methods and modern computational resources make it possible to accurately solve complex systems of mathematical equations, which describe the processes occurring in a structure under the influence of certain factors, as well as to describe the behavior of materials with complex nonlinear mathematical models and to account for geometric and physical nonlinearity. It should be noted that the accuracy of the numerical solution is mainly determined by the accuracy of the input data, one of the important components of which are mathematical models of material behavior. Some structures and structural elements during operation may be subjected to intensive impact or explosive loads. Such situations can arise both as a result of abnormal emergencies resulting from human errors, faults of equipment, natural effects, and as a result of targeted human actions. Some of the structural elements, due to their functional purpose, are designed to reduce the effects of pulse loads (for example, passive and active vehicle safety systems, protective containers for the transport of hazardous substances, striking elements such as bullets and projectiles, etc.). To equip and verify phenomenological behavior models used in the calculation of the stress–strain state, an extensive database on the dynamic properties of materials is required. In the field of dynamic testing of materials, there are practically no standardized test methods and commercially available test equipments. It should be noted that the dynamic properties of a number of traditional and, especially, new materials have not been studied enough. Therefore, the design of these critical objects of automotive, aviation, energy, and other types of equipment is performed using static properties (or data of well-known foreign analogues), which leads to the irrational design of structures experiencing pulse loads. In this regard, the methodological study of high-speed deformation and failure of practically important structural materials is an essential and high-demand task.

2.2 Methods of Experimental Research

The most popular tool for studying the processes occurring in samples under high rate loading is currently a technique based on the use of measuring bars, known as the Split Hopkinson Pressure Bar (SHPB) method [1]. In the review papers [2, 3], numerous bibliography describing the history of this method is presented. The working range for the strain rate of this method is from 10^2 to 10^4 c^{-1} . The SHPB method is relatively easy to implement and is well-grounded in terms of theory.

2.2.1 Tests of Samples Under Uniaxial Compression

The use of a split Hopkinson bar for compression tests was first proposed by Davis [4, 5] and almost simultaneously by Kolsky [6]. The mathematical model of the SHPB is a system of three bars: two “hard” and long thin bars and a “soft”, short sample between them (Fig. 2.1). In one of the bars, a one-dimensional elastic compression wave $\varepsilon^I(t)$ is generated by the impact of the striker. This wave propagates through the bar at a velocity C . When the sample is reached, the wave is splitted up due to the difference in acoustic stiffness ρC of the bar and sample materials, as well as the areas of their cross sections. A part of it is reflected back $\varepsilon^R(t)$, and the other part passes through the sample into the second bar as a compression wave $\varepsilon^T(t)$. At the same time, the specimen undergoes an elastic–plastic deformation, while the bars are elastically deformed. The amplitudes and shapes of pulses $\varepsilon^R(t)$ and $\varepsilon^T(t)$ are determined by the ratio of the acoustic stiffness of the bars and sample materials, as well as the response of the sample material to the applied dynamic load. By registering using the strain gauges the elastic deformation pulses in measuring bars, using the formulas proposed by Kolsky, one can determine stresses, deformations, and strain rates in a sample as a function of time.

We will give, without deriving, the basic relations that allow us to determine the strain rate, strain, and stress histories in the sample based on the signals recorded in the measuring bars [6]:

$$\dot{\varepsilon}_s(t) = \frac{1}{L_0} (C^I (\varepsilon^I(t) - \varepsilon^R(t)) - C^T \varepsilon^T(t))$$

$$\varepsilon_s(t) = \int_0^t \dot{\varepsilon}_s(\tau) d\tau$$

$$\sigma_s(t) = \frac{1}{A_0} E^T A^T \varepsilon^T(t)$$

here, A_0 , L_0 are initial cross-sectional area and sample length; C^I , E^I , A^I , C^T , E^T , A^T are bar sound speed, modulus of elasticity, and cross-sectional area of loading (with index I) and supporting (with index T) bars, respectively.

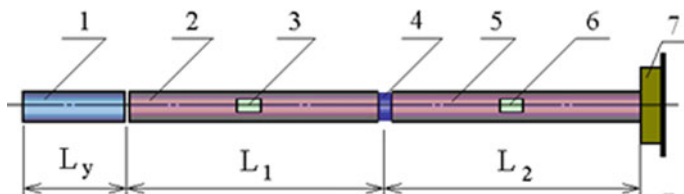


Fig. 2.1 Experimental setup: 1—striker; 2—incident bar; 3, 6—strain gauges, 4—specimen; 5—support bar; 7—damper

It should be noted that these are the so-called “technical” values, since the strength and elongation here are related to the initial dimensions of the sample. To construct a true strain diagram for large strains, the stress and strain values are corrected. True stress is calculated by the formula:

$$\sigma_S^T(t) = \sigma_S(t) \cdot (1 - \varepsilon_S(t))$$

The true (logarithmic) deformation is determined by the expression:

$$\varepsilon_S^T(t) = \ln(1 - \varepsilon_S(t))$$

The true strain rate is calculated as follows:

$$\dot{\varepsilon}_S^T(t) = \frac{\dot{\varepsilon}_S}{1 - \varepsilon_S(t)}$$

Then, from the obtained parametric dependences $\sigma_S(t)$, $\varepsilon_S(t)$ and $\dot{\varepsilon}_S(t)$, time is excluded as a parameter, and a deformation diagram $\dot{\varepsilon}_S \sim \varepsilon_S$ of a specific sample with a known dependence is constructed, which is used to control the change in the strain rate in the process of deformation or to evaluate the influence of the history strain rate on the deformation diagram of the sample under loading with a pulse of complex shape.

2.2.2 Shear Experiments

To obtain deformation diagrams under shear conditions, a modification of the SHPB was proposed [7]. The experimental setup is shown in Fig. 2.2.

In the process of testing, a sample of a special form is loaded as usual in the “loading bar—supporting tube” system (Fig. 2.3).

The time dependence of the shear strain is determined by the expression:

$$\gamma(t) = \frac{\int_0^t (C^I \cdot (\varepsilon^I(\tau) + \varepsilon^R(\tau)) - C^T \cdot \varepsilon^T(\tau)) d\tau}{h}$$

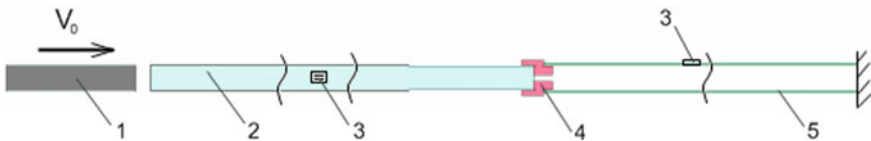


Fig. 2.2 Experimental setup for shear testing: 1—striker, 2—loading bar, 3—strain gauge, 4—ring sample, 5—supporting tube

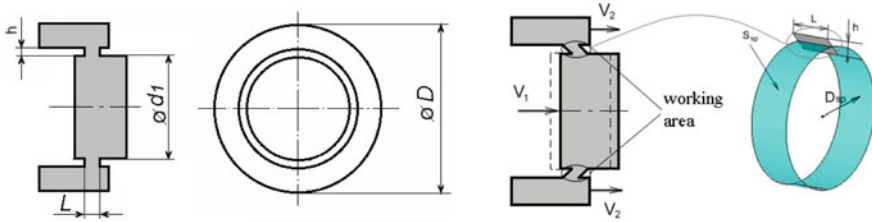


Fig. 2.3 Sample on ring shear

here, h is the height of the working part of the sample.

The shear stress on the basis of the pulse recorded in a supporting tube is determined by the formula:

$$\tau(t) = \frac{E \cdot A \cdot \varepsilon^T(t)}{\pi \cdot D_{sp} \cdot L}$$

here $D_{sp} = \frac{d_1 + (d_1 + 2 \cdot h)}{2} = d_1 + h$, E and A are elastic modulus and cross-sectional area of a measuring tube.

To compare the diagrams obtained in the test with diagrams, which were obtained under tension and compression, it is necessary to use the equivalent values of strain and stress using the Mises criterion:

$$\varepsilon_{\text{eqv}} = \frac{\gamma}{\sqrt{3}}$$

$$\sigma_{\text{eqv}} = \sqrt{3} \cdot \tau$$

2.2.3 Determination of the Dynamic Characteristics of Friction

To determine the dynamic coefficient of friction, a simple but effective method was proposed [7, 8] based on the modified Kolsky method with the use of a measuring tube instead of a supporting bar (Fig. 2.4).

In the experiments, a stressful connection (tight fit) of two parts (core sleeve and female jacket) with guaranteed contact preloading is used. Details cover each other with contact on a cylindrical surface. Prestressing can be implemented by mechanical pressing or thermal fit. It is preferable to use thermal fit, since in this case the microrelief of the surface of the mating elements remains almost unchanged. When using a thermal fit due to the difference in diameters of the female and male parts before assembly, some (controlled) prestress is created (negative clearance).

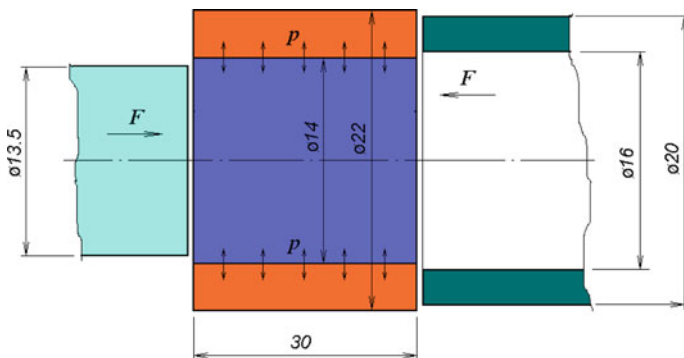


Fig. 2.4 Experimental scheme of dynamic “pressing-out”

The contact between the mating parts occurs on a cylindrical surface with a diameter d and a length l . The magnitude of the negative clearance δ is determined by taking into account the difference in the diameters of the female and male parts.

The pressure p on the contact surface for the assembly as shown in Fig. 2.4 is connected with the δ by formulas:

$$p = \frac{\delta}{\left(\frac{c_1}{E_1} + \frac{c_2}{E_2}\right) \cdot d}$$

$$c_1 = \frac{d^2 + d_1^2}{d^2 - d_1^2} - \nu_1$$

$$c_2 = \frac{d_2^2 + d^2}{d_2^2 - d^2} + \nu_2$$

here, E_1 and E_2 are the moduli of longitudinal elasticity, ν_1 and ν_2 are the values of the Poisson's ratio of female and male details, respectively. The inner diameter of the sleeve in the experiments $d_1 = 0$. In this case, the formula for calculating p is simplified.

The axial force F is determined when the assembly is loaded between the ends of the split Hopkinson bar (similar to the extrusion process) using the formula:

$$F = EA_b \varepsilon_t(t)$$

where E and A_b are, respectively, the modulus of elasticity and the cross-sectional area of the supporting bar (tube); $\varepsilon_t(t)$ is the transmitted deformation pulse.

The friction coefficient μ at axial force F and pressure p on the contact surface is determined as follows:

$$\mu = \frac{F}{p\pi dl}$$

where d is the diameter of the mating surface and l is its length.

Numerical analysis and justification of the described experimental scheme are carried out in [7].

2.2.4 Determining the Deformation Curves and Strength Characteristics Under High-Speed Tension

The classical version of the SHPB for compression tests is the most studied and theoretically justified, however, this type of testing does not allow determining the number of practically important strength characteristics of materials, such as ultimate tensile stress and ultimate characteristics of plasticity. In addition, the behavior of a material can significantly differ from various types of stress–strain state, therefore, the determination of deformation diagrams under tension is also an important stand-alone task. Various experimental setups for dynamic tension of samples designed by using the technique of measuring bars are described in [9–14]. The main difference between these modifications is in the method of generating a tensile pulse load.

In the present work the well-known Split Hopkinson Tension Bar method [15] was used to register the processes in the samples during high strain rate tensile experiments. Scheme of a setup with a gas gun for creating a direct tensile wave in the split Hopkinson pressure bar is shown in the Fig. 2.5. Sample 1 was fixed in measuring bars 2 and 3 using a threaded joint 4. Recording of strain pulses in bars was carried out by gauges 5. Loading tensile pulse 5 was formed by the impact of the tubular striker 6 on the anvil 8. Acceleration of the striker 6 in the barrel 7 was due to the compressed air energy 9, which was supplied when the pneumatic valve 10 was opened. The strain pulses in loading and output bars were used to obtain forces acting on the specimen during the experiment and history of the specimen's interface displacements. These values were calculated using formulas proposed by Kolsky.

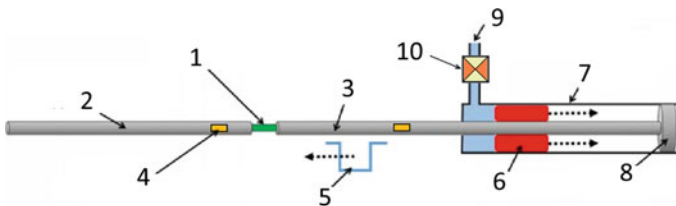


Fig. 2.5 Scheme of a setup with a gas gun for creating a direct tensile wave

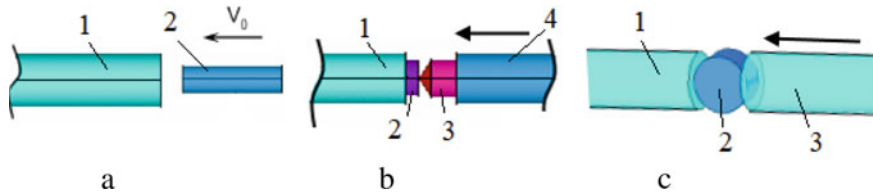


Fig. 2.6 Verification experiments

2.2.5 High-Temperature Experiments

For testing at elevated temperatures (≤ 350 °C), a compact tube-type stove was used, which was put on the measuring bars in the sample installation area. To control the sample temperature, an HC thermocouple was used.

2.2.6 Verification Experiments

According to the results of the experimental studies carried out using the developed program, the parameters of mathematical models that are part of the software systems for calculating the stress–strain state and strength of dynamically loaded structures and their elements are determined.

To test mathematical models, a system of experiments for the verification has been developed [16] (Fig. 2.6): a modified Taylor test (a), dynamic penetration of indenters with conical and hemispherical head parts (b), and high-speed diametric compression of viscoplastic samples (c), which uses measuring bars to register the force response of samples to dynamic deformation in the process of loading as a function of time. These data are used together with the residual form of the samples after dynamic loading when comparing the results of virtual and field experiments. In Fig. 2.6a, the numbers indicate as follows: 1—measuring bar; 2—Taylor bar. In Fig. 2.6b: 1 and 4—measuring bars; 2—sample; 3—indenter. In Fig. 2.6c: 1 and 3—measuring bars; 2—sample.

2.3 Experimental Results

2.3.1 Deformation Curves

Using an experimental setup [17] with a split Hopkinson pressure bar (SHPB), samples made of titanium alloys VT6, VT8, and VT20 were tested. The effect of the strain rate and temperature on the material deformation diagram was studied. It is usually not possible to obtain the compressive strength characteristics of metallic

materials, which, as a rule, have significant plastic properties, therefore, the results of dynamic tests under uniaxial tension are used to assess the strength characteristics and ultimate plasticity characteristics δ and ψ . All tests were carried out on high-strength steel measuring bars with a diameter of 20 mm. For loading a steel striker of 300 mm long was used, which was accelerated to the required speed in the barrel of a 20 mm caliber gas gun.

Figures 2.7, 2.8, 2.9, 2.10, 2.11, and 2.12 show the average diagrams of titanium alloys VT6, VT8, and VT20, obtained at different temperature-speed test modes.

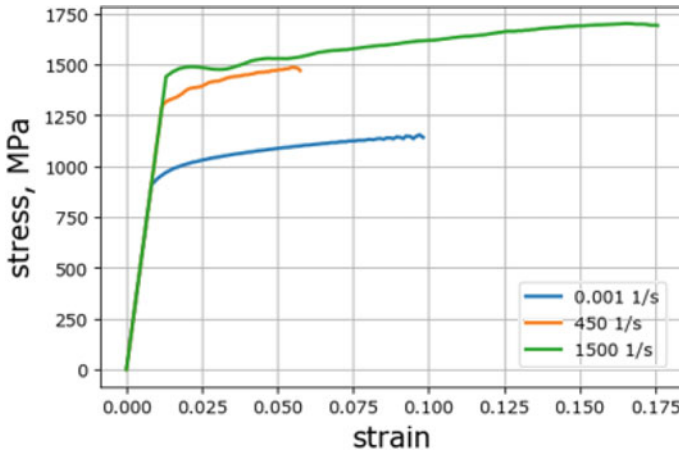


Fig. 2.7 VT6. Strain rate dependence

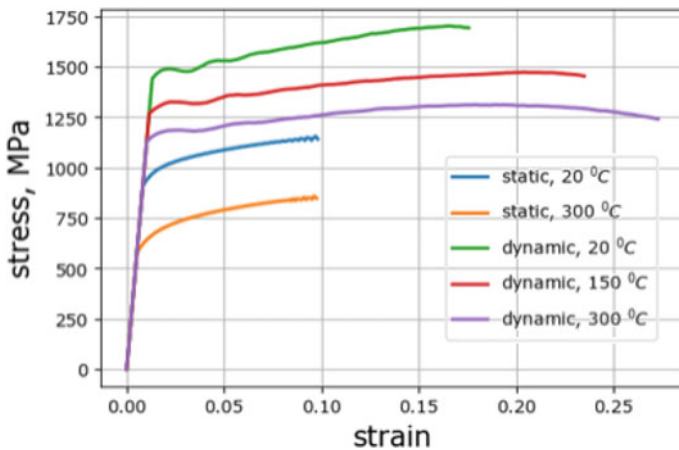


Fig. 2.8 VT6. Temperature dependence

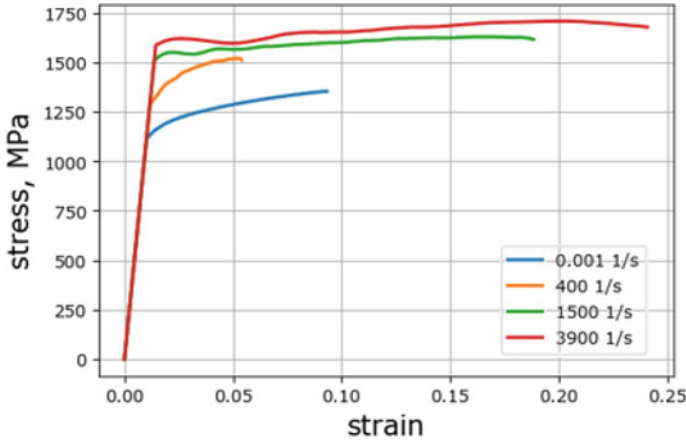


Fig. 2.9 VT8. Strain rate dependence

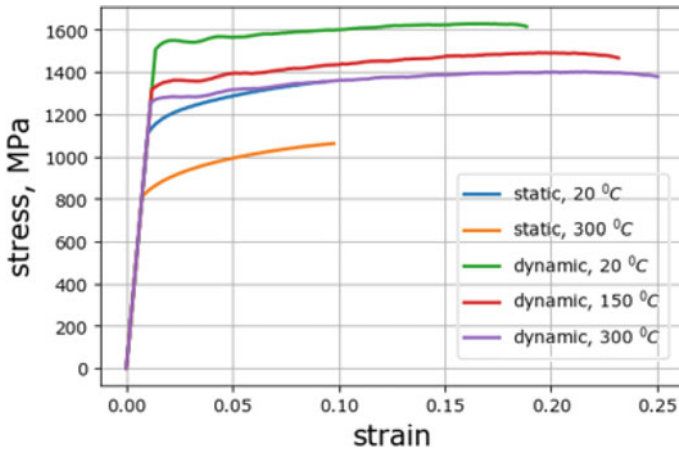


Fig. 2.10 VT8. Temperature dependence

It is clearly seen that both the strain rate and temperature have a significant effect on the dynamic properties of the studied alloys: the flow stress increases with increasing strain rate, while with increasing temperature it decreases.

Figure 2.13 compares the plastic parts of the deformation curves of the tested alloys. It can be seen that the slopes of the VT8 and VT20 titanium curves are very close, however, the flow stress for the VT20 alloy was 15% lower. VT6 alloy has a large strain hardening compared to other materials.

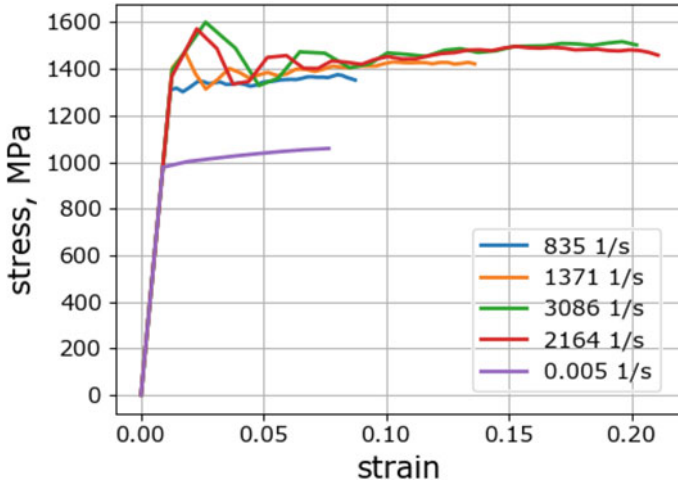


Fig. 2.11 VT20. Strain rate dependence

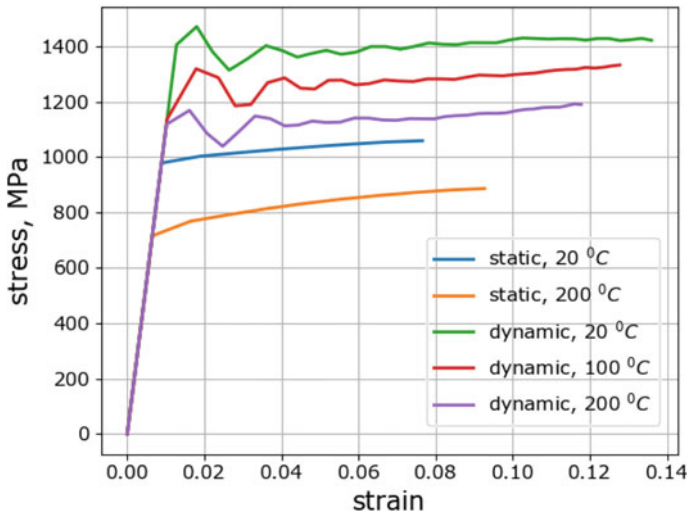


Fig. 2.12 VT20. Temperature dependence

2.3.2 Ultimate Failure Characteristics

The ultimate characteristics of plasticity of VT6, VT8, and VT20 alloys were determined in high strain rate tests. The loading mode was varied by changing the initial velocity of the striker. The ultimate failure characteristics (elongation after rupture δ and relative narrowing after rupture ψ) were determined by measuring the sample after the test as follows:

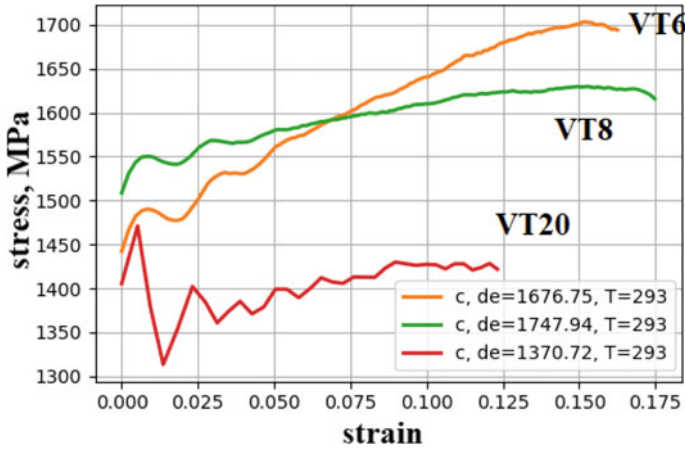


Fig. 2.13 Comparison of different materials

$$\delta = \frac{l - l_0}{l_0} \cdot 100\%$$

$$\psi = \frac{d_0^2 - d^2}{d_0^2} \cdot 100\%$$

where l_0 and l are the initial length of the working part of the sample and the length of the working part of the sample after the test, respectively, d_0 и d are the initial diameter of the sample and the diameter of the sample in the neck after rupture.

The ultimate plastic deformation of fracture can be estimated by the formula [7]:

$$\varepsilon_p^f = \ln\left(\frac{100}{100 - \psi}\right)$$

Figures 2.14, 2.15, and 2.16 show the rate and temperature dependences of the ultimate plastic strain for the studied alloys.

It is seen that with increasing strain rate and temperature, a slight increase in ultimate plastic strain occurs.

Figure 2.17 compares the strain rate dependences of the ultimate plastic deformation of different materials. It can be noted that in the dynamic range of strain rates the failure of the studied materials occurs at similar values of plastic deformation. According to static tests, the most fragile is VT6 alloy, while the most plastic is the VT8 alloy.

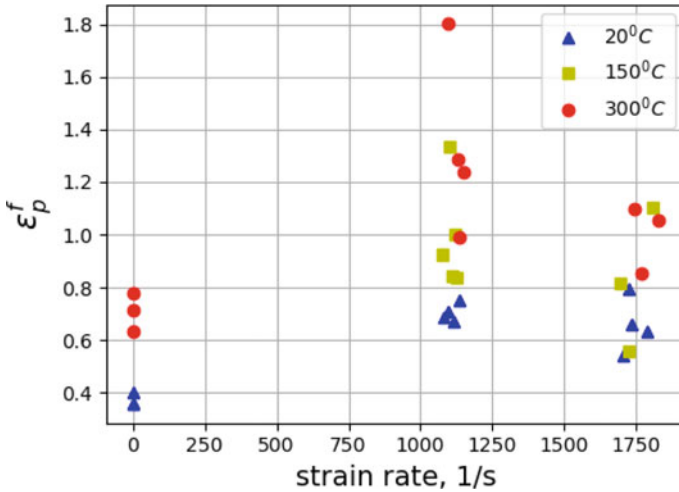


Fig. 2.14 The rate and temperature dependences of the ultimate plastic strain for VT6

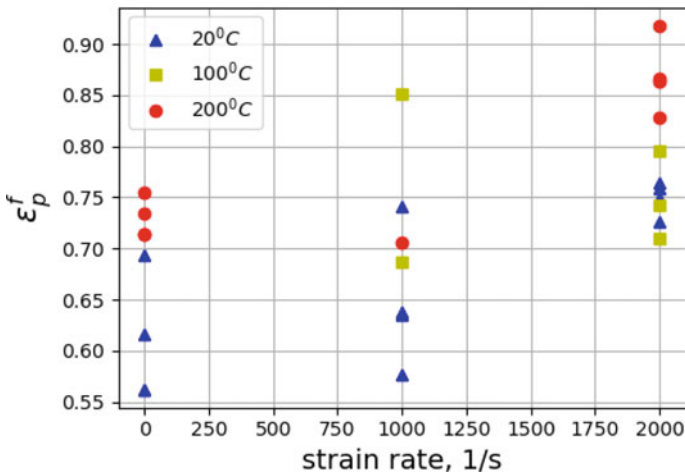


Fig. 2.15 The rate and temperature dependences of the ultimate plastic strain for VT8

2.3.3 Results of the Study of Dynamic Friction

To determine the dynamic coefficient of friction, a modification of the SHPB, previously described and specially designed, and the samples, in the form of “core-jacket” with a tight thermal fit with a guaranteed interference, were used. Tests for pairs VT-6-VT-6 and VT-6-AK4-1 were carried out at different temperatures. In assemblies of the second type, the core was made of titanium alloy, and the jacket was made of aluminum. To assess the influence of the contact pressure of the rubbing surfaces on

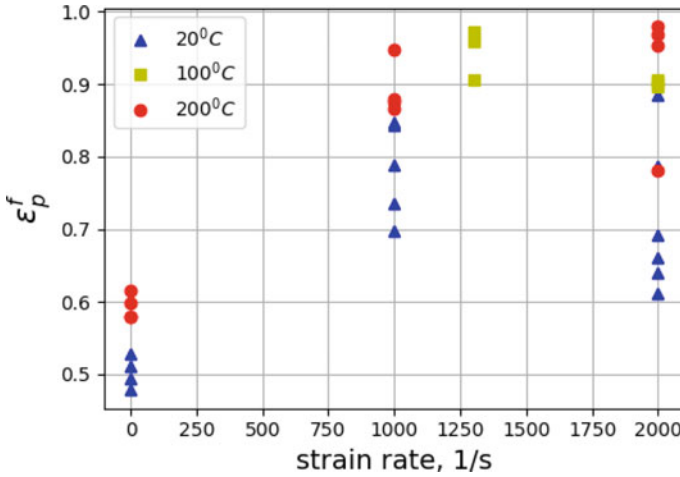
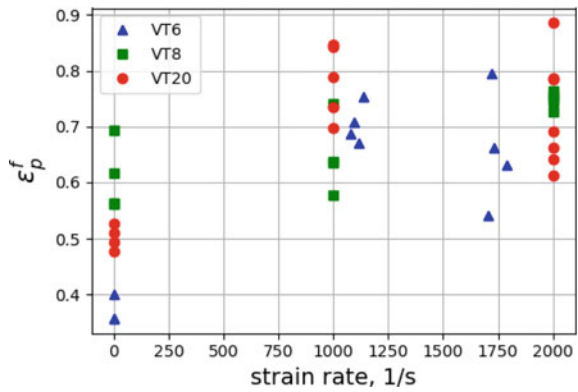


Fig. 2.16 The rate and temperature dependences of the ultimate plastic strain for VT20

Fig. 2.17 Materials comparison



the friction coefficient, assemblies with different preloads (from 0.014 to 0.028 mm negative clearance) are tested. The core diameter averaged ~ 14 mm, the outer diameter of the jacket was 20 mm, and the length of the core was equal to the length of the jacket and was 15 mm.

It should be borne in mind that when assemblies made of different metals are heated, the value of the initial static preload will change, since the coefficient of linear thermal expansion α for the components of the assembly may be different.

The radial displacement of the points of a hollow cylinder subjected to temperature loading can be described by the expression:

$$U_r = \frac{1 + \nu}{1 - \nu} \cdot \frac{\alpha}{r} \cdot \left[\int_a^r \Delta T \cdot r \cdot dr + \frac{(1 - \nu) \cdot r^2 + a^2}{b^2 - a^2} \cdot \int_a^b \Delta T \cdot r \cdot dr \right]$$

where ν and α are Poisson’s ratio and linear temperature expansion coefficient of cylinder material, respectively, a and b are inner and outer cylinder radii, ΔT is temperature increment. If we consider the temperature field within the sample volume to be constant, which is the case with prolonged (static) heating of the assembly, then this formula is much simpler and allows one to determine the change of the cylinder radius R (outer radius for the insert and the inner radius of the holder) when changing temperature ΔT :

$$\Delta R = \frac{1}{2} \cdot \frac{(1 + \nu) \cdot (2 - \nu)}{1 - \nu} \cdot \alpha \cdot \Delta T \cdot R$$

Based on this formula, it is possible to determine the dimensions of the parts constituting the assembly after heating. For titanium–titanium assemblies, the value of the initial tension when heated remains almost unchanged, since the components of the assembly have the same coefficients of linear temperature expansion. However, for the titanium–aluminum assemblies, it is completely different. The coefficient of temperature expansion for aluminum ($\alpha = 22 \times 10^{-6} \text{ deg}^{-1}$) is more than twice as many as the corresponding value for titanium ($\alpha = 8.9 \times 10^{-6} \text{ deg}^{-1}$), therefore when the assembly is heated, “titanium–aluminum” with tightness = 0.03 mm (which corresponds to the maximum interference) up to 200 °C due to different temperature deformations, this tension disappears, moreover, a gap of ~0.02 mm appears between its parts. The critical temperature at which the tension value of $\delta = 0.03 \text{ mm}$ disappears completely is ~130 °C. In this regard, tests of titanium–aluminum assemblies were carried out at elevated temperatures only with maximum tension and only at temperatures of +75 °C and +100 °C.

A characteristic view of the force, recorded in the measuring tube, as a function of time is shown in Fig. 2.18. According to the obtained dependences, the sliding forces F_{sl} were determined (some average value in the time range of 35–55 μs). It should be noted that the magnitude of sliding friction is determined rather arbitrarily, since the

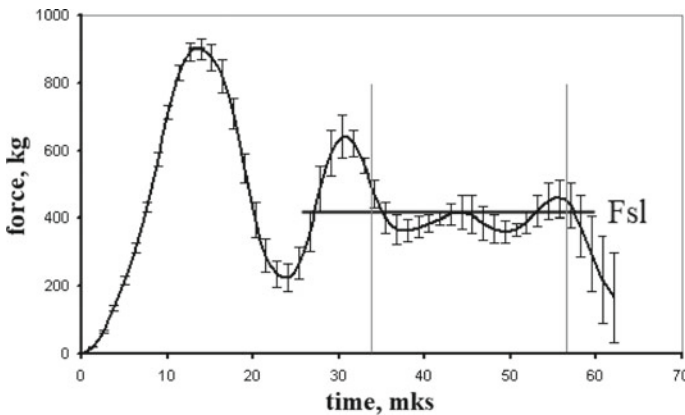


Fig. 2.18 Sliding force determination

sliding process itself is unstable and has stick-slip nature. It consists of several cycles of stress accumulation on the contact surface, shear components of the assembly with the discharge of stresses, motion stop, stress re-accumulation, etc.

Further, for certain values of F_{sl} , for a known fit, the friction coefficients are calculated as $\mu_{sl} = \frac{F_{sl}}{P \cdot S}$ where P is the known seating pressure, S is the contact surface area of the core and the jacket.

The values of the friction coefficients obtained at normal and elevated temperatures for titanium–aluminum pairs are shown in Figs. 2.19 and 2.20. In Fig. 2.20 blue markers indicate the results obtained at room temperature, the red ones at a temperature of 200 °C.

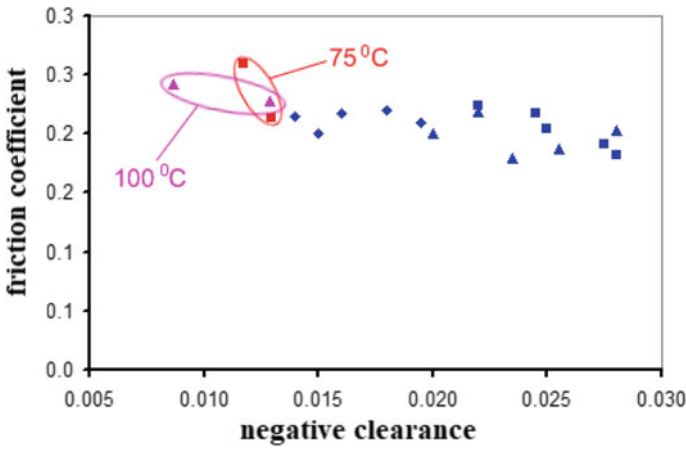


Fig. 2.19 Friction coefficients for Ti–Al pair

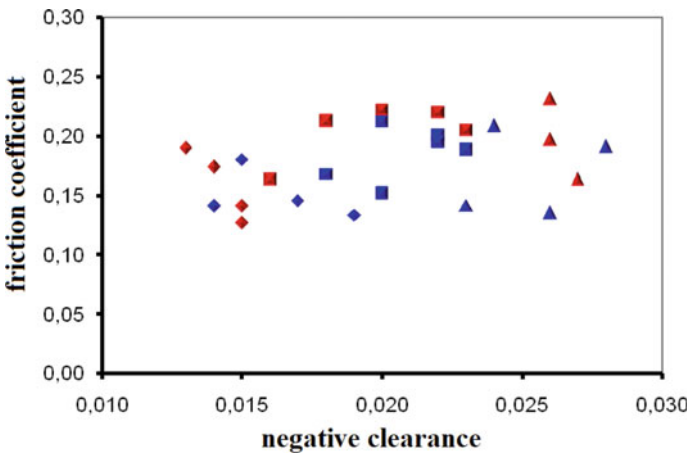


Fig. 2.20 Friction coefficients for Ti–Ti pair

Table 2.1 Friction coefficients

Pair of materials	Room temperature	High temperature
«Ti–Al»	0.205	0.236
«Ti–Ti»	0.17	0.187

It can be seen from the figures that in the studied range of loads, the coefficient of sliding friction is practically independent of either the prestress value or the temperature.

Table 2.1 shows the average values of the dynamic coefficient of friction.

2.4 Modeling the Properties of the Materials

According to the results of experimental studies of the behavior of titanium alloys under static and dynamic loading, the parameters of the Johnson-Cook model were determined. In this model, the yield stress is determined as a function of plastic strain, strain rate and temperature, and has the form [18]:

$$\sigma = (A + B \cdot \varepsilon_p^n) \cdot f_2(\dot{\varepsilon}^*) \cdot \left(1 - \frac{T - T_0}{T_m - T_0}\right)$$

The multiplier characterizing the strain rate hardening can take one of the following forms:

- Johnson-Cook's classic formulation [18]:

$$f_2 = 1 + C \cdot \ln(\dot{\varepsilon}^*)$$

- Hugh Kang model [19]:

$$f_2 = 1 + C \cdot \ln(\dot{\varepsilon}^*) + C_2 \cdot \ln(\dot{\varepsilon}^*)^2$$

- Alain-Rule-Jones model [20]:

$$f_2 = (\dot{\varepsilon}^*)^C$$

- Cooper-Simonds model [21]

$$f_2 = 1 + \left(\frac{\dot{\varepsilon}^*}{C}\right)^{\frac{1}{p}}$$

Since in the Johnson-Cook equation the effects of plastic strain hardening, strain rate hardening, and temperature softening are multiplied, this model poorly describes

diagrams in which the slope of the plastic part decreases with increasing strain rate, because the function f_2 scales as A (flow stress at zero plastic deformation) and B (responsible for the slope of the plastic part of the curve). Therefore, a modification is additionally considered, which is mathematically expressed by the equation:

$$\sigma = \sigma_A + B \cdot e^{-(\beta_0 - \beta_1 \ln(\dot{\varepsilon}))T} + A \cdot \varepsilon^n \cdot e^{-(\alpha_0 - \alpha_1 \ln(\dot{\varepsilon}))T}$$

where $\sigma_A, B, \beta_0, \beta_1, A, n, \alpha_0, \alpha_1$ are model parameters.

The parameters for the investigated alloys obtained by the approximation of experimental results are summarized in Tables 2.2, 2.3, 2.4, and 2.5.

The deviation of the mathematical model from the experimental data is characterized by the parameter R^2 , which is calculated by the formula:

$$R^2 = 1 - \frac{\sum (Y_i - \hat{Y}_i)^2}{\sum Y_i^2 - \frac{(\sum Y_i)^2}{N}}$$

where Y_i are experimental values, \hat{Y}_i are values calculated by the model, and N is the number of points. The closer the value of R^2 to unity, the better the model describes the experimental data.

Table 2.2 Model parameters for VT6

	JC	HK	ARJ	CS	
A	1067	1044	1047	333	MPa
B	796	760	765	241	MPa
n	0.46	0.44	0.44	0.43	–
C	0.03	0.0295	0.03	2.34×10^{-8}	–
C2/p	–	0.00054	–	23.4	–
m	0.8	0.8	0.8	0.8	–
R^2	0.991	0.991	0.991	0.991	

Table 2.3 Model parameters for VT8

	JC	HK	ARJ	CS	
A	1148	1110	1116	323	MPa
B	1760	1592	1567	458	MPa
n	1.06	1.01	1	1	–
C	0.03697	0.0365	0.0363	2.6×10^{-8}	–
C2/p	–	0.00085	–	19.7	–
m	0.88	0.87	0.87	0.87	–
R^2	0.975	0.975	0.975	0.975	

Table 2.4 Model parameters for VT20

	JC	HK	ARJ	CS	
A	1111	1070	1095	657	MPa
B	1093	955	1036	584	MPa
n	0.797	0.75	0.78	0.75	–
C	0.0266	0.0255	0.026	1197	–
C2/p	–	0.00095	–	15.56	–
m	0.8	0.8	0.8	0.8	–
R ²	0.96	0.96	0.96	0.96	

Table 2.5 Modified model parameters for materials studied

	VT6	VT8	VT20	
σ_A	528	546	635	MPa
B	1895	1539	1368	MPa
β_0	0.0045	0.0035	0.0039	–
β_1	0.00022	0.00022	0.000205	–
A	699	1237	1692	MPa
N	0.426	0.83	0.773	–
α_0	–0.000156	0.000255	0.0014	–
α_1	4.97×10^{-5}	5.03×10^{-5}	3.04×10^{-5}	–
R ²	0.994	0.976	0.96	

Table 2.6 The range of loading conditions in which the parameters of the models are obtained

	VT6	VT8	VT20
Strain rate, 1/s	0.01–1600	0.005–1800	0.005–2200
T, °C	20–300	20–200	20–200

Table 2.6 indicates the range of loading conditions in which the parameters of these models are obtained. Points outside this range are extrapolations; therefore, the efficiency of the models outside the specified ranges is not guaranteed.

2.5 Verification of Mathematical Models

These models were verified by experiment on the high rate penetration of indenters with conical and spherical heads. As an example, Figs. 2.21, 2.22, 2.23, and 2.24 show a comparison of the results of field and numerical experiments for material VT-8. The error in plastic imprint diameter prediction is no more than 8%. The numerical experiment gives a smaller diameter, which is due to the presence in the

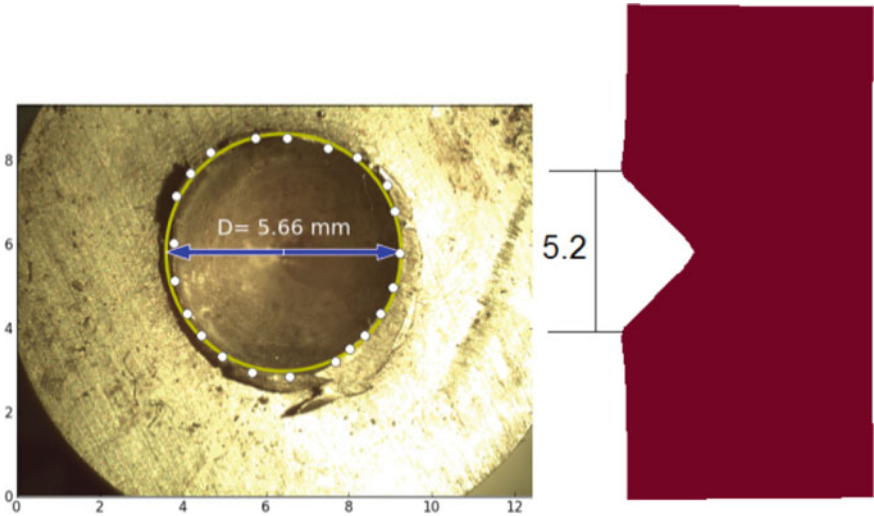


Fig. 2.21 Comparison of imprints in full-scale and numerical experiments for the alloy VT8. Indentation, cone

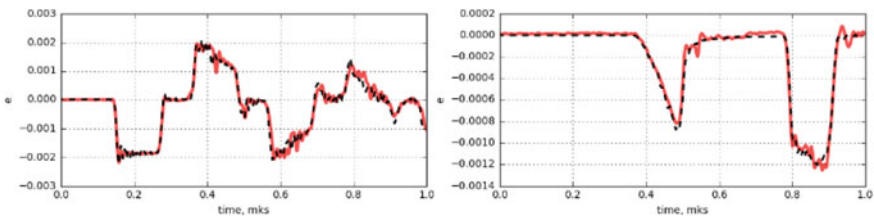


Fig. 2.22 Comparison of deformation pulses in measuring bars in full-scale and numerical experiment for alloy VT8, cone: on the left is the loading bar, on the right is the supporting bar

field test of a large number of loading cycles, while in the numerical experiment only 3 loading cycles were taken into account. A good agreement of the data from the measuring bars is obtained (see Figs. 2.22 and 2.24). In Figs. 2.22 and 2.24, the solid lines correspond to the results of the field tests, the dotted lines correspond to the numerical simulation.

Thus, it is possible to ascertain the sufficient accuracy and reliability of the description of the constructed models of the deformation of the real behavior of the investigated alloys.

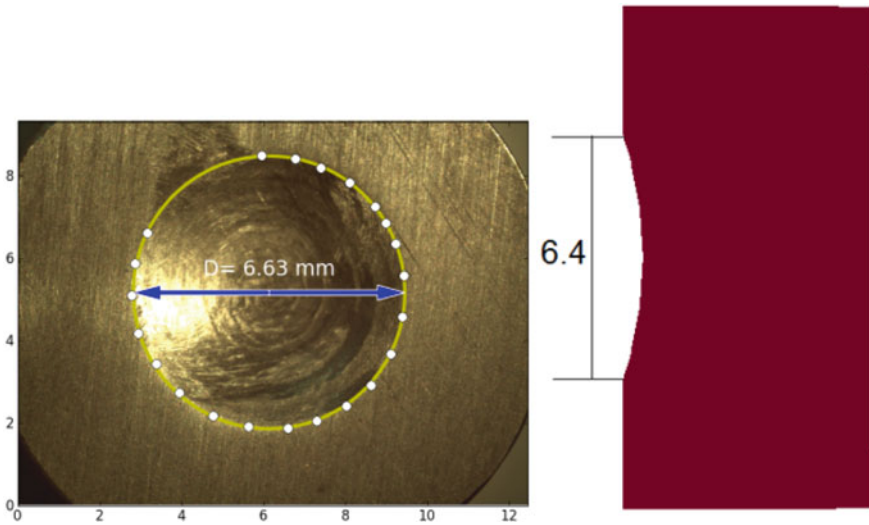


Fig. 2.23 Comparison of imprints in full-scale and numerical experiments for the alloy VT8. Indentation, sphere

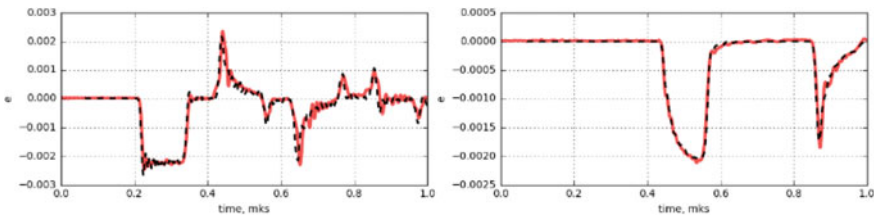


Fig. 2.24 Comparison of deformation pulses in measuring bars in full-scale and numerical experiment for alloy VT8, sphere: on the left is the loading bar, on the right is the supporting bar

2.6 Conclusions

For several titanium alloys (VT-6, VT-8, and VT-20), a comprehensive study of the behavior under high rate loading conditions was carried out. Deformation curves and ultimate characteristics of plasticity, as well as their dependences on temperature and strain rate, are determined. The friction coefficients at a high sliding velocity (about 20 m/s) for pairs of Ti–Al and Ti–Ti materials are determined. On the basis of the obtained experimental data, mathematical models were constructed that describe the behavior of the yield surface radius under various loading conditions—strain rate and temperature. These models were verified using an experiment on the dynamic penetration of indentors of various shapes into samples under study.

It should be noted that the modern integrated approach to the problems of high rate deformation employed in the present paper has shown its effectiveness for analyzing the processes of high rate deformation of structural materials.

Acknowledgments The experimental results were supported by a grant of the Russian Science Foundation (16-19-10237-P). The determination of the parameters of the mathematical model and computational experiment was supported by the Grant of the President of the Russian Federation for young scientists (MD-1221.2019.8).

References

1. Kolsky, H.: An investigation of the mechanical properties of materials at very high rates of loading. *Proc. Phys. Soc. London, Sect. B* **62**, 676–700 (1949)
2. Field, J.E., Walley, S.M., Bourne, N.K., Huntley, J.M.: Experimental methods at high strain rate. *J. Phys. IV, Colloque C3, Dymat*, 3–22 (1994)
3. Bacon, C., Lataillade, J-L.: Development of the Kolsky-Hopkinson techniques and applications for non-conventional testing. In: Nowacki, W.K., Klepaczko, J.R. (eds.) *New Experimental Methods in Material Dynamics and Impact. Trends in Mechanics of Materials*. Warsaw, pp 1–58 (2001)
4. Davies, R.M.: A critical study of the Hopkinson pressure bar. *Philos. Trans. R. Soc. (London) A* **240**, 375–457 (1948)
5. Davies, R.M.: A simple modification of the Hopkinson pressure bar. In: *Proceedings of 7th International Congress on Applied Mechanics*, vol. 1, p. 404 (1948)
6. Kolsky, H.: An investigation of the mechanical properties of material at very high rates of loading. *Proc. Phys. Soc. (London)* **62B**, 676–700 (1949)
7. Konstantinov, Y.A.: Experimental and numerical investigation of behavior of constructional materials under dynamic loading, PhD Thesis, Nizhny Novgorod (2007)
8. Bragov, A., Konstantinov, A., Lomunov, A., Shmotin, Yu., Kruszka, L.: Experimental definition of dynamic friction (DYMAT-2009). *J. Phys. IV*. 619–624 (2009)
9. Hauser, F.E.: Techniques for measuring stress-strain relations at high strain rates. *Exp. Mech.* **6**(8), 395–402 (1966)
10. Eskandari, H., Nemes, J.A.: Dynamic testing of composite laminates with a tensile split hopkinson bar. *J. Composite Mat.* **34**(4), 260–273 (2000)
11. Lindholm, U.S., Yeakley, L.M.: High strain-rate testing: tension and compression. *Exp. Mech.* **8**(1), 1–9 (1968)
12. Nicholas, T.: Tensile testing of materials at high rates of strain. *Exp. Mat.* **21**(5), 177–185 (1981)
13. Caverzan, A., Cadoni, E., di Prisco, M.: Tensile behaviour of high performance fibre-reinforced cementitious composites at high strain rates. *Int. J. Impact Eng* **45**, 28–38 (2012)
14. Jiang, B., Zhang, R.: Tensile properties in the through-thickness direction for a carbon fiber woven reinforced composite at impact loading rate. *J. Phys. IVFrance* **134**, 1071–1075 (2006)
15. Bragov, A., Konstantinov, A., Kruszka, L., Lomunov, A., Filippov, A.: Dynamic properties of stainless steel under direct tension loading using a simple gas gun. *EPJ Web Conf.* **183**(2018). <https://doi.org/10.1051/epjconf/201818302035>
16. Konstantinov, A.Y.: A modern experimental-theoretical approach to rationally , noveltechnological objects. *Mat. Phys. Mech.* **28**, 106–109 (2016)
17. Bragov, A.M., Konstantinov, A.Y., Lomunov, A.K., Yuzhina, T.N., Filippov, A.R.: Experimental complexes for investigation of behavior of materials at a strain rate of $5 \times 10^2 \div 10^5$ s⁻¹. *MATEC Web Conf.* **226**(3024) (2018). <https://doi.org/10.1051/matecconf/201822603024>

18. Johnson, G.R., Cook, W.H.: A constitutive model and data for metals subjected to large strains, high strain rates and high temperatures. In: 7th International Symposium on ballistics, pp. 541–547 (1983)
19. Huh, H., Kang, W.J.: Crash-worthiness assessment of thin-walled structures with the high-strength steel sheet. *Int. J. Veh. Des.* **30**(1/2), 1–21 (2002)
20. Allen, D.J., Rule, W.K., Jones, S.E.: Optimizing material strength constants numerically extracted from taylor impact data. *Exp. Mech.* **37**, 333–338 (1997)
21. Cowper, G.R., Symonds, P.S.: Strain Hardening and Strain Rate Effects in the Impact Loading of Cantilever Beams. Brown University, Applied Mathematics Report (1958)

Chapter 3

Direct and Inverse Problems for Interface Crack Identification in Layered Media



Alexander N. Galybin

Abstract This study is devoted to the problem of damage detection in layered media. A package of dissimilar elastic layers is considered. Continuity conditions for the stress and displacement vectors are accepted on the interfaces between the layers. The package can be bonded to elastic half-plane and this interface may be damaged by an interfacial crack that can be of normal mode or shear mode or combined mode. It is suggested that strain/displacement measurements are accrued on the stress-free part of the external boundary. These data are used further on as input into a model that can detect the presence of interfacial cracks and predict delamination. The problem is reduced to the Cauchy initial problem for the complex potentials used in plane problems of elasticity and then solved by applying the Fourier transform. This problem is conditionally ill-posed, as it possesses unstable solutions, which can make impossible crack detection, as the noise in measured strains can be greater than the strain caused by interfacial cracks, and thus they could be indistinguishable. A possibility of crack detection is discussed for a special example.

Keywords Layered media · Inverse problems · Interface cracks · Integral equations · Integral transforms

3.1 Introduction

This study is aimed at the problem of debonding detection on the interfaces between dissimilar layers. Such problems often occur, they could be observed in engineering (e.g. coatings or FGM structures), geomechanics (layered rocks), biomechanics (live tissues) and other areas. There exist several routine methods, such as X-ray, ultrasonic tomography, frequency analysis, strain/displacement monitoring and so on. Some are suitable for different practical situations but cannot be applied to others for different

A. N. Galybin (✉)

The Schmidt Institute of Physics of the Earth (IPE RAS), Moscow, Russia

e-mail: a.n.galybin@gmail.com

Don State Technical University, Rostov-on-Don, Russia

© Springer Nature Switzerland AG 2020

S. M. Aizikovich et al. (eds.), *Modeling, Synthesis and Fracture of Advanced Materials for Industrial and Medical Applications*, Advanced Structured Materials 136,

https://doi.org/10.1007/978-3-030-48161-2_3

reasons. This means that further developments of existing methods and extension of the scope of their application are a timely problem in different fields of human activity. Here we continue the development of a mathematical basis for the strain/displacement monitoring technique for the sake of stress analysis and damage detection.

There are many papers that deal with standard formulations of boundary value problems, BVP, for media consisting of dissimilar elastic layers. This study focuses on inverse formulations although the standard (direct) formulations are also considered but as auxiliary ones that could be used for the generation of synthetic data for the back analysis. Here we employ a general approach based on the Fourier transform, which is an effective tool in the stress analysis of layered structures. It is appropriate for one layer, i.e. for an elastic strip, see [1], as well as for a package of layers. In the monograph by Shel'jakov [2], one can find a general method capable of dealing with 2D and 3D layered structures involving the Fourier transform and matrix algorithms and also some solutions for the standard formulations of the BVP of elasticity. His method is used further on but has been modified considerably by utilising the Fourier transforms for the complex potentials in the plane theory of elasticity and applied for solving inverse problems.

The inverse problem considered in this study belongs to a wide class of incorrectly posed BVP that is overdetermined on a part of the boundary and underdetermined on the rest of it. Shvab [3] referred such BVP as the (\mathbf{u}, \mathbf{p}) problem, which indicates that both displacement, \mathbf{u} , and stress, \mathbf{p} , vectors are known on a part of the boundary and nothing is known outside of it. It was proved that this problem has a unique solution and therefore is conditionally ill-posed. There are some other formulations that can be reduced to the (\mathbf{u}, \mathbf{p}) problem, see [4–8].

One can note that the (\mathbf{u}, \mathbf{p}) problem is basically the Cauchy initial problem for the system of differential equations of plane elasticity that can easily be solved by using finite differences. However, due to the nature of the inverse problem, its solution is unstable with respect to small variations of initial conditions, which requires the application of special regularisation techniques as detailed in [9]. It has been shown, e.g. [10, 11], that the SVD regularisation is an effective tool for providing stability of solutions especially for medium-size systems of linear algebraic equations that can be arrived at after discretisation of the corresponding system of integral equations. In a recent paper by Galybin and Rogerson [12], it has been shown that the inverse (\mathbf{u}, \mathbf{p}) problem for an elastic strip can be reduced to the inversion of the Stieltjes integral and the SVD regularisation provides a satisfactory solution at least for several model examples considered there. The present paper essentially generalises the results obtained in [12] for the strip. Here we consider a package consisting of dissimilar layers and discuss the possibility of crack detection on the interfaces between the layers given that the strain monitoring on the stress-free part of the external boundary is subjected to measurement errors.

3.2 Preliminaries

3.2.1 Kolosov–Muskhelishvili Formulas

The Kolosov–Muskhelishvili formulas for the stress and displacement components in a Cartesian coordinate system Oxy are as follows [13]:

$$\begin{aligned} P &\equiv \frac{\sigma_{xx} + \sigma_{yy}}{2} = \Phi(z) + \overline{\Phi(z)}, \\ D &\equiv \frac{\sigma_{yy} - \sigma_{xx}}{2} + i\sigma_{xy} = \bar{z}\Phi'(z) + \Psi(z), \\ 2GW &\equiv 2G(u_x + iu_y) = \kappa\phi(z) - z\overline{\Phi(z)} - \overline{\psi(z)}. \end{aligned} \quad (3.1)$$

Here, σ_{xx} , σ_{yy} , σ_{xy} are stress components, P is mean stress, D is complex stress deviator, $W = u_x + iu_y$ is complex displacement vectors with the components u_x , u_y along the x and y axes, respectively, G is shear modulus, $\kappa = (3-4\nu)$ for the plain stress and $\kappa = (3-\nu)/(1+\nu)$ for the plane stress conditions, ν is Poisson's ratio, and $\Phi(z) = \phi'(z)$, $\Psi(z) = \psi'(z)$ are complex potentials (holomorphic functions of a complex variable $z = x+iy$).

For straight boundaries, it is convenient [14] to replace the potential $\Psi(z)$ by a new unknown holomorphic function $\Omega(z)$ as follows:

$$\Omega(z) = z\Phi'(z) + \Phi(z) + \Psi(z). \quad (3.2)$$

Then the expression for the complex stress deviator takes the form

$$D(z, \bar{z}) = (\bar{z} - z)\Phi'(z) - \Phi(z) + \Omega(z). \quad (3.3)$$

By differentiating the third formula in (3.1) with respect to the variable x and making use of (3.2)–(3.3), one obtains the following expressions for the derivative of the displacement vector, $w = W'$, and its complex conjugate, $\bar{w} = \bar{W}'$, in terms of the holomorphic functions $\Phi(z)$ and $\Omega(z)$:

$$2Gw = \kappa\Phi(z) - \overline{\Omega(z)} + (\bar{z} - z)\overline{\Phi'(z)}, \quad 2G\bar{w} = \kappa\overline{\Phi(z)} - \Omega(z) - (\bar{z} - z)\Phi'(z). \quad (3.4)$$

The sum of the first and the second formulas in (3.1) followed by complex conjugation results in the following two equivalent relationships:

$$\begin{aligned} \sigma &\equiv \sigma_{yy} + i\sigma_{xy} = \overline{\Phi(z)} + \Omega(z) + (\bar{z} - z)\Phi'(z), \\ \bar{\sigma} &\equiv \sigma_{yy} - i\sigma_{xy} = \Phi(z) + \overline{\Omega(z)} - (\bar{z} - z)\overline{\Phi'(z)}. \end{aligned} \quad (3.5)$$

Now the expressions for the complex potentials $\Phi(z)$ and $\Omega(z)$ in terms of the stress and displacement vectors are found from (3.4) and (3.5) as follows:

$$(\kappa + 1)\Phi(z) = \bar{\sigma} + 2Gw, \quad (3.6)$$

$$(\kappa + 1)\Omega(z) = \kappa\sigma - 2G\bar{w} + (\kappa + 1)(z - \bar{z})\Phi'(z). \quad (3.7)$$

The form of (3.6) remains on the boundary while the latter term in (3.7) vanishes when $y = 0$ and therefore the boundary values of the complex potentials can be presented in the form:

$$(\kappa + 1)\Phi(x) = \overline{\sigma(x, 0)} + 2Gw(x, 0), \quad (3.8)$$

$$(\kappa + 1)\Omega(x) = \kappa\sigma(x, 0) - 2G\overline{w(x, 0)}. \quad (3.9)$$

We further assume the boundary values specified by (3.4) and (3.5) to be known on a part of the boundary.

3.2.2 Fourier Transforms

The Fourier transform, $\mathbf{F}(\cdot)$ (abbreviated as the FT hereafter), and its inverse, $\mathbf{F}^{-1}(\cdot)$, are specified as follows [15]:

$$\mathbf{F}(Y(x)) \equiv \hat{Y}(s) = \int_{-\infty}^{\infty} Y(x)e^{-isx} dx, \quad \mathbf{F}^{-1}(\hat{Y}(s)) \equiv Y(x) = \frac{1}{2\pi} \int_{-\infty}^{\infty} \hat{Y}(s)e^{isx} ds, \quad (3.10)$$

where s is a real parameter, $\text{Im}(s) = 0$. The FT of the derivative is

$$\mathbf{F}(Y'(x)) = is\hat{Y}(s). \quad (3.11)$$

The FT for complex conjugated functions is

$$\mathbf{F}(\overline{Y(x)}) = \overline{\hat{Y}_0(s)} = \int_{-\infty}^{\infty} \overline{Y(x)}e^{-isx} dx = \overline{\int_{-\infty}^{\infty} Y(s)e^{isx} ds} = \overline{\hat{Y}(-s)}. \quad (3.12)$$

If $Y_0(x)$ is a real-valued function then $\overline{\hat{Y}_0(s)} = \hat{Y}_0(-s)$.

Application of the FT with respect to the variable x to any holomorphic function $H(z) = H(x,y)$ results (due to the Cauchy–Riemann equations) in the following relationships for the transforms of the complex potentials:

$$\begin{pmatrix} \hat{\Phi}(s, y) \\ \hat{\Omega}(s, y) \end{pmatrix} = e^{-ys} \begin{pmatrix} \hat{\Phi}(s, 0) \\ \hat{\Omega}(s, 0) \end{pmatrix}. \tag{3.13}$$

Applying complex conjugation to (3.13) one finds from (3.11) that

$$\begin{pmatrix} \overline{\hat{\Phi}(-s, y)} \\ \overline{\hat{\Omega}(-s, y)} \end{pmatrix} = e^{ys} \begin{pmatrix} \overline{\hat{\Phi}(-s, 0)} \\ \overline{\hat{\Omega}(-s, 0)} \end{pmatrix}. \tag{3.14}$$

Relationships (3.13) and (3.14) are frequently used further on.

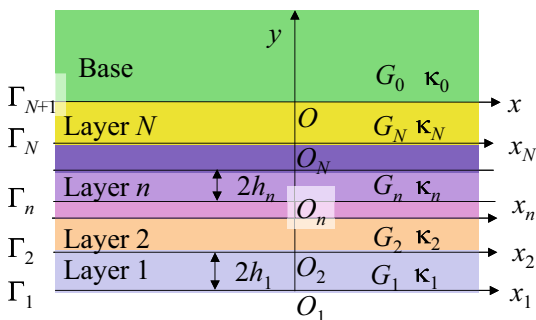
3.3 Problem Formulation

Let us consider a package consisting of N different elastic layers characterised by thickness $2h_n$ and elastic constants G_n and κ_n , where $n = 1, 2 \dots N$ and the subscript designates the layer number. The package of layers can be attached to an elastic base considered as a half-plane whose moduli are G_0 and κ_0 . This configuration includes the external boundary Γ_1 and N interfaces Γ_{n+1} ($n = 1, 2 \dots N$) between dissimilar materials as shown in Fig. 3.1.

Each n -th layer is described in a local coordinate system $O_n x_n y$ as the subdomain $\{-\infty < x_n < \infty, 0 < y < 2h_n\}$. Displacement and stress vectors and complex potentials in every subdomain are linked by the Kolosov–Muskhelishvili formulas (see subsection above) and marked by subscripts n in accordance with the layer number, respectively, $w_n(x_n, y)$, $\sigma_n(x_n, y)$, $\Phi_n(x_n + iy)$, $\Omega_n(x_n + iy)$, for the base we use $n = 0$.

It is assumed that the layers are fully bonded to each other, which implies continuity of the stress and displacement vectors on the interfaces Γ_{n+1} ($n = 1, 2 \dots N$). On the interface Γ_{N+1} the stress vector is also continuous while the displacements

Fig. 3.1 The package of N dissimilar elastic layers bonded to the base



can be discontinuous in the case of partial delamination over a part of the interface, say on an interval (a, b) . This zone can be viewed as an open crack or a sliding zone or a combination of both.

In order to distinguish the stress and displacement vectors acting on the interfaces from those acting inside the subdomains, we omit their second argument and use, respectively, the notations $\sigma_n(t)$ and $w_n(t)$. Then the continuity conditions between the adjacent layers can be presented as follows:

$$\sigma_{n+1}(t) = \sigma_{n+1}(t, 0) = \sigma_n(t, 2h_n), \quad n = 1 \dots N, \quad t \in \Gamma_{n+1}, \quad (3.15)$$

$$w_{n+1}(t) = w_{n+1}(t, 0) = w_n(t, 2h_n), \quad n = 1 \dots N - 1, \quad t \in \Gamma_{n+1}. \quad (3.16)$$

In the case of delamination on the interface Γ_{N+1} , the condition (3.16) is valid outside (a, b) and the following condition is imposed on the density of the displacement jump:

$$\int_a^b (w_0(x, 0) - w_N(x, 2h_N)) dx = 0, \quad (3.17)$$

which provides single-valuedness of the displacements.

It is assumed that the boundary Γ_1 is loaded by concentrated forces P_j applied at the points t_j ($j = 1 \dots J$). Moreover, the displacements (and hence their contour derivatives) are also known on the whole boundary with exception of points t_j . Therefore, we further consider a Cauchy type problem with the initial conditions

$$\sigma(t, 0) = \sum_{j=0}^J P_j \delta(t - t_j) = \sigma_1(t), \quad w(t, 0) = w_1(t), \quad t \in \Gamma_1, \quad (3.18)$$

where $\delta(t)$ is the Dirac delta function.

It is evident that such formulation belongs to a wide class of incorrectly posed problems of plane elasticity as the number of scalar conditions on the free boundary is equal to four, which exceeds the required number of two conditions necessary for correct formulation. Instead, no conditions are set on the interface Γ_{N+1} apart from the continuity of the stress vector (3.15) and condition (3.17). This suggests that the general problem for the package of dissimilar layers bonded to the base can be decomposed into two sub-problems. The first one is the Cauchy type problem for inhomogeneous elastic strip consisting of N layers made of dissimilar materials, while the second is the problem for the elastic half-plane with underspecified boundary conditions on the interval (a, b) and overspecified on the rest of Γ_{N+1} as both stress and displacement vectors will be known there from the solution of the first sub-problem.

Both sub-problems belong to the class of conditionally ill-posed problems, which means that they possess unique solutions but these can be unstable with respect to small variations in the boundary conditions. The latter are inherent for engineering applications involving displacements (or strain) monitoring. Therefore, in calculation, the function $w_1(t)$ in (3.18) can be modelled as the sum of ideal displacements $w^{\text{ideal}}(t)$ (these should be obtained from the solution of a correctly posed problem) and random noise of certain intensity ε , i.e.

$$w_1(t) = w^{\text{ideal}}(t) + \text{Noise}(t), \quad t \in \Gamma_1, \quad (3.19)$$

where $\text{Noise}(t)$ is a function that generates for every point t a random noise that can be modelled by uniformly distributed random numbers or by normally distributed errors with zero mean or by other means.

For the sake of crack (delamination) detection, the solution to the first sub-problem could be sufficient in the cases when the calculated normal stresses on Γ_{N+1} comply with the typical stress profile near the crack, as has been demonstrated in [12] for the case of a single strip. However, if delamination occurs as a sliding zone then the stresses may not have large gradients near the crack tips and therefore it would be desirable to analyse the solution of the general problem. It should be noted that the general problem becomes overspecified and therefore it may not possess a solution if the delamination on the interface Γ_{N+1} does not exist. It has been shown for the problem for a coating fully bonded to a substrate [12] that in such a case the boundary conditions of the type (3.18) cannot be selected independently but should satisfy certain integral relationships. The latter can also be used to identify the integrity of the layered structure. We consider further both sub-problems and also provide necessary solutions to the fundamental problems for the elastic strip that can be used for modelling of displacement monitoring in accordance with (3.19).

3.4 Direct Boundary Value Problems for an Elastic Strip

This section presents solutions of three fundamental boundary value problems for an elastic strip with the boundaries $\Gamma_1 = \{z = t : -\infty < t < \infty\}$ and $\Gamma_2 = \{z = t + 2ih : -\infty < t < \infty\}$. These solutions play an auxiliary role for the present study as they can serve for forming the data on strain monitoring on the stress-free boundary. These solutions can be found in [1] and [16] for the stress–displacement distributions on the strip boundaries. We present full solutions in terms of the FT of the complex potentials, which enable one to analyse the stress state at any point in the strip.

Problem 1 The strip is subjected to normal and tangential stresses $\sigma_1(x)$ on Γ_1 and the tangential derivatives of the displacements $w_2(x)$ on Γ_2 .

Let us apply the FT to (3.4) and (3.5) and use the properties in (3.11)–(3.12) to obtain

$$2G\overline{\hat{w}(-s, y)} = \kappa\overline{\hat{\Phi}(-s, y)} - \hat{\Omega}(s, y) - 2sy\hat{\Phi}(s, y), \quad (3.20)$$

$$\hat{\sigma}(s, y) = \overline{\hat{\Phi}(-s, y)} + \hat{\Omega}(s, y) + 2sy\hat{\Phi}(s, y). \quad (3.21)$$

Then on $y = 0$:

$$\hat{\sigma}_1(s) = \overline{\hat{\Phi}_1(-s)} + \hat{\Omega}_1(s), \quad (3.22)$$

while on $y = 2h$:

$$2G\overline{\hat{w}_2(-s)} = \kappa e^{2hs}\overline{\hat{\Phi}_1(-s)} - e^{-2hs}\left[4hs\hat{\Phi}_1(s) + \hat{\Omega}_1(s)\right]. \quad (3.23)$$

In (3.22) and (3.23) we introduced the following notations:

$$\hat{\Phi}_1(s) = \hat{\Phi}(s, 0), \quad \hat{\Omega}_1(s) = \hat{\Omega}(s, 0). \quad (3.24)$$

and used (3.13)–(3.14).

Excluding $\hat{\Omega}_1(s)$ from the system (3.22)–(3.23) one finds

$$\hat{\Omega}_1(s) = \hat{\sigma}_1(s) - \overline{\hat{\Phi}_1(-s)}, \quad (3.25)$$

$$2G\overline{\hat{w}_2(-s)} + e^{-2hs}\hat{\sigma}_1(s) = (\kappa e^{2hs} + e^{-2hs})\overline{\hat{\Phi}_1(-s)} - 4hse^{-2hs}\hat{\Phi}_1(s). \quad (3.26)$$

Complex conjugation of (3.19) followed by the replacement of the variable s by $-s$ leads to the following system for the determination of $\hat{\Phi}_1(s)$:

$$\begin{cases} -4hse^{-2hs}\hat{\Phi}_1(s) + (\kappa e^{2hs} + e^{-2hs})\overline{\hat{\Phi}_1(-s)} = e^{-2hs}\hat{\sigma}_1(s) + 2G\overline{\hat{w}_2(-s)} \\ (\kappa e^{-2hs} + e^{2hs})\hat{\Phi}_1(s) + 4hse^{2hs}\overline{\hat{\Phi}_1(-s)} = e^{2hs}\overline{\hat{\sigma}_1(-s)} + 2G\hat{w}_2(s) \end{cases}. \quad (3.27)$$

From (3.20) it follows that

$$\hat{\Phi}_1(s) = \frac{e^{hs}}{\Delta_1(s)} \begin{bmatrix} (\kappa e^{2hs} + e^{-2hs})(e^{hs}\overline{\hat{\sigma}_1(-s)} + 2Ge^{-hs}\hat{w}_2(s)) - \\ -4hs(e^{-hs}\hat{\sigma}_1(s) + 2Ge^{hs}\overline{\hat{w}_2(-s)}) \end{bmatrix}, \quad (3.28)$$

$$\Delta_1(s) = (\kappa e^{2hs} + e^{-2hs})(\kappa e^{-2hs} + e^{2hs}) + (4hs)^2.$$

Therefore for $0 \leq y \leq 2h$

$$\hat{\Phi}(s, y) = \frac{e^{(h-y)s}}{\Delta_1(s)} \begin{bmatrix} (\kappa e^{2hs} + e^{-2hs})(e^{hs}\overline{\hat{\sigma}_1(-s)} + 2Ge^{-hs}\hat{w}_2(s)) - \\ -4hs(e^{-hs}\hat{\sigma}_1(s) + 2Ge^{hs}\overline{\hat{w}_2(-s)}) \end{bmatrix}, \quad (3.29)$$

The FT of the potential $\Omega(z)$ is found by substitution of (3.28) into (3.25) followed by multiplication by $\exp(-ys)$, i.e. as $\hat{\Omega}(s, y) = e^{-ys}(\hat{\sigma}_1(s) - \overline{\hat{\Phi}_1(-s)})$, which gives

$$\hat{\Omega}(s, y) = e^{-ys} \hat{\sigma}_1(s) - \frac{e^{-(h+y)s}}{\Delta_1(s)} \left[(\kappa e^{-2hs} + e^{2hs}) \left(e^{-hs} \hat{\sigma}_1(s) + 2Ge^{hs} \overline{\hat{w}_2(-s)} \right) + 4hs \left(e^{hs} \overline{\hat{\sigma}_1(-s)} + 2Ge^{-hs} \hat{w}_2(s) \right) \right]. \quad (3.30)$$

Therefore the solution of the mixed boundary value in terms of the FT is complete.

Problem 2 The stress vectors $\sigma_1(x)$ and $\sigma_2(x)$ are given on Γ_1 and Γ_2 , respectively.

In this case, one has the system consisting of Eq. (3.22) on the boundary $y = 0$ and the following one on $y = 2h$

$$\hat{\sigma}_2(s) = e^{2hs} \overline{\hat{\Phi}_1(-s)} + e^{-2hs} \left(\hat{\Omega}_1(s) + 4hs \hat{\Phi}_1(s) \right). \quad (3.31)$$

Excluding $\hat{\Omega}_1(s)$ from the system (3.22), (3.31) and using a similar approach as in the problem above one arrives at the following system for the determination of $\hat{\Phi}_1(s)$

$$\begin{cases} 4hse^{-2hs} \hat{\Phi}_1(s) + 2 \sinh(2hs) \overline{\hat{\Phi}_1(-s)} = \hat{\sigma}_2(s) - e^{-2hs} \hat{\sigma}_1(s) \\ 2 \sinh(2hs) \hat{\Phi}_1(s) + 4hse^{2hs} \overline{\hat{\Phi}_1(-s)} = e^{-2hs} \overline{\hat{\sigma}_1(-s)} - \overline{\hat{\sigma}_2(-s)}. \end{cases} \quad (3.32)$$

The solution of this system is found as follows:

$$\begin{aligned} \hat{\Phi}_1(s) &= \frac{e^{hs}}{2\Delta_2(s)} \left[\sinh(2hs) \left(e^{-hs} \overline{\hat{\sigma}_2(-s)} - e^{hs} \overline{\hat{\sigma}_1(-s)} \right) + 2hs \left(e^{hs} \hat{\sigma}_2(s) - e^{-hs} \hat{\sigma}_1(s) \right) \right], \\ \Delta_2(s) &= (2hs)^2 - \sinh^2(2hs). \end{aligned} \quad (3.33)$$

Therefore

$$\hat{\Phi}(s, y) = \frac{e^{(h+y)s}}{2\Delta_2(s)} \left[\sinh(2hs) \left(e^{-hs} \overline{\hat{\sigma}_2(-s)} - e^{hs} \overline{\hat{\sigma}_1(-s)} \right) + 2hs \left(e^{hs} \hat{\sigma}_2(s) - e^{-hs} \hat{\sigma}_1(s) \right) \right] \quad (3.34)$$

The solution for $\hat{\Omega}_1(s)$ follows from (3.25) and conjugated (3.33). Thus

$$\hat{\Phi}(s, y) = e^{-ys} \hat{\sigma}_1(s) + \frac{e^{-(h+y)s}}{2\Delta_2(s)} \left[\sinh(2hs) \left(e^{hs} \hat{\sigma}_2(s) - e^{-hs} \hat{\sigma}_1(s) \right) + 2hs \left(e^{-hs} \overline{\hat{\sigma}_2(-s)} - e^{hs} \overline{\hat{\sigma}_1(-s)} \right) \right]. \quad (3.35)$$

Problem 3 The displacement vectors $w_1(x)$ and $w_2(x)$ are given on Γ_1 and Γ_2 , respectively.

In this case, one has the system consisting of Eq. (3.23) on the boundary $y = 2h$ and the following one on $y = 0$

$$2G\overline{\hat{w}_1(-s)} = \kappa\overline{\hat{\Phi}_1(-s)} - \hat{\Omega}_1(s). \quad (3.36)$$

We further solve (3.36) for $\hat{\Omega}_1(s)$ and substitute it into (3.23) to obtain the following system for the determination of $\hat{\Phi}_1(s)$

$$\begin{cases} -e^{-2hs}4hs\hat{\Phi}_1(s) + 2\kappa\sinh(2hs)\overline{\hat{\Phi}_1(-s)} = 2G(\overline{\hat{w}_2(-s)} - \overline{\hat{w}_1(-s)}e^{-2hs}) \\ -2\kappa\sinh(2hs)\hat{\Phi}_1(s) + e^{2hs}4hs\overline{\hat{\Phi}_1(-s)} = 2G(\hat{w}_2(s) - \hat{w}_1(s)e^{2hs}) \end{cases}. \quad (3.37)$$

The solution of (3.37) is found in the form

$$\hat{\Phi}_1(s) = \frac{Ge^{hs}}{\Delta_3(s)} \begin{bmatrix} \kappa\sinh(2hs)(\hat{w}_2(s)e^{-hs} - \hat{w}_1(s)e^{hs}) - \\ -hs(\overline{\hat{w}_2(-s)}e^{hs} - \overline{\hat{w}_1(-s)}e^{-hs}) \end{bmatrix}, \quad \Delta_3(s) = (2hs)^2 - \kappa^2\sinh^2(2hs). \quad (3.38)$$

Therefore for $0 \leq y \leq 2h$

$$\hat{\Phi}(s, y) = \frac{Ge^{(h-y)s}}{\Delta_3(s)} \begin{bmatrix} \kappa\sinh(2hs)(\hat{w}_2(s)e^{-hs} - \hat{w}_1(s)e^{hs}) - \\ -hs(\overline{\hat{w}_2(-s)}e^{hs} - \overline{\hat{w}_1(-s)}e^{-hs}) \end{bmatrix}. \quad (3.39)$$

The solution for $\hat{\Omega}_1(s)$ follows from (3.36) and conjugated (3.39). Thus

$$\hat{\Omega}(s, y) = -2Ge^{-ys}\overline{\hat{w}_1(-s)} - \kappa\frac{Ge^{-(h+y)s}}{\Delta_3(s)} \begin{bmatrix} \kappa\sinh(2hs)(\overline{\hat{w}_2(-s)}e^{hs} - \overline{\hat{w}_1(-s)}e^{-hs}) - \\ -hs(\hat{w}_2(s)e^{-hs} - \hat{w}_1(s)e^{hs}) \end{bmatrix}. \quad (3.40)$$

In this section, we presented the solutions for a single strip for three fundamental (direct) boundary value problems in terms of the FT of the complex potentials. They are given by Eqs. (3.29)–(3.30), (3.33)–(3.35), (3.39)–(3.40).

3.5 Solution of the Cauchy Problem for the Inhomogeneous Strip

Let us consider the n th layer that is an elastic strip with the boundaries $\Gamma_n = \{z = t : -\infty < t < \infty\}$ and $\Gamma_{n+1} = \{z = t + 2ih_n : -\infty < t < \infty\}$.

The boundary values of the complex potentials in accordance with (3.6)–(3.9) have the form

$$(\kappa_n + 1)\Phi_n(x, 0) = \overline{\sigma_n(x)} + 2G_n w_n(x), \quad (3.41)$$

$$(\kappa_n + 1)\Phi_n(x, 2h_n) = \overline{\sigma_{n+1}(x)} + 2G_n w_{n+1}(x), \quad (3.42)$$

$$(\kappa_n + 1)\Omega_n(x, 0) = \kappa_n \sigma_n(x) - 2G_n \overline{w_n(x)}, \quad (3.43)$$

$$(\kappa_n + 1)\Omega_n(x, 2h_n) = \kappa_n \sigma_2(x) - 2G_n \overline{w_2(x)} + 4ih_n(\kappa_n + 1)\Phi'_n(x, 2h_n). \quad (3.44)$$

Applying the FT to (3.41), (3.42) one obtains the following equations:

$$(\kappa_n + 1)\hat{\Phi}_n(x, 0) = \overline{\hat{\sigma}_n(-s)} + 2G_n \hat{w}_n(s), \quad (3.45)$$

$$(\kappa_n + 1)\hat{\Phi}_n(s, 2h_n) = \overline{\hat{\sigma}_{n+1}(-s)} + 2G_n \hat{w}_{n+1}(s), \quad (3.46)$$

$$(\kappa_n + 1)\hat{\Omega}_n(s, 0) = \kappa_n \hat{\sigma}_n(s) - 2G_n \overline{\hat{w}_n(-s)}, \quad (3.47)$$

$$(\kappa_n + 1)\hat{\Omega}_n(s, 2h_n) = \kappa_n \hat{\sigma}_{n+1}(s) - 2G_n \overline{\hat{w}_{n+1}(-s)} - 4h_n s \left(\overline{\hat{\sigma}_{n+1}(-s)} + 2G_n \hat{w}_{n+1}(s) \right). \quad (3.48)$$

Then one can use (3.13)–(3.14) to find the relationships between the combinations of the stress and displacement vectors on the interfaces as follows:

$$\overline{\hat{\sigma}_{n+1}(-s)} + 2G_n \hat{w}_{n+1}(s) = e^{-2h_n s} \left(\overline{\hat{\sigma}_n(-s)} + 2G_n \hat{w}_n(s) \right), \quad (3.49)$$

$$\begin{aligned} \kappa_n \hat{\sigma}_{n+1}(s) - 2G_n \overline{\hat{w}_{n+1}(-s)} - 4h_n s \left(\overline{\hat{\sigma}_{n+1}(-s)} + 2G_n \hat{w}_{n+1}(s) \right) &= \\ &= e^{-2h_n s} \left(\kappa_n \hat{\sigma}_n(s) - 2G_n \overline{\hat{w}_n(-s)} \right). \end{aligned} \quad (3.50)$$

Substitution of (3.49) into (3.50) leads to

$$\begin{aligned} \kappa_n \hat{\sigma}_{n+1}(s) - 2G_n \overline{\hat{w}_{n+1}(-s)} = \\ = e^{-2h_n s} \left[\kappa_n \hat{\sigma}_n(s) - 2G_n \overline{\hat{w}_n(-s)} + 4h_n s \left(\overline{\hat{\sigma}_n(-s)} + 2G_n \hat{w}_n(s) \right) \right]. \end{aligned} \quad (3.51)$$

Let us present the system of Eqs. (3.49) and (3.51) in the matrix form

$$\begin{pmatrix} \hat{\sigma}_{n+1}(s) \\ \overline{\hat{w}_{n+1}(-s)} \end{pmatrix} = \mathbf{A}(2h_n s, \kappa_n, G_n) \begin{pmatrix} \hat{\sigma}_n(s) \\ \overline{\hat{w}_n(-s)} \end{pmatrix} + \mathbf{B}(2h_n s, \kappa_n, G_n) \begin{pmatrix} \overline{\hat{\sigma}_n(-s)} \\ \hat{w}_n(s) \end{pmatrix}, \quad (3.52)$$

where it is denoted as

$$\mathbf{A}(q, \kappa, G) = \cosh(q) \begin{pmatrix} 1 & 0 \\ 0 & 1 \end{pmatrix} + \frac{\sinh(q)}{\kappa + 1} \begin{pmatrix} 1 - \kappa & 4G \\ \frac{\kappa}{G} & \kappa - 1 \end{pmatrix}, \quad (3.53)$$

$$\mathbf{B}(q, \kappa, G) = \frac{2qe^{-q}}{\kappa + 1} \begin{pmatrix} 1 & 2G \\ -\frac{1}{2G} & -1 \end{pmatrix}. \quad (3.54)$$

Complex conjugation of (3.52) gives

$$\begin{pmatrix} \overline{\hat{\sigma}_{n+1}(-s)} \\ \hat{w}_{n+1}(s) \end{pmatrix} = \mathbf{B}(-2h_n s, \kappa_n, G_n) \begin{pmatrix} \hat{\sigma}_n(s) \\ \overline{\hat{w}_n(-s)} \end{pmatrix} + \mathbf{A}(-2h_n s, \kappa_n, G_n) \begin{pmatrix} \overline{\hat{\sigma}_n(-s)} \\ \hat{w}_n(s) \end{pmatrix} \quad (3.55)$$

Note that the matrices \mathbf{A} and \mathbf{B} are real-valued, therefore their complex conjugations are found by changing the Fourier parameter s by $-s$.

Now, one can form the 4×4 matrix as follows:

$$\begin{pmatrix} \hat{\sigma}_{n+1}(s) \\ \overline{\hat{w}_{n+1}(-s)} \\ \hat{\sigma}_{n+1}(-s) \\ \hat{w}_{n+1}(s) \end{pmatrix} = \begin{pmatrix} \mathbf{A}(2h_n s, \kappa_n, G_n) & \mathbf{B}(2h_n s, \kappa_n, G_n) \\ \mathbf{B}(-2h_n s, \kappa_n, G_n) & \mathbf{A}(-2h_n s, \kappa_n, G_n) \end{pmatrix} \begin{pmatrix} \hat{\sigma}_n(s) \\ \overline{\hat{w}_n(-s)} \\ \overline{\hat{\sigma}_n(-s)} \\ \hat{w}_n(s) \end{pmatrix}. \quad (3.56)$$

This system allows one to calculate the stress and displacement vectors on the $(n + 1)$ th interface through their values on the n th interface. Therefore, the solution for the $(N + 1)$ th interface is found by the recurrent formula below:

$$\begin{pmatrix} \hat{\sigma}_{n+1}(s) \\ \overline{\hat{w}_{n+1}(-s)} \\ \hat{\sigma}_{n+1}(-s) \\ \hat{w}_{n+1}(s) \end{pmatrix} = \begin{pmatrix} \mathbf{A}(s) & \mathbf{B}(s) \\ \mathbf{B}(-s) & \mathbf{A}(-s) \end{pmatrix} \begin{pmatrix} \hat{\sigma}_1(s) \\ \overline{\hat{w}_1(-s)} \\ \overline{\hat{\sigma}_1(-s)} \\ \hat{w}_1(s) \end{pmatrix}, \quad (3.57)$$

where the matrix of the system is the product of matrixes specified for each layer as shown below

$$\begin{pmatrix} \mathbf{A}(s) & \mathbf{B}(s) \\ \mathbf{B}(-s) & \mathbf{A}(-s) \end{pmatrix} = \prod_{n=1}^N \begin{pmatrix} \mathbf{A}(2h_n s, \kappa_n, G_n) & \mathbf{B}(2h_n s, \kappa_n, G_n) \\ \mathbf{B}(-2h_n s, \kappa_n, G_n) & \mathbf{A}(-2h_n s, \kappa_n, G_n) \end{pmatrix}. \quad (3.58)$$

The column in the right-hand side is found from the FT of the boundary conditions (3.18)–(3.19) that can be presented in the form:

$$\hat{\sigma}_1(s) = \sum_{j=1}^J P_j e^{-ist_j}, \quad \hat{w}_1(s) = \hat{w}_1^{\text{ideal}}(s) + \mathbf{E}. \quad (3.59)$$

Here \mathbf{E} designates a symbolic operator that models scattering of the data in the Fourier space and the transformation $\mathbf{F}(\delta(x)) = 1$ is taken into account.

Let δ be the variation of the solution due to measurement errors. Then as follows, from (3.57) and (3.58), the errors in the solution on the $(N + 1)$ th interface can be estimated as follows

$$\begin{aligned} \delta \begin{pmatrix} \hat{\sigma}_{N+1}(s) \\ \hat{w}_{N+1}(-s) \end{pmatrix} &= \mathbf{A}(s) \delta \begin{pmatrix} \hat{\sigma}_1(s) \\ \hat{w}_1(-s) \end{pmatrix} + \mathbf{B}(s) \delta \begin{pmatrix} \overline{\hat{\sigma}_1(-s)} \\ \hat{w}_1(s) \end{pmatrix} = \varepsilon \begin{pmatrix} a_{11}(s) & a_{12}(s) \\ a_{21}(s) & a_{22}(s) \end{pmatrix} \begin{pmatrix} 0 \\ \hat{\mathbf{E}} \end{pmatrix} + \\ &+ \varepsilon \begin{pmatrix} b_{11}(s) & b_{12}(s) \\ b_{21}(s) & b_{22}(s) \end{pmatrix} \begin{pmatrix} 0 \\ \mathbf{E} \end{pmatrix} = \varepsilon \begin{pmatrix} a_{12}(s) & b_{12}(s) \\ a_{22}(s) & b_{22}(s) \end{pmatrix} \begin{pmatrix} \mathbf{E} \\ \hat{\mathbf{E}} \end{pmatrix}. \end{aligned} \quad (3.60)$$

This formula shows that the solution in the Fourier space depends on the data continuously, which, in general, manifests stability of the solution provided that the norm of the matrix in (3.60) is bounded.

One may possibly note that the error operator \mathbf{E} could routinely be removed by any standard procedure of data smoothing especially if uniformly or normally distributed random numbers with zero mean are used for modelling errors. This, for instance, is achieved by applying the fast Fourier transform procedure to (3.19) followed by zeroing all elements in the array of Fourier coefficients that are responsible for high frequencies. It would obviously work if one were able to separate the ideal displacements from noise, which does not sound realistic. Therefore, after smoothing the displacement vector would still contain errors caused by smoothing the “ideal” part of the cumulative data despite the noise filtered out.

3.6 Inverse Problem of Crack Detection

3.6.1 An Interface Crack

We further consider the case of inhomogeneous strip partly debonded from the upper half-plane as shown in Fig. 3.2.

The result of the previous section demonstrates that the solution for both stress and displacement vectors on the interface between the strip and the base is found with certain errors. On the other hand, if on the boundary the stresses σ_0 and displacements w_0 are known exactly, they should satisfy the following complex equation that can be deduced from two real integral equations presented in [17]

$$\frac{\kappa_0 - 1}{2} \sigma_0(x) - \frac{\kappa_0 + 1}{2\pi i} \int_{-\infty}^{+\infty} \frac{\sigma_0(t)}{t - x} dt - 2G_0 \overline{w_0(x)} = 0, \quad \text{Im}(x) = 0. \quad (3.61)$$

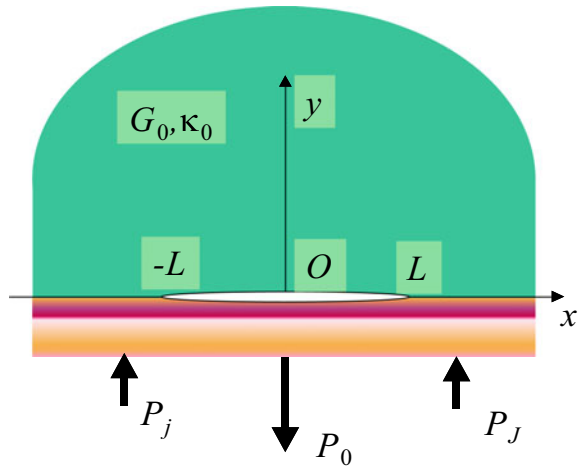
Application of the FT to (3.61), taking into account that the integral in (3.61) is of the convolution type and the FT of its kernel is $\mathbf{F}(x^{-1}) = -i\pi \text{sgn}(s)$, results in

$$2G_0 \widehat{w_0}(-s) = \left(\frac{\kappa_0 - 1}{2} - \frac{\kappa_0 + 1}{2} \text{sgn}(s) \right) \widehat{\sigma_0}(s). \quad (3.62)$$

This condition serves as a criterion of the full bonding of the strip and the base provided that σ_0 and w_0 are replaced, due to continuity, by the stresses σ_{N+1} and displacements w_{N+1} , respectively, calculated by the exact formula in (3.57).

For modelling, we need the ideal displacements on Γ_1 that enter into boundary conditions (3.19) and their FT (3.59). These can be obtained from (3.57) by assuming the continuity conditions and by rearranging equations in (3.57), which leads to

Fig. 3.2 Inhomogeneous strip partly debonded from the substrate



the following relationships between the stress and displacement vectors on the boundaries Γ_1 and Γ_N

$$\begin{pmatrix} \hat{\sigma}_0(s) \\ \hat{\sigma}_0(-s) \end{pmatrix} - \begin{pmatrix} a_{11}(s) & b_{11}(s) \\ b_{11}(-s) & a_{11}(-s) \end{pmatrix} \begin{pmatrix} \hat{\sigma}_1(s) \\ \hat{\sigma}_1(-s) \end{pmatrix} = \begin{pmatrix} a_{12}(s) & b_{12}(s) \\ b_{12}(-s) & a_{12}(-s) \end{pmatrix} \begin{pmatrix} \overline{\hat{w}_1(-s)} \\ \hat{w}_1(s) \end{pmatrix}, \\ \begin{pmatrix} a_{21}(s) & b_{21}(s) \\ b_{21}(-s) & a_{21}(-s) \end{pmatrix} \begin{pmatrix} \hat{\sigma}_1(s) \\ \hat{\sigma}_1(-s) \end{pmatrix} = \begin{pmatrix} \hat{w}_0(-s) \\ \hat{w}_0(s) \end{pmatrix} - \begin{pmatrix} a_{22}(s) & b_{22}(s) \\ b_{22}(-s) & a_{22}(-s) \end{pmatrix} \begin{pmatrix} \overline{\hat{w}_1(-s)} \\ \hat{w}_1(s) \end{pmatrix}. \quad (3.63)$$

Any of these equations can be used to generate the data for w_1 ; the former equation is suitable if one uses the solution of fundamental Problem 2 presented by (3.33)–(3.35); the latter is suitable if Problem 1, Eqs. (3.29)–(3.30), is used.

As soon as the distribution for w_1 has been generated, one can find the solution for σ_0 and w_0 and check if they satisfy (3.62). This means the following equality should be satisfied exactly if the noise is absent

$$\mathbf{C}(s) \left[\mathbf{A}(s) \begin{pmatrix} \hat{\sigma}_1(s) \\ \hat{w}_1(-s) \end{pmatrix} + \mathbf{B}(s) \begin{pmatrix} \overline{\hat{\sigma}_1(-s)} \\ \hat{w}_1(s) \end{pmatrix} \right] = 0, \quad (3.64)$$

where

$$\mathbf{C}(s) = (\beta_0(s), -2G_0), \quad \beta_0(s) = \frac{\kappa_0 - 1}{2} - \frac{\kappa_0 + 1}{2} \text{sgn}(s). \quad (3.65)$$

If the measurements of displacements w_1 contain errors, then (3.64) should be satisfied approximately. It has been discussed already that the noise could be filtered out but this still does not guaranty that we know the displacement w_1 accurately enough in order to conclude on possible delamination of the interface. As additional information one can analyse the profile of σ_0 that should correspond to typical stress distributions near the cracks, in particular, high gradient could help to localise crack tips and low level of stresses could be associated with the delamination zone. Better results can be obtained if one uses not only the continuity conditions but takes into account the influence of the interface crack from direct modelling. This is discussed in the next subsection for a simplified example.

The continuity conditions also can be used to reveal that the following function:

$$\beta(s) = \frac{G_{\text{eff}}}{G_0} \beta_0(s) = \frac{G_{\text{eff}}}{G_0} \begin{cases} \kappa_0, & s < 0 \\ -1, & s > 0 \end{cases}. \quad (3.66)$$

This is the only one that controls dissimilarity of elastic properties, where G_{eff} can be considered as the effective shear modulus of the homogeneous strip.

3.6.2 Example: Discussion of Possibility of Crack Detection

Let us consider a bi-material structure which bases in much stiffer than the coating. Thus, we can assume that one side of the coating is clumped and therefore $w_2(t) = 0$ on Γ_2 . The boundary Γ_1 is stress-free apart from the origin where it is subjected to a concentrated load of intensity P_0 acting normal to the surface, i.e. $\sigma_1(t) = P_0\delta(t)$, $\text{Im}P_0 = 0$.

Firstly we solve the direct problem in order to generate synthetic measurements of the displacements on the stress-free surface of the coating. By applying the FT one finds the following boundary conditions for the direct Problem 1

$$\hat{\sigma}_1(s) = P_0, \quad \hat{w}_2(s) = 0 \quad (3.67)$$

Then the solution for $\mathbf{F}(\Phi(z))$ in (3.29), which is valid for $0 \leq y \leq 2h$, assumes the form:

$$\hat{\Phi}(s, y) = \frac{e^{(h-y)s} P_0}{\Delta_1(s)} [(\kappa e^{2hs} + e^{-2hs})e^{hs} - 4hse^{-hs}]. \quad (3.68)$$

The FT transforms of w_1 and σ_2 are found from the FT of (3.6) by taking into account that $w_2 = 0$

$$2G\overline{\hat{w}_1(-s)} = -P_0 + \frac{e^{-2hs} P_0(\kappa + 1)}{\Delta_1(s)} (\kappa e^{-2hs} + e^{2hs} + 4hse^{2hs}), \quad (3.69)$$

$$\hat{\sigma}_2(s) = \frac{P_0(\kappa + 1)}{\Delta_1(s)} (\kappa e^{-2hs} + e^{2hs} + 4hse^{2hs}). \quad (3.70)$$

It follows from (3.69) and (3.70) that

$$2G\overline{\hat{w}_1(-s)} = -P_0 + e^{-2hs} \hat{\sigma}_2(s) \quad \text{or} \\ \hat{\sigma}_2(s) = e^{2hs} \left(P_0 + 2G\overline{\hat{w}_1(-s)} \right). \quad (3.71)$$

This equation can be used as the condition for examining the integrity of the interface if σ_2 is smaller than the tensile strength. The normalised distributions of the stresses σ_2/P_0 and the derivatives of the displacements $2Gw_1/P_0$ are shown in Figs. 3.3 and 3.4, respectively, for the case $\kappa = 1.8$ and $2h = 1$. The inverse FT have been calculated numerically, directly for σ_2 as its image has exponential order, see (3.70), while for w_1 has been calculated as the sum of analytically found inverse of $\beta_0(s)$, see (3.65), with the numerically calculated inverse of the difference of $\mathbf{F}(2Gw_1)$ in (3.69) and $\beta_0(s)$.

It is evident from Figs. 3.3 and 3.4 that the maximum tensile stress occurs at point $x = 0$ that lies opposite to the point of application of the concentrated load. This maximum is equal to $0.808P_0$ and then the normal stress rapidly decreases to $0.015P_0$

Fig. 3.3 Profiles of the normal (solid) and shear (dashed) stresses normalised by P_0 for $\kappa = 1.8$ and $2h = 1$

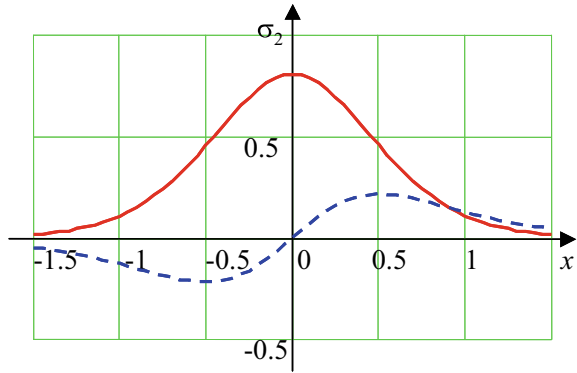
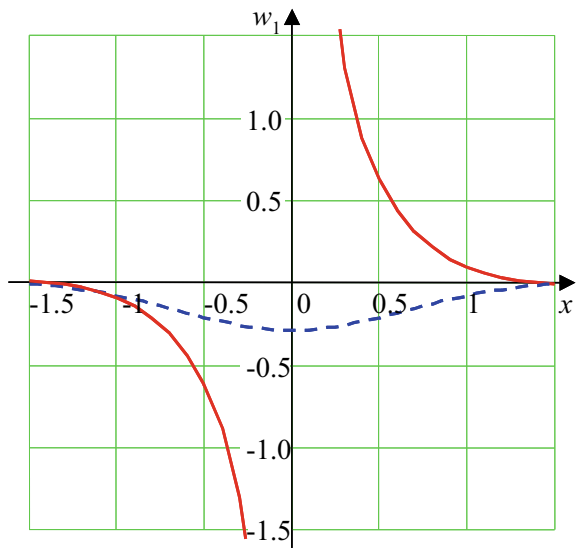


Fig. 3.4 Profiles of the derivatives of the normal (solid) and tangential (dashed) displacements along the stress-free surface for $P_0/2G = 1$, $\kappa = 1.8$ and $2h = 1$



at the points $x = \pm 1.5$. The shear stresses have extrema of about $\pm 0.22P_0$ at the points $x = \pm 0.5$. Delamination may occur at any of these three points depending on the tensile and shear strengths of the interface and can propagate along the interface. It can be modelled as a combined open-shear crack of the length $2L$. In this case, the condition $w_2 = 0$ will be valid only outside the crack.

Let us consider the second problem assuming $\sigma_1 = 0$ and $w_2 = 0$ outside $|x| > L$ while within it is an odd unknown function which FT being denoted as $\mu(s)$

$$\hat{\sigma}_1(s) = 0, \quad 2G\hat{w}_2(s) = \mu(s). \tag{3.72}$$

Then (3.29) becomes

$$\hat{\Phi}(s, y) = \frac{e^{(h-y)s}}{\Delta_1(s)} \left[(\kappa e^{2hs} + e^{-2hs}) e^{-hs} \mu(s) - 4hs e^{hs} \overline{\mu(-s)} \right]. \quad (3.73)$$

Let us find the FT of w_1 and its complex conjugate from the FT of (3.6) taking into account that $\sigma_1 = 0$

$$2G\hat{w}_1(s) = \frac{\kappa + 1}{\Delta_1(s)} \left[(\kappa e^{2hs} + e^{-2hs}) \mu(s) - 4hs e^{2hs} \overline{\mu(-s)} \right], \quad (3.74)$$

$$2G\overline{\hat{w}_1(-s)} = \frac{\kappa + 1}{\Delta_1(s)} \left[4hs e^{-2hs} \mu(s) + (\kappa e^{-2hs} + e^{2hs}) \overline{\mu(-s)} \right]. \quad (3.75)$$

Solution of (3.74) and (3.75) for μ gives

$$\begin{aligned} (\kappa + 1)\mu(s) &= -2G \left((\kappa e^{-2hs} + e^{2hs}) \hat{w}_1(s) + 4hs e^{2hs} \overline{\hat{w}_1(-s)} \right), \\ (\kappa + 1)\overline{\mu(-s)} &= 2G \left(4hs e^{-2hs} \hat{w}_1(s) - (\kappa e^{2hs} + e^{-2hs}) \overline{\hat{w}_1(-s)} \right). \end{aligned} \quad (3.76)$$

Now one can find $\mathbf{F}(\sigma_2)$ from the FT of (3.6) in the form

$$\hat{\sigma}_2(s) = -\overline{\mu(-s)} + \frac{e^{2hs}(\kappa + 1)}{\Delta_1(s)} \left[(\kappa e^{-2hs} + e^{2hs}) \overline{\mu(-s)} + 4hs e^{-2hs} \mu(s) \right]. \quad (3.77)$$

It follows from (3.75) and (3.77) that

$$\hat{\sigma}_2(s) = -\overline{\mu(-s)} + 2G e^{2hs} \overline{\hat{w}_1(-s)}. \quad (3.78)$$

By superposition of these two solutions, one can find the distributions of the total stresses acting on the interface and the derivative of the total displacements on the stress-free surface. The relationship between their FT is as follows:

$$\hat{\sigma}_2(s) = -\overline{\mu(-s)} + e^{2hs} \left(P_0 + 2G \overline{\hat{w}_1(-s)} \right). \quad (3.79)$$

Here σ_2 is the sum of the solutions obtained above, which correspond to the aggregated boundary conditions (3.67) and (3.72)

$$\hat{\sigma}_1(s) = P_0, \quad 2G\hat{w}_2(s) = \mu(s), \quad (3.80)$$

while the FT of the function w_1 is found approximately by displacement monitoring. It should be noted that it is not realistic to separate measurements of w_1 into two parts that correspond to the problems considered above, as we have no information about the existence of a delamination in advance. Therefore, the crack diagnostics depends on the level of measurement errors. In the case of an intact interface theoretically, $\mu = 0$ and the solution for the contact stresses on Γ_2 is given by formula (3.71). However, if the displacement measurements of w_1 include errors specified by

unknown function E then $w_1 = w_1^{\text{ideal}} + E$ and (3.71) assume the form somewhat similar to (3.79), namely

$$\hat{\sigma}_2(s) = \overline{\hat{E}(-s)} + e^{2hs} \left(P_0 + 2G\overline{\hat{w}_1^{\text{ideal}}(-s)} \right). \quad (3.81)$$

Now it is evident that cracks can be detected if their contribution to the stress field determined by the crack opening displacements, COD, is greater than the level of errors determined by the function E . In this case, the errors can be filtered out by employing, for example, the fast Fourier transform technique with the use of a windowing function that rejects low values in the frequency domain. In the Fourier space, this merely means that if the norm of the function $\|\mu\|$ in (3.79) is essentially greater than the norm of $\|\mathbf{F}(E)\|$ in (3.81) then crack detection is possible; otherwise, the crack cannot be distinguished from noise in the data.

It is evident from Fig. 3.4 that the derivative of COD becomes small on the distances from the point of load application of the order of the coating thickness, i.e. for $|x| > 1$ the level of noise could be higher than the level of measured strains. Therefore, it can be recommended to conduct measurements as close as possible to the point of load application. For example, if we assume 5% errors for the configuration depicted in Fig. 3.4, then the interval where the noise is smaller than the tangential strain is $(-1.155, 1.155)$ while for the normal deflection it is even narrow $(-1.125, 1.125)$. Thus, the reasonable interval of measurements can be estimated as $(-1, 1)$.

For a rough estimation of the detectable COD, let us model delamination by a pair of dislocations of the magnitudes $\pm\omega_0$ with the cores placed at points $t = \pm 1$. Thus, $w_2(t) = -i\omega_0 \frac{d}{dt} \frac{\text{sgn}(t+1) - \text{sgn}(t-1)}{2}$ and $\omega_0 > 0$ can be associated with the dimensionless mean normal COD over the delamination; the minus sign is due to opposite direction of the crack opening with respect to the direction of the y -axis. By applying the FT one finds

$$\hat{\sigma}_1(s) = P_0, \quad 2G\hat{w}_2(s) = \mu(s) = 2G\omega_0 \sin(s). \quad (3.82)$$

Since the sin function is bounded, it becomes obvious that the crack detection would be possible if the level of errors does not exceed the normalised average COD. It is evident from Fig. 3.4 that the derivative of COD becomes small on the distances from the point of load application of the order of the coating thickness.

3.7 Conclusions

The problem of crack detection on the interface between dissimilar layered media has been analysed in this study on the basis of direct and inverse formulations for a multilayered 2D package. The modelling assumes that the strain/displacement measurements are conducted on the stress-free surface of the external boundary that

is loaded by a set of known concentrated loads. Therefore, the mathematical problem is overdetermined and as a result, possesses unstable solutions and manifests itself as the Cauchy initial value problem formulated in terms Kolosov–Muskhelishvili complex potentials.

The solutions of both direct and inverse problems have been found in analytical form by applying the Fourier transform. All fundamental direct BVP have an auxiliary role for this study. They are used in order to generate synthetic data of the strain measurements on the stress-free surface. The solution of the Cauchy problem is found for the package of dissimilar layers that form an inhomogeneous strip that can be bonded to a base modelled by a half-plane made of a different material. If the interface between the strip and the base is fully bonded, then the measured displacements should satisfy the conditions of continuity of the displacement and stress vectors and therefore they cannot be set independently. This condition is considered as a criterion of fully bonding. If the criterion is not satisfied, this can be viewed as the indication of partial delamination of the materials on their interface. However, given that the strain measurements include some noise this can also be considered as “a false warning”. In order to illustrate this situation, an example has been considered to discuss what level of measurement errors can be acceptable for crack detection.

Acknowledgements This work was supported by the grant of the Government of the Russian Federation No. 14.Z50.31.0046.

References

1. Ufyjand, J.S.: Integral Transforms in Problems of the Elasticity Theory. Nauka, Leningrad (1968). in Russian
2. Shevljakov, Y.A.: Matrix Algorithms in the Theory of Elasticity of Inhomogeneous Media. Vischa Schola, Kiev-Odessa (1977). in Russian
3. Shvab, A.A.: Incorrectly posed static problems of elasticity. *Solid Mech.* **24**, 98–106 (1989)
4. Kubo, S.: Inverse problems related to the mechanics and fracture of solids and structures. *JSME Int. J.* **31**, 157–166 (1988)
5. Gao, Z., Mura, T.: Elasticity problems with partially overspecified boundary conditions. *Int. J. Eng. Sci.* **29**(6), 685–692 (1991)
6. Yeih, W.C., Koya, T., Mura, T.: An inverse problem in elasticity with partially overspecified boundary conditions. I. Theoretical approach. *Trans. ASME J. Appl. Mech.* **60**, 595–600 (1993)
7. Hsieh, S.C., Mura, T.: Nondestructive cavity identification in structures. *J. Solids Struct.* **30**(12), 1579–1587 (1993)
8. Bonnet, M., Constantinescu, A.: Inverse problems in elasticity. *Inverse Prob.* **21**, R1–R50 (2005)
9. Tikhonov, A.N., Arsenin, V.Y.: *Solution of Ill-posed Problems*. Winston, Wiley, New York (1977)
10. Marin, L., Lesnic, D.: Boundary element solution for the Cauchy problem in linear elasticity using singular value decomposition. *Comput. Methods Appl. Mech. Eng.* **191**(6), 257–270 (2002)
11. Galybin, A.N.: Determination of softening law by measuring crack opening displacements. In: Dyskin, A.V., et al. (eds.) *Structural Integrity and Fracture*, pp. 35–41. Lisse, The Netherlands, Swets & Zeitlinger B.V. (2002)

12. Galybin, A.N., Rogerson, G.A.: Ill-posed problem of the Cauchy type for an elastic strip. *Math. Mech. Solids* **24**(9), 2986–2998 (2019)
13. Muskhelishvili, N.I.: *Some Basic Problems of the Mathematical Theory of Elasticity*. P. Noordhoff, Groningen, the Netherlands (1963)
14. Erdogan, F., Gupta, G.: The stress analysis of multi-layered composites with a flaw. *Jnt. J Solids Struct.* **7**(8), 39–61 (1971)
15. Bateman, H., Erdelyi, A.: *Tables of Integral Transforms*. McGraw-Hill, New York (1954)
16. Khrapkov, A.A.: *Wiener-Hopf Method in Mixed Elasticity Theory Problems*. VNIIG, Sankt-Peterburg (2001)
17. Johnson, K.L.: *Contact Mechanics*. Cambridge University Press (1985)

Chapter 4

Experimental and Clinical Investigation of Carbon Nanostructural Material for Orthopaedic Applications



George Sh. Golubev, Valery N. Varavka, and Michael B. Rodin

Abstract New carbon nanostructured material is an ideal candidate for bone defects substitution and development of fundamental approaches for conventional orthopaedic surgery. Experiment on rats has been performed, which demonstrated biological compatibility with bone. Some characteristics of biocomposite at the bone-to-implant interface have been described. Mechanical properties of a wedge-shaped implant were tested under static and cyclic loading conditions. The need in compression between bone and implant has been shown. Clinical application of some special-shaped implants for substituting large bone defects and axial bone disorders has been performed. The excellent clinical and economic prospects of new carbon nanostructural implants have been demonstrated.

Keywords Carbon nanostructured materials · Biocomposites · Bone defects substitution

4.1 Introduction

Research and development of the new materials for bone defects substitution depend on some essential paradigms: the similarity of biomechanical properties of the new material to ones of bone, the ability to transform to the host's bone tissue, and the

G. Sh. Golubev (✉)

Department of Trauma and Orthopaedic Surgery, Rostov State Medical University,
Nahichevansky av., 29, Rostov-on-Don 344022, Russian Federation
e-mail: dovegg@mail.ru

V. N. Varavka

Research and Education Centre "Materials", Don State Technical University, pl. Gagarina 1,
Rostov-on-Don 344000, Russian Federation
e-mail: varavkavn@gmail.com

M. B. Rodin

Department of Orthopaedic Surgery, Rostov City Center of Trauma and Orthopaedic Surgery,
Rostov-on-Don, Russian Federation
e-mail: rodin_mihail@mail.ru

© Springer Nature Switzerland AG 2020

S. M. Aizikovich et al. (eds.), *Modeling, Synthesis and Fracture of Advanced Materials for Industrial and Medical Applications*, Advanced Structured Materials 136,
https://doi.org/10.1007/978-3-030-48161-2_4

minimal host's immune response. Reconstruction of the critical bone defect is a multipurpose clinical problem. It has several ways to resolve, including an external fixation with bone transport, massive bone autografts, and amputations [1]. Synthetic materials open new directions to success bone defects substitution. Experimental and clinical investigations report successful implementations of calcium phosphate bioceramics, titanium sponges, and tantalum scaffolds as bioinert implants [2, 3].

Carbon implants have gained attention during several last years. Development of some new technologies to produce different types of carbon composites has given researchers a possibility to use them for small joints arthroplasty, osteosynthesis, and bone defects substitution. The main features of carbon implants are minimal cellular reaction and possibilities to manage biomechanical properties of implants at the design stage, as shown in experimental and clinical studies [4, 5].

4.2 Types of Carbon Materials and Implants for Orthopaedic Applications

Several classes of artificial carbon materials are known. They differ according to patterns of the pyrolytic process leading to carbon sedimentation with different carbon grids. One can find some samples' description of carbon materials for orthopaedic surgery on (Fig. 4.1).

The process of pyrolytic carbon-carbon composites' production consists of carbon fibre object modelling, then carbonizing at 1000 °C in nitrogen, impregnating with phenolic resin and graphitizing at 2200 °C in argon. Pyrolytic carbon deposits from propane in a tumbling bed reactor. The technology described above enables a very smooth glass-like surface of implants. That is why pyrolytic carbon implants are widely used for small joint arthroplasty since the early 1980s [7–10]. Hand and foot surgery are the fields where properties of pyrolytic carbon implants have adequate clinical statistics. The main problems revealed are squeaking and bad osseointegration leading to aseptic instability of implants with revision rate up 39% [8–11].

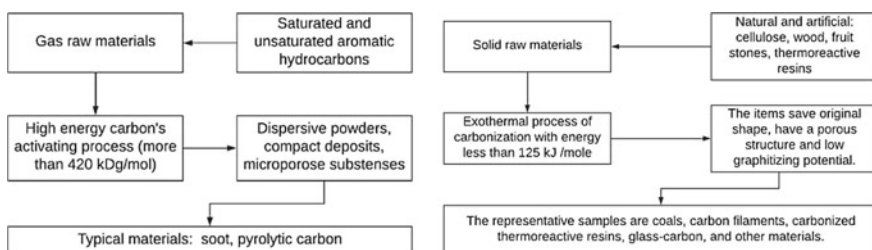


Fig. 4.1 Creation of carbon materials from gas and solid raw sources (adapted from [6])

Some impressive clinical results were obtained with the pyro-condensed fabric frameworks. Small-size packages in the form of plates were created based on fabrics with the different elastic modulus of carbon filaments. Authors investigated low-modular URALS-TM/4 and high-modular UT-900 fabrics. Crafted package was stitched on the sewing machine by low-modular carbon filament of the URALS-N or URALS-NSH brand with the distance between lines of 5–10 mm. Availability of the third coordinate in a framework provides an increase in inter-laminar strength of carbon–carbon composite materials. The research of mechanical and structural characteristics carbon–carbon composite materials revealed rather high values at materials with an apparent density not lower than 1.35–1.45 g/cm³. Mechanical characteristics of carbon–carbon composite materials were determined by standard methods, and they were similar to the bone's ones [12]. Also, authors report numerous procedures to substitute cranium defects, but a substitution of loading parts of the skeleton was rare, and implants were removed due to undescribed failures.

The successful development of carbon-fabric hip endoprosthesis stem has been previously described. The stem was manufactured by hot pressing at 380 °C and average pressure 10 atm (Fig. 4.2). The researchers emphasize that this type of stems has properties that are equal to bone's modules. Animal tests show that forces' distribution between carbon stem and the femur bone is much better compared to titanium stem [13].

Fig. 4.2 Composite carbon hip stem (Fig. 25 from [13])



4.3 Carbon Nanostructured Materials

Carbon nanostructured materials based on nanotubes and carbon nanofibers attract growing attention due to their structural and mechanical characteristics. These well-ordered hollow nanostructures consist of carbon atoms bonded to each other via sp^2 bonds. Excellent mechanical properties and high thermal conductivity are the results of such bonding. Graphene layers are rolled into cylinders and form carbon nanotubes. If graphene sheets are curved at some angle to create stacks of nanocones, they form nanofiber (Fig. 4.3). Characteristics of one- and multilayer nanotubes are relatively well known. They have incredibly high mechanical strength (Young's modulus varies between 410 and 4150 GPa with mean value 1800 GPa). The dependence of Young modulus on nanotubes radius and quality of the shape are also known [14, 15].

The porous structure of carbon nanostructural materials makes it possible to use them as a scaffold for bone defects substitution. One can suppose that such implants shorten the bed rest period, lower the cost of rehabilitation, and social impact of disability.

Carbon nanostructural implants (CNI) are being manufactured by NanoTechMed Plus, Russia, according to TY 9398-001-30422885-2014 and Certificate of accordance № POCC RU.HM41.H01487 (valid since 30.11.2017 to 30.11.2020, № 0071740). This carbon-to-carbon composite consists of the threads reinforcing basis, which represents a framework from vertical and horizontal slices of the cores formed from carbon filaments (Fig. 4.3) that connects layers one to each other.

Some stages of the carbon nanoimplants production are shown in Fig. 4.4. According to the technology described, the fabrication of the carbon implants consists of four main steps:

1. Production of rod elements by binding carbon fibres with polymer resin.
2. Rod elements assembly to form the skeleton of composite material.
3. Carbon matrix synthesizing in the reinforcing skeleton's pores.
4. Mechanical processing of the carbon composite block to produce the implants for specific needs.

Synthesis of a carbon nanostructural matrix from gaseous hydrocarbons provides its high purity. The composite consists entirely of carbon. The lack of metals and

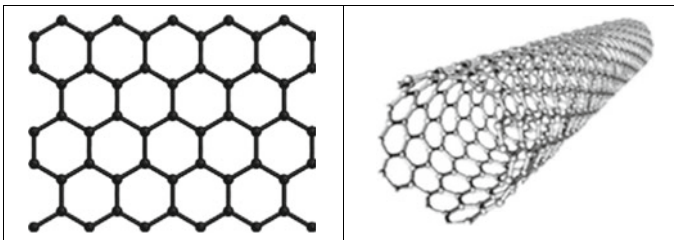


Fig. 4.3 Graphene sheet (on the left) and graphene nanotube (on the right)

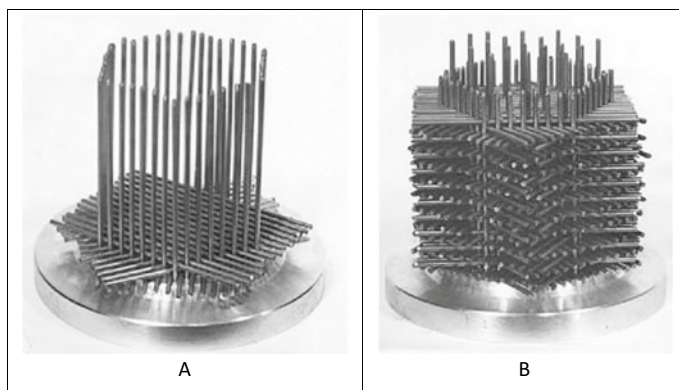


Fig. 4.4 Assembly of a framework from carbon threads (A—the starting layer; B—the framework just before transfer to reactor). Reproduced from [16]

other impurities in the material significantly influences biocompatibility. The energy dispersive X-ray analysis of the material confirms its composition (Fig. 4.5).

Mechanical characteristics of CNI approach to bone ones. The porosity of the material is not less than 20 volume %, and the size of each pore varies between 100 and 1000 microns. The compression strength is not less than 30 MPa, the compression Young modulus is not less than 1.5 GPa, density is between 1.4 and 1.78 g/cm³, and the mean size of graphite particles is not more than 30 nm. A mass fraction of reinforcing fibres in the mass of a matrix is not less than 0.4 [17]. Comparative data on mechanical properties of CNI and bone are shown in Table 4.1.

The data prove that the strength of carbon implants exceeds bone strength at axial loading and bending. This feature enables the application of implants for bone defects substitution. The material is diamagnetic; hence, it does not prevent MRI and physiotherapeutic methods after the procedure. Thus, these materials are very important for orthopaedic application, owing to the extreme mechanical properties and the carbon's biocompatibility [18].

4.4 Testing of Carbon Nanostructural Material's Properties

Relevance of the described relatively new carbon nanostructural material evaluation as the subject for multipurpose application at orthopaedic surgery was substantiated above. The most interesting fields are the quality of biocomposite at the implant–bone interface, methods to improve integration of the implant to the bone, and technologies of massive bone defects substitution by CNI.

Experimental estimation of bone tissue reaction and osteoconductive features of CNI was done *in vivo*. Wedge osteotomy of a femur bone was performed in experimental circumstances on 26 white rats (control = 6, experiment = 21). The

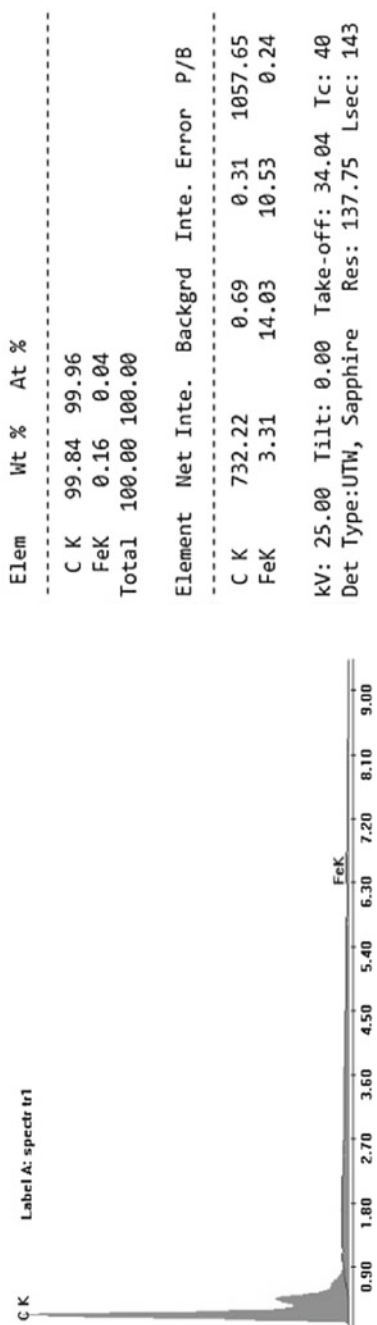


Fig. 4.5 EDAX spectrum of carbon nanostructural implant produced by TY 9398-001-30422885-2014 (authors' material)

Table 4.1 CNI and bone strength characteristics at different types of loading

Type of loading	Sample	Section size, mm	Strength, GPa	Type of destruction
Compression	Rib's body	14 × 7	1.23	Cortical fracture
	Rib's angle	(12 × 10) + (14 × 8)	1.23	Cortical fracture at the vertex of an angle
	Iliac crest	(19 × 15) + (20 × 15)	2.01	Shift with consequent fracture
	CNI	10 × 10	6.03	Destruction of the loaded part
Bending	Rib's body	14 × 7	0.15	Rupture of cortical layer
	Rib's angle	(12 × 10) + (14 × 8)	0.51	Rupture of cortical layer
	Iliac crest	(19 × 15) + (20 × 15)	0.93	Rupture of cortical layer
	CNI	10 × 10	1.65	Stratification of an implant

experiment was approved by the Ethic Council of Rostov State Medical University and followed demands of European Convention [19, 20]. Wedge-shaped ($h = 4$ mm, $r = 3$ mm, $\alpha = 12^\circ$) implants were crafted from the carbon nanomaterial described above.

Left or right side for osteotomy was chosen randomly. At control group, osteosynthesis performed after osteotomy. At experimental animals, wedge-shaped defect was substituted with carbon wedge. In both cases, the osteosynthesis was performed with compression by shape-memory brackets. Rats were withdrawn from the experiment in 3 months. The “bone-implant-bone” samples were prepared for consequent investigations.

Mechanical properties of the “bone-wedge-bone” block evaluated by a 3-point bending test. Both ends of the resected 20 mm “bone-implant-bone” cylinder were rigidly fixed on the table of testing machine P₃M-0,1 (Metrotest Ltd., Moscow). The central part was loaded until fracture between implant and bone occurred.

Morphological estimations were carried out with the field emission scanning electron microscope Zeiss Crossbeam 340 (Carl Zeiss Microscopy GmbH, Germany). The microelements distribution in the samples was measured by energy dispersive X-ray analysis with the use of Oxford Instruments X-Max 80. Samples were coated with a thin layer of carbon. The experiment's data is shown in Table 4.2.

The toughness of zone between implants and bone fragments depends of clinical features of consolidation (mean $Tou_{nonun} = 9.10$ MPa, $Tou_{consolid} = 50.82$ MPa, Welsh p -value = 0.001, where Tou_{nonun} is the toughness of non-united “bone-to-implant” samples, $Tou_{consolid}$ is the toughness of clinically consolidated samples, the square of side plane of implant was 0.01118 cm²).

Table 4.2 Results of double-side femur bone osteotomies

R.no	Gender	Weight, g	Eside	Type	Compl	Consolid	Tou, MPa
I	m	363	R	E	0	Consolid	46.05
II	m	490	R	E	1	Nonun	3.22
III	m	300	R	E	0	Nonun	1.18
IV	m	337	R	E	1	Consolid	51.52
V	m	375	R	C	0	Consolid	55.81
VI	m	371	R	E	0	Consolid	48.73
VII	m	302	L	E	0	Consolid	48.62
VIII	m	239	R	E	0	Nonun	0.86
IX	m	420	L	E	0	Consolid	45.30
X	m	219	R	E	0	Consolid	45.83
XI	m	356	L	E	1	Nonun	0.43
XII	m	530	L	E	0	Nonun	0.97
XIII	m	358	R	E	0	Consolid	50.88
XIV	m	330	R	E	0	Nonun	5.26
XV	m	346	L	E	0	Consolid	50.23
XVI	m	334	L	E	0	Consolid	45.94
XVII	m	330	R	E	0	Consolid	48.09
XVIII	m	340	R	E	0	Nonun	51.84
XIX	m	345	L	E	0	Consolid	46.80
XX	m	350	L	E	0	Consolid	48.94
XXI	m	338	R	E	0	Consolid	46.80
XXII	m	338	R	C	0	Consolid	56.89
XXIII	m	343	L	C	0	Consolid	60.11
XXIV	m	339	L	C	0	Consolid	56.89
XXV	m	357	R	C	0	Consolid	56.67
XXVI	m	359	L	C	0	Consolid	55.49

Comments: *R.no*—animal's ID; *Gender*—animal's gender; *Weight*—animal's weight, g; *Eside*—“experimental” side; *Type*—*E*(xperiment), *C*(ontrol); *Compl*—purulent complication, 1—if Yes, 0—if No; *Consolid*—X-ray, consolidation; *Tou*—sample's toughness, MPa

Comparison between toughness at control and experimental cases shows significant differences between them ($Tou_{\text{contr}} = 56.97$ MPa, $Tou_{\text{exp}} = 47.68$ MPa, Welsh p -value = $2.689e-07$).

Detailed visualization of the bone–implant interface shows the interposition of connective tissue between these two objects (refer to Fig. 4.6). The thickness of connective tissue layers depends on the fracture's consolidation or nonunion status of the sample.

Ca²⁺ and P distribution in thickness of an implant was used to estimate penetration of bone tissue. These characteristics for sample 9 are shown in Fig. 4.7.

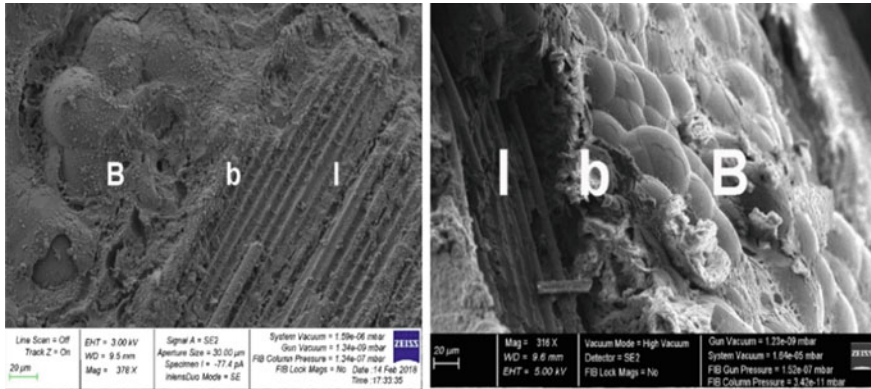


Fig. 4.6 Bone-to-implant border (B—bone, I—implant, b—bone to implant border). On the left: sample 2, full consolidation. On the right: sample 4, nonunion

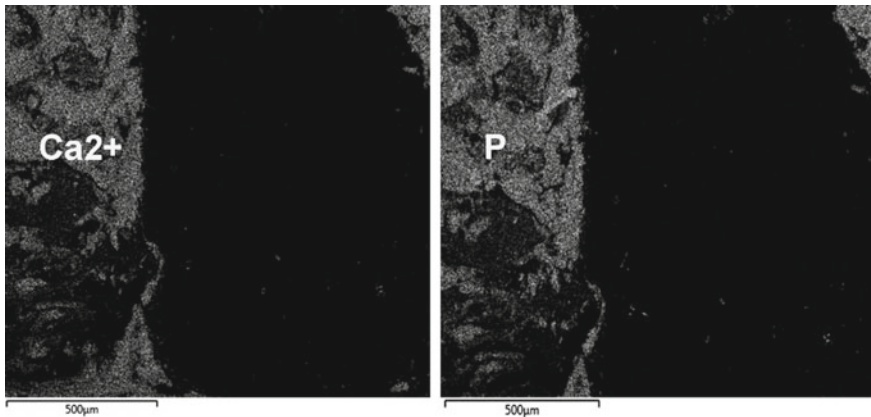


Fig. 4.7 Sample 9. Distribution of Ca²⁺ (blue, on the left) and P (green, on the right)

The obtained data enable to suppose that the quality and the thickness of the biocomposite zone at the bone–implant interface predetermine clinical results of bone substitution. Integration of bone-to-implant in the investigated cases takes place in a very thick layer. Moreover, the absence of microelements inside the body of implants confirms that the implant structure is too subtle. Increasing porosity of material and creation of transverse channels can improve bone conduction and scaffold quality of carbon nanoimplants. This hypothesis was confirmed by data published in [4, 5]. Carbon nanomaterials must be investigated thoroughly to resolve some known issues: increasing callus formation inside and over implants; improving the visibility of these radiolucent materials.

4.5 Biomechanical Properties and Clinical Applications of Carbon Nanostructural Implants

One must differentiate two essential applications of carbon implants: substitution of significant bone defects and correction of wedge-like defects. The most often applications of novice implants are bone osteotomies, nonunions, and osteomyelitis. As the primary stability of CNI is unknown for the most types of implant types, the investigation of primary stability for the wedge-type implant was performed.

Open-wedge high tibial osteotomy was performed on wet calf's tibial bone. According to clinical recommendations, osteotomy was modelled at a "safe zone," and the distal part was moved to get 5 degrees valgus. The defect was filled with specially designed wedge-shape CNI without fixation. Compression forces of peroneal and tibial muscles modelled by rubber strips to reproduce compression of 1.114 MPa. Proximal and distal epiphyses were cut transversally to adapt them to plates of the INSTRON 8801, 5982 servohydraulic testing systems (Fig. 4.8).

The listed loading regimens used:

1. Static compression up to 882 N.
2. Dynamic compression up to 882 N.
3. Cyclic compression from 294 N to 882 N with frequencies 2 Hz and 8 Hz.

Three cycles of static loading (1) were performed. As one can see at diagram 1 (Fig. 4.9) the implant gets its position between bone fragments. Friction force



Fig. 4.8 High tibial osteotomy model (left) is installed to loading machines INSTRON 8801 (middle) and INSTRON 5982 (right)

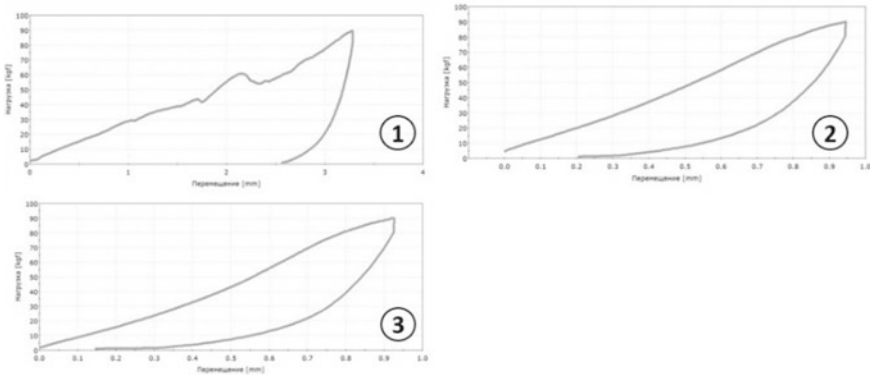


Fig. 4.9 Static loading of the model up to 883 N

increased due to impaction of the implant to bone while the system bone-implant-bone becomes stable. For the first time this process' lasted for 113 s, the second and the third cycles lasted 43 s. On static loading, the system was stable according to diagrams 2, 3 (Fig. 4.9).

Dynamic compression shows deformation and destabilization of the bone-to-implant system. The maximal loading 883 N was achieved in 4.5–4.6 s at the first and the second cycle. At the third loading to 823 N destabilization occurred and the system collapsed (Fig. 4.10). Deformation of the model was 9.2 mm at destruction.

Experimental data show that the wedge-shape CNI implant can be used for correction of axial limb disorders. The necessary condition to enable primary stability of the bone–implant system is preloading.

Cycling compressive loading with the force range from 294 N to 883 N demonstrated residual stability of the preloaded by force of $342\text{ N} \pm 49\text{ N}$ bone–implant system. This data suggests that one must stabilize the implant by orthopaedic devices

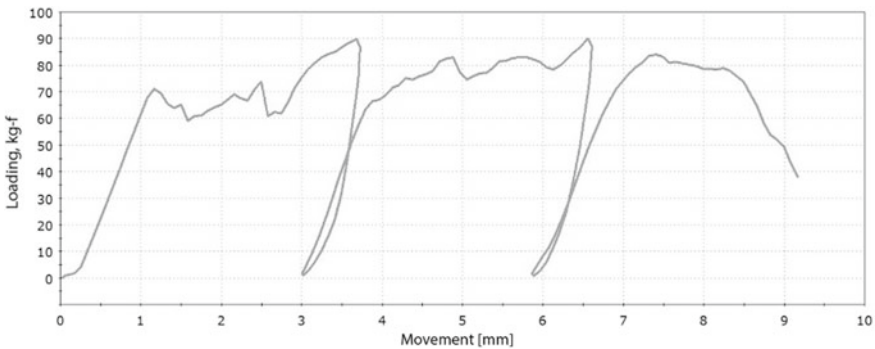


Fig. 4.10 Dynamic loading to destruction

to enable optimal conditions for biocomposite formation at the bone-to-implant border.

Experimental data show that wedge-shape CNI implant can be used for correction of limbs axial disorders. The necessary condition to enable primary stability of the bone–implant system is preloading. Methods of osteosynthesis enable additional stability.

4.6 Clinical Applications of Carbon Nanostructural Implants

4.6.1 Long Bones Defects

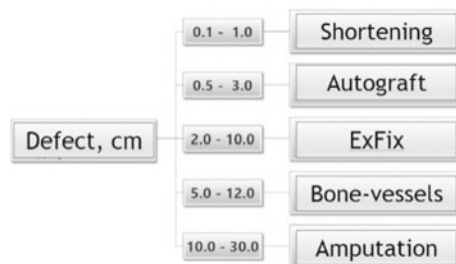
Each defect is unique in several parameters: the bacteriological landscape of a wound; narrow “therapeutic window” to perform full reconstruction of the gap; the existence of a set of options for reconstruction and uncertainty of criteria for their choice. Hence, special treatment of bone defects represents a complex problem. Combinations of the osteoplasty with a cast or external fixator fixation, AO-plating, distraction osteogenesis according to Ilizarov, bone autografts are the methods of choice. And there are no process that guarantees a good result [21–23]. Algorithm of convenient methods’ choice for bone defects treatment depending on the gap’s size is shown in Fig. 4.11.

Defects more exceptional than 60 mm often are followed by traumatization of the main neurovascular brunches, skin, and muscle defects. Substitution’s options on such defects are limited by external fixation, endoprosthetic replacement, allografting. The frequency of failures is high, especially when substituting humeral bone’s defects.

The case below demonstrates the possibility of substituting large humerus bone defects by CNI implants.

30 y/o woman (ID: KO30f) got multiple combined explosive trauma. After primary treatment and infection elimination, she admitted to the hospital with the

Fig. 4.11 Algorithm of bone defects’ substitution depending on gap size (based on literature and clinical experience)



defect of middle and distal thirds of the right humeral shaft (7.5 cm), primarily stabilized by uniaxial external fixation device. She also had neuropathy of a radial nerve with primary deficiency of sensitivity, combined contracture of the right elbow joint; nonunion of proximal 1/3 of the right ulna and foreign matters in soft tissues of the right shoulder joint, and damage of external plantar nerve of the right foot.

On admission, the forearm was fixed at an angle 90° by an external fixation device. Rotation of a forearm was impossible. There was an irregular soft tissue defect at the internal surface of the right shoulder (14×1.4 cm). ROM of the wrist joint and metacarpal joints were limited, muscle force was at 3 points. The sensitivity of 1, 2, 3 fingers was violated (Fig. 4.12).

The specially designed CNI was prepared for implantation from the raw rod having the initial form of a block sized 15.6×150 mm with the rounded sides. The implant was saturated with Gentamycin solution (5 mg per kilogram of patient's weight, 250 mg netto).

Under combined local anaesthesia, an external fixation device was dismantled, lateral approach to the humeral bone executed, and debridement performed. The implant pressed intramedullary into proximal and distal fragments with excellent primary stability. AO-plating was used to increase the strength of the system (Fig. 4.13). The skin wound closed.

The postoperative period was uneventful. Change of structure of bone tissue and signs of osseointegration in the field of introduction CNI to the marrow canal appeared in 2 months. Full functional rehabilitation occurred in 3 months (Fig. 4.14).

The case KO30f demonstrates the excellent economic effect of the bone gap substitution by CNI. Indeed, bone transport by external fixation devices gets T_{month}

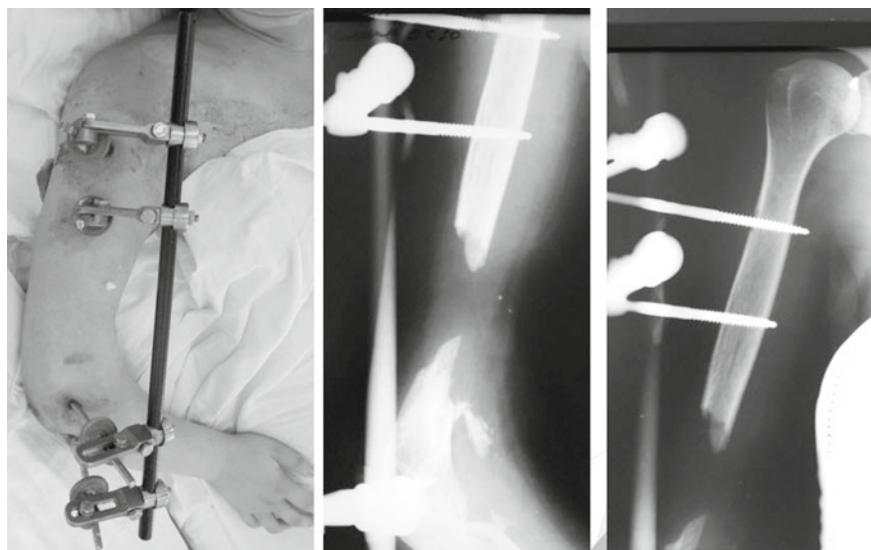


Fig. 4.12 Shoulder external view and X-ray data on admission (KO30f)

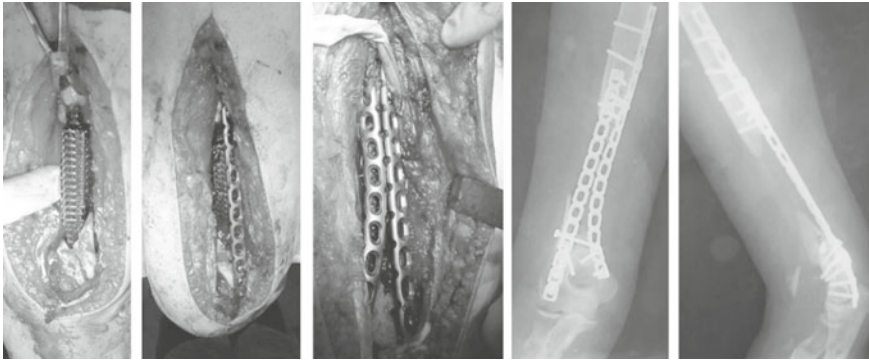


Fig. 4.13 Case KO30f. Stages of bone gap substitution

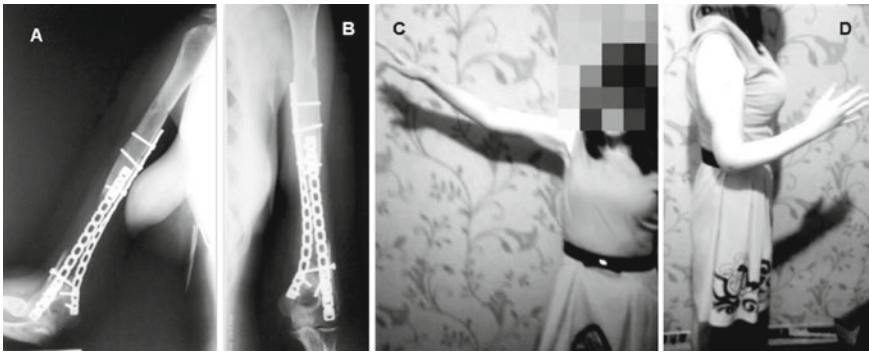


Fig. 4.14 Case KO30f. X-ray control (A, B) and arm function in 3 months (C, D)

$= k * l + t_{\text{cons}}$, where $k = 1.5$ is the statistically curtailed coefficient, l is the size of a defect, cm; $t_{\text{cons}} = 4$ is the average duration of consolidation to get mechanical toughness of regenerate enabling axial loading. For the considered case $T_{\text{month}} = 1.5 * 7.5 + 4 \approx 15.5$ months. According to [24] the average treatment's cost of one such event is up to \$100,000. Substitution of the defect of 7.5 cm with full functional rehabilitation in 3 months opens new horizons for similar complicated cases.

4.6.2 Bone Axial Disorders

Case 2. 62 y older man (SKK62m) with severe varus distal shin deformity. He had an open fracture of the distal metaphysis of tibia and fibula bones on the right at age 12 y/o. The treatment by plaster splinting was performed. The deformity started just after the trauma and notably increased 3 years before admission to the department.



Fig. 4.15 Case SKK62m. From left to right: a general view and X-rays (A–C) before the procedure; X-rays and general view (D–F) after 12 months. CNI is shown in circle (D)

Pain and progressive functional disorders were the main reasons to look for limb reconstruction.

During the procedure osteotomies of tibial and fibular bones were performed with axial correction. Wedge-like tibia's defect was filled with CNI implant. Primary fixation was augmented with the plate. The good functional result achieved in 1 year (Fig. 4.15).

4.7 Conclusion

Biomechanical, experimental, and clinical evaluation of the new carbon nanostructural material proved its high mechanical durability. This feature allows stable primary fixation in any bone gap. Due to clinical demands, the stability can be increased by additional plating or compression by external fixation devices.

The porosity of CNI allows us to saturate them by medicines. This feature enables the use of implants to fill osteomyelitic cavities and defects when impregnating implants with antibiotics and other additional bioactive materials.

The orthopaedic surgeon must follow some simple rules to get optimal results with CNI:

- careful preoperative planning;
- access to CNI of the necessary size;
- axial alignment;
- rigid implant primary fixation + osteosynthesis = early restoration of function.

Some additional investigations are necessary to simplify the fabrication of unique shape implants to increase porosity for the best osteoconduction. Regardless, new carbon nanostructural implants reduce the length of medical rehabilitation and lower the cost of hospital treatment.

Acknowledgments Morphology and elemental analysis were performed at the Laboratory for Electron and Optic Microscopy, Research and Education Centre “Materials,” Don State Technical University (<http://nano.donstu.ru>).

References

1. Nauth, A., Schemitsch, E., Norris, B., Nollin, Z., Watson, J.T.: Critical-size bone defects: is there a consensus for diagnosis and treatment? *J. Orthop. Trauma* **32**(3), S7–S11 (2018)
2. Faria, P.E.P., Carvalho, A.L., Felipucci, D.N.B., Wen, C., Sennerby, L., Salata, L.A.: Bone formation following implantation of titanium sponge rods into humeral osteotomies in dogs: a histological and histometrical study. *Clin. Implant Dent. Relat. Res.* **12**(1), 72–79 (2010)
3. Rumian, Ł., Reczyńska, K., Wrona, M., Tiainen, H., Haugen, H.J., Pamuła, E.: The influence of sintering conditions on microstructure and mechanical properties of titanium dioxide scaffolds for the treatment of bone tissue defects. *Acta Bioeng. Biomech.* **17**(1), 3–9 (2015)
4. Hak, D.J., Mauffrey, C., Seligson, D., Lindeque, B.: Use of carbon-fiber-reinforced composite implants in orthopedic surgery. *Orthopedics* **37**(12), 825–830 (2014)
5. Chua, M., Chui, C.K.: Probabilistic predictive modelling of carbon nanocomposites for medical implants design. *J. Mech. Behav. Biomed. Mater.* **44**, 164–172 (2015)
6. Schuric, A.G.: *The Artificial Carbon Materials*. Public house of Perm State University, Perm (2009)
7. Peškoř, V., Klězl, Z., Balík, K., Adam, M.: Biomechanical and biological properties of the implant material carbon-carbon composite covered with pyrolytic carbon. *J. Mater. Sci. Mater. Med.* **11**(12), 793–798 (2000)
8. McGuire, D.T., White, C.D., Carter, S.L., Solomons, M.W.: Pyrocarbon proximal interphalangeal joint arthroplasty: outcomes of a cohort study. *J. Hand Surg. Eur.* **37**(6), 490–496, Jul (2012)
9. Chan, K., Ayeni, O., McKnight, L., Ignacy, T.A., Farokhyar, F., Thoma, A.: Pyrocarbon versus silicone proximal interphalangeal joint arthroplasty. *Plast. Reconstr. Surg.* **131**(1), 114–124 (2013). Jan
10. Ceruso, M., Pfanner, S., Carulli, C.: Proximal interphalangeal (PIP) joint replacements with pyrolytic carbon implants in the hand. *EFORT Open Rev.* **2**(1), 21–27 (2017)
11. Sweets, T.M., Stern, P.J.: Pyrolytic carbon resurfacing arthroplasty for osteoarthritis of the proximal interphalangeal joint of the finger. *J. Bone Jt. Surg. Ser. A* **93**(15), 1417–1425 (2011)
12. Sinani, I.L., Shchurik, A.G., Osorgin, Y.K., Bushuyev, V.M.: Carbon-carbon composites for orthopaedics and traumatology. *Russ. J. Biomech.* **2**(56), 74–82 (2012)
13. Bandoh, S., et al: The development of composite stem for hip joint, An application of composite materials for medical implant device. *ICCM Int. Conf. Compos. Mater.* pp. 1–9 (2007)
14. Krishnan, A., Dujardin, E., Ebbesen, T.: Young’s modulus of single-walled nanotubes. *Phys. Rev. B - Condens. Matter Mater. Phys.* **58**(20), 14013–14019 (1998)
15. Tran, P.A., Zhang, L., Webster, T.J.: Carbon nanofibers and carbon nanotubes in regenerative medicine. *Adv. Drug Deliv. Rev.* **61**(12), 1097–1114 (2009)
16. Rudskoy, A.I., Belov, I.M., Gordeev, S.K., Barzinskii, O.V., Kondrat’ev, S.Y.: Carbon nanostructured implants for substituting bone defects and process of their production. *Met. Sci. Heat Treat.* **60**(1–2), 18–23 (2018)
17. Gordeev, S.K.: Nanoporous and nanofragmental carbon composite materials. In: Benedek, G., Milani, P., Ralchenko, V.G. (eds.) *Nanostructured Carbon for Advanced Applications* NATO Science Series, Springer Science+Business Media, B.V., pp. 71–78 (2001)
18. Salernitano, E., Migliaresi, C.: Composite materials for biomedical applications: a review. In: *Composite Materials*. Springer-Verlag London, pp. 233–243 (2003)

19. Alemanno, G.: COUNCIL DECISION of 22 July 2003 concerning the conclusion of the protocol of amendment to the European convention for the protection of vertebrate animals used for experimental and other scientific purposes. **2002** (July 2002), 538–540 (2003)
20. European convention for the protection of vertebrate animals used for experimental and other scientific purposes. *Cets.* **170**, 123 (1986)
21. Grubor, P., Milicevic, S., Grubor, M., Meccariello, L.: Treatment of bone defects in war wounds: retrospective study. *Med. Arch.* **69**(4), 260 (2015)
22. Azzam, W., Atef, A.: Our experience in the management of segmental bone defects caused by gunshots. *Int. Orthop.* **40**(2), 233–238 (2016). Feb
23. Bari, M.M., Ahmed, M.U., Hossain, M.B., Chowdhury, F.R., Siddiqui, M.A.: Treatment of non union of humerus using G. A. Ilizarov technique. *Mymensingh Med. J.* **13**(1), 36–38 (2004). Jan
24. Lowenberg, D.W., Buntic, R.F., Buncke, G.M., Parrett, B.M.: Long-term results and costs of muscle flap coverage with Ilizarov bone transport in lower limb salvage. *J. Orthop. Trauma* **27**(10), 576–581 (2013). Oct

Chapter 5

Nanoindentation Derived Mechanical Properties of Human Enamel and Dentine Subjected to Etching with Different Concentrations of Citric Acid



Evgeniy A. Kislyakov, Roman V. Karotkiyan, Evgeniy V. Sadyrin,
Boris I. Mitrin, Diana V. Yogina, Artur V. Kheygetyan,
and Stanislav Yu. Maksyukov

Abstract In the present paper, the mechanical characteristics (reduced Young's modulus and indentation hardness) were measured for three sound human enamel and dentine samples using nanoindentation. Each sample was subjected to 60 s exposure in citric acid with varying concentration (0.5 wt.%, 3 wt.%, 5 wt.%). Each sample is a longitudinal section obtained from a single human maxillary molar. For each sample, a series of characteristic curves for the dependence of indentation depth on indentation load (load-displacement curves) for both enamel and dentine were obtained.

Keywords Nanoindentation · Mechanical properties · Enamel · Dentin · Citric acid

E. A. Kislyakov (✉) · R. V. Karotkiyan · E. V. Sadyrin · B. I. Mitrin
Don State Technical University, 1 Gagarin Sq., Rostov-on-Don 344000, Russia
e-mail: evgenka_95@mail.ru

R. V. Karotkiyan
e-mail: valker94@gmail.com

E. V. Sadyrin
e-mail: ghostwoode@gmail.com

B. I. Mitrin
e-mail: boris.mitrin@gmail.com

D. V. Yogina · A. V. Kheygetyan · S. Yu. Maksyukov
Rostov State Medical University, 29 Nakhichevansky Lane, Rostov-on-Don 344022, Russia
e-mail: dianaturbina@mail.ru

A. V. Kheygetyan
e-mail: artur5953@yandex.ru

S. Yu. Maksyukov
e-mail: kafstom2.rostgmu@yandex.ru

5.1 Introduction

The dependence of the mechanical properties of teeth tissues on various types of acids has been studied for quite a long time. There are known issues of clinical [1] and laboratory [2–4] cases of changes emerging in enamel and dentine under the influence of heavily consumed products containing acids (or demonstrating increased level of pH). In such cases, an erosion of tooth areas leading to a violation of occlusion [5] may occur. Nevertheless, acids are widely used in dentistry as components of adhesive systems [6–8]. An adhesive system is a set of liquids used to fix dental materials to hard tooth tissues [7, 8]. Usually, before sealing, the dental clinician uses adhesive to remove the smear layer [9]. Today, orthophosphoric acid is widely used as the basis for adhesive systems. When applying orthophosphoric acid, it is difficult to control the degree and depth of demineralization of enamel and dentine [10]. This leads to the fact that the applied adhesive does not completely fill the open dentine tubules, and this in turn does not ensure the formation of a full-fledged hybrid layer. Also the clinical cases where it was not possible to remove all orthophosphoric acid are known, which led to the formation of an “acid mine” [11]. With the advent of adhesive systems of the 6th and 7th generation, the use of orthophosphoric acids was decreased, since self-etched adhesives [12] appeared.

Usage of citric acid in the composition of self-etching adhesives or as a component of adhesive system may allow more control over the process of removing the smear layer on the tooth area subjected to sealing. Thus, the aim of the present study was to compare the mechanical characteristics (reduced Young’s modulus and indentation hardness) measured for three sound human enamel and dentine samples subjected to 60 s exposure in citric acid of varying concentration (0.5 wt.%, 3 wt.%, 5 wt.%). The mechanical characteristics were obtained using the nanoindentation test device.

5.2 Materials and Methods

5.2.1 *Sample Preparation*

Three human enamel samples were obtained from a single maxillary molar extracted from a patient (male, 21 years old) in the dental department of Rostov State Medical University clinic for orthodontic reasons (the patient provided informed consent, local independent ethics committee of Rostov State Medical University approved the study (statement 15/9 from October 3, 2019)). For disinfection reasons, the tooth was subjected to the 1% NaClO solution for 10 min. After this procedure, the tooth was stored in Hanks’ Balanced Salt Solution (HBSS) at 4 °C to prevent demineralization. The thymol granules were added to the HBSS to prevent fungal growth (the ratio of thymol to HBSS was 1:1000). A gradual grinding and polishing procedure was carried out with a reduction in the size of the abrasive on the each step (down to

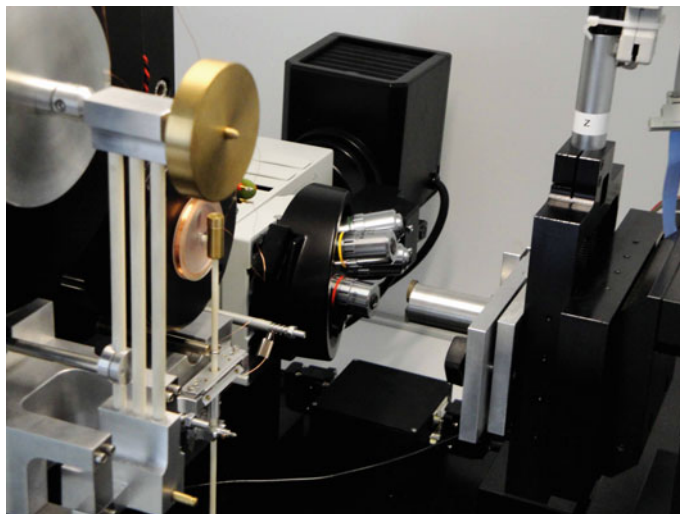


Fig. 5.1 The Nanotest 600 chamber interior, featuring the loading cell, optical microscope, and a sample mounted to the sample holder

0.05 μm). After each step, ultrasonic treatment was performed for 5 min to remove residual abrasive materials from the prepared surface.

5.2.2 Nanoindentation

Nanoindentation device Nanotest 600 Platform 3 (Micro Materials, UK) was used for the testing of the samples (Fig. 5.1). The experiments were conducted in a closed chamber at a constant temperature of $27.0 \pm 0.2^\circ\text{C}$. In all the experiments, the maximum indentation load was 50 mN and the diamond Berkovich indenter was used. For each sample, twenty indentations were made at a distance of 25 μm from each other, the results were averaged. The positions for the indentations were chosen using the optical microscope integrated into the nanoindentation device. Between the indentations each sample was wet with saline droplets using a syringe pump Terufusion TE-332 (Terumo, Belgium) inside the chamber.

5.3 Results

As a result of the experiments, the series of characteristic curves for the dependence of indentation depth on indentation load (load-displacement curves) were constructed (Figs. 5.2, 5.3, 5.4, 5.5, 5.6, and 5.7). The processing of the load-displacement curves

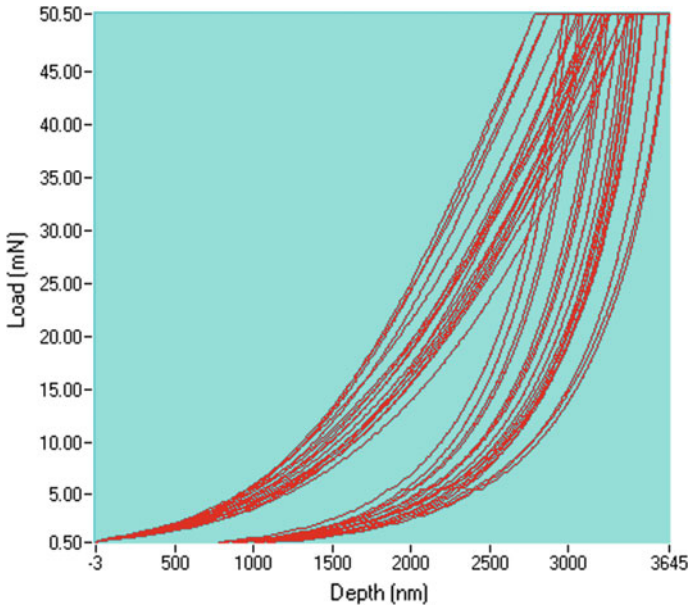


Fig. 5.2 Series of load-displacement curves for the dentine of the sample subjected to 0.5 wt.% citric acid concentration

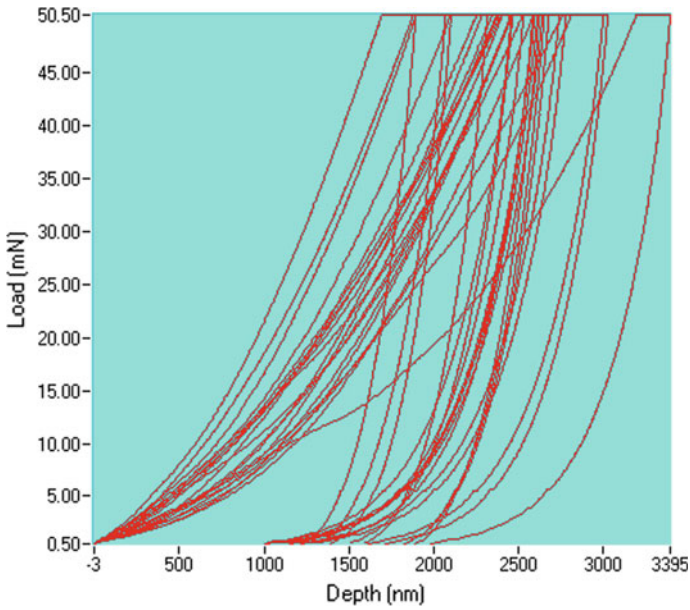


Fig. 5.3 Series of load-displacement curves for the dentine of the sample subjected to 3 wt.% citric acid concentration

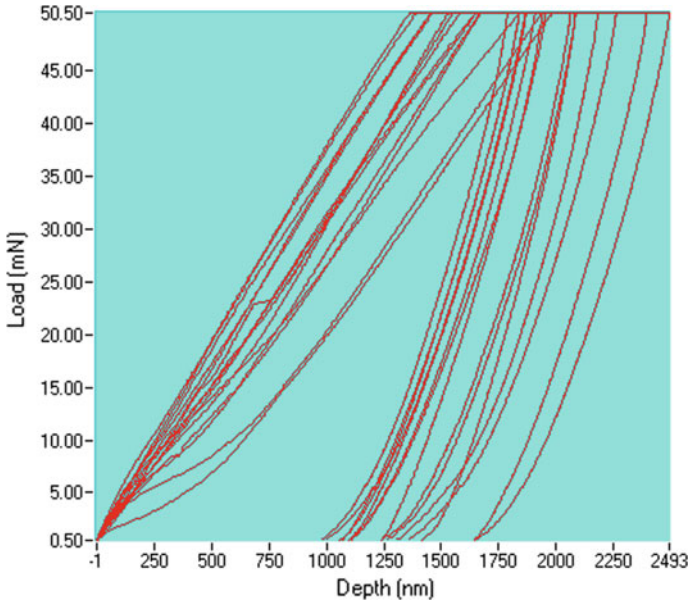


Fig. 5.4 Series of load-displacement curves for the dentine of the sample subjected to 5 wt.% citric acid concentration

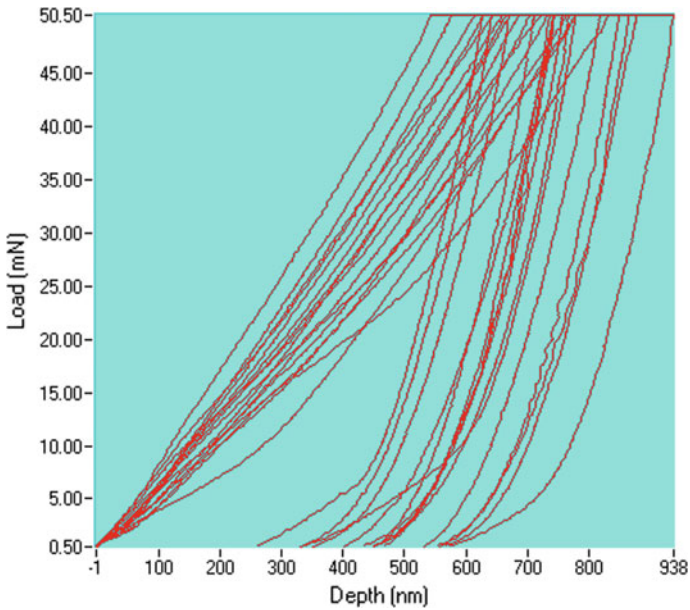


Fig. 5.5 Series of load-displacement curves for the enamel of the sample subjected to 0.5 wt.% citric acid concentration

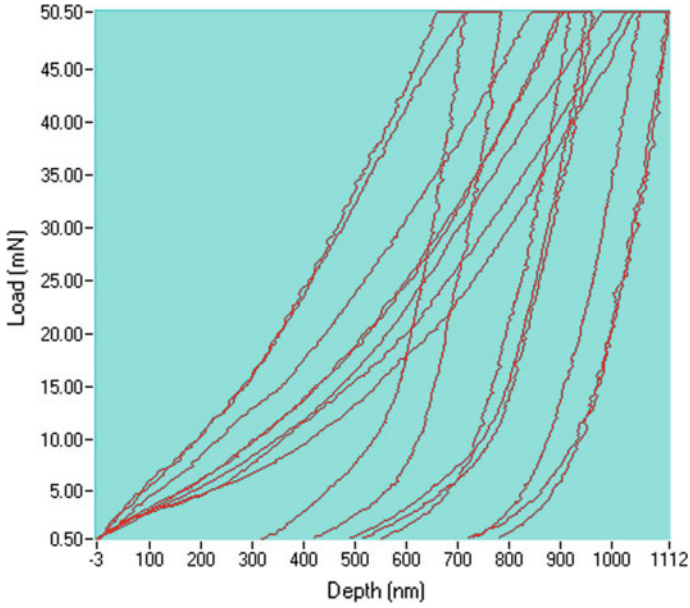


Fig. 5.6 Series of load-displacement curves for the enamel of the sample subjected to 3 wt.% citric acid concentration

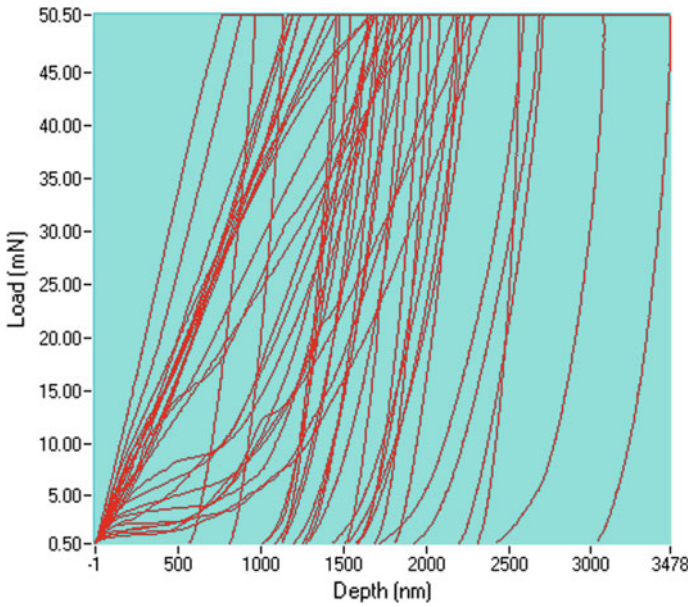


Fig. 5.7 Series of load-displacement curves for the enamel of the sample subjected to 5 wt.% citric acid concentration

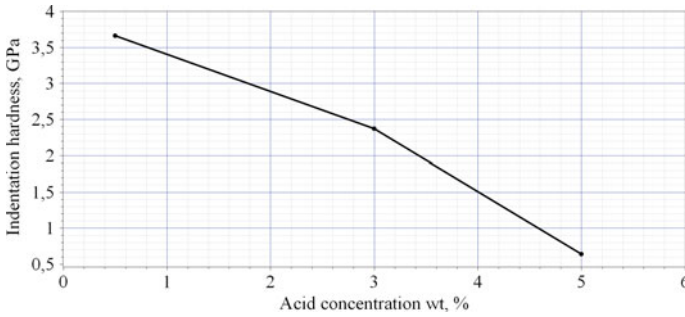


Fig. 5.8 Dependence of the indentation hardness on citric acid concentration

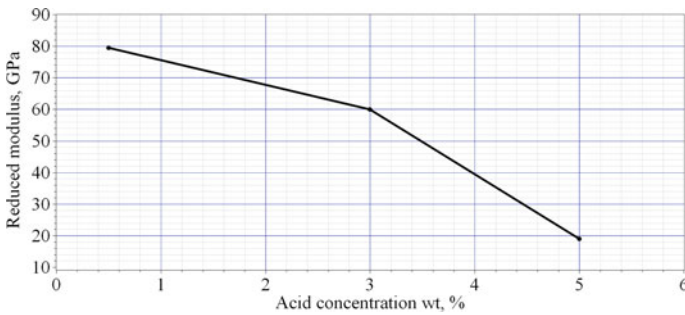


Fig. 5.9 Dependence of the reduced Young's modulus on citric acid concentration

was conducted using Oliver—Pharr method [13]. The dependence of the change in mechanical properties (reduced Young's modulus, indentation hardness) of the human tooth enamel on the concentration of citric acid was established. Figures 5.8 and 5.9 demonstrate the dependence of the reduced Young's modulus and indentation hardness correspondingly on the citric acid concentration. Values of reduced Young's modulus and indentation hardness are given in the Table 5.1. According to them, an increase in the concentration of citric acid leads to a decrease in Young's modulus and indentation hardness, which is caused by the dissolution of the main component for both enamel and dentine, hydroxyapatite, under the aggressive influence of the highest concentrations of citric acid. Due to the small number of samples, no specific correlation was found between the mechanical characteristics of the dentine and the acid concentration.

5.4 Discussion

Acid etching technique with orthophosphoric acid is widespread in the dental practice. A 15s etching of both dentine and enamel is usually sufficient to obtain the

Table 5.1 Dependence of the reduced Young's modulus and indentation hardness on the citric acid concentration

Acid concentration, wt. %	0.5%	3%	5%
<i>Enamel</i>			
Young's modulus E (GPa)	79.43 ± 11.49	59.91 ± 14.16	18.93 ± 9.32
Indentation hardness H (GPa)	3.67 ± 0.92	2.37 ± 0.85	0.64 ± 0.5
<i>Dentin</i>			
Young's modulus E (GPa)	4.46 ± 0.56	9.12 ± 2.63	0.32 ± 0.09
Indentation hardness H (GPa)	0.20 ± 0.03	2.36 ± 0.55	0.09 ± 0.02

desired results [14] for the clinician. When using this acid, it is necessary to take into account the uncontrolled degree of etching. On the other hand, citric acid possesses mildly aggressive impact on the tooth surface, which results in the slower dissolution of the hydroxyapatite crystallites. This gave us a possibility to observe the process of demineralization of the surface structure of dentine and enamel from the mechanical point of view. This feature may give the possibility for dental clinicians to control the etching process to a higher extent comparing to other acids as well. Probably, if the observations made in the present paper will be consistent for a variety of teeth belonging to different patients, the citric acid may become a component of the adhesive systems in the future (or a component for other dental procedures).

5.5 Conclusion

The dependencies were established between the mechanical characteristics of human tooth enamel and the concentration of citric acid, applied to the tooth surface. The increase in the concentration of citric acid leads to the decrease in the Young's modulus and indentation hardness for the samples under study. No such correlation was found for dentine in this study. For the further study of the influence of such an acid on the mechanical properties of human teeth, it is necessary to conduct a similar study on a much larger number of samples with approximately same initial mineral density of enamel and dentine.

Acknowledgments The research was supported by Russian Foundation for Basic Research grants no. 19-07-01259, 18-07-01397. E.V. Sadyrin was supported by the scholarship of the President of the Russian Federation no. SP-3672.2018.1. Nanoindentation experiments were made in the Nanocenter of Research and Education Center "Materials", Don State Technical University (<http://nano.donstu.ru>).

References

1. Gambon, D.L., Brand, H.S., Amerongen, A.N.: Soft drink, software and softening of teeth—a case report of tooth wear in the mixed dentition due to a combination of dental erosion and attrition. *Open Dent. J.* **4**, 198–200 (2010)
2. Marshall Jr., G.W., Wu-Magidi, I.C., Watanabe, L.G., Inai, N., Balooch, M., Kinney, J.H., Marshall, S.J.: Effect of citric acid concentration on dentin demineralization, dehydration, and rehydration: atomic force microscopy study. *J. Biomed. Mater. Res.* **42**(4), 500–507 (1998)
3. Saeki, K., Marshall, S.J., Gansky, S.A., Marshall, G.W.: Etching characteristics of dentin: effect of ferric chloride in citric acid. *J. Oral Rehabil.* **28**(4), 301–308 (2001)
4. Lippert, F., Parker, D.M., Jandt, K.D.: Susceptibility of deciduous and permanent enamel to dietary acid-induced erosion studied with atomic force microscopy nanoindentation. *Eur. J. Oral Sci.* **112**(1), 61–66 (2004)
5. Huysmans, M.C.D.N.J.M., Chew, H.P., Ellwood, R.P.: Clinical studies of dental erosion and erosive wear. *Caries Res.* **45**(1), 60–68 (2011)
6. Sofan, E., Sofan, A., Palaia, G., Tenore, G., Romeo, U., Migliau, G.: Classification review of dental adhesive systems: from the IV generation to the universal type. *Ann. di Stomatol.* **8**(1), 1–17 (2017)
7. Takamizawa, T., Barkmeier, W.W., Tsujimoto, A., Scheidel, D.D., Erickson, R.L., Latta, M.A., Miyazaki, M.: Effect of phosphoric acid pre-etching on fatigue limits of self-etching adhesives. *Oper. Dent.* **40**(4), 379–395 (2015)
8. Giannini, M., Makishi, P., Ayres, A.P.A., Vermelho, P.M., Fronza, B.M., Nikaido, T., Tagami, J.: Self-etch adhesive systems: a literature review. *Braz. Dent. J.* **26**(1), 3–10 (2015)
9. Pashley, D.H., Tao, L., Boyd, L., King, G.E., Horner, J.A.: Scanning electron microscopy of the substructure of smear layers in human dentine. *Arch. Oral Biol.* **33**(4), 265–270 (1988)
10. Scheffel, D.L., Tenuta, L.M., Cury, J.A., Hebling, J.: Effect of acid etching time on demineralization of primary and permanent coronal dentin. *Am. J. Dent.* **25**(4), 235–238 (2012)
11. Pini, N.I.P., Sundfeld-Neto, D., Aguiar, F.H.B., Sundfeld, R.H., Martins, L.R.M., Lovadino, J.R., Lima, D.A.N.L.: Enamel microabrasion: An overview of clinical and scientific considerations. *World J. Clin. Cases: WJCC* **3**(1), 34–41 (2015)
12. Helvey, G.A.: Adhesive dentistry: the development of immediate dentin sealing/selective etching bonding technique. *Compend. Contin. Educ. Dent.* **32**(9), 22–24 (2011)
13. Oliver, W.C., Pharr, G.M.: An improved technique for determining hardness and elastic modulus using load and displacement sensing indentation experiments. *J. Mater. Res.* **7**, 1564–1583 (1992)
14. Zafar, M.S., Ahmed, N.: The effects of acid etching time on surface mechanical properties of dental hard tissues. *Dent. Mater. J.* **34**(3), 315–320 (2015)

Chapter 6

Experimental and Theoretical Solution of the Problem on the Generating of Fatigue Wear in Heterogeneous Materials and Coatings



Oleg V. Kudryakov, Valery N. Varavka, Igor Yu. Zabiya, and Natalia I. Bronnikova

Abstract The process of nucleation of fatigue wear in industrial alloys and ion-plasma coatings under the influence of high-speed discrete droplet flow is investigated. The results obtained relate to the stage of microstructural mechanics of fatigue fracture. This stage precedes the stage of the steady growth of fatigue cracks, which is described by the continuum mechanics of fatigue failure (for example, by the Paris–Erdogan concept). Processes of formation of fatigue defects in materials and coatings with a heterogeneous structure are considered on the base of the dislocations theory. A computational–analytical model for determining the moment of formation of a defect (cracks, pores, microcrater) of critical size depending on the parameters of droplet impacts is proposed and theoretically substantiated. The model is universal in its application to various materials and coatings, in which the mechanisms for the nucleation of defects are of a dislocation nature. The correspondence of the results of numerical experiments in the framework of the developed model to the results of bench tests is shown. The data testifying to the high compliance of the results of the application of the proposed model and the well-known fatigue model of Murakami–Endo for steels and alloys in conditions of droplet impacts are given. At the same time, the results obtained using both models for thin high-strength ion-plasma coatings contradict each other.

O. V. Kudryakov · V. N. Varavka (✉) · I. Yu. Zabiya · N. I. Bronnikova
Don State Technical University, Gagarin Square 1, Rostov-on-Don 344000, Russian Federation
e-mail: varavkavn@gmail.com

O. V. Kudryakov
e-mail: kudryakov@mail.ru

I. Yu. Zabiya
e-mail: zabiyaigor@gmail.com

N. I. Bronnikova
e-mail: makarovani88@mail.ru

6.1 Introduction

In several of our previous works [1–4], attempts were made to quantify the ability of materials and coatings to resist the action of external shock cyclic loads. In particular, it was possible to create a computational and analytical model that was tested under the conditions of a liquid droplet impacts [5, 6]. However, the model we developed did not differentiate the behavior of a material or coating at the stages of nucleation and development of destruction. The stage of nucleation is very problematically identified in the experiment. In our model, it was estimated using empirical coefficients that did not have a universal theoretical justification, which can be considered an obvious drawback of the model. Therefore, this work aims to provide a more in-depth theoretical consideration of the stage of the nucleation of defects in the material, leading to its wear and destruction, as well as the creation on this basis of a calculating methodics to determine the moment of nucleation of cracks or pores in various materials and coatings under cyclic loading.

The peculiarity of the process under study is that the hydrodynamics of the impact of a drop on a smooth metal surface includes two components—mechanical and cavitation [2, 7, 8]. In the long process of multiple drip impacts, the fate of the metal surface is of the greatest interest, since this issue affects the problem of wear resistance and durability of products and components of various equipment operating under conditions of droplet impingement erosion: turbine, ventilation, agrotechnical, aviation, cryogenic equipment. From this point of view, the cavitation component generates a maximum of the internal stress in the material during a single collision, which can be considered as a separate loading cycle [2, 8]. And the mechanical component is realized in the form of the cyclical nature of these loads falling into one point. Thus, the degradation of the material in case of multiple droplet impacts can be considered as a fatigue process. In our previous works, it was shown that, depending on the composition and structure of the material, the initial stages of its destruction can proceed through various mechanisms. In such ductile metallic materials as, for example, austenitic steel, the formation of primary wear craters occurs through the nucleation and development of fatigue porosity. Quantitative estimates of this wear mechanism were developed based on Goodman's fatigue model [2]. In durable materials such as martensitic steel, for example, wear craters are formed by initiating and developing fatigue cracks. A quantitative assessment of their subcritical growth was performed on the basis of the Paris–Erdogan fatigue theory [5, 6, 9]. In both cases, the estimates were based on the use of extensive parameters (specific porosity, length of crack, and crack growth rate), which is generally a characteristic of fracture mechanics approaches. This paper considers mainly the intensive parameters that determine the internal processes of nucleation and development of fatigue pores or cracks in materials of different nature during the formation of wear under conditions of high-cycle droplet impacts. Consideration of the behavior of dislocations under these conditions or the influence of microstructural elements on the assessment of the wear resistance of materials is typical of metal physics and materials science approaches. The complementary (synthesis) approaches of fracture mechanics and

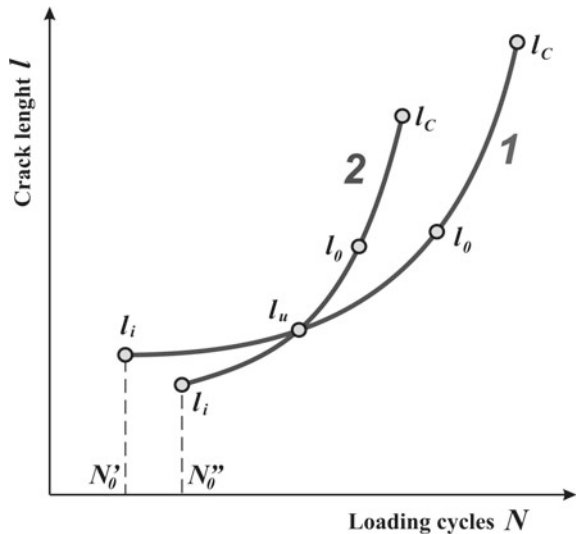
materials science are aimed at forming a more complete and detailed physical and theoretical picture of the wear of materials during droplet impingement erosion, as well as at improving the accuracy of its applied estimates, which is the purpose of this work.

6.2 Conditions for Initiation of Destruction (Wear) Under Droplet-Impact Cyclic Effects

With the calculating apparatus of fatigue failure at the stage of stable growth of a crack up to its critical size, the situation is not bad: there is a choice among various models with the help of which one can analyze the stage of propagation of the fatigue cracks in materials of various nature. But in relation to the crack initiation stage there are serious gaps, primarily due to the difficulties of instrumental fixation of cracks in the early stages of development.

In the general case, on the curve of fatigue failure of a material, several characteristic points can be distinguished, shown in Fig. 6.1: l_i —theoretical crack start; l_u —instrumentally determined crack start; l_0 —initial crack size; l_C —critical crack size. The value of l_u is determined by the capabilities of the equipment used (microscope, ultrasound scanner, etc.). Obviously, the value of l_u does not depend on the nature and properties of the material; therefore, in Fig. 6.1, the point l_u on the curves of ductile and durable materials coincides. The point l_0 on the fatigue curve of the material marks the beginning of a steady crack growth, which up to the point l_C can be described by a relatively simple relationship, for example, the Paris equation [5, 9]. Point l_C characterizes the beginning of the catastrophic destruction of the

Fig. 6.1 Schematic dependence of the length of the fatigue crack l on the number of loading cycles N for ductile (1) and durable (2) materials



material. Determining the value of l_C is most important from the point of view of the safe operation of materials, products, and structures. Therefore, the value of l_C is the most researched and appears in many theories of fracture mechanics. The l_i point is the least studied, since it lies below the instrumental threshold and, strictly speaking, cannot be determined experimentally. However, to create a complete model of the formation of wear, a method for determining its nucleation stage in the form of l_i is necessary. In the present work, this method is implemented in the form of a theoretical concept, a calculating apparatus, and checking their adequacy on the basis of indirect experimental data. It should also be noted that under cyclic loading (including under drop-impact action), fatigue processes in a material or coating, depending on their nature, can initiate wear in the form of cracks, pores, or microcraters. In this paper, the geometry of the fatigue defect that is being formed is not differentiated and is not a subject of consideration and analysis in the computational and analytical model.

As the initial experimental base of the process of destruction under droplet impacts, we used our own and literary [10–12] test data obtained at the unique scientific test bench “Erosion-M” of NRU-MPEI (Moscow) [13]. According to the results of these tests, the experimental critical value of the impact velocity is recognized as $V_0^{\text{cr.}} \approx 150$ m/s (for alloys based on Fe and Ti). At smaller values of the impact rate V_0 , wear of the experimental samples was not observed. However, a special study of this issue was not carried out. In this regard, for the theoretical justification of the values, it is proposed to refer to the works [14, 15], in which the impact of a metal plate with a fixed target is considered. When reaching $V_0^{\text{cr.}}$ in the target, the process of plastic flow of the metal is initiated, the front of which at the same time begins to move with velocity V_P :

$$V_0^{\text{cr.}} = \sqrt{\frac{\sigma_T}{\rho \cdot \left[1 - \left(\frac{V_P}{C_0}\right)^2\right]}} \quad (6.1)$$

where σ_T —target material yield strength; ρ —target material density; C_0 —the speed of sound in the target material.

Expression (6.1) is obtained for explosive (i.e., impact) conditions. It includes only the quantities characterizing the target. Therefore, there are no restrictions preventing the use of expression (6.1) for the conditions of any impact character, including the collision of a water drop with a metal surface of the target.

The criteria character of expression (6.1) determines its mathematical meaning. Thus, from the physical point of view, the impact velocity V_0 becomes critical when the process of plastic deformation starts in the target. From the mathematical point of view, the critical value of the velocity V_0 corresponds to its exit from the complex plane into the real numerical axis when using the inverse relationship $V_P = f(V_0^{\text{cr.}})$. Based on this, $V_0^{\text{cr.}}$ can be determined by taking $V_P = 0$.

To find the value of V_0^{cr} under a droplet impact, we choose pure α -iron as the target material. The choice of material is due to the fact that such a highly plastic material, which has not been subjected to hardening (thermal or deformation) treatment and does not contain hardening phases, has a priori minimal resistance to droplet impingement erosion. Consequently, the value V_0^{cr} for such a material will be the smallest of all possible structural variants of metallic materials. That is, it will be most consistent with the concept of a critical impact velocity.

We first define the value of C_0 for a pure α -Fe. Let us determine the sound velocity in a metal as the velocity of a longitudinal wave in an isotropic solid (without taking into account various wave attenuation mechanisms associated with structural inhomogeneity) [16, p. 133]:

$$C_0 = \sqrt{\frac{E \cdot (1 - \nu)}{\rho \cdot (1 + \nu) \cdot (1 - 2\nu)}} \quad (6.2)$$

where E —Young’s modulus of the target material; ν —Poisson’s ratio.

For a pure α -Fe [16]: $\rho = 7874 \text{ kg/m}^3$; $E = 200 \text{ GPa}$; $\nu = 0.28$; $\sigma_T = 170 \text{ MPa}$. Then in accordance with the expression (6.2) we get $C_0 = 5698 \text{ m/s}$, and taking into account the expression (6.1) under the condition $V_p = 0$: $V_0^{\text{cr}} = 146.936 \text{ m/s}$. The obtained value V_0^{cr} corresponds to the experimental bench test data for iron-based alloys, obtained both in [10–12] and in our research [17–20].

Thus, the obtained value V_0^{cr} represents the boundary of the onset of plastic deformation processes in the material, which, in turn, are determined by the processes of formation and interaction of dislocations. The accumulation of microplastic deformation (in the form of dislocations) in materials under cyclic loads leads to the formation of fatigue defects (cracks, pores, microcraters)—wear start points. Therefore, the condition $V_0 > 146.936 \text{ m/s}$ determines the possibility of nucleation and development of the destruction and wear of a metal target (in iron-based alloys), which can be expressed on the physical and mathematical concepts of the theory of dislocations.

6.3 Theoretical Bases of Quantitative Estimates for the Stage of Microstructural Fracture Mechanics Under Droplet Impacts

The difficulties in assessing the stage of initiation of fracture and wear during cyclic shock liquid-drop impacts are associated not only with the instrumental determination of nuclei of cracks or pores. At this stage, the presence of structural elements in the material does not allow to represent it as a continuous continuum and to use linear fracture mechanics for calculations, for example, the Paris–Erdogan fatigue theory. Therefore, in the mechanics of fracture, the initial stage of the nucleation of fatigue defects is distinguished into a special stage of “microstructural fracture mechanics”,

which proceeds until the defect reaches the size $l_k = (4 \dots 10) \cdot d$, where d is the size of the structural element of the material [21, p. 107–110]. In this regard, the analytical assessment of the stage of the generation of fatigue defects requires, above all, a material science approach. The task is to find the calculated expression for the number of droplets impacts N_3 , necessary for the formation of a fatigue defect of critical size in the material.

In the general case, the equation for the number of collisions N_3 should include three components: mechanical, kinetic, and structural.

The mechanical component implies the number (density) of mobile dislocations ρ_m arising during a single drop collision. In the process of repeated collisions, the number of moving dislocations increases. They move in a metal matrix along slip planes under the action of shear stresses σ_s until they form flat clusters with critical density ρ_{cr} on the nearest insurmountable barriers. Let us take as $\rho_{cr} = 10^{16} \text{ m}^{-2}$ —the dislocation density, the excess of which leads to spontaneous breaking of the interatomic bonds in the metal and the formation of the crack origin. Then the mechanical component of the number of collisions will be expressed as $N_3 = f(\rho_{cr}/\rho_m)$.

The kinetic component of the number of collisions N_3 takes into account the dependence of the dislocation energy on its velocity V_d . The impact force causes mobile dislocations to slide at high speed. It is known from the theory of dislocations that as the speed of a dislocation increases, its energy increases in accordance with an expression similar to Einstein's expression for bodies moving at speeds close to the speed of light. Only the limit for the dislocation velocity is the speed of sound in a crystal C_0 , at which the dislocation energy becomes infinite. Therefore, taking into account the specifics of a droplet impacts, the kinetic component of the number of collisions will be expressed as $N_3 = f(V_d/C_0)$.

The structural component of the number of collisions N_3 has two aspects. The first is that the movement of dislocations upon impact is limited by the size of the structural element of the metal matrix within which a free path of dislocations is possible. In the general case, the grain size of metal D is considered as such an element. Another aspect involves the fact that various obstacles for dislocation movement can exist within the grain: particles of secondary phases, small-angle boundaries, dislocations fixed by atmospheres, packing defects, crystal lattice resistance (Peierls stress). Therefore, the structural component of the number of collisions should take into account both of these aspects and will be a function of two variables $N_3 = f(D, \Delta G)$, where ΔG is Gibbs free energy to activate the process of overcoming an obstacle within a structural element D by a moving dislocation. The mechanism for overcoming an obstacle depends on the nature of the obstacle, which determines the ΔG value for each specific case of the material structure (its classification is given below).

It follows from the above that all components of the desired number of collisions N_3 affect the process of the formation of a fatigue defect at the same time—with each collision. This fact determines the commutative nature of the interaction of mechanical, kinetic, and structural components. Then in the most general form, N_3 will be defined by the following expression:

$$N_3 = \frac{\rho_{cr}}{\rho_m} \cdot \sqrt{1 - \left(\frac{V_d}{C_0}\right)^2} \cdot \frac{D}{l_0} \cdot e^{-\frac{\Delta G}{kT}} \quad (6.3)$$

where $k = 1.38 \times 10^{-23}$ J/K is a Boltzmann constant; T —thermodynamic temperature, K; l_0 —the path traveled by mobile dislocations in one loading cycle (single impact).

Expression (6.3) is obtained on the basis of the theory of dislocations and is rather a theoretical concept than a calculation technique. To use expression (6.3) when evaluating the durability of materials under cyclic liquid-drop collisions, it is necessary to disclose the values included in it (such as ρ_m , V_d , l_0 , ΔG) through the measured parameters of the collision, for example, the impact velocity V_0 and the drop size R_0 .

6.4 Main Design Parameters for the Nucleation Stage of Destruction and Wear Under Drip-Impact Cyclic Loading

The process of formation of flat dislocation clusters, described above as the process of formation of fatigue defects (cracks, pores), is a particular case of the processes of plastic deformation and hardening. In these processes, the strain rate (hardening) V_{def} is determined by the density of mobile dislocations ρ_m and the sliding speed of dislocations V_d by the well-known expression:

$$V_{def} = \rho_m \cdot b \cdot V_d \quad (6.4)$$

where b is a Burgers vector.

In turn, the value of ρ_m at the steady-state stage of plastic flow is solely a function of stress σ_s and temperature. The simplest relationship, consistent with theory and experiment. [22, p. 25]:

$$\rho_m = \alpha \cdot \left(\frac{\sigma_s}{\mu \cdot b}\right)^2 \quad (6.5)$$

where μ is a shear modulus; α —constant coefficient taken in normal conditions is approximately equal to 1.

As the stress σ_s in expression (6.5), we consider the shear stress in the slip plane, under the action of which the displacement of moving dislocations occurs. The stress σ_s can be expressed in terms of the impact parameters. To do this, consider the stress distribution in the surface layer of the metal target in the center of the impact zone during a single loading cycle (drip collision), shown in Fig. 6.2 and already presented in some of our works (see, for example, [2]). In Fig. 6.2, the stress σ is expressed in relative units $\rho_0 \cdot c_0 \cdot V_0$, called the hydraulic shock approximation, where ρ_0 is the

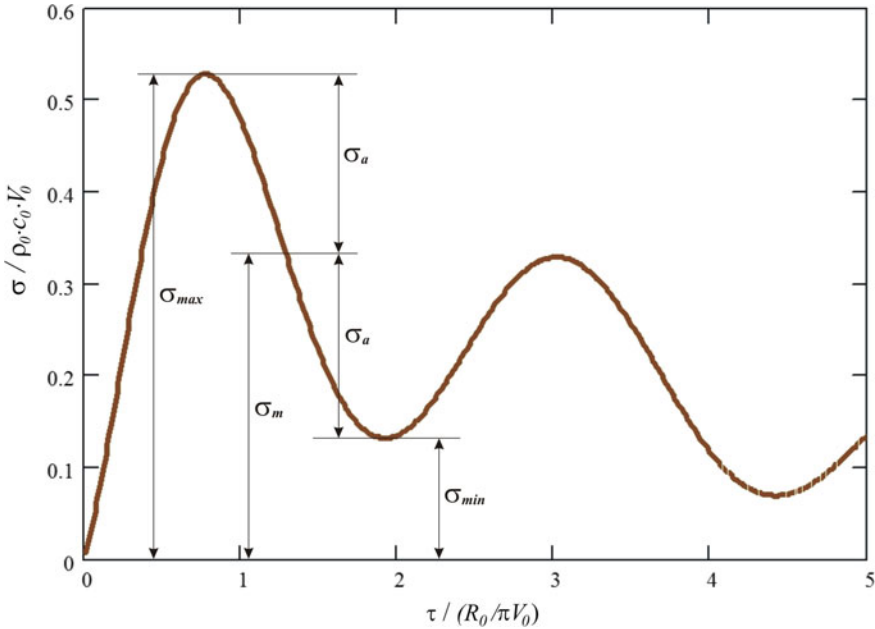


Fig. 6.2 Stress distribution σ in time τ for the period of the one drip-impact cycle (in relative units)

density of the unperturbed fluid, and c_0 is the sound velocity in the fluid under normal conditions (for water $\rho_0= 1000 \text{ kg/m}^3$, $c_0 = 1500 \text{ m/s}$).

Figure 6.2 shows the main design parameters of stress characteristic of fatigue models: maximum σ_{max} , minimum σ_{min} , and median σ_m . We assume that the dislocation slip occurs during the entire time of the loading cycle (collision) with a length of $\tau = 2 \cdot R_0 / V_0$ at a stress of $\sigma_m = 0,33 \cdot \rho_0 \cdot c_0 \cdot V_0$. To go from the applied external stress σ_m to the shear stress in the slip plane σ_s , we use the Schmidt–Boas law for a polycrystal:

$$\sigma_m = M_p \cdot \sigma_s \tag{6.6}$$

where M_p is Taylor’s factor: $M_p= 2.9$ for bcc lattice, $M_p= 3.06$ for fcc lattice [22, p. 30].

Then, taking into account the expression (6.6), the stress σ_s in formula (6.5) will be expressed through the parameters of the collision:

$$\sigma_s = \frac{0.33 \cdot \rho_0 \cdot c_0 \cdot V_0}{M_p} \tag{6.7}$$

During shock loading (including explosion), the strain rate reaches very large values ($V_{def} > 10^2 \text{ s}^{-1}$). In this case, plastic deformation is controlled by phonon and electronic braking of dislocations. The speed of movement of dislocations for these

conditions is determined by the drag coefficient B by the expression [22, p. 31]:

$$V_d = \sigma_s \cdot b / B \quad (6.8)$$

where the values of the braking coefficient B are in a rather narrow interval $10^{-5} \dots 10^{-4}$ N s/m², for further calculations we accept $B = 10^{-4}$ N s/m².

Thus, in the basic expression (6.3), the calculated values of all quantities included in the mechanical and kinetic components of N_3 are determined. In the structural component N_3 , the free path of dislocations in one drip-impact cycle is defined as $l_0 = V_d \cdot \tau$ and, taking into account expressions (6.7) and (6.8), is written as

$$l_0 = \frac{0.66 \cdot R_0 \cdot \rho_0 \cdot c_0 \cdot b}{B \cdot M_p} \quad (6.9)$$

The determination of the energy of passage of structural obstacles by ΔG dislocations requires a more detailed analysis.

From classical works on the theory of dislocations [22–24], it is known that the energy ΔG is a function of the stress σ_s and depends on the shape and distribution of obstacles, as well as on the field of internal stresses between obstacles. In general, the value of ΔG in Eq. (6.3) can be represented as

$$\Delta G(\sigma_s) = \Delta F \cdot \left(1 - \frac{\sigma_s}{\sigma_\tau}\right) \quad (6.10)$$

where ΔF is the activation energy of the process of overcoming an obstacle without the application of external stress, the value of ΔF actually determines the strength of the obstacles in terms of passing them by dislocation; σ_τ is the internal stress that exists in the material and allows dislocations to pass an obstacle with minimum values of ΔG ; the flow stress of a solid at $T = 0$ K is taken as σ_τ .

The values of σ_τ and ΔF are the properties of the material and, in general, they are expressed through its basic physical characteristics of μ and b :

$$\sigma_\tau = \alpha_1 \cdot \mu \cdot b / l; \Delta F = \alpha_2 \cdot \mu \cdot b^3 \quad (6.11)$$

The coefficients α_1 and α_2 in expression (6.11) classify obstacles by their strength, and the value l represents the distance between the obstacles. There is a fairly tight correlation between these parameters. Thus, strong or large particles of secondary phase precipitates are determined by the coefficient $\alpha_2 = 2$, and the linear average statistical distance between the precipitates is taken as l . Medium strength obstacles are, for example, small, cut by dislocations, precipitates, and forest dislocations, formed, for example, during deformation hardening. Such obstacles have a coefficient $\alpha_2 = (0.2 \dots 1.0)$, and as l is taken the distance between dislocations, that is $l = 1 / \sqrt{\rho_d}$. Low-strength obstacles include atoms of an element dissolved in a

lattice (for example, during quenching) or Peierls resistance of a lattice (with a relatively low dislocation density ρ_d). In this case, $\alpha_2 < 0.2$, and the value of l has a size commensurate with the Burgers vector b .

In the framework of the above classification, the deterministic inverse relationship is observed between the values of σ_τ and ΔF : as the strength of obstacles increases, the stress in the lattice between obstacles σ_τ weakens, and accordingly the energy to overcome obstacles ΔF increases. The coefficient α_1 relates the classification of obstacles to the free path of dislocations, determined by the value of the structural element D (for example, the grain size). The physical meaning of the coefficient α_1 is not completely clear and requires a wider discussion beyond the framework of this work. According to the results of our research, including numerical experiments, it can be said that for compact metallic materials in which dislocation interactions are determined by the type of microstructure and the free path of dislocations are always greater than the distance between dislocations ($D > 1/\sqrt{\rho_m}$), the coefficient α_1 in expressions (6.11) can be not used, there is $\alpha_1 = 1$. The coefficient α_1 , other than one, is relevant for nanomaterials and nanostructured coatings (see below). That is, for this category of materials the coefficient α_1 in expression (6.11) acts as a regulator of the value of the Burgers vector. This fact may indirectly indicate that plastic deformation in nanomaterials is carried out with the participation of partial or grain-boundary dislocations.

Thus, formulas (6.5)–(6.11) expand the theoretical expression (6.3) into the design plane and allow us to determine the number of loading cycles (drip impacts) necessary for the formation of a fatigue defect of critical size. Since the theoretical model used is based on the theory of dislocations, then such a defect will be understood as a local increase in the dislocation density to a critical level $\rho_{cr} \geq 10^{16} \text{ m}^{-2}$. In real metals and alloys, this level is usually achieved in the form of flat dislocation clusters at impermeable barriers: at the ends of the braked slip bands, on grain boundaries, on incoherent boundaries of large inclusions, etc. The high degree of lattice deformation in these regions relaxes by breaking interatomic bonds and forming free interfaces. If this happens by the pure shear mechanism (usually in durable metals and alloys), a crack is formed. If according to a more complicated mechanism, for example, shear with torsion (usually in ductile materials), then the pore is formed.

It should also be noted that all values determined by formulas (6.5)–(6.11) are calculated on the basis of either the known reference characteristics of the material (μ , b , M_p) or the measured process parameters (V_0 , R_0). This allows us to consider the system of expressions (6.3)–(6.11) as a fully practical computational–analytical model for determining the critical moment of the generation of fracture and wear in a material or coating with a known structure under drip-impact cyclic loading.

6.5 Application of Calculation Model

6.5.1 Compact Materials (Metals and Alloys)

Consider some of the results of numerical experiments obtained in the framework of the proposed analytical model.

Table 6.1 shows the values of the critical velocity of collisions, obtained using expressions (6.1) and (6.2). These values should not be considered as absolute, because in expressions (6.1) and (6.2) such an important impact parameter as the droplet size R_0 was not taken into account. However, these values can be used as a relative comparative wear resistance of various materials under conditions of drip-impact cyclic loading, taking the default value of R_0 equal and fixed.

The relative comparative data of the calculated values V_0^{cr} from Table 6.1 as a criterion for the durability of materials and the experimental values of the relative erosion resistance m_0 under the conditions of drip-impact cyclic loading, obtained during bench tests [12, 17–20], are shown in Fig. 6.3. Among the calculated data as in the unit, the critical velocity of the collision of pure iron was taken (ferrite structure in Fig. 6.3). The duration of the incubation period m_0 of the wear curve of austenitic steel 08Cr18Ni10Ti is taken among the experimental data per unit [17, 18], since the authors did not have an experimental value for pure iron. The experimental value of 1.56 is the average for several titanium alloys that are similar in chemical composition [12]. Normalization of the calculated and experimental values was carried out independently of each other. Among the results shown in Fig. 6.3, the following are noteworthy:

- (1) the calculated and experimental data have uniform distribution patterns among materials with different structure;

Table 6.1 The minimum calculated values of the impact velocity V_0^{cr} required to initiate the destruction and wear in various metallic materials under droplet impact

№	Material	Characteristics of material				Calculated parameters	
		Density ρ , kg/m ³	Young's modulus E , GPa	Poisson's ratio ν	Yield strength σ_y , MPa	C_0 , m/s	V_0^{cr} , m/s
1.	Fe	7874	200	0.28	170	5698	146.9
2.	Ti	4505	110	0.33	300	6015	258.1
3.	Al	2689	70	0.31	22	6007	90.5
4.	Co	8900	206	0.32	300	5755	183.6
5.	20Cr13 (sorbite structure)	7670	218	0.30	640	6186	288.9
6.	08Cr18Ni10Ti	7900	196	0.29	205	5702	161.1

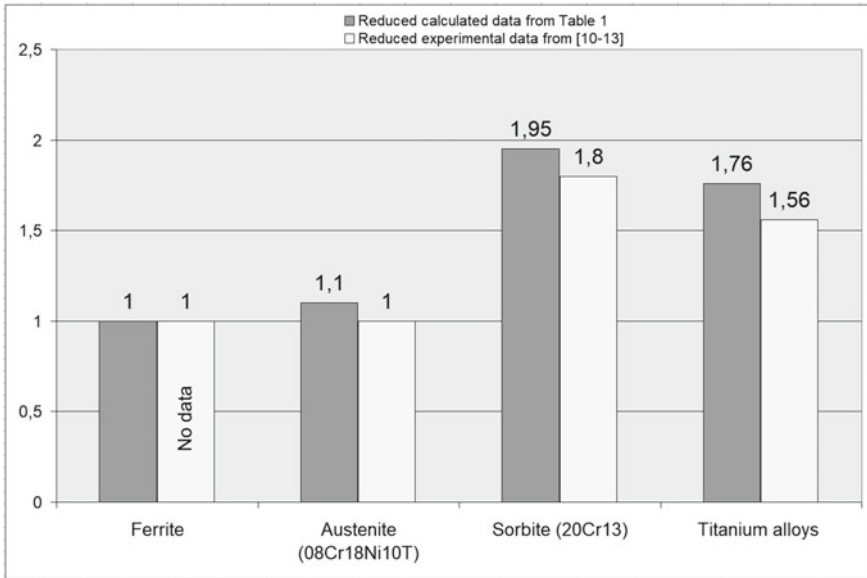


Fig. 6.3 Comparative data of the erosion resistance of various materials (the reduced calculated and experimental values)

(2) the obtained normalized calculated and experimental values of each material are very close.

The given data for calculating the critical velocity of collisions V_0^{cr} do not claim to be the main result of the work, but rather are an intermediate stage. Nevertheless, the result of this stage, in our opinion, deserves attention and further more in-depth studies. In addition, an important fact is that the calculated values V_0^{cr} clearly demonstrate its dependence on the structure for Fe-based alloys. In Table 6.1 (lines no. 1, 5, 6) three different structural types of such alloys are presented:

- pure metal α -Fe (bcc lattice);
- deeply alloyed solid solution based on γ -Fe (austenite steel 08Cr18Ni10T with fcc lattice);
- heterogeneous sorbite structure in a steel 20Cr13 (metal matrix of ferrite with dispersed particles of cementite).

The structural factor is one of the main parameters in the above analytical model—in expressions (6.3)–(6.11). It is this parameter that distinguishes the proposed model from many models based on fatigue theories or theories of continuum mechanics, where material heterogeneity is usually ignored. We believe that at the initial stages of destruction, the structural features of the material should not only be taken into account, but also, perhaps, play a decisive role. The results of numerical experiments, shown below, are designed to confirm this thesis against the background of comparative experimental data.

Table 6.2 presents the results of using expressions (6.3)–(6.11) for Fe-based alloys with different structural morphologies. Let us clarify the values of some parameters given in Table 6.2. The distance between obstacles l in the path of mobile dislocations in ferrite and austenite is taken as the distance between dislocations, that is $l = 1/\sqrt{\rho_d}$. Given the high plasticity of these solid solutions, their dislocation density is relatively small $\rho_d = 10^{11} \text{ m}^{-2}$, which gives $l \approx 3 \text{ }\mu\text{m}$. In hardened steel, the dislocation density is close to critical $\rho_{cr} = 10^{16} \text{ m}^{-2}$, which not only gives the value of the structural parameter $l \approx 0.01 \text{ }\mu\text{m}$ in Table 6.2, but also changes the method for calculating the number of droplet impacts in the original model (6.3).

For durable materials, for example, for strongly deformed or hardened alloys (including 20Cr13 with martensitic structure), in expression (6.3) the first three factors turn into one. Since the critical dislocation density ρ_{cr} in such materials has already been achieved, the concept of mobile dislocations ρ_m and the concept of their mobility lose their meaning. In numerical form, this is expressed as: $\rho_{cr}/\rho_m = 1$; $V_d = 0$; $D = l_0 = 1/\sqrt{\rho_{cr}}$. As for the exponent in expression (6.3), it retains its meaning with the values of the parameters α_2 and l given in Table 6.2. In order for a crack to born in such a structure, the cyclic loading must overcome the existing stresses in a saturated dislocation medium and to form a defect of shear nature [22, 25]. Considering the above, expression (6.3) for hardened steel (and for similar durable materials) will look like

$$N_3 = \left(\frac{\mu}{\sigma_s}\right)^2 \cdot e\left(-\frac{\Delta F}{kT}\right) \cdot \left(1 - \frac{\sigma_s}{\sigma_c}\right) \quad (6.12)$$

The experimental values shown in Table 6.2 characterize the incubation period for the erosive wear of the material m_0 . This value includes both the stage of the nucleation of a defect (cracks, pores, microcrater), and the stage of its development before the start of mass loss by the sample. It is not possible to instrumentally identify in experimental values of m_0 the number of collisions occurring only at the nucleation stage. Therefore, N_3 values are exclusively calculated. The contribution of the nucleation stage to the total value is characterized by the coefficient $\alpha_0 = N_3/m_0$.

In addition to the numerical values presented in Table 6.2, the model makes it possible to obtain the dependences of the number of collisions N_3 , which is necessary for the nucleation of a fatigue defect (cracks, pores, microcrater), on the velocity of collisions V_0 at fixed values of the droplet size R_0 . Some variants of such dependencies are presented in Fig. 6.4.

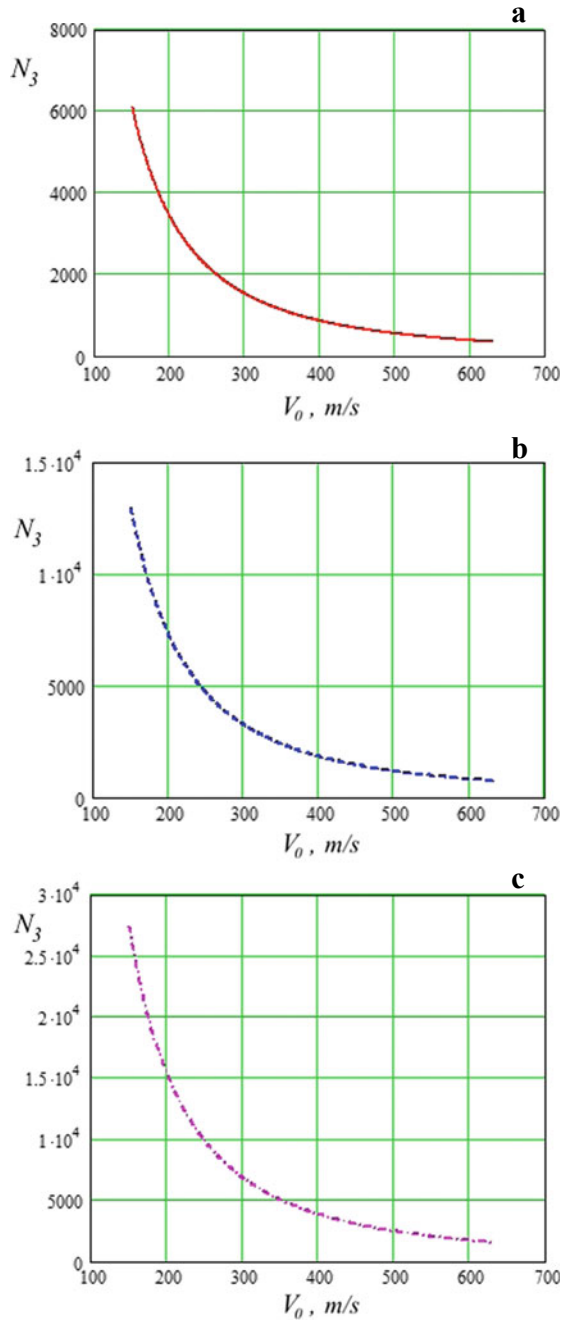
The results show that the calculated data N_3 does not contradict the experiment (bench test data m_0). They also demonstrate compliance with the basic canons of fracture mechanics. In particular, the coefficient α_0 characterizes the nucleation energy with respect to the destruction of energy. In ductile metallic materials (armco, austenite, sorbite), the nucleation energy of fatigue cracks is substantially less than the energy of their growth. In durable alloys (martensite), the nucleation energy is almost always higher than the growth energy. Our data in Table 6.1 show that in steel 20Cr13 with the martensitic structure the stage of nucleation of the fatigue defect N_3

Table 6.2 Experimental m_0 and calculated N_3 values of the number of collisions* for Fe-based alloys

Alloy (structure)	Structure parameters					Impact parameters for initial data						
	Lattice Type (Taylor's factor M_p)	α_1	D, m^{-6}	l, m^{-6}	$V_0 = 250 \text{ m/s};$ $R_0 = 0.55 \text{ mm}$	Calculations		Experiment		$V_0 = 340 \text{ m/s};$ $R_0 = 0.32 \text{ mm}$		
						N_3	α_0	m_0	N_3	α_0	N_3	α_0
Armco Fe (ferrite)	bcc (2.9)	0.5	100	3.0		2197	–	–	1187	–	–	–
08Cr18Ni10Ti (austenite)	fcc (3.06)	0.5	100	3.0		2446	0.253	9680	1322	0.154	8597	
20Cr13 (sorbite)	bcc (2.9)	2.0	100	0.35–0.50		4655	0.280	16630	3742	0.254	14768	
20Cr13 (martensite)	tetragonal (2.95)	0.02	0.01	0.01		9844	0.550	17861	5705	0.470	12140	

*—The table shows the values of the numbers of droplet impacts that fall in one point (defined in the software of the test bench)

Fig. 6.4 Dependencies of the number of collisions N_3 on the velocity of collision V_0 at $R_0 = 0.55$ mm for the initiation of cracks in Fe-based alloys with different structures: Armco iron, ferrite (a); steel 20Cr13, sorbite (b); steel 20Cr13, martensite (c)



is about half of the entire incubation period of formation of wear m_0 : $\alpha_0 = 0.47$ and 0.55 for the impact speeds $V_0 = 340$ m/s and 250 m/s, respectively. Whereas for the same steel with a sorbite structure, the coefficient α_0 is half as much.

The calculated dependencies in Fig. 6.4 also correspond to experimental reality. They are located asymptotically with respect to the values of $V_0 \approx 100..0.150$ m/s (our numerical experiment did not study this area in detail). The correspondence to the real experiment lies in the fact that it is known from bench tests that when $V_0 < 150$ m/s in iron-based alloys, no wear is observed (this aspect is discussed in detail in the second part of this work). That is, the asymptotics of the graphs in Fig. 6.4 confirms this empirical fact by showing that at the indicated low speeds of droplet impacts, no fatigue defects of critical size are formed.

The generally accepted universal analytical models of drop impact, combining microstructural and continuum fracture mechanics, are not available to date. Therefore, in our opinion, it will be interesting to compare the results obtained in the framework of the considered computational model with the existing universal fatigue models. Such models, combining the structural and strength properties of materials, may include the well-known and discussed model proposed by Y. Murakami and his colleagues [26–29]. The model, in particular, establishes a semi-empirical dependence of the threshold value of the stress concentration factor ΔK_{th} for crack non-propagation (under conditions of tension-compression or rotation with bending) on the hardness HV and the parameter $\sqrt{\text{area}}$ [27]:

$$\Delta K_{th} = \alpha_3 \cdot (HV + 120) \cdot (\sqrt{\text{area}})^{1/3} \quad (6.13)$$

where α_3 is a coefficient characterizing the localization region and the geometry of the fatigue defect (in the case of coatings, the surface defect in the form of a pore or a crack is determined by the value $\alpha_3 = 3.3 \times 10^{-3}$); HV —Vickers indenter hardness (kg mm^{-2}); $\sqrt{\text{area}}$ is the square root of fatigue defect area (μm).

Expression (6.13) relates the microstructure and imperfection of the material (coefficient α_3 and a parameter $\sqrt{\text{area}}$) with its strength properties (HV). It was obtained on the basis of numerous experimental data, a microscopic study of the processes of crack initiation, and a numerical analysis of a three-dimensional stressed state. Of particular interest here is the parameter $\sqrt{\text{area}}$ entered by Y. Murakami and M. Endo. It represents the square root of the area of the projection of the defect (or crack) on a plane perpendicular to the direction of the maximum tensile stress.

The parameter $\sqrt{\text{area}}$ can be determined from expression (6.13) for the materials we studied. The value of ΔK_{th} for cyclic loading with the effective stress σ and with the crack origin of length l (which is already existing in the material) are determined from the following conditions:

$$\begin{aligned} K_{\max} &= \sigma_{\max} \sqrt{\pi \cdot l}; \quad K_{\min} = \sigma_{\min} \sqrt{\pi \cdot l} \\ &\text{for } \sigma_{\min} > 0 \text{ and } K_{\min} = 0 \text{ for } \sigma_{\min} \leq 0 \end{aligned} \quad (6.14)$$

$$\Delta K_{th} = K_{max} - K_{min} = \Delta\sigma \cdot \sqrt{\pi \cdot l} \quad (6.15)$$

In accordance with Fig. 6.2 under the considered conditions of drip-cyclic loading in expression (6.15) should be taken:

$$\Delta\sigma = \sigma_{max} - \sigma_{min} = (0.528 - 0.134) \cdot \rho_0 \cdot c_0 \cdot V_0 = 0.394 \cdot \rho_0 \cdot c_0 \cdot V_0 \quad (6.16)$$

The parameters $\sqrt{\text{area}}$ in expression (6.13) and l in expression (6.15) have very close geometry, physical meaning, and dimension. This also follows from [27–29], where it was shown that small cracks, defects, and nonmetallic inclusions having the same square root value from the projection area ($\sqrt{\text{area}}$) have the same effect on the fatigue limit, regardless of various stress concentration factors. Then, for the estimated calculations in the case of droplet impacts, in our case, with a certain degree of approximation, we can assume that these parameters are equivalent. With this in mind, a joint solution of expressions (6.13)–(6.16) can determine the maximum values of the fatigue defect for various materials, under which the development of these defects under given conditions of collisions (V_0 and R_0 parameters) will not occur. This follows from the threshold essence of ΔK_{th} , which determines the non-propagation of cracks. Without going into details of the joint solution of expressions (6.13)–(6.16), we give the calculation formula for finding the parameter $\sqrt{\text{area}}$ for the case of drip-cyclic loading (6.17), as well as the results of calculations presented in Fig. 6.5.

$$\sqrt{\text{area}} = \left[\frac{\alpha_3 \cdot (HV + 120)}{0.394 \cdot \rho_0 \cdot c_0 \cdot V_0 \cdot \sqrt{\pi}} \right]^{2/3} \quad (6.17)$$

The results obtained in Fig. 6.5 can be compared with the data in Table 6.1. Thus, for the values of the critical velocity of impacts from Table 6.1, by expression (6.17) and the dependences of Fig. 6.5 we obtain: $\sqrt{\text{area}} = 3.0 \mu\text{m}$ —for ferrite (at $V_0^{cr} = 147 \text{ m/s}$); $\sqrt{\text{area}} = 3.1 \mu\text{m}$ —for austenite (at $V_0^{cr} = 161 \text{ m/s}$); $\sqrt{\text{area}} = 2.6 \mu\text{m}$ —for sorbite (at $V_0^{cr} = 289 \text{ m/s}$). Within the framework, both of our models and in the model of Y. Murakami, the obtained values for the given materials are threshold values. That is, with smaller sizes of fatigue defects, the destruction and wear of materials under drip-cyclic loading will not develop. In accordance with Fig. 6.1, the obtained parameter $\sqrt{\text{area}}$ values lie between the points l_u and l_0 on curve 1 (since all three materials under consideration belong to the category of ductile). Such defects are detected by microscopic examination ($l > l_u$), but do not lead to sustained crack growth ($l < l_0$). These data are consistent with the experimental results of our previous work [5, 6].

In addition to the estimated and geometric characteristics, the obtained calculated data testify to the varying effectiveness of the hardening mechanisms in the process of droplet impact. Despite the close threshold values of the parameter $\sqrt{\text{area}} \approx 2.5... 3.0 \mu\text{m}$ for all three considered materials, they are achieved at

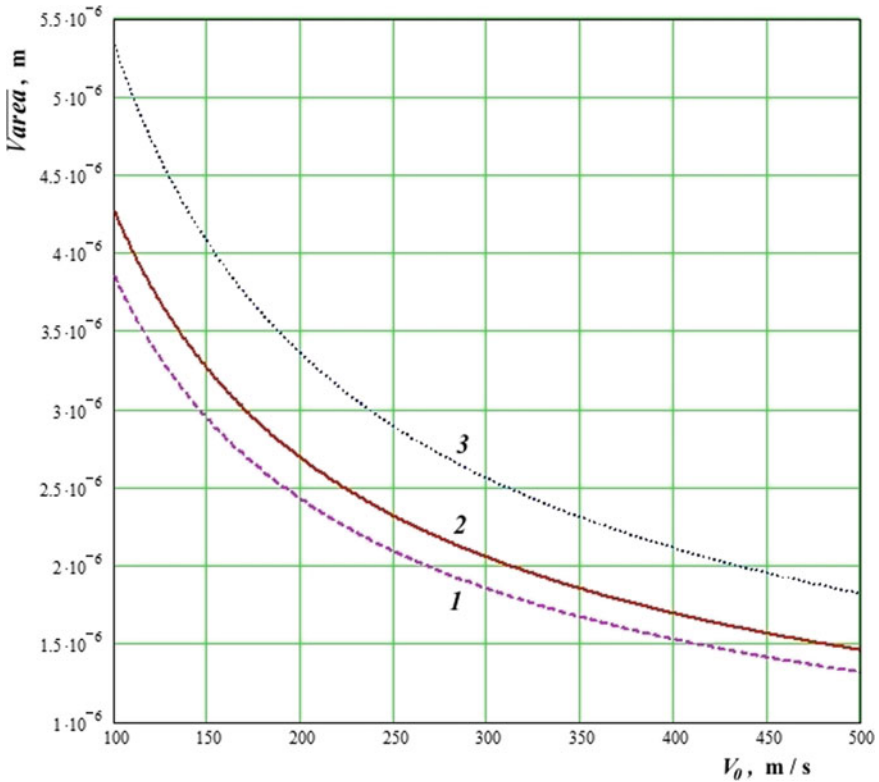


Fig. 6.5 Dependences of the maximum size of the fatigue defect $\sqrt{\text{area}}$ on the impact velocity V_0 (the drop size is fixed: $R_0 = 0.55$ mm), in which the development of destruction in the material does not occur: 1—Armco iron (ferrite structure); 2—steel 08Cr18Ni10T (austenite structure); 3—steel 20Cr13 (structure of sorbite)

different values of the velocity of collisions V_0^{cr} . The higher efficiency of the dispersion hardening mechanism, which is dominant in the sorbite structure, provides an almost twofold excess of the parameter V_0^{cr} compared to the ferritic and austenitic structures, where the solid solution hardening mechanism is dominant.

6.5.2 Coatings

Approbation of the computational model was also carried out for vacuum ion-plasma coatings of different composition and structure. The choice of coatings was due primarily to the difference in the behavior of dislocations in such coatings to identify the capabilities of the computational model. So in the coatings of pure Ti and

Table 6.3 The main physics and mechanical characteristics of the coatings used in the calculations [1, 16, 22]

Coating composition	Characteristics of the coating material					
	Density ρ , kg/m ³	Young's modulus E , GPa	Poisson's ratio ν	Shear modulus μ , GPa	Burgers vector b , 10 ⁻¹⁰ m	Lattice Type (Taylor's factor M_p)
Pure Ti	4505	110	0.33	41.5	2.92	hcp (6.5)
Monolayer TiN	5430	429	0.23	174	2.995	fcc (3.06)
3D-composite of TiAlSi-system	3840	148	0.24	60	3.9	fcc (3.06)

of stoichiometric titanium nitride TiN, the dislocation is braked by the grid resistance (Peierls stress). However, the dislocations themselves and their behavior in the metal and in ceramics are different. With a larger value of the Burgers vector, the dislocations in ceramics, in accordance with the Peierls–Nabarro theory, have a smaller width. Therefore, the value of ρ_{cr} in ceramics is about half an order of magnitude higher than in metals. This has a certain effect on the calculation results. And, speaking of ceramics, you should pay special attention to the proportion of covalent bonds. If it prevails, then the dislocations in such ceramics have a very small width; they are not mobile and become active only at temperatures above 1500–2000 °C. Such ceramics, for example, include AlN or SiC. Titanium nitride TiN refers to metal-like nitrides with a mixed ion-metal bond, dislocations in such ceramics, as in the TiAlSi system, are very mobile, which determines the applicability of the proposed model to such systems.

The main characteristics of the coatings used in the calculations are listed in Table 6.3. The structure of the investigated coatings is presented in Fig. 6.6.

In the coating of pure titanium with a hexagonal lattice in the framework of the model under consideration, the process of nucleation of fracture is determined by the phonon and electronic resistance of the lattice to the dislocation slip. The braking of dislocations occurs at the grain boundaries or on the surface of the substrate. Therefore, the distance between dislocations is taken as the distance l at which dislocations are decelerated by the Peierls stress σ_τ , that is, $l = 1/\sqrt{\rho_d}$. Considering the high ductility of pure titanium, the dislocation density is relatively small $\rho_d = 10^{11} \text{ m}^{-2}$, which gives $l \approx 3 \text{ }\mu\text{m}$ (Table 6.4).

In the TiN coating with the fcc lattice, the braking mechanism is also determined by the lattice resistance. But, unlike pure Ti, the value of l is determined by the distance between mobile dislocations, so l depends on the impact's stress σ_s and is a calculated value.

In the TiAlSi system coating, the dislocation is braked by dispersed particles, ordered (modulated) arranged in the coating volume (Fig. 6.6c). The average statistical distance between them is about 50 nm. In the calculations, the mechanism of

Fig. 6.6 Structure of coatings in cross section, scanning electron microscopy: TiN coating with a Ti sublayer 0.3 μm (a); coating of the TiAlSi system with the modulated structure of a 3D-nanocomposite at various magnifications (b, c)

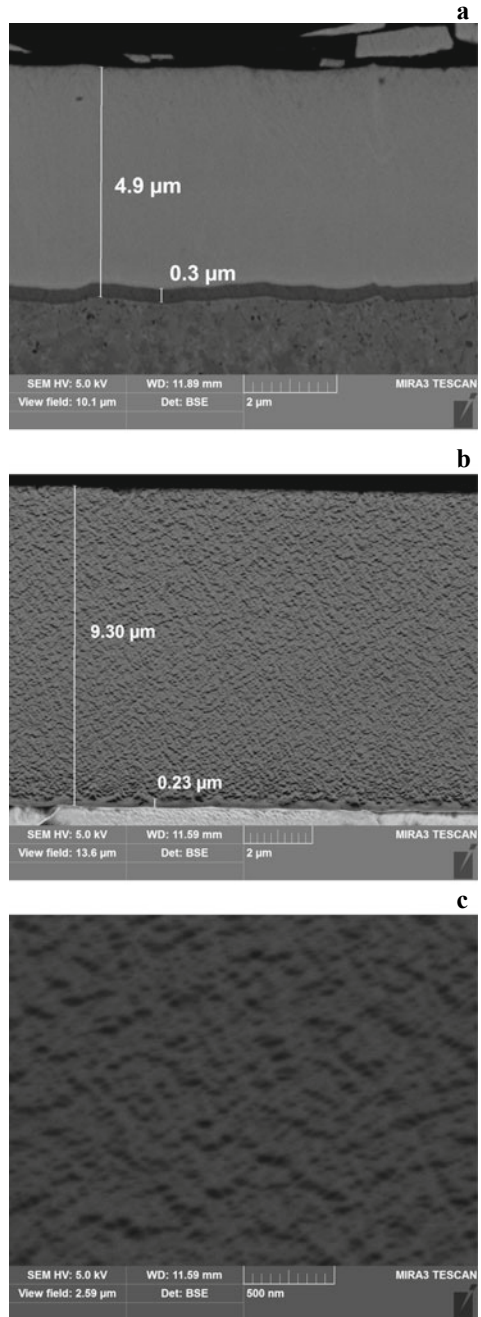


Table 6.4 Experimental m_0 and calculated N_3 values of the number of collisions* for various types of vacuum ion-plasma coatings

Coating composition	Structure parameters			Impact parameters for initial data $V_0 = 250$ m/s; $R_0 = 0.55$ mm		
	α_2	l, m^{-6}	D, m^{-6}	Calculations		Experiment
				N_3	α_0	m_0
Pure Ti	0.5	3.0	6.1	4051	0.283	14310
Monolayer TiN	0.025	1.05	4.9	6952	0.242	28760
3D-composite of TiAlSi-system	2.0	0.05	9.3	16730	0.445	37650

*—The table shows the values of the numbers of droplet impacts that fall in one point (defined in the software of the test bench)

interaction of dislocations with strengthening particles was not regulated. In connection with this uncertainty, the value of the coefficient α_1 in expression (6.11) for the TiAlSi system coating was calculated as $\alpha_1 = l \cdot \sqrt{\rho_m}$, whereas for the other coatings it was assumed $\alpha_1 = 1$.

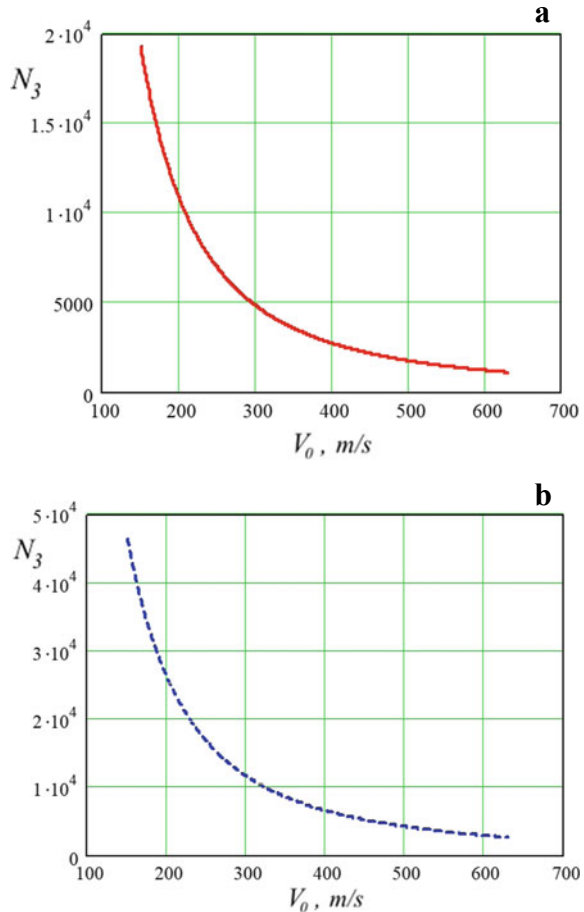
Calculations show that under impact loads of droplet collisions, the free path of dislocations during a single loading cycle (collision) for all the coatings under consideration significantly exceeds the size of the limiting structural factor. For example, in TiN, it exceeds the thickness of the experimental coating D by more than an order of magnitude. In the TiAlSi 3D-composite, it is almost an order of magnitude larger than the distance between the dispersed hardening particles. When analyzing the coatings, this circumstance made it possible to exclude the factor D/l_0 from the main design expression (6.3).

The results of numerical experiments in the framework of the considered model and the data of bench tests of the coatings are shown in Table 6.4. The experimental values shown in Table 6.4 characterize the incubation period for the erosive wear of the coatings m_0 . This value includes both the stage of the nucleation of a defect (cracks, pores, microcrater), and the stage of its development before the start of mass loss by the sample. It is not possible to instrumentally identify in experimental values of m_0 the number of collisions occurring only at the nucleation stage; therefore, the N_3 values are exclusively calculated. The contribution of the nucleation stage to the total value is characterized by the coefficient $\alpha_0 = N_3/m_0$.

In addition to the numerical values presented in Table 6.4, the model makes it possible to obtain the dependencies of the number of collisions N_3 , necessary for the nucleation of a fatigue defect in the coating, on the velocity of collisions V_0 for fixed values of the drop size R_0 . Some variants of such dependencies for the investigated coatings are presented in Fig. 6.7.

The results show that it is the structural parameters that determine the wear resistance under conditions of contact cyclic loads. The main structural principle that can significantly increase the wear resistance of coatings is limiting the mobility of dislocations. The implementation of this principle in coatings allows, among other

Fig. 6.7 Dependencies of the number of collisions N_3 on V_0 at $R_0 = 0.55$ mm, necessary for the initiation of fatigue cracks in coatings of different composition: monolayer of TiN (**a**); 3D-composite of TiAlSi system (**b**)



things, to increase the contribution of the N_3 nucleation stage of fatigue defects ($\alpha_0 = 0.445$) to the overall level of wear resistance m_0 .

The solution of the problem of generating fatigue wear proposed by us in this work concerns only the stage of formation of a fatigue defect—the origin of destruction and wear. The solution is based on the dislocation concept, which takes into account the interaction of dislocations with each other and with obstacles of various nature, and therefore it belongs to the field of microstructural fracture mechanics. However, one should not assume that the stage of microstructural fracture mechanics ends with the formation of a fatigue microdefect of a critical size (cracks, pores). It seems that the boundary between the stages of microstructural and continual fracture mechanics is not easy to determine. This is indicated by some of our experimental data. For example, at the stage of sustainable development of cracks under conditions of a drop-impact cyclic impact, the discrete nature of the development of fatigue cracks in coatings at the initial stage of their growth attracts attention. Features of the growth

of such cracks are shown in Fig. 6.8—they represent a chain of narrow pores. Each such structural element (segment) of the crack is about 0.5–0.75 μm. If the dislocation concept is extended to this stage of coating destruction, then at a dislocation density

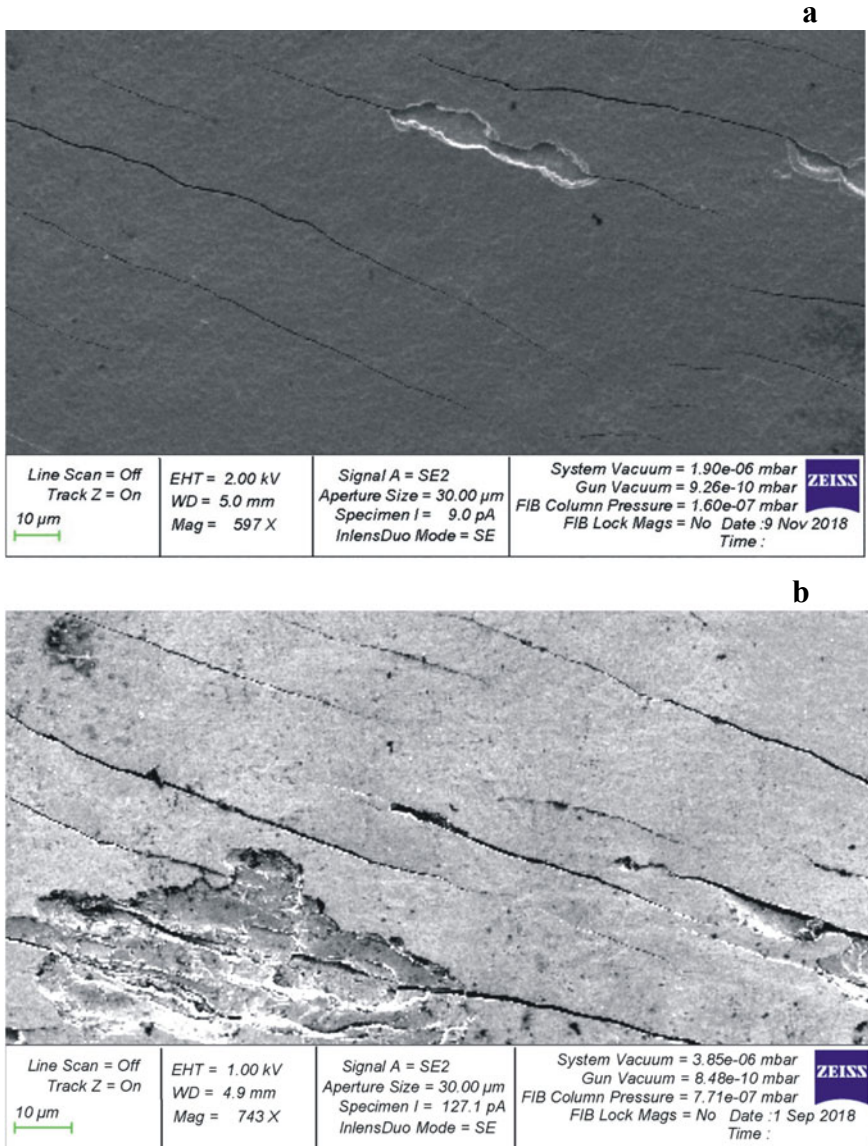


Fig. 6.8 The initial stages of the coatings destruction under drip-cyclic loading (TiAlSi system; scanning electron microscopy): the beginning of the growth stage of fatigue cracks (a); the beginning of the breaking of the coating (b)

providing a material rupture ($\rho_{cr} \approx 10^{16} \text{ m}^{-2}$), the distance between the dislocations in a pile-up of the crack fragment will be about 10 nm. In this case, a cluster of critical size should consist of 50–70 dislocations. A simple calculation shows that in the area of the head dislocation of such a cluster, the stresses will be about 20 GPa, that is, they will exceed the hardness of the coating and lead to its rupture. A violation of the continuity of the coating (rupture) initiates the promotion of the crack. Due to the formation of a new crack edge, the stress of the dislocation cluster relaxes below the critical value, since the deformation energy of the cluster zone is distributed as the surface energy of the banks of the formed crack segment. Under the action of subsequent droplet impacts in the plasticity zone at the tip of the crack, structural dislocations form a new cluster of dislocations until their density reaches a critical value and does not lead to a new rupture. With continued drip-impact effects, this process is constantly reproduced, determining the discrete nature of the advancement of the fatigue crack. Moreover, as follows from the described mechanism, the rate of crack propagation is determined by the structure of the material (coating) in the form of barriers that brake dislocations.

Suppose that the specified segments of cracks are equivalent to a parameter $\sqrt{\text{area}}$ in the model of J. Murakami, considered earlier for compact materials. From this point of view, a decrease in the threshold value of the size of the fatigue defect (segment) with an increase in hardness (the hardness of the coatings is several times higher than the hardness of the steels under consideration) within the framework of this model looks natural. However, the results of numerical experiments for coatings performed by expressions (6.13)–(6.17), similar to the steels considered above, did not give a satisfactory agreement with the experimental data. Apparently, with respect to thin highly hard coatings, both our model and the model of Y. Murakami need to be refined, taking into account the influence of the substrate and specific mechanisms of destruction of coatings.

6.6 Conclusion

The results of the performed studies demonstrate that in the absence of instrumental methods for accurately determining the duration of the stage of wear nucleation, the proposed analytical model can be used for this purpose. The model has a versatility of application with respect to various materials and coatings, the mechanisms for the nucleation of fatigue defects (cracks, pores, microcraters) in which they have a dislocation nature. Therefore, under normal conditions, the model is not applicable to ceramic materials with a high proportion of covalent bonds. Another limitation of using the model is, perhaps, too high sensitivity of the exponential factor in the basic expression (6.3) of the model. A small error in determining the numerical values of $\alpha_1, \alpha_2, \sigma_s$ or l in expression (6.3) does not allow obtaining results that are adequate to the experimental data. An important applied result of the work should be considered a clear demonstration of the fact that the targeted design of the coating's structure can significantly increase its durability (data in Table 6.2). The theoretical principles of the organization of the coating's structure described in the paper and the model for their calculation are forming the methodological foundations of such design.

It should be noted that, despite the satisfactory results of testing the proposed model for materials and coatings with different types of structure, it does not have absolute universality. In the presented results of numerical experiments (Tables 6.1, 6.2, 6.3, and 6.4; Figs. 6.4, 6.5, and 6.7) such materials and coatings were used, in which the mechanisms for the nucleation of fatigue defects (cracks, pores, micro-craters) are determined by the slip and interaction of full lattice dislocations. Such mechanisms are observed in compact materials with high values of the stacking fault energy, and in nanostructured materials and coatings, with sizes of structural elements (grains) of more than 30 nm. When the size of the structure elements is within 10... 30 nm, according to the classification of Cheng and others [30], the main carriers of plastic deformation are partial dislocations, which are generated at the grain boundaries. The motion and interaction of partial lattice dislocations lead to the formation of stacking faults. For such materials and coatings, as well as for compact materials with a low stacking fault energy, the model can be supplemented taking into account the stage of motion of partial dislocations and the stage of formation of stacking faults. As for nanomaterials with grain sizes less than 10 nm, within the framework of the dislocation approach, grain-boundary dislocations can be considered as carriers of deformation [30]. However, due to the specificity of the concept of grain-boundary dislocations and the incompleteness of their theory, the authors do not see the possibility of extending the proposed model to similar materials, as well as to materials with a covalent chemical bond type.

Acknowledgements The work was carried out with financial support from Russian Foundation for Basic Research (project code 18-08-00546).

References

1. Varavka, V.N., Kudryakov, O.V., Ryzhenkov, A.V.: In: Parinov, I.A. (ed.) *Piezoelectrics and Nanomaterials: Fundamentals, Developments and Applications*, p. 105. Nova Science Publishers, New York (2015)
2. Varavka, V.N., Kudryakov, O.V.: Regularities of steel wear under the impact of discrete water-droplet stream, Part I: Initial stage of droplet-impingement erosion. *J. Frict. Wear* **36**(1), 71 (2015)
3. Varavka, V.N., Kudryakov, O.V.: Regularities of steel wear under the impact of discrete water-droplet stream. Part II: Stage of the developed droplet-impingement erosion. *J. Frict. Wear* **36**(2), 153 (2015)
4. Kudryakov, O.V., Varavka, V.N.: Integrated indentation tests of metal-ceramic nanocomposite coatings. *Inorg. Mater.* **51**(15), 1508 (2015)
5. Varavka, V.N., Kudryakov, O.V., Bronnikova, N.I., Zabiya, I.Yu., Rubanov, V.V.: Development of the Paris-Erdogan model for the quantitative evaluation of the wear resistance of materials under dynamic contact with a discrete liquid-drop flow. *MATEC Web Conf.* **226**, 03005 (2018)
6. Kudryakov, O.V., Varavka, V.N., Zabiya, I.Y., Bronnikova, N.I.: Ocenka erozionnoy stoykosti uprochnennykh metallicheskikh splavov v usloviyakh kapleudarnogo vozdeystviya (in Russ., Erosion resistance assessment of hardened metal alloys under conditions of drop impact). *Vestnik DSTU.* **18**(1), 6 (2018) (in Russian)
7. Chizhov, A.V., Shmidt, A.V.: Impact of a high-velocity drop on an obstacle. *J. Techn. Phys.* **70**, 18 (2000)
8. Haller, K., Ventikos, Y., Poulidakos, D., Monkewitz, P.: Computational study of high-speed liquid droplet impact. *J. Appl. Phys.* **92**, 2821 (2002)

9. Paris, P., Erdogan, F.: A critical analysis of crack propagation laws. *ASME, J. Basic Eng.* **85**(4), 528–533 (1963). <https://doi.org/10.1115/1.3656900>
10. Seleznev, L.I., Ryzhenkov, V.A.: Erosion wear of structural materials. *Technol. Met.* **10**(3), 19 (2007) (in Russian)
11. Seleznev, L.I., Ryzhenkov, V.A., Mednikov, A.F.: Phenomenology of erosion wear of constructional steels and alloys by liquid particles. *Therm. Eng.* **57**(9), 741 (2010)
12. Ryzhenkov, V.A., Lebedeva, A.I., Mednikov, A.I.F.: Erosion wear of the blades of wet-steam turbine stages: Present state of the problem and methods for solving it. *Therm. Eng.* **58**(9), 713 (2011)
13. Anonymous. Experimental complex of unique stands “Hydro-impact stand Erosion-M”. National Research University “Moscow Power Engineering Institute”, Russia (2019).
14. Trykov, Y.P., Shmorgun, V.G., Gurevich, L.M.: Deformation of Layered Composites (VolSTU, Volgograd, 2001), p. 33 (in Russian)
15. Trykov, Y.P., Shmorgun, V.G.: Properties and Efficiency of Layered Composites (VolSTU, Volgograd, 1999), p. 190 (in Russian)
16. Babichev, A.P., Babushkina, N.A., Bratkovskiy, A.M., et al.: In: I.S. Grigoriev, E.Z. Meilikhov (eds.) *Physical Quantities: Reference Book* (Energoatomizdat, Moscow, 1991), p. 1232 (in Russian)
17. Ryzhenkov, V.A., Kachalin, G.A., Mednikov, A.F., Mednikov, A.L.F., Kudryakov, O.V., Varavka, V.N.: Kinetika zarozhdeniya i razvitiya erozionnogo razrusheniya poverkhnosti staley pri kapleudarnom vozdeystvii (in Russ., Kinetics of the nucleation and development of the steel’s surface erosional destruction under droplet impingement impacts), *Nadezhnost’ i bezopasnost’ energetiki*, (1), 67–71 (2012)
18. Varavka, V.N., Kudryakov, O.V.: Strength and high-plasticity materials fracture mechanisms under discrete water-droplet flow. *Vestnik DSTU.* **11**(8-2), 1376–1384 (2011)
19. Kudryakov, O.V., Varavka, V.N.: Mekhanizmy formirovaniya erozionnogo iznosa metallicheskikh materialov pri vysokoskorostnykh kapel’nykh soudareniyakh: Chast’ 1 (in Russ., Mechanisms of forming erosive wear of metal materials in process of high-speed droplet impact: Part 1), *Materialovedenie* (5), 36–43 (2012)
20. Kudryakov, O.V., Varavka, V.N.: Mekhanizmy formirovaniya erozionnogo iznosa metallicheskikh materialov pri vysokoskorostnykh kapel’nykh soudareniyakh: Chast’ 2 (in Russ., Mechanisms of forming erosive wear of metal materials in process of high-speed droplet impact: Part 2), *Materialovedenie*, (6), 14–19 (2012)
21. Botvina, L.R.: Destruction: Kinetics, Mechanisms, General Laws. In: I.I. Novikov (eds.) *(Science, Moscow, 2008)*, p. 334 (in Russian)
22. Frost, H.J., Ashby, M.F.: *Deformation-Mechanism Maps. The Plasticity and Creep of Metals and Ceramics* (Pergamon Press, Oxford, 1982), p. 328
23. de Meester, B., Yin, C., Doner, M., Conrad, H.: In: Li, J.C.M., Mukherjee, A.K.(eds.) *Rate Processes in Plastic Deformation* (A.S.M., 1973)
24. Hirth, J.P., Lothe, J.: *Theory of Dislocations* (McGraw Hill, 1968), p. 600
25. Hedström, P.: Deformation and Martensitic Phase Transformation in Stainless Steels (Luleå University of Technology, Department of Applied Physics and Mechanical Engineering, Division of Engineering Materials Sweden, 2007), p. 160
26. Murakami, Y.: *Metal Fatigue: Effects of Small Defects and Nonmetallic Inclusions*. Yokendo Ltd, Tokyo (1993)
27. Murakami, Y., Endo, M.: Effects of defects, inclusions and inhomogeneities on fatigue strength. *Int. J. Fatigue* **16**, 163 (1994)
28. Murakami, Y., Beretta, S.: Small defects and inhomogeneities in fatigue strength: experiments, models and statistical implications. *Extremes* **2**(2), 123 (1999)
29. Āman, M., Tanaka, Y., Murakami, Y., Remes, H., Marquis, G.: Fatigue strength evaluation of small defect at stress concentration. *Proced. Struct. Integr.* **7**, 351–358 (2017). 3rd International Symposium on Fatigue Design and Material Defects, FDMD 2017, ISSN 2452-3216, <https://doi.org/10.1016/j.prostr.2017.11.099>. <http://www.sciencedirect.com/science/article/pii/S2452321617304559>
30. Cheng, S., Spencer, J.A., Milligan, W.W.: Strength and tension/compression asymmetry in nanostructured and ultrafine-grain metals. *Acta Mater.* **51**, 4505 (2003)

Chapter 7

Interface Frictional Behaviour of Aluminium and Iron Powder Compacts at Room Temperature



Pragat P. Marathe, Kanhu C. Nayak, Prashant P. Date,
and Sergei Alexandrov

Abstract Compacts from aluminium and iron powders were compressed under various loads such that their cylindrical surfaces touched that of the concentrically placed sleeve around the compact. Further compression led to the development of frictional conditions between the compact and the sleeve. The variation of frictional force depended on the ductility of the material and the particle shape. The interfacial coefficient of friction showed no dependence on the material, and showed a power law relation with the axial force. The surface roughness (R_a) values varied along the height of the compacted aluminium powder sample from 4.5 to 6.64 microns, while the hardness ranged from 24 Hv to 11 Hv.

Keywords Aluminium powder · Contact area · Friction · Friction test · Hardness · Roughness · Steel powder

7.1 Introduction

Powder compacts, when extruded to the final shape involve significant frictional forces between the container and the surface of the compact. They undergo free bulging under compression until a slightly barrelled cylindrical surface comes in contact with the walls of the tool. Further compression enhances the normal force

P. P. Marathe · K. C. Nayak · P. P. Date (✉)

Department of Mechanical Engineering, Indian Institute of Technology Bombay, Mumbai
400076, India
e-mail: ppdate@gmail.com

P. P. Marathe
e-mail: ppm1991@gmail.com

K. C. Nayak
e-mail: nayakkanhu83@gmail.com

S. Alexandrov (✉)
Ishlinsky Institute for Problems in Mechanics, Russian Academia of Sciences, 101-1 Prospect
Vernadskogo, 119526 Moscow, Russia
e-mail: sergei_alexandrov@yahoo.com

© Springer Nature Switzerland AG 2020

S. M. Aizikovich et al. (eds.), *Modeling, Synthesis and Fracture of Advanced Materials for Industrial and Medical Applications*, Advanced Structured Materials 136,
https://doi.org/10.1007/978-3-030-48161-2_7

exerted by the radially outward movement of the compact, leading to an increase in frictional forces causing considerable shear deformation at the interface (and consequent work hardening of the surface layers). Increase in compressive loading would cause the shear surface to move into the body of the billet. A thin sheared layer would appear on the cylindrical surface of the billet (sample). With an increase in the temperature, the shear strength of the billet would drop and the thin shear layer would form at much lower loads at the periphery of the billet. Besides, at high temperature, the distribution of the strain rate across the thickness of the shear layer would depend upon the nature of the interface. The generation of narrow hardened layers in the vicinity of frictional interfaces in metal machining and deformation processes is of interest due to the effect of these layers on the performance of machined parts and structures [1, 2]. Hardened (or fine grain) layers formed during deformation processes has been studied experimentally in [3–11]. One of the difficulties with studying such deformation behaviour is that the state of strain there is far away from that in conventional tests. Another difficulty is that several conventional models of plasticity predict singular behaviour of the actual velocity field in the vicinity of surfaces with high friction. For perfectly plastic materials having a yield criterion independent of hydrostatic stress, it has been shown in [12] that the quadratic invariant of the strain rate tensor approaches infinity and follows an inverse square root rule near maximum friction surfaces. The behaviour of the quadratic invariant of the strain rate tensor controlling the evolution of material properties is in qualitative agreement with experimental results on the generation of narrow hardened layers near friction surfaces. The main result reported in [12] has been extended to several models of plasticity in [13], where the double shearing model has been considered (the double shearing model has been proposed in [14]), [15] wherein a model of anisotropic plasticity, and [16, 17] wherein a model of viscoplasticity has been considered. Conventional constitutive equations used for describing the evolution of material properties cannot be combined with these theoretical results due to the singularity in the velocity field. To this, a novel approach has been recently proposed in [18]. The theoretical basis of this approach is the strain rate intensity factor introduced in [12]. To further develop this approach, it is necessary to design and carry out a number of non-conventional tests. One such possible tests is proposed in the present paper.

Solid and dry friction contacts are developed at the surface between the tool and the workpiece during the extrusion process. The mechanisms of friction present in tool–workpiece interaction are on account of the formation of adhesive bonds (called molecular interactions) and the elastic and plastic deformation (called mechanical interaction). The friction at the tool–workpiece interface is the outcome of the sum total of molecular and mechanical interaction. To understand the frictional phenomena, recently some friction tests have been proposed, such as high-pressure friction test [19] torsion friction test and high-speed friction test [20]. The high-speed friction test was used for developing the sticking friction at the die and workpiece interface for different workpiece temperatures [21]. Properties like hardness and size of the surface grains were investigated for extruded AA6060 alloy. A thin hard layer with a small grain size (compared to the centre of the extruded workpiece) was generated near the friction surface. Further, this friction test has been used by some

for extrusion of aluminium and magnesium alloy to understand the tool–workpiece interface friction behaviour [22]. They analysed the evolution of microstructure at different combinations of temperatures and friction speeds. In addition, they studied the microhardness near the friction surface.

However, in the entire test as mentioned in the literature, only solid wrought metallic workpieces have been used in the study of interface friction. It is necessary to understand the phenomena of friction in metallic powders in the powder metallurgy technique. Here, many methods like powder extrusion, powder forging and powder rolling are used to make products.

The present work is about the frictional behaviour of aluminium (Al) powder samples and those compacted from iron powder at room temperature. Low to moderate compressive loads were deployed and the frictional force was measured at the room temperature. In addition, hardness and roughness properties were determined and examined to know the effect of friction. A theoretical solution for the test conducted has been proposed in [23], where a model of viscoplasticity has been employed.

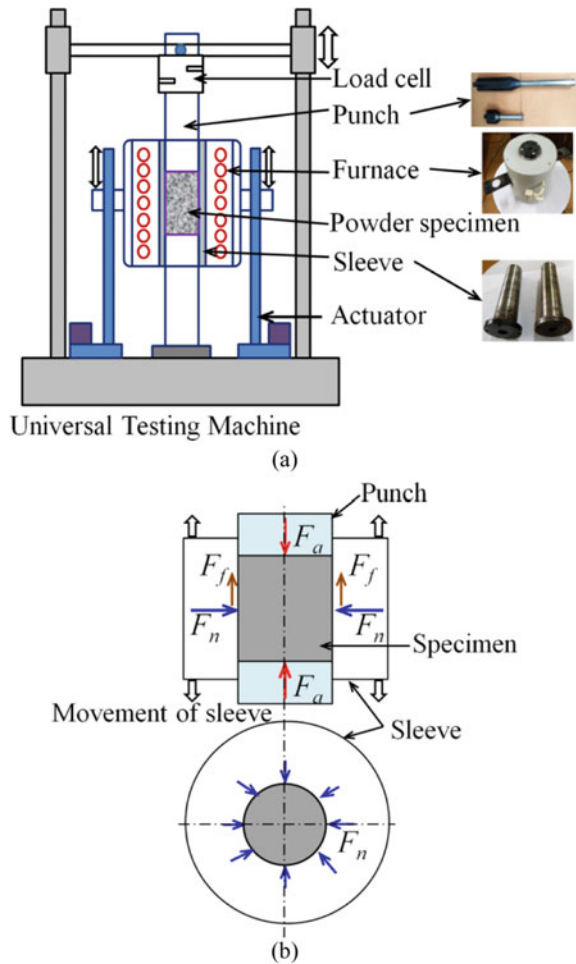
7.2 Experimental Procedure

Two sets of powder compacted samples were fabricated. The first set of the samples of green density 5.2 g/cc was compacted from pure iron powder; the second one set of green density of 2.1 g/cc was compacted from aluminium powder (Fe-0.1%, Mn-0.02%, Ti-0.03%, Cu- 0.02% Si-0.1% and balance Al). Iron powder was purchased from Industrial Metal Powders Pvt. Ltd, Pune-412216, India while the aluminium powder was purchased from Loba Chemie Pvt. Ltd, Mumbai-400005, India.

The tool consisted of two opposing punches between which the sample was compressed. The compressed sample and the punches were surrounded by a metallic sleeve to contain (enclose) the sample completely (Fig. 7.1a). The top punch was longer than the bottom punch. On compressing the sample, an increase in the diameter would be prevented by the cylindrical surface of the sleeve surrounding the sample, generating a normal force, F_n (acting radially) between the cylindrical surface of the sleeve and that of the sample in contact. Figure 7.1b illustrates different forces such as friction force (F_f), normal force (F_n) and axial force (F_a) acting on the specimen during the experiment. The direction of the frictional force (Fig. 7.1b) on the contact surface of the specimen was measured during the vertical (upward and downward) movement of the sleeve with respect to the specimen.

Determining the area of contact is an important step. For this, a blue colour was applied all over the cylindrical surface using indelible ink. The blue coloured cylindrical compacted sample was axially compressed in between the top and the bottom punches surrounded by the sleeve. Wherever tool–sample contact occurred, the ink was removed, and it remained behind on the sample in the other regions (Fig. 7.2). This enabled delineating regions of tool–workpiece contact from the non-

Fig. 7.1 Schematic diagram of the process: **a** experimental setup and **b** various forces on the specimen

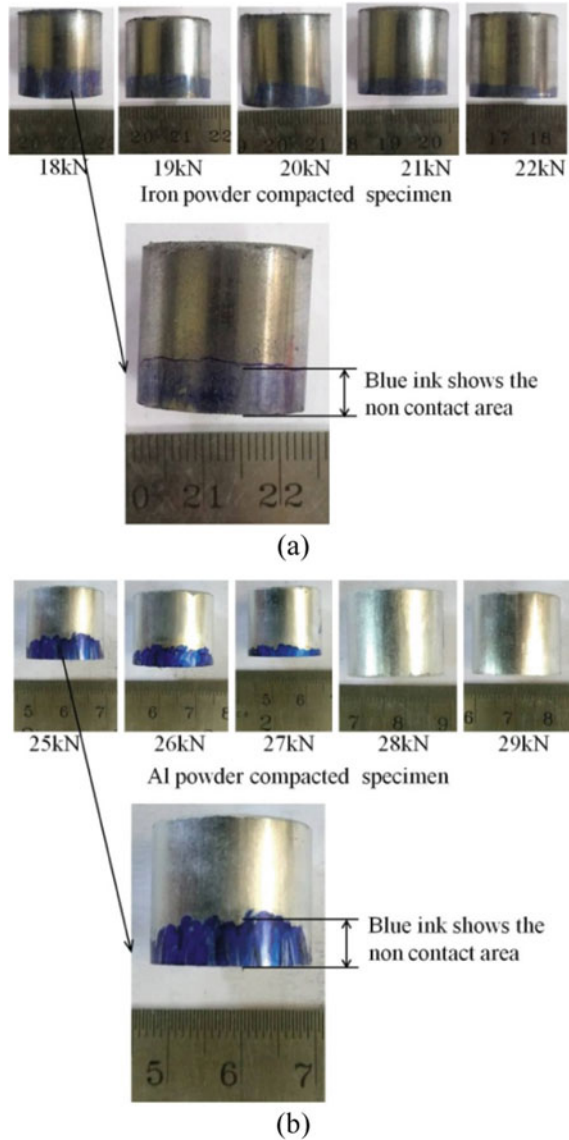


contacting ones. The maximum axial load varied from 25 to 29kN for aluminium-compacted samples, whereas, for iron, it ranged from 18 to 22kN.

Thereafter, the sleeve was lifted up slowly using a separate arrangement at about 1 mm/s. The (frictional) force versus time chart was recorded by the Tinius Olsen tensile testing machine (Supplier: Tinius Olsen India Pvt. Ltd, Delhi-201305, India). The specimens after axial compression under different loads are shown in Fig. 7.2a, b. As the sleeve was moved relative to the compressed sample, a peak in the load was observed as shown in Fig. 7.3a, b. This corresponds to the frictional force. The area of contact and the normal stress (calculated from the axial stress) was used to determine the normal force.

This, together with the frictional force measured, was used to estimate the coefficient of friction.

Fig. 7.2 Close up view of the tested sample for: **a** iron and **b** aluminium

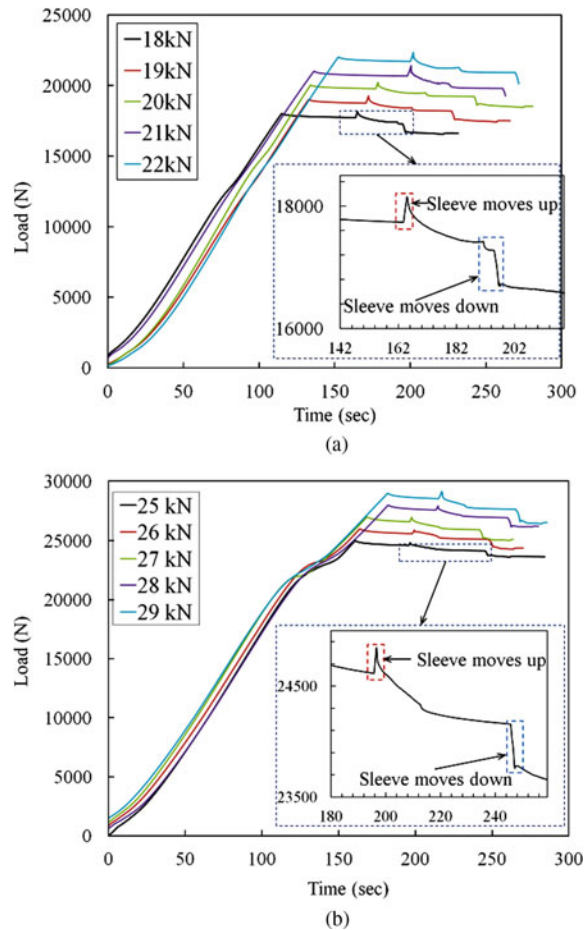


Contrary to expectations, the area of contact was found to be non-uniform (Fig. 7.2a, b).

The load due to friction was found to be higher when the sleeve was moved up as compared to when the sleeve was moved down (Fig. 7.3).

This procedure was repeated for two different materials (iron and aluminium), and each experiment was performed twice at each axial load for iron powder compacted samples, and thrice for aluminium powder compacted samples. The coefficient of

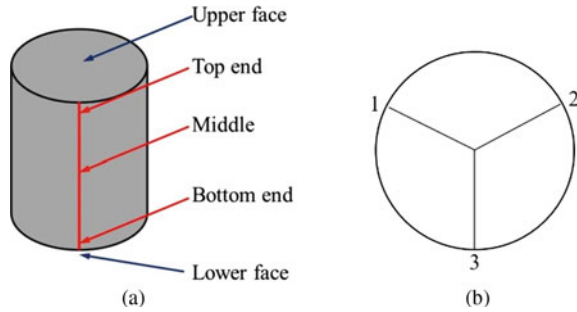
Fig. 7.3 Short load peaks in the load peaks in the load time curves noticed from the load time recording and differences in the frictional load depending on which way the sleeve was moved for: **a** iron and **b** aluminium



friction on the cylindrical surface was determined in each case and the corresponding hardness at the contact interface was measured (Fig. 7.4).

Surface roughness and surface hardness were measured for the samples deformed. The surface roughness was measured on the cylindrical surface using a Zeta optical profilometer, whereas the Vicker’s hardness was measured using a standard hardness tester (Vicker microhardness, HMVw). The compacted sample was reversed (turned upside down) when mounting it on the setup for the friction test. Hence the face at the top end of the sample during compaction was as the bottom during the friction test. The top end during compaction showed the highest hardness and density of packing of the particles, and this was on the lower platen for the friction test. A decrease in hardness measured on the cylindrical surface is observed due to the cylindrical surface getting abraded by the deformed (hardened) particles on the surface dislodged by friction during the friction experiment.

Fig. 7.4 Scheme of measuring hardness and surface roughness for the flat and the cylindrical surfaces of the sample: **a** three positions along the axis and **b** three locations along the circumference for a given location along the axis



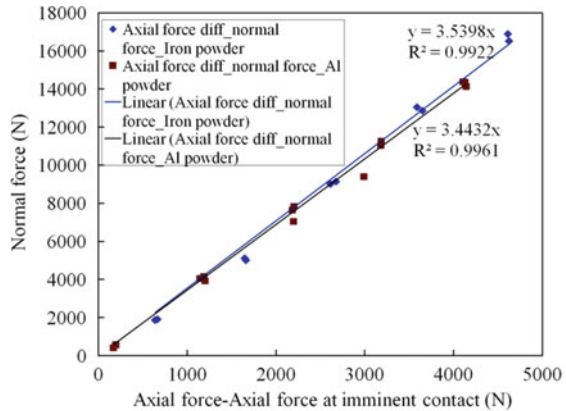
Thus the metallic powders were compacted to cylinders of 20 mm diameter using a pair of flat platens and a plastic sheet as a solid lubricant between the platen and the workpiece.

7.3 Results and Discussion

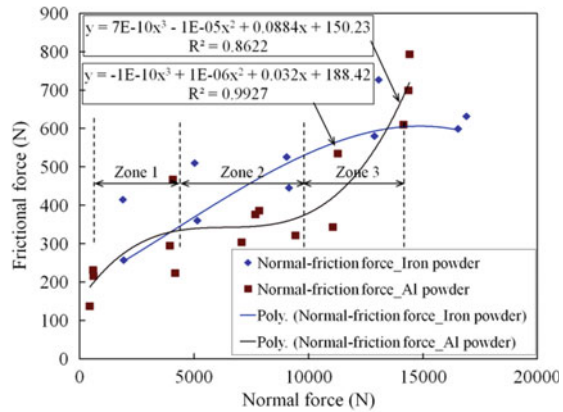
In the friction test, as the axial load increased, as expected, the diameter of the sample also increased. One would expect the surface roughness to increase with free bulging due to increasing circumferential strain. This would be expected to cause a larger frictional coefficient at the time of contact with the sleeve. However, the axial loading increased the contact pressure between the cylindrical surfaces of the sample and the sleeve, and so did the normal force on the surface. This increased the real area of contact as the asperities got flattened. This showed up as a decreasing coefficient of friction. The specimen surface roughened by the initial free bulging got smoothed in the area of contact. In this experiment, the percentage area of contact and the rate at which it approaches a value of 100% depends on the ductility (compressibility) of the powder. The aluminium powder, for instance, is more easily deformable compared to the iron powder. Hence, the percentage of the specimen contact area in aluminium powder sample approaches closer to 100%, and increases faster than in case of the iron powder.

The axial force in excess of that needed for imminent contact is the cause for the normal force of contact between the workpiece and the sleeve. The normal force is seen to increase linearly with this excess axial force (Fig. 7.5a). The rate of increase of the normal force is greater for iron powder than that for the aluminium powder. The maximum value of the normal force attained is greater for the iron compact compared to the aluminium compact. This is because, part of the energy of compression is used in deforming the powder particles, which serves to densify the aluminium powder compact. Thus, the rate of increase in the normal force is relatively lower for aluminium powder compacts than that of iron powder. Inevitably, the shape of the powder particles would also influence this parameter. However, the two curves

Fig. 7.5 Relations between different forces: **a** normal force varying with axial force and **b** frictional force varying with normal force



(a)



(b)

in Fig. 7.5a are very close as the nature of the curve is determined largely by the configuration of the experiment.

The Frictional force–Normal force curve (Fig. 7.5b) for aluminium shows three zones of frictional behaviour. The frictional coefficient, which can be seen as the slope of the Frictional force–Normal Force curve, shows an initial high value followed by a sharp drop. This is followed by a gentle drop in the coefficient of friction consistent with a practically constant slope of the Frictional force–Normal force curve. An increase in the frictional coefficient depicted by a rise in the frictional force in zone 3 (at higher compressive loads) is not observed in the variation of the frictional coefficient seen in Fig. 7.5b.

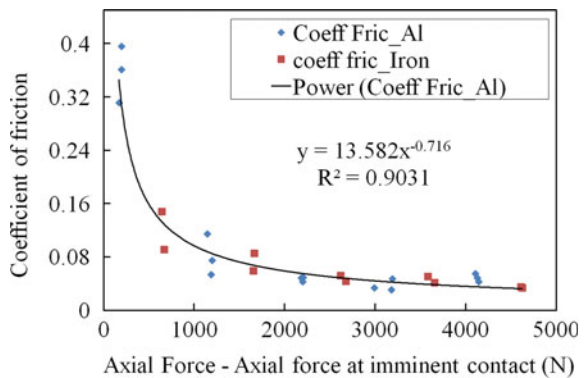
Comparatively, in case of iron powder, the increase in the frictional force occurs at a decreasing rate with an increase in the normal force. This indicates a decrease in the coefficient of friction. The iron powder does not show a three-stage behaviour as shown by the aluminium powder.

At increasing axial forces, the increasing normal force on the surface of the sleeve would increase and deflect the sleeve. At relatively larger loads, the elastic deflection of the sleeve would be the highest. While measuring the frictional force, as the sleeve is lifted (moved upwards axially), the point of contact on the sleeve will change thereby bringing an undeflected portion of the sleeve in contact with the sample maintained under a certain compressive load. Considering that the elastic deflection in aluminium would be much greater than that in steel (due to a greater stored elastic energy being recovered), this would lead to a greater ‘frictional force’ being measured in aluminium powder compact, despite flattening of the asperities on the cylindrical surface of the sample. Additionally, interlocking (proportional to the normal force) of the surface roughness profile of compacted soft, deformable aluminium particles with that of the steel sleeve would also lead to such an observation. With regard to iron powder, the loads involved are much greater, but the phenomenon of flattening of surface asperities of a free bulging iron compact on contact with the sleeve, and interlocking of the particles at the surface with the roughness profile of the sleeve would be far less effective than what was observed with aluminium powder which is softer and more deformable and compliant compared to iron. As a result, the frictional force increases with increasing axial (and hence normal) force in aluminium and much greater scatter is also observed in the measured frictional force in view of the reasons just discussed.

The surface roughness (R_a) values measured on the cylindrical surface along the height of the sample ranged between 4.5 and 6.64 microns, and the hardness ranged from 24 Hv to 11 Hv in the aluminium samples. Such a variation is consistent with the fact that the cylindrical surface gets abraded during the friction experiment leading to the removal of hardened particles from the surface especially from places where the density of packing is relatively low.

In Fig. 7.6, it is seen that the variation of coefficient of friction with the axial force in both Al and steel powders lies on the same curve. Hence, the frictional behaviour of the two materials is seen to be very similar after a relatively large surface contact between the sample and the sleeve. This clearly indicates an overwhelming influence

Fig. 7.6 Coefficient of friction with an increase in axial force for the two metal powders



of the powder properties and the forming conditions, compared to the material, on the development of the coefficient of friction.

Despite the above, the frictional forces between the cylindrical surfaces of the samples (compacted from aluminium or iron powder) and the tool are very different. The frictional force at large axial force is seen to rise rapidly in case of aluminium compared to that for iron (Fig. 7.7).

The area of contact depends strongly on the nature of the powder (Fig. 7.8). Aluminium being a more easily deformable (softer) material shows a greater area of contact compared to that in an iron powder compact.

Powder morphology too has a strong influence on the interlocking among particles. Together with a greater yield strength, this explains a relatively lower contact area in case of steel powder compared to that of aluminium.

Figure 7.9a, b show the particle morphology for the aluminium powder (a) and the iron powder (b). Both the powders show a bimodal particle size, i.e. particles which can be divided into two classes—the small-sized particles and the large-sized ones. The Al particles have a rounded shape and have well-rounded edges, while those of

Fig. 7.7 Frictional force varying with the axial force for powder compacts of iron and aluminium

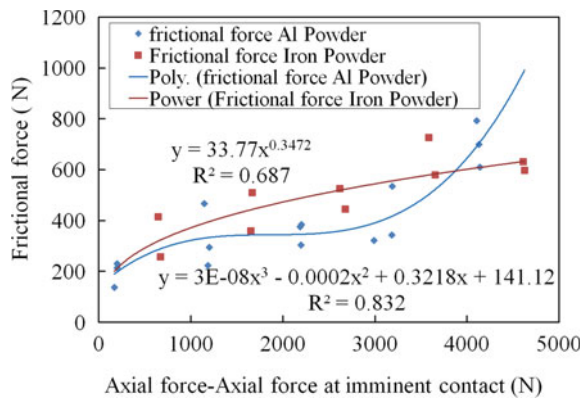


Fig. 7.8 Percentage area of contact with increasing axial load

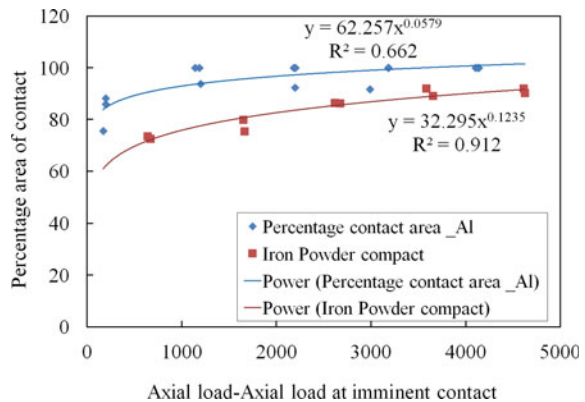
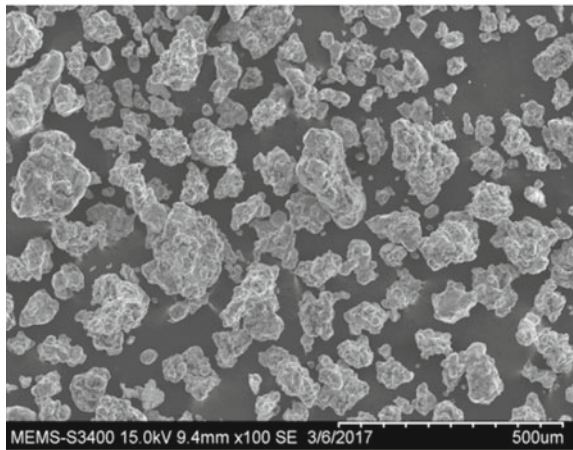


Fig. 7.9 Powder particle morphology of (a) aluminium powder and (b) iron powder used in the study



(a)



(b)

iron are irregular in shape and show edges which are not rounded. This influences the interlocking among particles, and interparticle friction. Hence the compaction load in case of the iron powder increases without a significant increase in the percentage of area in contact with the sleeve. Besides, a relatively lower deformability of the iron particles leads to fragmentation of these particles under load.

The magnitude of the normal force (as a consequence of the axial load) would be subject to frictional resistance among particles. Hence, large scatter is observed in the variation of the frictional force with respect to the axial force for iron powder.

7.4 Conclusions

From the foregoing observations and discussions, the following conclusions emerge:

1. The various observations made with regard to the contact behaviour of the aluminium and steel powder compacts on the basis of the axial friction test are well explained in light of results from the various investigations
2. The area of contact of the sample with the sleeve was always greater for aluminium powder compacts compared to those of iron powder.
3. The coefficient of friction decreases with an increase in the axial force, irrespective of the material, on account of flattening of asperities under an increasing normal force.
4. The surface hardness after the friction test was found to be lower on account of the removal of the hardened particles on the surface of the powder compacted samples.
5. The interface conditions at the room temperature strongly depend on the material of the powder, the particle morphology, and the prior work hardening, i.e. strain experienced by the particles.

Acknowledgments The funding under the DST (INT/RUS/RFBR/P-214) for the experimental work conducted at IIT Bombay and RFBR (Project number 17-51-45085) is gratefully acknowledged.

References

1. Griffiths, B. J., Furze, D. C.: Tribological advantages of white layers produced by machining. *ASME J. Tribol.* **109**(2), 338–342 (1987). <https://doi.org/10.1115/1.3261363>
2. Choi, Y. (2010). Influence of a white layer on the performance of hard machined surfaces in rolling contact. *Proc. Inst. Mech. Eng. Part B J. Eng. Manufact.* **224**(8), 1207–1215. <https://doi.org/10.1243/09544054JEM1847>
3. Kim, Y.-T., Ikeda, K.: Flow behavior of the billet surface layer in porthole die extrusion of aluminum. *Metallurg. Mater. Trans. A* **31**, 1635–1643 (2000). <https://doi.org/10.1007/s11661-000-0173-4>
4. Murai, T., Matsuoka, S., Miyamoto, S., Oki, Y.: Effects of extrusion conditions on microstructure and mechanical properties of AZ31B magnesium alloy extrusions. *J. Mater. Process. Technol.* **141**, 207–212 (2003). [https://doi.org/10.1016/S0924-0136\(02\)01106-8](https://doi.org/10.1016/S0924-0136(02)01106-8)
5. Kajino, S., Asakawa, M.: Effect of “additional shear strain layer” on tensile strength and microstructure of fine drawn wire. *J. Mater. Process. Technol.* **177**, 704–708 (2006). <https://doi.org/10.1016/j.jmatprotec.2006.04.108>
6. Sasaki, T.T., Morris, R.A., Thompson, G.B., Syarif, Y., Fox, D.: Formation of ultra-fine copper grains in copper-clad aluminum wire. *Scripta Mater.* **63**, 488–491 (2010). <https://doi.org/10.1016/j.scriptamat.2010.05.010>
7. Thirumurugan, M., Rao, S.A., Kumaran, S., Rao, T.S.: Improved ductility in ZM21 magnesium–aluminium macrocomposite produced by co-extrusion. *J. Mater. Process. Technol.* **211**, 1637–1642 (2011). <https://doi.org/10.1016/j.jmatprotec.2011.05.005>

8. Li, X., Zu, G., Ding, M., Mu, Y., Wang, P.: Interfacial microstructure and mechanical properties of Cu/Al clad sheet fabricated by asymmetrical roll bonding and annealing. *Mater. Sci. Technol. A.* **529**, 485–491 (2011). <https://doi.org/10.1016/j.msea.2011.09.087>
9. Hwang, Y.-M., Huang, T.-H., Alexandrov, S.: Manufacture of gradient microstructures of magnesium alloys using two—stage extrusion dies. *Steel Res. Int.* **86**, 956–961 (2015). <https://doi.org/10.1002/srin.201400571>
10. Alexandrov, S., Jeng, Y.-R., Hwang, Y.-M. (2015). Generation of a fine grain layer in the vicinity of frictional interfaces in direct extrusion of AZ31 alloy. *Trans. ASME J. Manuf. Sci. Eng.* **137**, Paper 051003. <https://doi.org/10.1115/1.4030267>
11. Alexandrov, S., Sidjanin, L., Vilotic, D., Movrin, D., Lang, L.: Generation of a layer of severe plastic deformation near friction surfaces in upsetting of steel specimens. *Metals* **8**, Article 71. <https://doi.org/10.3390/met8010071>
12. Alexandrov, S., Richmond, O.: Singular plastic flow fields near surfaces of maximum friction stress. *Int. J. Non-Linear Mech.* **36**(1), 1–11 (2001). [https://doi.org/10.1016/S0020-7462\(99\)00075-X](https://doi.org/10.1016/S0020-7462(99)00075-X)
13. Alexandrov, S., Lyamina, E.: Singular solutions for plane plastic flow of pressure-dependent materials. *Dokl. Phys.* **47**(4), 308–311 (2002). <https://doi.org/10.3103/S0025654413060071>
14. Spencer, A.J.M.: A theory of the kinematics of ideal soils under plane strain conditions. *J. Mech. Phys. Solids* **12**, 337–351 (1964). [https://doi.org/10.1016/0022-5096\(64\)90029-8](https://doi.org/10.1016/0022-5096(64)90029-8)
15. Alexandrov, S., Jeng, Y.-R.: Singular rigid/plastic solutions in anisotropic plasticity under plane strain conditions. *Cont. Mech. Therm.* **25**(5), 685–689 (2013). <https://doi.org/10.1007/s00161-013-0304-y>
16. Alexandrov, S., Mustafa, Y.: Singular solutions in viscoplasticity under plane strain conditions. *Meccanica* **48**(9), 2203–2208 (2013). <https://doi.org/10.1007/s11012-013-9736-5>
17. Alexandrov, S., Mustafa, Y.: Quasi-static axially symmetric viscoplastic flows near very rough walls. *Appl. Math. Model.* **39**(15), 4599–4606 (2015). <https://doi.org/10.1016/j.apm.2014.12.052>
18. Goldstein, R.V., Alexandrov, S.E.: An approach to prediction of microstructure formation near friction surfaces at large plastic strains. *Phys. Mesomech.* **18**, 223–227 (2015). <https://doi.org/10.1134/S1029959915030066>
19. Hora, P., Gorji, M., Berisha, B.: Modeling of friction phenomena in extrusion processes by using a new torsion-friction test. *Key Eng. Mater.* **491**, 129–135 (2012). <https://doi.org/10.4028/www.scientific.net/KEM.491.129>
20. Sanabria, V., Mueller, S., Reimers, W.: A new high speed friction test for extrusion processes. *Key Eng. Mater.* **585**, 33–39 (2014). <https://doi.org/10.4028/www.scientific.net/KEM.585.33>
21. Sanabria, V., Mueller, S., Reimers, W.: Microstructure evolution of friction boundary layer during extrusion of AA 6060. *Procedia Eng.* **81**, 586–591 (2014). 11th International Conference on Technology of Plasticity, Nagoya. <https://doi.org/10.1016/j.proeng.2014.10.044>
22. Sanabria, V., Mueller, S., Gall, S., Reimers, W.: Investigation of friction boundary conditions during extrusion of aluminium and magnesium alloys. *Key Eng. Mater.* **611**, 997–1004 (2014). <https://doi.org/10.4028/www.scientific.net/KEM.611-612.997>
23. Alexandrov, S., Date, P.P.: An alternative interpretation of axial friction test results for viscoplastic materials. *Mech. Time Depend. Mater.* **22**(2), 259–271 (2018). <https://doi.org/10.1007/s11043-017-9372-x>

Chapter 8

In Vitro Degradation Test of Gd-, Si-Substituted Hydroxyapatite



Elizaveta A. Mukhanova, Ekaterina S. Ivanyutina, Maxim Yu. Stupko, and Irina V. Rybal'chenko

Abstract Synthetic hydroxyapatite is involved in osteogenesis when using as an implant. Different substitutions in the hydroxyapatite (HAp) can change the low rate of degradation and solubility of pure hydroxyapatite as well as other physical, chemical, and biological properties. We synthesized single-phase $\text{Ca}_8\text{Gd}_2(\text{PO}_4)_4(\text{SiO}_4)_2(\text{OH})_2$ (Gd, Si-HAp) by coprecipitation and investigated its behavior in model solutions: water, simulated body fluid and physiological saline solution (0.9% NaCl). Morphology of samples before and after degradation confirmed that flake-like crystals of initial Gd, Si-HAp is a preferable form for the further precipitation of HAp crystals with needle-like morphology the same as in human body. The degradation rate of substituted Gd, Si-HAp in comparison with pure HAp is higher in different solutions and the rate of nucleation is apparently slower as we can see in a series of in vitro degradation tests.

Keywords Hydroxyapatite · Simulated body fluid · Gadolinium

E. A. Mukhanova (✉) · E. S. Ivanyutina · M. Yu. Stupko · I. V. Rybal'chenko
Chemistry Department, Southern Federal University, 344090 7 Zorge St, Rostov-on-Don, Russian Federation
e-mail: kand@sfedu.ru

E. S. Ivanyutina
e-mail: creamjug@yandex.ru

M. Yu. Stupko
e-mail: 4maxst@gmail.com

I. V. Rybal'chenko
e-mail: riv@sfedu.ru

E. A. Mukhanova
Don State Technical University, 344000, Pl. Gagarina 1, Rostov-on-Don, Russian Federation

8.1 Introduction

Hydroxyapatite (HAp) plays a special (central) role in orthopedic and dental medicine (applications) as the major component of human bones and teeth [1–5]. Recent studies have shown that substituted HAp such as silicon-substituted hydroxyapatite (SiHAp) possesses new physical, chemical, and biological properties, [6–10]. Silicon plays an important role in cartilage and bone growth as microelement [11] and influences hydroxyapatite microstructure resulting in smaller crystal size and improved bioactivity and biocompatibility [10]. Lanthanides are other dopants that can also change HAp properties. For example, organic complexes with lanthanum are the potential orally available bone resorption inhibitors because they have less toxic effect than cisplatin and have a lack of disturbance in the HAp structure upon binding [2, 12–22]. The complexes of lanthanides may act as antioxidants or pro-oxidants and take part in free radicals homeostasis [23], have anticancer [24] and anticoagulation activities [25]. Gd³⁺-doped hydroxyapatite could emit ultraviolet (UV) radiation at 313 nm and suits for treatment of skin diseases like psoriasis, vitiligo, atopic dermatitis (eczema) and other photoresponsive skin disorders [26]. Lanthanide ions including Eu³⁺ and Gd³⁺ ideally substitute Ca²⁺ in apatite structure and affect the bone remodeling cycle. These ions are used in some multifunctional drug delivery systems with *in vitro* and *in vivo* bio-imaging [16]. Ag⁺ and Gd³⁺ substituted hydroxyapatite nanoparticles can be a contrast agent for multimodal imaging of bone–tissue interface [16, 27, 28].

A contradiction in the data on the possible degree of substitution of calcium for gadolinium can be outlined: Yasukawa et al. [29] stated that atomic ratios Gd/(Gd+Ca) can be only 0.01 but in [30] $x = 1.4$. Li et al. [22] stated that composition with $x = 2$ has Gd(OH)₃ as a side product. In patent [28] solid solutions' end for Ca_{10-x}Gd_x(PO₄)_{6-y}(SiO₄)_y(OH)_{2+x-y} belong to intervals $0 < y < 1.1$ and $0 < x < 1.1$. The materials with composition Ca₉M(PO₄)₅(SiO₄)_Y with M = Ln and Y = F, O, OH is known as mineral britholite and belongs to the apatite group.

The purpose of our study was to define a probability of getting pure phase Gd-, Si-doped hydroxyapatite with britholite structure, composition Ca₈Gd₂(PO₄)₄(SiO₄)₂(OH)₂ (Gd-, Si-HAp) and estimate bioactivity of this material by investigation of its biodegradation/bioresorption *in vitro*. Bioactivity for bone and dental implants implies the ability to form a layer of HAp on the implant surface instead of fibrous tissue during biodegradation/bioresorption processes. The importance of such studies is underlined by the fact that the time of bioresorption of HAp is one of the main characteristics for the practical application in medical devices and it depends on many factors: composition, chemical surface structure, porosity, crystal size, characteristics of the patient, and so on. Although the use of simulated body fluid (SBF) is controversial [31], Kokubo et al. [32] and Zadpoor [33] substantiated evidence of the possible correlation between behavior in solutions and bioactivity. These authors claimed that examination of a material in SBF is useful for predicting the *in vivo* bone bioactivity and can be used for screening bone bioactive materials before animal testing. For our purposes, we have tested degradation of Gd, Si-HAp

in water, physiological saline solution (0.9% NaCl), and SBF to predict the behavior of the material in future tests and to estimate their need.

8.2 Material and Method

8.2.1 Synthesis

$\text{Ca}_8\text{Gd}_2(\text{PO}_4)_4(\text{SiO}_4)_2(\text{OH})_2$ have been synthesized using the precipitation method [34]. To remove water from $\text{Ca}(\text{NO}_3)_2 \cdot n\text{H}_2\text{O}$, it was heated at 200 °C and then dissolved in distilled water. Gd_2O_3 was consequently dissolved in HNO_3 under stirring to obtain $\text{Gd}(\text{NO}_3)_3$ and added in $\text{Ca}(\text{NO}_3)_2$ solution. Then the appropriate amounts of sodium silicate $\text{Na}_2\text{SiO}_3 \cdot 9\text{H}_2\text{O}$ were added in this solution as a soluble source of silicon. Finally, the 17 M H_3PO_4 solution was added. After mixing for one minute, pH of the solution was maintained at 10.0 by adding NH_4OH solution. Afterward, the reaction mixture was heated to 70 °C and stirred for 3 days. The white precipitate was collected by filtration, fully washed and dried at 150 °C for 2 h, and then calcinated at $T = 800$ °C for 1 hour. Pure HAp also has been synthesized at the same conditions for comparison.

8.2.2 Degradation Test

$\text{Ca}_8\text{Gd}_2(\text{PO}_4)_4(\text{SiO}_4)_2(\text{OH})_2$ was soaked in water because the process of dissolution of HAp is very similar to bone resorption and caries processes [35]. The stimulating effect of dopants on the growth of new bone tissue ceramics was evaluated by immersing the samples in water, physiological saline solution (0.9% NaCl) [36–38], and SBF. The SBF solution was prepared according to the procedure described in [39].

In vitro tests were carried out at the temperature 37 °C for 28 days. After soaking, the samples were removed, filtrated, and dried at room temperature.

The extent of Ca^{2+} dissolution was evaluated by complexometric titration with EDTA using Eriochrome Black T as the indicator [40]. The presence of Gd^{3+} ion was evaluated by complexometric titration with EDTA using xylenol orange as the indicator [41]. No traces of Gd^{3+} were detected in solution after treatment.

8.2.3 Characterization

X-ray diffraction (XRD) is carried out for phase identification using ARL X'TRA diffractometer with $\text{CuK}\alpha$ ($\lambda = 1.5406$ Å) radiation. The XRD peaks are recorded in

2θ range of $5\text{--}70^\circ$. The surface morphology and microstructure of the samples before and after incubation in SBF was investigated by Scanning Electron Microscopy with JEOL JSM 6390 LA.

8.2.4 Statistical Analysis

Student's t-test was conducted to determine statistical significance among groups, and statistical significance was considered to be a p -value < 0.05 .

8.3 Results and Discussion

8.3.1 XRD Analyses

We analyzed the X-ray diffraction pattern of all samples before and after the degradation test (Fig. 8.1a–d). The main phase of all ceramics was found to be hydroxyapatite. The halo ring on (b) and (c) points out the presence of an amorphous phase or phase with low crystallinity.

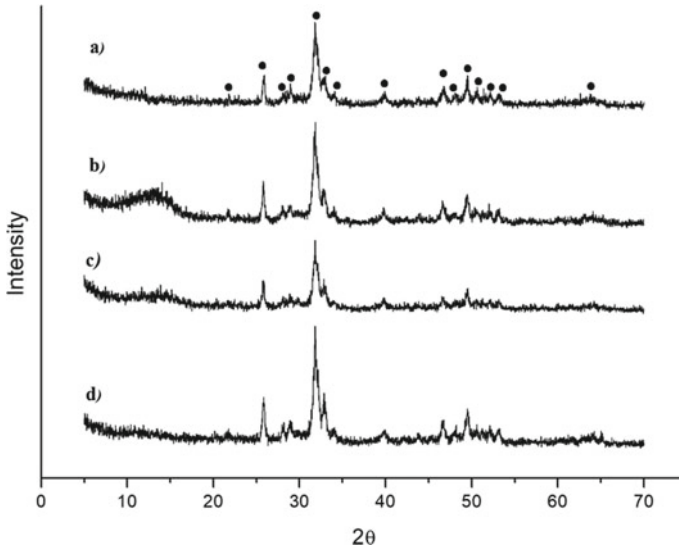


Fig. 8.1 XRD patterns of the samples: **a** $\text{Ca}_8\text{Gd}_2(\text{PO}_4)_4(\text{SiO}_4)_2(\text{OH})_2$; **b** after soaking in 0.9% NaCl; **c** after soaking in water; **d** after soaking in SBF. Black circles mark hydroxyapatite. #card 09-0432 (HAp) 32-0163 and britholite Gd, Si-HAp with hydroxyapatite structure [42]

The amorphous phase may consist of hydrated calcium phosphates involving polymeric silicate species and a few carbonate anions. The average crystallite size estimated from the full width at half maximum of the diffraction peak by the Scherrer equation in all three solutions is 58 ± 6 nm for initial Gd, Si-HAp, 110 ± 4 nm for SBF-treated, 108 ± 2 nm for water-treated and 102 ± 6 nm for NaCl-treated. In the same conditions, pure HAp has a size of about 50 nm [43, 44]. Substitution ions (Gd^{3+} and Si^{4+}) can change centers of crystallization on the HAp surface during resorption and recrystallization. We think that detailed modeling of this process can explain this feature in our next work.

The XRD studies have shown that Gd^{3+} has been successfully doped into no other crystalline phases that were detected besides this (hydroxyapatite phase). The silicon stabilizes HAp structure as described in britholite [42] and the degree of substitution of Ca to Gd is higher than that described in [17]. Probably the degree of substitution can be more than $x = 2$ and it can alter the physicochemical properties of the material. XRD patterns demonstrate that the samples after degradation/resorption are the mixture of apatite-like phases. They have promising potential for applications in the bone or dental implants according to [33].

8.3.2 SEM Analyses

We compared the morphology of crystals Gd, Si-HAp before and after 10 days of SBF soaking. SEM images of the ceramics before resorption show that particles, which consist of crystallites, have an average size of 90–100 μm and 20–30 μm (Fig. 8.2a). At a higher resolution (Fig. 8.2b), we estimated the size of the single flake-like crystallites in the group as about 1–1.5 μm that could be beneficial for bone growth [45]. The shape of the crystallites proves the high crystallinity of the obtained sample. We observed pores in the particles with a linear size of about 0.5–1.5 μm . Pore sizes are directly related to bone formation since they provide surface and space for cell adhesion and bone ingrowth. The pores of this size are suitable for vascularization ingrowths, while 100–300 μm pore sizes are suitable for bone regeneration [46].

On the graph of Gd, Si-HAp crystals after soaking in SBF, we detected visible differences in the shape and size. In the graph with $\times 100$ resolution (Fig. 8.2c), we noted that large (20–100 μm) and small (1–10 μm) crystallites generate aggregates up to 500 μm . We supposed that large aggregates of crystallites have formed by filling the pores during remineralization. The new hydroxyapatite layer consists of individual nonporous needle-like crystals with a size of up to 5 μm (Fig. 8.2d). The needle-like crystals are the most common morphology of calcium phosphates in bone [47].

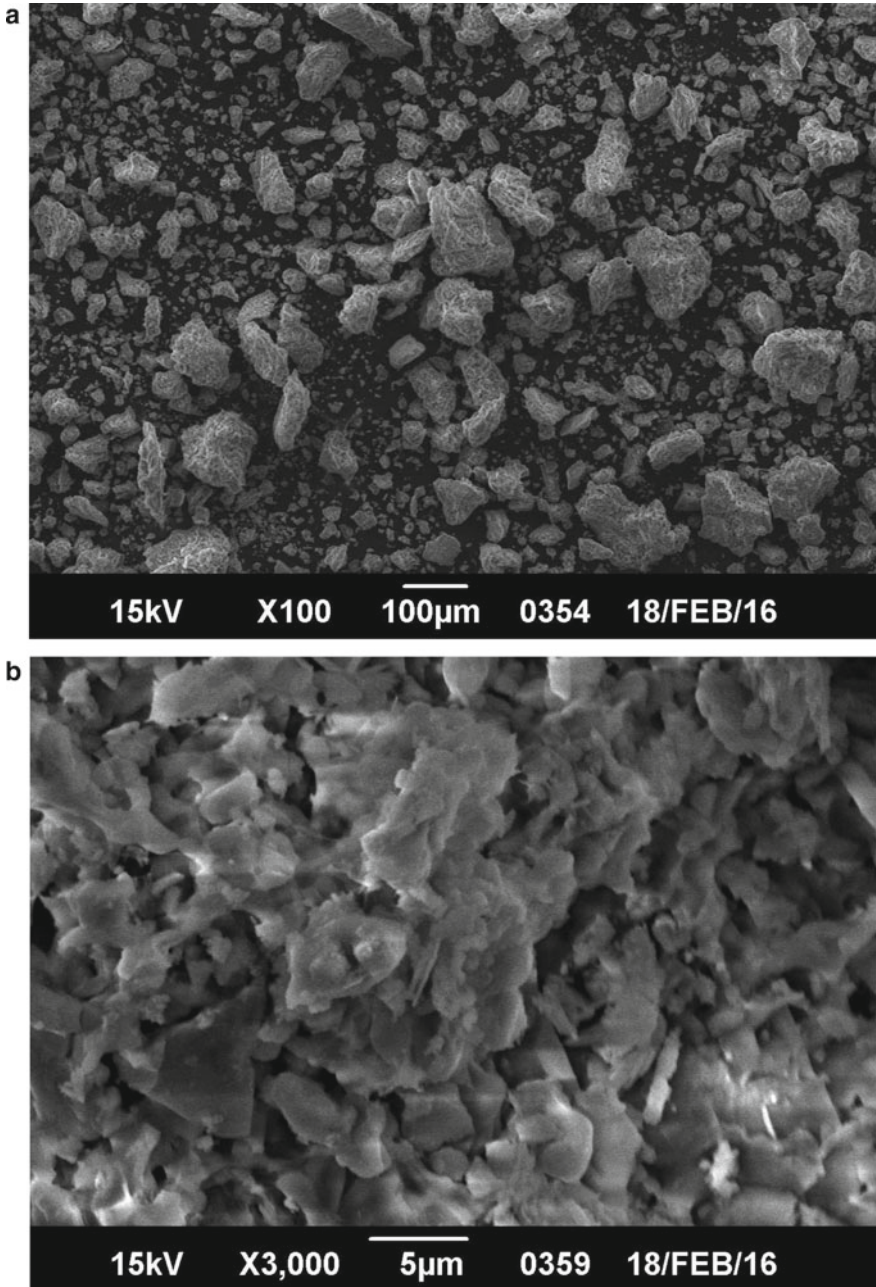


Fig. 8.2 a, b SEM images of samples before soaking in SBF for 10 days, c, d SEM images of samples after soaking in SBF for 10 days

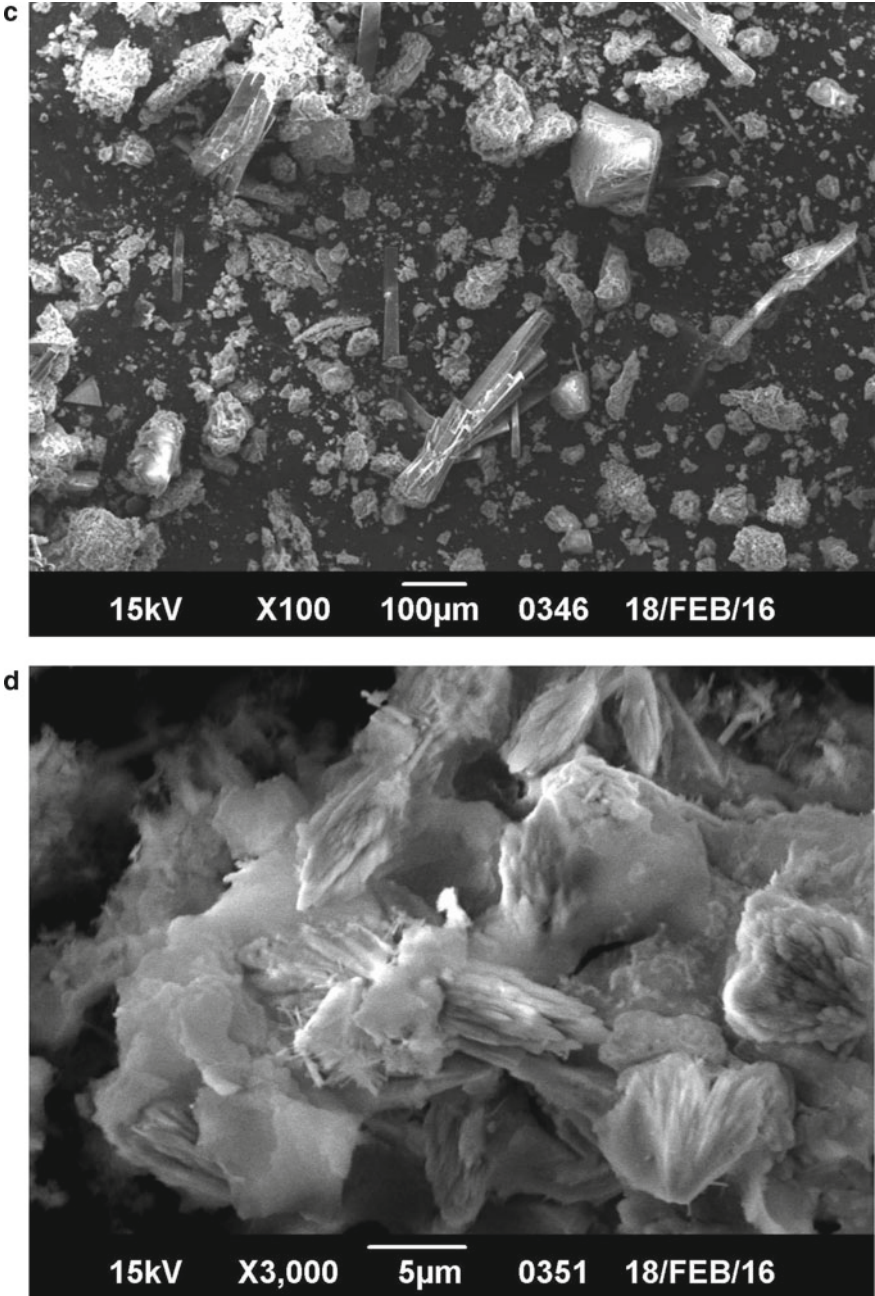


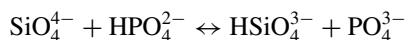
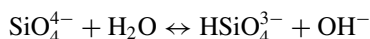
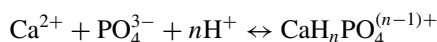
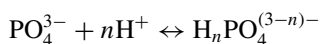
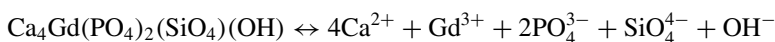
Fig. 8.2 (continued)

Table 8.1 Calcium content change after soaking in different modeling liquids after 10 days

Sample	%w Ca in solid phase	%w Ca in initial solution	
	H ₂ O	NaCl	SBF
Gd, Si-HAp	-13	-10	-20
HAp	-0.97	-0.95	-68

8.3.3 *In Vitro Degradation Study*

The following reactions describe general equilibria of different stages of non-substituted HAp dissolution (degradation) [48, 49] and hydrolysis of Gd³⁺ and SiO₄⁴⁻ ions [50, 51].



To determine degradation, we analyzed the calcium quantity in supernatants (Table 8.1). We found that 0.9% of NaCl soaking led to smaller changes in calcium concentration in comparison with water or SBF. Both this result and XRD pattern show an opportunity for remineralization connecting with the salting-out effect [52] in comparison with water. Soaking in SBF led to a decrease of the Ca²⁺-content in solution due to bonding in the new hydroxyapatite layer (Table 8.1). When using SBF, there is an initial amount of calcium in the solution. The percent of calcium content in the supernatant after pure HAp-SBF immersing is lower in comparison with the initial solution. We decided that the nucleation time in substituted HAp is lower and this is consistent with the investigation of bioactive glasses [53]. Authors [53] suggested that the ability to form the apatite layer decreases as the ionic field strength increases.

Thus, in this study, we investigated the degradation/resorption of Ca₈Gd₂(PO₄)₄(SiO₄)₂(OH)₂ in vitro. The behavior of the sample in three different solutions allows us to assume the bioactivity of this material. Our degradation experiments in water support our first finding of this sample activity during resorption in

SBF. Rate and degree of degradation in water and 0.9% NaCl solution were higher in the synthesized sample than in pure HAp, obtained in the same conditions to the comparison. The higher hydrolysis of silicate in comparison with phosphate can explain this fact. As it was said before (Table 8.1), the concentration of calcium in SBF solution has changed less in substituted HAp than in pure HAp. Either a higher rate of degradation or a slower rate of nucleation can explain this. We suppose that both contribute to the degradation/resorption process. The presence/absence of other ions can control the different degradation's degree in the model solutions. Further kinetics study of this degradation can specify details.

Our second finding is that $\text{Ca}_8\text{Gd}_2(\text{PO}_4)_4(\text{SiO}_4)_2(\text{OH})_2$ can form a hydroxyapatite layer on its surface in SBF. The results of XRD and SEM analyses of sample soaking in SBF solution support possible bioactivity of material because only apatite-like phase presents diffraction pattern and new crystals can be seen on SEM pictures.

One limitation of our study is that our experiment was held in air and some substitution of CO_3^{2-} for OH^- is possible. It is hard to evaluate a degree of such substitution in our conditions, but the influence of the effect on properties is insignificant as human HAp is always carbonate-substituted [54]. HAp can absorb NO_3^- ions during synthesis through precipitation and this ability limits clearness of future toxicological tests. Finding another soluble nontoxic precursor for gadolinium cation has practical importance for further applications.

8.4 Conclusion

We prepared Gd, Si-HAp with the structure of britholite by a coprecipitation method and investigated its behavior in water, physiological saline solution (0.9% NaCl), and SBF. To the best of our knowledge, this is the first experimental confirmation that the degree of substitution can reach $x = 2$. Our results show that doped Gd, Si-HAp has higher degradation rate in different solutions and an apparently slower rate of nucleation as we can see in a series of in vitro degradation/resorption tests. Hydrolysis of silicates and phosphates regulates these processes and the rate of nucleation relates to the ionic field strength of the substituting cation. The presence/absence of other ions can control different degradation in the model solutions. Further kinetics experiment needs to study the detailed mechanism. We confirmed that flake-like crystals of initial material are the preferable form to precipitate HAp crystals with needle-like morphology as in the human body. These tests allow one to predict that this material could expose bioactivity under biological in vitro and in vivo tests after synthesis modification and could be suitable for bone regeneration.

Acknowledgments This research was supported by the grant of the Government of Russian Federation no. 14.Z50.31.0046.

References

1. Dorozhkin, S.V.: Bioceramics of calcium orthophosphates. *Biomaterials*. **31**(7), 1465–1485 (2010)
2. Adzila S., Murad M., Sopyan I.: Doping metal into calcium phosphate phase for better performance of bone implant materials. *Recent Patents Mater. Sci.* **5**(1), 18–47 (2012)
3. Balasundaram, G., Webster, T.J.: A perspective on nanophase materials for orthopedic implant applications. *J. Mater. Chem.* **16**(38), 3737 (2006)
4. Swetha, M., Sahithi, K., Moorthi, A., Srinivasan, N., Ramasamy, K., Selvamurugan, N.: Biocomposites containing natural polymers and hydroxyapatite for bone tissue engineering. *Int. J. Biol. Macromol.* **47**, 1–4 (2010)
5. Olszta, M.J., Cheng, X., Jee, S.S., Kumar, R., Kim, Y.-Y., Kaufman, M.J., Douglas, E.P., Gower, L.B.: Bone structure and formation: a new perspective. *Mater. Sci. Eng. R: Rep.* **58**(3–5), 77–116 (2007)
6. Porter, A.E., Patel, N., Skepper, J.N., Best, S.M., Bonfield, W.: Effect of sintered silicate-substituted hydroxyapatite on remodelling processes at the bone–implant interface. *Biomaterials* **25**(16), 3303–3314 (2004)
7. Marchat, D., Zymelka, M., Coelho, C., Gremillard, L., Joly-pottuz, L., Babonneau, F., Esnouf, C., Chevalier, J., Bernache-assollant, D.: Accurate characterization of pure silicon-substituted hydroxyapatite powders synthesized by a new precipitation route. *Acta Biomater.* **9**(6), 6992–7004 (2013)
8. Camaioni, A., Cacciotti, I., Campagnolo, L., Bianco, A.: Silicon substituted hydroxyapatite for biomedical applications. In: Mucalo M (ed) *Hydroxyapatite for biomedical applications*. Woodhead Publishing Elsevier Limited Edition, Oxford, pp 343–373 (2015)
9. Leventouri, T.: Neutron powder diffraction studies of silicon-substituted hydroxyapatite. *Biomaterials* **24**(23), 4205–4211 (2003)
10. Arcos, D., Rodríguez-Carvajal, J., Vallet-Regí, M.: Silicon incorporation in hydroxylapatite obtained by controlled crystallization. *Chem. Mater.* **16**(11), 2300–2308 (2004)
11. Seaborn, C.D., Nielsen, F.H.: Effects of germanium and silicon on bone mineralization. *Biol. Trace Elem. Res.* **42**(2), 151–164 (1994)
12. Barta, C.A., Sachs-Barrable, K., Jia, J., Thompson, K.H., Wasan, K.M.: Lanthanide containing compounds for therapeutic care in bone resorption disorders. *Orvig C*
13. Boanini, E., Gazzano, M., Bigi, A.: Ionic substitutions in calcium phosphates synthesized at low temperature. *Acta Biomater.* **6**, 1882–1894
14. Li, X., Zeng, H., Teng, L., Chen, H.: Comparative investigation on the crystal structure and cell behavior of rare-earth doped fluorescent apatite nanocrystals. *Mater. Lett.* **125**, 78–81 (2014)
15. Chen, F., Huang, P., Zhu, Y.J., Wu, J., Zhang, C.L., Cui, D.X.: The photoluminescence, drug delivery and imaging properties of multifunctional $\text{Eu}^{3+}/\text{Gd}^{3+}$ dual-doped hydroxyapatite nanorods. *Biomaterials*. **32**(34), 9031–9039 (2011)
16. Liu, Z., Wang, Q., Yao, S., Yang, L., Yu, S., Feng, X., Li, F.: Synthesis and characterization of $\text{Tb}^{3+}/\text{Gd}^{3+}$ dual-doped multifunctional hydroxyapatite nanoparticles. *Ceramics Int.* **40**(2), 2613–2617 (2014)
17. Yasukawa, A., Kandori, K., Tanaka, H., Gotoh, K.: Preparation and structure of carbonated calcium hydroxyapatite substituted with heavy rare earth ions. *Mater. Res. Bull.* **47**, 1257–1263 (2012)
18. Yasukawa, A., Gotoh, K., Tanaka, H., Kandori, K.: Preparation and structure of calcium hydroxyapatite substituted with light rare earth ions. *Colloids Surf. A : Physicochem. Eng. Asp.* **393**, 53–59 (2011)
19. Fleet, M.E., Liu, X., Pan, Y.: Site preference of rare earth elements in hydroxyapatite $[\text{Ca}_{10}(\text{PO}_4)_6(\text{OH})_2]$. *J. Solid State Chem.* **149**(2), 391–398 (2000)
20. Cawthray, J.F., Creagh, A.L., Haynes, C.A., Orvig, C.: Ion exchange in hydroxyapatite with lanthanides. *Inorg. Chem.* **54**(4), 1440–1445 (2015)

21. Cipreste, M.F., Peres, A.M., Cotta, A.A.C., Aragón, F.H., de Antunes, A.M., Leal, A.S., Macedo, W.A.A., de Sousa, E.M.B.: Synthesis and characterization of 159Gd-doped hydroxyapatite nanorods for bioapplications as theranostic systems. *Mater. Chem. Phys.* **181**, 301–311 (2016)
22. Li, Y., Ooi, C.P., Philip, Hong Ning, C., Aik Khor, K.: Synthesis and characterization of Neodymium(III) and Gadolinium(III)-Substituted Hydroxyapatite as Biomaterials. *Int. J. Appl. Ceram. Technol.* **6**(4), 501–512 (2009)
23. Valcheva-Traykova, M., Saso, L., Kostova, I.: Involvement of Lanthanides in the free radicals homeostasis. *Curr. Topics Med. Chem.* **14**(22), 2508–2519 (2014)
24. Xu, Z.-Q., Mao, X.-J., Jia, L., Xu, J., Zhu, T.-F., Cai, H.-X., Bie, H.-Y., Chen, R.-H., Ma, T.: Synthesis, characterization and anticancer activities of two lanthanide(III) complexes with a nicotinohydrazone ligand. *J. Mol. Struct.* **1102**, 86–90 (2015)
25. Xu, X., Liu, Q., Xie, Y.: Metal ion-induced stabilization and refolding of anticoagulation factor II from the Venom of *Agkistrodon acutus* †. *Biochemistry* **41**(11), 3546–3554 (2002)
26. Mokoena, P.P., Nagpure, I.M., Kumar, V., Kroon, R.E., Olivier, E.J., Neethling, J.H., Swart, H.C., Ntwaeaborwa, O.M.: Enhanced UVB emission and analysis of chemical states of Ca₅(PO₄)₃OH:Gd³⁺, Pr³⁺ phosphor prepared by co-precipitation. *J. Phys. Chem. Solids* **75**(8), 998–1003 (2014)
27. Madhumathi, K. Sampath Kumar, T.S., Sanjeed, T M.: Silver and gadolinium ions co-substituted hydroxyapatite nanoparticles as bimodal contrast agent for medical imaging. *Biocerami. Dev. Appl.* **4**(2), 1–4 (2014)
28. Gibson, I.R., Skakle, J., Smith, N., Buckland, T.: Biomedical materials, Patent US20100322867 (23.12.2010)
29. Yasukawa, A., Kandori, K., Tanaka, H., Gotoh, K.: Preparation and structure of carbonated calcium hydroxyapatite substituted with heavy rare earth ions. *Mater. Res. Bull.* **47**(5), 1257–1263 (2012)
30. Get'man, E.I., Loboda, S.N., Tkachenko, T.V., Yablochkova, N.V., Chebyshev, K.A.: Isomorphous substitution of samarium and gadolinium for calcium in hydroxyapatite structure. *Russ. J. Inorg. Chem.* **55**(3), 333–338 (2010)
31. Bohner, M., Lemaître, J.: Can bioactivity be tested in vitro with SBF solution? *Biomaterials* **30**, 2175–2179 (2009)
32. Kokubo, T., Takadama, H.: How useful is SBF in predicting in vivo bone bioactivity? *Biomaterials* **27**, 2907–2915 (2006)
33. Zadpoor, A.A.: Relationship between in vitro apatite-forming ability measured using simulated body fluid and in vivo bioactivity of biomaterials. *Mater. Sci. Eng. C.* **35**(1), 134–143 (2014)
34. Nayak, A.K.: Hydroxyapatite synthesis methodologies: an overview. *Int. J. ChemTech Res.* **2**(2), 974–4290 (2010)
35. Christoffersen, J., Christoffersen, M.R., Kjaergaard, N.: The kinetics of dissolution of calcium hydroxyapatite in water at constant pH. *J. Cryst. Growth.* **43**(4), 501–511 (1978)
36. Okayama, S., Akao, M., Nakamura, S., Shin, Y., Higashikata, M., Aoki, H.: The mechanical properties and solubility of strontium-substituted hydroxyapatite. *Bio-Med. Mater. Eng.* **1**(1), 11–7 (1991)
37. Chen, Z.F., Darvell, B.W., Leung, V.W.H., Chen, Z.F.: Hydroxyapatite solubility in simple inorganic solutions. *Arch. Oral Biol.* **49**(5), 359–367 (2004)
38. Kim, S.B., Kim, Y.J., Yoon, T.L., Park, S.A., Cho, I.H., Kim, E.J., Kim, I.A., Shin, J.W.: The characteristics of a hydroxyapatite-chitosan-PMMA bone cement. *Biomaterials* **25**(26), 5715–5723 (2004)
39. Oyane, A., Kim, H.-M., Furuya, T., Kokubo, T., Miyazaki, T., Nakamura, T.: Preparation and assessment of revised simulated body fluids. *J. Biomed. Mater. Res.* **65A**(2), 188–195 (2003)
40. Dasgupta, S., Sinha, B.C., Rawat, N.S., Dasgupta, S.: Stepwise complexometric determinations of calcium and magnesium in lime and magnesia bearing materials. *Trans. Indian Ceram. Soc.* **41**(1), 14–16 (2014)
41. Barge, A., Cravotto, G., Gianolio, E., Fedeli, F. Barge, A.: How to determine free Gd and free ligand in solution of Gd chelates. A technical note. *Contrast Media Mol. Imag.* **1**(5), 184–188 (2006)

42. Arcos, D., Rodríguez-Carvajal, J., Vallet-Regí, M.: Crystal-chemical characteristics of Silicon–Neodymium substituted hydroxyapatites studied by combined X-ray and neutron powder diffraction. *Chem. Mater.* **17**(1), 57–64 (2005)
43. Yin, N., Chen, S.Y., Ouyang, Y., Tang, L., Yang, J.X., Wang, H.P.: Biomimetic mineralization synthesis of hydroxyapatite bacterial cellulose nanocomposites. *Prog. Nat. Sci.: Mater. Int.* **21**(6), 472–477 (2011)
44. Karamian, E., Khandan, A., Eslami, M., Gheisari, H., Rafiaei, N.: Investigation of HA nanocrystallite size crystallographic characterizations in NHA, BHA and HA pure powders and their influence on biodegradation of HA. *Adv. Mater. Res.* **829**, 314–318 (2013)
45. Wang, H.X., Guan, S.K., Wang, X., Ren, C.X., Wang, L.G.: In vitro degradation and mechanical integrity of Mg-Zn-Ca alloy coated with Ca-deficient hydroxyapatite by the pulse electrodeposition process. *Acta Biomater.* **6**(5), 1743–1748 (2010)
46. Jongwattanapisan, P., Charoenphandhu, N., Krishnamra, N., Thongbunchoo, J., Tang, I.M., Hoonsawat, R., Smith, S.M., Pon-On, W.: In vitro study of the SBF and osteoblast-like cells on hydroxyapatite/ chitosan-silica nanocomposite. *Mater. Sci. Eng. C* **31**(2), 290–299 (2011)
47. Ferraz, M.P., Monteiro, F.J., Manuel, C.M.: Hydroxyapatite nanoparticles : a review of preparation methodologies. *J. Appl. Biomater.* **2**(2), 74–80 (2004)
48. Dorozhkin, S.V.: A review on the dissolution models of calcium apatites. *Prog. Cryst. Growth Charact. Mater.* **44**(1), 45–61 (2002)
49. Bengtsson, A., Sjöberg, S.: Surface complexation and proton-promoted dissolution in aqueous apatite systems. *Pure Appl. Chem.* **81**(9), 1569–1584 (2009)
50. Shikina, N.D., Zotov, A.V., Volchenkova, V.A.: The solubility of Gd(2)Ti(2)O(7) and the hydrolysis of Gd(3+) in acidic solutions at 250A degrees C and saturation vapor pressure. *Geochem. Int.* **47**(4), 372–379 (2009)
51. Hayakawa, S., Kanaya, T., Tsuru, K., Shirosaki, Y., Osaka, A., Fujii, E., Kawabata, K., Gasqueres, G., Bonhomme, C., Babonneau, F., Jäger, C., Kleebe, H.-J.: Heterogeneous structure and in vitro degradation behavior of wet-chemically derived nanocrystalline silicon-containing hydroxyapatite particles. *Acta Biomater.* **9**(1), 4856–4867 (2013)
52. Rootare, H.M., Deitz, V.R., Carpenter, F.G.: Solubility product phenomena in hydroxyapatite-water systems. *J. Colloid Sci.* **17**(3), 179–206 (1962)
53. Branda F., Arcobello-Varlese, F., Costantini, A., Luciani, G.: Effect of the substitution of M2O3 (M = La, Y, In, Ga, Al) for CaO on the bioactivity of 2.5CaO·2SiO2 glass. *Biomaterials* **23**(3), 711–716 (2002)
54. Taylor, D. Fracture and repair of bone: a multiscale problem. *J. Mater. Sci.* **42**(21), 8911–8918 (2007)

Chapter 9

Mechanical Properties of Microposit S1813 Thin Layers



Andrey L. Nikolaev, Boris I. Mitrin, Evgeniy V. Sadyrin,
Vladimir B. Zelentsov, Adair R. Aguiar, and Sergei M. Aizikovich

Abstract Microposit S1813 is very popular photoresist due to high resolution, simplicity of deposition methods, and high adhesion to semiconductors. The least controlled parameter of photoresist thin films deposition is the tanning process, where everything depends on the operator and therefore it is quite difficult to ensure perfect reproducibility of the process. In this work, we studied thin films of Microposit S1813, deposited by spin coating on silicon substrates, and then tanned in 30, 45, 60, 75, and 90 s at 110 °C. The thickness of the films was studied using optical microscopy. The waviness and surface roughness were investigated by atomic force microscopy. To evaluate the mechanical properties of Microposit S1813 thin films, the nanoindentation method in the quasistatic mode was used. The results obtained will help to determine the region of the indenter-sample contact area as well as the measurement error, which is necessary for modern analytical mathematical models used to study the mechanical characteristics of multilayer coatings.

A. L. Nikolaev (✉) · B. I. Mitrin · E. V. Sadyrin · V. B. Zelentsov · S. M. Aizikovich
Don State Technical University, 1 Gagarin Sq., Rostov-on-Don 344000, Russia
e-mail: andreynicolaev@eurosites.ru

B. I. Mitrin
e-mail: boris.mitrin@gmail.com

E. V. Sadyrin
e-mail: ghostwoode@gmail.com

V. B. Zelentsov
e-mail: vbzelen@gmail.com

S. M. Aizikovich
e-mail: aguiarar@sc.usp.br

A. R. Aguiar
University of Sao Paulo, Sao Paulo, Brazil
e-mail: saizikovich@gmail.com

9.1 Introduction

The explosive growth of the semiconductor industry was caused by the constant desire to reduce semiconductor devices. Minimum element sizes or critical dimensions of semiconductor devices in mass production decreased from 10 mm more than 30 years ago to less than 100 nm in 2005. Minimization of semiconductor devices allowed to obtain a lot of complex equipment.

The tendency toward minimization was possible thanks to the photolithography process, based on the use of special photosensitive polymer materials called photoresists. Currently, the positive photoresist Microposit S1813 is widely used in the manufacture of modern micro- and nanodevices [1]. The advantages of this photoresist include the simplicity of application methods and high adhesion to semiconductor materials.

However, to obtain maximum resolution, high control of the deposition, tanning, and drying parameters is required. These operations can be combined into cycles, so the photoresist is subjected to loads, which can ultimately lead to cracking and destruction. The surface roughness, film thickness, as well as its mechanical properties also greatly contribute to the resolution of the photoresist.

In this work, optical microscopy was used to measure the thickness of the Microposit S1813 coatings, because thin films of the photoresist react quite violently to the electron beam in a scanning electron microscope. The waviness and roughness of the surface of the photoresist cause scattering at the exposure stage, which leads to diffraction and blurring of the film boundaries after development. In addition, these parameters also affect the indentation accuracy. To measure the amount of waviness and surface roughness, the method of atomic force microscopy was chosen.

Currently, nanoindentation is used to study the mechanical properties of microstructures, such as hardness and elastic modulus, due to its accuracy and simplicity. Photoresist films are a viscoelastic material, therefore, for their exhaustive study, it is necessary to use a dynamic indenter loading scheme [2]. However, one of the important applications of photoresist is to determine the real contact zone of the indenter with the sample. To do this, a thin film of photoresist is applied to the test sample and illuminated while holding the indenter at maximum force, so part of the thin film of the photoresist is in the shadow and penumbra of the indenter. Then the photoresist is developed and the resulting print is examined. For such studies, it is important to know the real properties of a particular photoresist of a certain thickness for a reliable interpretation of the indentation results. With the chosen formulation of the problem, the inapplicability of the dynamic mechanical analysis method is obvious. Therefore, it is necessary to use the quasistatic method. The quasistatic method of interpreting indentation data is based on the analysis of the curves of the indenter sinking versus the applied force [3, 4]. The most popular method for interpreting the results of nanoindentation using the Berkovich indenter is the Oliver–Farr method [5]. This method is used in a significant number of works devoted to the study of coatings for more than 20 years, starting from pioneering articles [6–8]. Currently, the approach is used to study the mechanical characteristics of topological insula-

tors [9], coatings for microelectronics [10], instruments for various purposes [11, 12], implants [13], thermal barrier coatings [14], self-organized films [15], films for improving tribological properties of materials [16], and others. Moreover, to analyze the experimental data obtained for thin films and heterogeneous in depth structures, researchers often resort to analytical [17–23, 25–27] and finite element modeling [28–32].

In this work, nanoindentation in a quasistatic mode is used to evaluate the mechanical properties of thin photoresist films deposited on silicon substrates. The obtained results will help to determine the region of the contact zone of the indenter with the sample, which is necessary for advanced analytical mathematical models used to study the mechanical characteristics of complex areas.

9.2 Materials and Methods

9.2.1 Sample Preparation

Thin films of photoresist are made by spin coating, as shown in Fig. 9.1. The photoresist is distributed on the substrate under the action of centrifugal force. This is the most common method of deposition polymer coatings, which gives a stable and reproducible result. The thickness of the resulting coating is influenced by the following deposition parameters: centrifuge rotation speed, time to set maximum rpm, and viscosity of the applied material.

In this study, the coating material is Microposit S1813 positive photoresist, and the substrate is a silicon (111) wafer. Before coating, the surface of the substrate is thoroughly cleaned with acetone, then the oxide layer is etched in hydrofluoric acid, and washed with deionized water. A portion of the photoresist with a volume of $10\mu\text{l}$ is dropped into the center of the rotating substrate, then the photoresist is evenly distributed on the substrate under the action of centrifugal force. The spin coating process consists of two stages. At the first stage, the photoresist is placed in the center of the substrate, rotating at 500 rpm. The center of the sample coincides with the axis of rotation of the centrifuge. After 5 s, the sample is accelerated to a

Fig. 9.1 Schematic illustration of the spin coating process

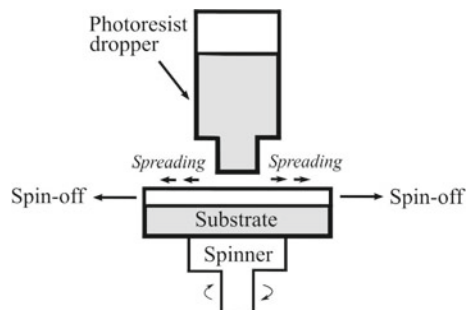
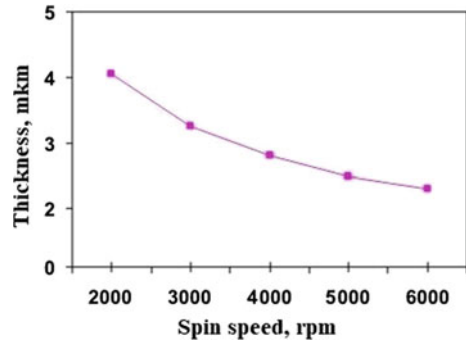


Fig. 9.2 Dependence of coating thickness on centrifuge rotation speed for Microposit S1813 photoresist. For measurements, the silicon substrate was cleaved



predetermined rotation speed and held there for 15 s. At the second stage, tanning of the coating occurs at a temperature of 110 °C in a dry oven. In this study, tanning times of 30–90 s were used with increments of 15 s. The thickness of the films made using different rotation speeds is shown in Fig. 9.2. It illustrates that the thickness decreases exponentially with rotation speed, where the film thickness is about 2.5 μm for 5000 rpm.

9.3 Results

9.3.1 Thickness Measurements

Optical measurements of the thickness of the deposited photoresist films were carried out using an Zeiss AXIO Vert A.1 inverted optical microscope. For measurements, a silicon substrate with deposited photoresist thin film was cleaved. Thickness measurements were made at the end of the cleavage, the results are presented in Fig. 9.3.

The samples obtained by the spin coating method showed excellent uniformity in thickness. In order not to clutter up the article with a large number of photographs, Fig. 9.3 shows only two samples with a maximum thickness (a) and a minimum thickness (b) of the photoresist.

9.3.2 AFM

The research of the dependence of surface roughness from the tanning time was conducted using Atomic Force Microscope (AFM) Nanoeducator (NT-MDT, Russia). For each of the five samples, the AFM images were taken in the $21 \times 21 \mu\text{m}$ scanning field. The surface roughness Ra for each of the images was measured using Gwyddion software (Czech Metrology Institute, Czech Republic) in three directions: horizontal, vertical, and diagonal. In each of the directions, five profiles were built. The average value of these five profiles was taken as absolute in this direction (Ra_{avg}).

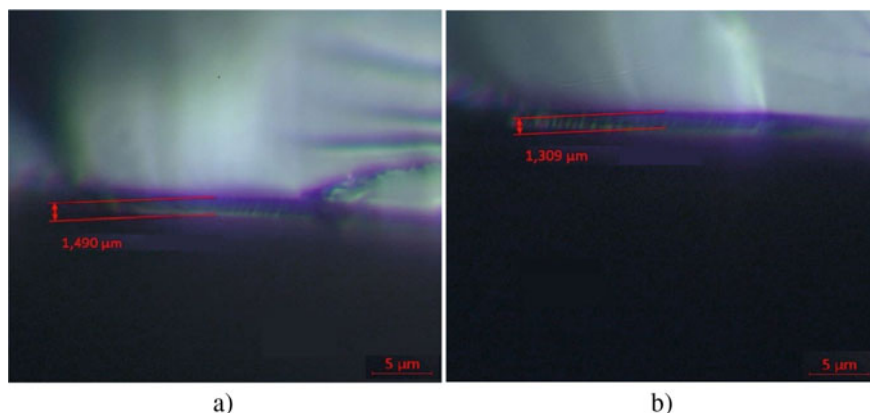


Fig. 9.3 Microposit S1813 thin films thickness images obtained by Zeiss AXIO Vert A.1 optical microscope for samples with 45 s (a) and 75 s (b) tanning time

The average value of roughness in three directions was taken as the absolute value of the roughness for a given surface (Ra_{absol}). All the profiles were constructed in such a manner to not contain the artifacts of deposition. The measurement results for the images in Fig. 9.4 are presented in Table 9.1.

No correlation was found between the tanning time and surface roughness of the photoresist films. The comparison of the maximum height value seems not to be valid, because of the presence of the artifacts of deposition on the AFM images. However, the AFM research revealed some important features of the tanning procedure:

- (1) the procedure allows to achieve smooth surface of the photoresist (> 10 nm) film regardless of the tanned time;
- (2) the most advanced surface topography with the highest value of Ra_{absol} was achieved by tanning the film for 75 s;
- (3) the smoothest surface with the lowest value of Ra_{absol} was achieved by tanning the film for 45 s.

9.3.3 Nanoindentation

Estimation of the mechanical characteristics of the films was conducted on Nanotest Platform 3 device (Micro Materials, UK) mounted on the anti-vibration table. The experiments were held in the closed chamber at a constant temperature of 27 ± 0.1 °C. For each of the five samples, 20 identical indentations were performed (maximum load was 5 mN, loading/dwell/unloading time was 30 s, and indenter contact velocity was $0.1 \mu\text{m/s}$), the results were averaged. In all the experiments, diamond Berkovich indenter was used. The results for Young's modulus and indentation hardness measurements are summarized in Table 9.2 and in Fig. 9.5.

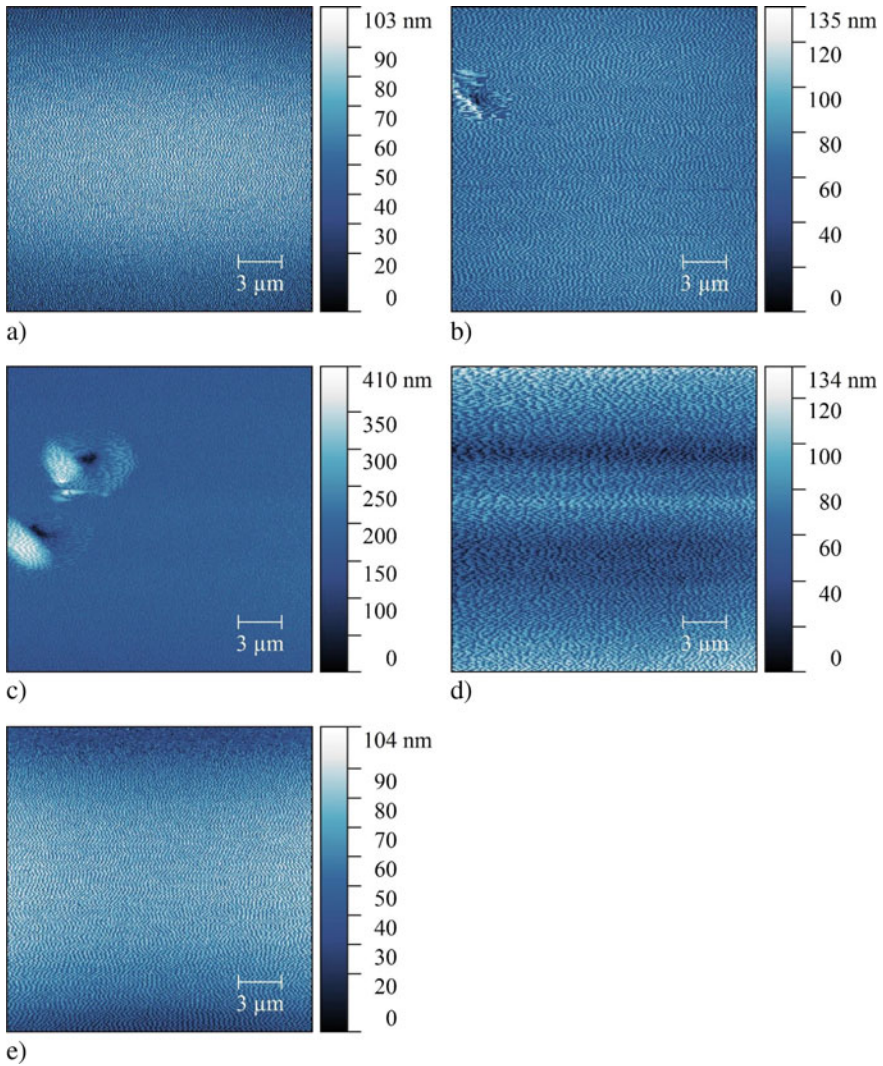


Fig. 9.4 Surface topography of the samples: **a** tanning time 30 s; **b** tanning time 45 s; **c** tanning time 60 s; **d** tanning time 75 s; **e** tanning time 90 s

As photoresist films are viscoelastic materials, the methodology of mechanical characteristic estimation provided in the paper is not fully representative because of creep and strain rate effects [33]. However, testing all the five samples with the same parameters and keeping in mind the fact that only one deposition parameter (tanning time) differs, one can make some conclusions by comparing the results for the samples with each other:

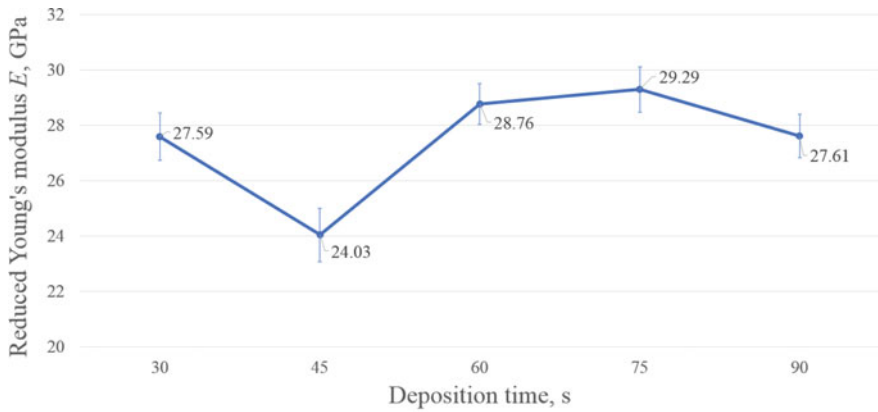
Table 9.1 Surface roughness summary

<i>t</i>	<i>n</i>	Horizontal		Vertical		Diagonal		<i>Ra</i> _{absol}
		<i>Ra</i> (<i>n</i>)	<i>Ra</i> _{avg}	<i>Ra</i> (<i>n</i>)	<i>Ra</i> _{avg}	<i>Ra</i> (<i>n</i>)	<i>Ra</i> _{avg}	
30	1	6.9	22.5	26.6	27.1	18.4	22.8	24.1
	2	6.4		27.1		21.3		
	3	7.3		26.6		21.3		
	4	7.6		28.7		28.4		
	5	7.5		26.5		24.3		
1	1	30.4	31.0	33.1	29.6	20.0	24.4	28.3
	2	31.5		28.7		27.0		
	3	30.0		25.8		20.7		
	4	27.8		28.9		30.4		
	5	35.3		31.3		23.8		
15	1	27.6	30.5	19.4	20.2	24.8	26.4	25.7
	2	30.1		17.0		32.8		
	3	31.6		20.4		21.8		
	4	35.6		18.4		32.1		
	5	27.6		26.0		20.5		
30	1	91.7	99.5	82.1	101.8	82.5	103.0	101.4
	2	153.0		125.3		103.6		
	3	107.4		110.9		147.8		
	4	67.0		110.1		110.2		
	5	78.5		80.4		70.9		
45	1	125.6	120.0	153.1	137.7	128.4	115.0	124.2
	2	137.9		133.8		115.9		
	3	133.2		86.4		126.4		
	4	104.3		153.3		126.6		
	5	99.2		161.8		77.6		
60	1	194.2	130.8	111.4	126.6	160.6	161.8	139.7
	2	142.0		145.6		150.6		
	3	94.5		123.8		130.3		
	4	133.1		134.4		187.0		
	5	90.1		117.9		180.6		

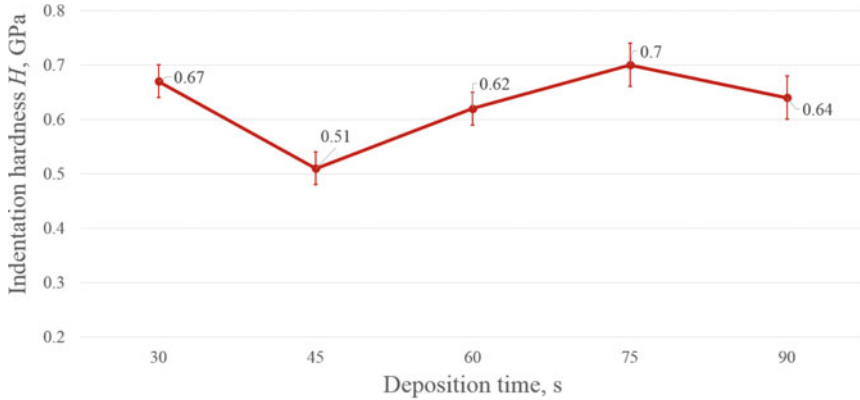
- (1) the procedure allows to achieve the photoresist with relatively small scattering of the mechanical properties;
- (2) the highest values of the reduced Young’s modulus and indentation hardness (along with the lowest maximum indentation depth) were obtained on the sample tanned for 75 s;
- (3) the lowest values of the reduced Young’s modulus and indentation hardness (along with the highest maximum indentation depth) were obtained on the sample tanned for 45 s;

Table 9.2 Mechanical properties of the samples

Deposition time (s)	Reduced Young's modulus E (GPa)	±	Indentation hardness H (GPa)	±	Maximum indentation depth h_{max} (nm)	±
30	27.59	0.85	0.67	0.03	508.12	10.03
45	24.03	0.96	0.51	0.03	578.4	14.8
60	28.76	0.74	0.62	0.03	523.28	13.38
75	29.29	0.82	0.70	0.04	493.08	11.72
90	27.61	0.78	0.64	0.04	518.9 3	14.38



a)



b)

Fig. 9.5 Mechanical properties of the samples: **a** reduced Young's modulus; **b** indentation hardness

9.4 Conclusion

All samples obtained by the spin coating technique have good thickness uniformity. This indicates a good reproducibility of the application of photoresist films and that a change in the tanning time from 30 to 90 s at a temperature of 110 °C does not affect the thickness of the resulting coating. From the results of AFM and nanoindentation research, we may suspect the surface microgeometry to influence the mechanical characteristics of the photoresist films as smoothest surface corresponded to the lowest values of mechanical properties, the most advanced surface—to the highest ones. However, due to the absence of the correlation between the deposition time and surface roughness, it is difficult to make clear what factor influences the surface roughness (and as a consequence the mechanical properties) at the stage of coating deposition. To find this out, further experimental work should be done with the statistical calculations.

Acknowledgments This research was supported by the Russian Science Foundation (RSF) through grant no. 19-19-00444.

References

1. Seidemann, V., Butefisch, S., Buttgebach, S.: Fabrication and investigation of in-plane compliant SU8 structures for MEMS and their application to micro valves and micro grippers. *Sens. Actuators* **97**, 457–461 (2002)
2. Odegard, G.M., Gates, T.S., Herring, H.M.: Characterization of viscoelastic properties of polymeric materials through nanoindentation. *Exp. Mech.* **45**, 130–136 (2005)
3. Beake, B.D., Leggett, G.J.: Nanoindentation and nanoscratch testing of uniaxially and biaxially drawn poly(ethylene terephthalate) film. *Exp. Mech.* **43**, 319–327 (2002)
4. Golovin, Y.I.: Nanoindentation and mechanical properties of solids in submicrovolumes, thin near-surface layers, and films. A review. *Phys. Solid State.* **50**(12), 2205–2236 (2008)
5. Pharr, G.M., Oliver, W.C.: Measurement of thin film mechanical properties using nanoindentation. *MRS Bull.* **17**(7), 28–33 (1992)
6. Tsui, T.Y., Pharr, G.M., Oliver, W.C., Chung, Y.W., Cutiongco, E.C., Bhatia, C.S., White, R.L., Rhodes, R.L., Gorbatskin, S.M.: Nanoindentation and nanoscratching of hard coating materials for magnetic disks. *MRS Online Proc. Libr. Arch.* **356** (1994)
7. Mencik, J., Quandt, E., Munz, D.: Elastic modulus of TbDyFe films—a comparison of nanoindentation and bending measurements. *Thin Solid Films* **287**(1–2), 208–213 (1996)
8. Suresh, S., Nieh, T.G., Choi, B.W.: Influence of phosphoric acid pretreatment on self-etching bond strengths. *Scr. Mater.* **41**(9), 951–957 (1999)
9. Lai, H.D., Jian, S.R., Tuyen, L., Le, P., Luo, C.W., Juang, J.Y.: Nanoindentation of Bi₂Se₃ thin films. *Micromachines* **9**(10), 518 (2018)
10. Xing, X., Wang, H., Xiao, G., Yang, S., Shu, X.: Impact of pH and application time of metaphosphoric acid on resin-enamel and resin-dentin bonding. *J. Mech. Behav. Biomed. Mater.* **80**, 235–245 (2018)
11. Vasiliev, A.S., Sadyrin, E.V., Mitrin, B.I., Aizikovich, S.M., Nikolaev, A.L.: Nanoindentation of ZrN coatings on silicon and copper substrates. *Russ. Eng. Res.* **38**(9), 735–737 (2018)
12. Horling, A., Hultman, L., Oden, M., Sjolen, J., Karlsson, L.: Mechanical properties and machining performance of Ti1 - xAlxN - coated cutting tools. *Surf. Coat. Technol.* **191**(2–3), 384–392 (2005)

13. Catauro, M., Bollino, F., Giovanardi, R., Veronesi, P.: Modification of Ti6Al4V implant surfaces by biocompatible TiO₂/PCL hybrid layers prepared via sol-gel dip coating: structural characterization, mechanical and corrosion behavior. *Mater. Sci. Eng.* **74**(3), 501–507 (2017)
14. Keshavarz, M., Idris, M.H., Ahmad, N.: Mechanical properties of stabilized zirconia nanocrystalline EB-PVD coating evaluated by micro and nano indentation. *J. Adv. Ceram.* **2**(4), 333–340 (2013)
15. Burlakova, V.E., Tyurin, A.I., Droган, E.G., Sadyrin, E.V., Pirozhkova, T.S., Novikova, A.A., Belikova, M.A.: Mechanical properties and size effects of self-organized film. *J. Tribol.* **141**(5), 051601 (2009)
16. Bemporad, E., Sebastiani, M., Staia, M.H., Cabrera, E.P.: Tribological studies on PVD/HVOF duplex coatings on Ti6Al4V substrate. *Surf. Coat. Technol.* **203**(5–7), 566–571 (2008)
17. Parinov, I.A., Chang, S.H., Gupta, V.K.: Advanced Materials. In: Proceedings of the International Conference on Physics and Mechanics of New Materials and Their Applications, PHENMA 2017, vol. 207. Springer Proceedings in Physics (2017)
18. Argatov, I.I.: Depth-sensing indentation of a transversely isotropic elastic layer: second-order asymptotic models for canonical indenters. *Int. J. Solids Struct.* **48**(25–26), 3444–3452 (2011)
19. Argatov, I.I., Sabina, F.J.: Small-scale indentation of an elastic coated half-space: the effect of compliant substrate. *Int. J. Eng. Sci.* **104**, 87–96 (2016)
20. Schwarzer, N.: The extended Hertzian theory and its uses in analyzing indentation experiments. *Philos. Mag.* **86**(33–35), 5179 (2006)
21. Chudoba, T., Schwarzer, N., Linss, V., Richter, F.: Determination of mechanical properties of graded coatings using nanoindentation. *Thin Solid Films* **469**, 239–247 (2004)
22. Vasiliev, A., Volkov, S., Aizikovich, S., Jeng, Y.R.: Axisymmetric contact problems of the theory of elasticity for inhomogeneous layers. *ZAMM-J. Appl. Math. Mech./Zeitschrift für Angewandte Mathematik und Mechanik* **94**(9), 705–712 (2014)
23. Guler, M.A., Erdogan, F.: Contact mechanics of graded coatings. *Int. J. Solids Struct.* **41**, 3856–3889 (2004)
24. Parinov, I.A., Chang, S.H., Jani, M.A.: Advanced Materials. In: Techniques, Physics, Mechanics and Applications, vol. 193. Springer Proceedings in Physics (2017)
25. Krenev, L.I., Aizikovich, S.M., Tokovyy, Y.V., Wang, Y.C.: Axisymmetric problem on the indentation of a hot circular punch into an arbitrarily nonhomogeneous half-space. *Int. J. Solids Struct.* **59**, 18–28 (2015)
26. Ma, J., Ke, L.L., Wang, Y.C.: Frictionless contact of a functionally graded magneto-electro-elastic layered half-plane under a conducting punch. *Int. J. Solids Struct.* **51**, 2791–2806 (2014)
27. Su, J., Ke, L.L., Wang, Y.C.: Axisymmetric frictionless contact of a functionally graded piezoelectric layered half-space under a conducting punch. *Int. J. Solids Struct.* **90**, 45–59 (2016)
28. Kot, M., Rakowski, W., Lackner, J.M., Major, L.: Analysis of spherical indentations of coating-substrate systems: experiments and finite element modeling. *Mater. Des.* **43**, 99–111 (2013)
29. Karimpour, M., Balint, D.S., Rzepiejewska-Malyska, K.A., Szerling, A., Michler, J., Lin, J.: An inverse method for extracting the mechanical properties of the constituent materials of a multilayer from nanoindentation data. *Comput. Mater. Sci.* **68**, 384–390 (2013)
30. Dean, J., Aldrich-Smith, G., Clyne, T.W.: Use of nanoindentation to measure residual stresses in surface layers. *Acta Mater.* **7**(59), 2749–2761 (2011)
31. Csanadi, T., Németh, D., Lofaj, F.: Mechanical properties of hard W-C coating on steel substrate deduced from nanoindentation and finite element modeling. *Exp. Mech.* **1–13**, (2016)
32. Gan, L., Ben-Nissan, B., Ben-David, A.: Modelling and finite element analysis of ultramicrohardness indentation of thin films. *Thin Solid Films* **290**, 362–366 (1996)
33. Chang, R.C., Chen, F.Y., Yang, P.: Dynamic mechanical properties of photo resist thin films. *J. Mech. Sci. Technol.* **21**(10), 1739 (2007)

Chapter 10

A Continual Model of Damage for Analyzing Long-Term Strength of Materials and Structural Elements



Ivan A. Volkov, Leonid A. Igumnov, and Svetlana Yu. Lutvinchuk

Abstract The issue of evaluating the strength and service life of critical engineering facilities with the exploitation properties characterized by multi-parametrical nonstationary thermal–mechanical effects is discussed. The main degradation mechanisms of structural materials (metals and their alloys), characteristic of such facilities, are examined. Basic requirements imposed on mathematical models of the above processes are formulated. In the framework of mechanics of damaged media (MDM), a mathematical model is developed, which describes processes of inelastic deformation and damage accumulation in the presence of creep. The MDM model consists of three interrelated parts: relations defining inelastic behavior of the material, accounting for its dependence on the failure process; equations defining damage accumulation kinetics; a strength criterion of the damaged material. The results of experimentally studying short-term creep of the VZh-159 heat-resistant alloy at constant temperatures and different stresses applied to the specimens are presented. Deformation and damage accumulation processes have been numerically analyzed; the obtained numerical results are compared with the data of full-scale experiments. The results of numerically modeling the carrying capacity of a nuclear power plant (NPP) reactor vessel in the conditions of a hypothetical accident are presented. The emergency was modeled by applying pressure modeling the effect of meltdown, constant internal pressure and temperature varying within the limits of the analyzed part of the reactor vessel. The analysis of the obtained numerical results reveals a number of characteristic features accompanying the process of deformation and failure of such facilities, related with time and location of the forming macrocracks, history of the stressed–strained state (SSS), damage degree in the failure zone, etc. In general, the results of comparing the numerical and experimental data make it

I. A. Volkov (✉) · L. A. Igumnov · S. Yu. Lutvinchuk
Research Institute for Mechanics, National Research Lobachevsky State University of Nizhny
Novgorod, 603950 Nizhny Novgorod, Russian Federation
e-mail: pmptmvgavt@yandex.ru

L. A. Igumnov
e-mail: igumnov@mech.unn.ru

S. Yu. Lutvinchuk
e-mail: litvinchuk@mech.unn.ru

possible to conclude that the proposed defining relations of MDM are reliable in accounting for the degradation of initial strength properties of materials according to the long-term strength mechanism and can be effectively used for evaluating long-term strength of structural elements under thermal–mechanical loading.

Keywords A continual model · Analyzing long-term strength · History of the stressed–strained state · Mechanics of damaged media

10.1 Introduction

In the course of their long service life, materials of structural elements of the equipment and systems of critical engineering facilities (CEF) with service lives of several tens of years (atomic power plants, oil-processing equipment, reservoirs for gaseous and liquefied chemical products, new generation aviation gas-turbine engines (GTE), plants (GTP), etc.), working in the conditions of nonstationary thermal–mechanical loading, accumulate microdefects leading to degradation of their initial strength characteristics, nucleation, and growth of cracks. For a considerable period of time, such changes develop implicitly. Besides, the most critical zones, determining the residual life of the elements, are, as a rule, inaccessible for nondestructive control means. To guarantee safe exploitation of CEFs and to prolong their life over normative time limits, it is required to control rates of development of damage levels in the most critical zones of structural elements (to evaluate spent life), as well as to forecast the development of such processes up to critical states (to evaluate residual life) [1].

Sudden strength failures of structural elements result from the degradation of the initial strength properties of structural materials due to damage accumulation under the effect of physical fields of various matures. In view of the locality of degradation processes, the working capacity of structural elements is determined by the service life of their most critical zones—zones with the highest rates of degradation of physical–mechanical properties of their structural materials. The parameters of such zones can greatly differ due to the difference in the properties of the materials themselves, design features, exploitation conditions, production technologies, etc.

At the design stage, ensuring safety, from the viewpoint of strength, is reduced to substantiating allowable time limits in the course of the designed service life for the initial conservative exploitation model of the facility (the loading history of a structural element incorporated in the design) with a margin for “not knowing” the true exploitation conditions, actual individual physical–mechanical and strength properties characteristic of the structural materials, limiting states, approximate character of computational methodologies, etc.

As damage accumulation processes are closely related to stressed–strained state (SSS) kinetics, the accuracy of numerical evaluations of strength and service life of structural elements will depend on how adequately the defining relations describe deformation processes in the critical zones of the structural elements in the given exploitation conditions. Such parameters of the viscoplastic deformation process as

length and type of the deformation trajectory, type and history of the stressed state, etc., substantially affect the rates of damage accumulation processes [2–4].

The currently available normative methods of evaluating service life of structural elements do not account for the actual processes taking place in materials. Elastic analysis used in the normative approach does not make it possible to account for actual characteristics of the viscoplastic deformation of materials, which, to a large degree, determine the service lives of structural elements [1]. In a general case, the strength of structures must take into account loading time and history. Then the failure criterion will be closely related to defining relations describing the failure process.

In this connection, it becomes necessary to develop new methods of evaluating service life of structural elements, based on corresponding equations of thermal-viscoplasticity, equations of damage accumulation and failure criteria, with comprehensively verifying them by corresponding full-scale and numerical experiments on laboratory specimens and numerically analyzing processes of deformation and failure of structural elements in exploitation conditions [1, 2, 5–8].

The most effective means to this end is the mathematical modeling of degradation processes of structural materials, using advanced models and methods of mechanics of damaged media (MDM) and fracture mechanics (FM) [2, 5–10]. Values of damage in accessible zones, obtained using numerical modeling, must be updated by means of periodic nondestructive control, using modern physical methods, of the state of material in accessible zones during shut-downs or maintenance of the facilities [11].

The results of numerous studies, where various metals were tested for long-term strength at different temperatures, loaded in pure tension, pure torsion, or combined torsion-tension, made it possible to conclude definitely that, in the conditions of a homogeneous stressed state, of all the possible equivalent stresses, it is either maximal principal stress or stress intensity (the second invariant of stress deviator), or a combination thereof, is the most appropriate one for determining long-term strength and comparing creep curves in different types of stressed states.

There exist publications experimentally substantiating the hypothesis of equivalency of creep process intensity (and long-term strength), based on the assumption of the existence of a unified curve of specific work of energy dissipation. Creep process intensity is understood to mean dissipated power [12]. To choose a particular type of equivalent stress for a given structural material, it is necessary to conduct additional experiments for creep and long-term strength in torsion or an experiment with combined torsion-tension of tubular specimens.

Durability curves are, as a rule, constructed for constant pressures (loads), whereas in practice stresses and temperatures vary according to rather complex laws. Hence, the problem of damage summation for quite irregular loading histories arises. In predicting time to failure in the conditions of variable stresses and temperatures, the crucial issue is the applicability of the results of tests conducted at constant stresses and temperatures. In engineering applications, the law of linear damage summation is generally used to this end, where each part of the spent life, or accumulated damage, is assumed to be independent of one another. Failure occurs when the sum of the parts of spent life is equal to unity. This law is widely used in engineering computations for the cases where structures work in the conditions of variable temperatures and

variable loading. Few attempts have been made to assess the accuracy of such analyses for variable stresses and variable temperatures separately, though even superficial analysis of damage accumulation kinetics reveals the evident difference. The currently available experimental programs have two main drawbacks. The first one is that creep failure is treated as a theoretical notion rather than an actual measurable physical phenomenon. The second drawback is connected with the fact that the experiments are aimed at verifying only one particular damage summation law, rather than at finding general laws of this process. Thus, for each of the test series (variable temperatures or stresses), it is only possible to determine whether the summation law is applicable, without being able to learn why it is inapplicable. The analysis of the available experimental data makes it possible to speak about a considerable effect of stress and temperature histories on long-term strength and to conclude that the linear damage summation law cannot be applied to the conditions of variable stresses and temperatures. A good correlation between room temperature hardness of a specimen loaded to creep and its long-term strength has been found. Comparison with a linear law of summation of relative durabilities reveals the following deviations [4]:

- creep damage accumulation in a tested alloy is not, in a general case, a linear function of preloading time;
- it is rather difficult to compare the damage state for the parts of the durability of equal duration, as the individual effect of each of the factors (temperature or stress) on the process of nucleation and growth of pores has not been studied. It was found, however, that, for each given component of durability, the total pore volume increases with the decreasing stress (at constant temperatures) and with the decreasing temperature (at constant stresses). For the same effect, during a part of durability, the softening degree (pore volume) increases with the decreasing stress but remains almost insensitive to temperature.
- there is no unified value of creep damage that always results in failure. Each combination of tests or exploitation conditions results in its own characteristic value of damage of failure.

The present paper, in the framework of mechanics of damaged media, develops a mathematical model of MDM, describing damage accumulation processes in structural materials (metals and their alloys) accompanying degradation mechanism due to developing creep strains in the conditions of multiaxial stressed states and arbitrarily complex regimes of thermal–mechanical loading. The processes of the long-term strength of the VZh-159 heat-resistant alloy have been numerically analyzed; the obtained numerical results were compared with the data from full-scale experiments.

The same model is used for numerically analyzing the carrying capacity of a nuclear power plant reactor vessel in the conditions of a hypothetical accident.

10.2 Defining Relations of Mechanics of Damaged Media

The present version of MDM is based on the following assumptions [2, 9]:

- the material of the medium is initially isotropic and free of any damage (only anisotropy due to deformation processes is accounted for; anisotropy of elastic properties due to damage processes in the material is not accounted for);
- tensor components of strains e_{ij} and strain rates \dot{e}_{ij} are a sum of “instant” and “time” components. The “instant” component consists of elastic components e_{ij}^e , \dot{e}_{ij}^e , independent of the deformation history and determined by the final state of the process, and plastic components e_{ij}^p , \dot{e}_{ij}^p depending on the deformation process history. The time component (creep strains e_{ij}^c , \dot{e}_{ij}^c) describes time dependence of the deformation processes at low loading rates;
- the evolution of equipotential creep surfaces is described by the change of its radius C_c and displacement of its center ρ_{ij}^c ;
- the elementary volume of the body changes elastically, i.e., $e_{ii}^p = e_{ii}^c = 0$;
- deformation processes characterized by small deformations are considered;
- the only structural parameter characterizing damage degree of the material on the macro-level is a scalar parameter ω —«damage degree» ($\omega_0 \leq \omega \leq \omega_f$);
- the effect of the accumulated damage degree on the deformation process of the material is accounted for by introducing effective stresses $\tilde{\sigma}_{ij}$.

The model of a damaged medium consists of three interrelated parts:

- relations defining the viscoplastic behavior of the material, accounting for its dependence on the failure process;
- equations describing damage accumulation kinetics;
- a strength criterion of the damaged material

(a) *Relations of thermal creep*

The relation between the tensor components of stresses and elastic strains is established using equations of thermal elasticity:

$$\begin{aligned} \sigma &= 3K[e - \alpha T]; \dot{\sigma} = 3K[\dot{e} - \dot{\alpha}T - \alpha\dot{T}] + \frac{\dot{K}}{K}\sigma, \\ \sigma'_{ij} &= 2Ge'_{ij}; \dot{\sigma}'_{ij} = 2Ge'_{ij}\frac{\dot{G}}{G}\sigma'_{ij}; e'_{ij} = e'_{ij} - e_{ij}^p - e_{ij}^c \end{aligned} \quad (10.1)$$

where σ , e are spherical and σ'_{ij} , e'_{ij} are deviatoric tensor components of stresses σ_{ij} and strains e_{ij} , respectively; $G(T)$ is shear modulus, $K(T)$ is the volumetric modulus of elasticity, $\alpha(T)$ is thermal expansion coefficient—a function of temperature T .

To describe creep processes, a family of equipotential creep surfaces F_c is introduced in the stress space, which has a common center ρ_{ij}^c and different radii C_c , determined by the current stressed state [12–15]:

$$F_c^{(i)} = S_{ij}^c S_{ij}^c - C_c^2 = 0, S_{ij}^c = \sigma'_{ij} - \rho_{ij}^c, i = 0, 1, 2 \dots \quad (10.2)$$

According to the associated law,

$$\dot{e}_{ij}^c = \lambda_c \frac{\partial F_c^{(i)}}{\partial S_{ij}^c} = \lambda_c S_{ij}^c, \quad (10.3)$$

where λ_c is the current surface $F_c^{(i)}$ determining the current stressed state S_{ij}^c .

Among these equipotential surfaces, a surface of radius \bar{C}_c can be found that corresponds to zero creep rate:

$$F_c^{(0)} = \bar{S}_{ij}^c \bar{S}_{ij}^c - \bar{C}_c^2 = 0, \bar{S}_{ij}^c = \bar{\sigma}'_{ij} - \rho_{ij}^c \quad (10.4)$$

where \bar{S}_{ij}^c and $\bar{\sigma}'_{ij}$ are a combination of stressed states \bar{S} corresponding (with a certain tolerance) to zero creep rate.

It is postulated that

$$\begin{aligned} \bar{C}_c &= \bar{C}_c(\dot{\lambda}_c, T); \dot{\lambda}_c = \left(\frac{2}{3} \dot{e}_{ij}^c, \dot{e}_{ij}^c \right)^{1/2}; \chi^c = \int_0^t \chi^c dt; \\ \lambda_c &= \lambda_c(\psi_c, T); \psi_c \left[\frac{(S_{ij}^c S_{ij}^c)^{1/2} - \bar{C}_c}{C_c} \right]; \lambda_c = \begin{cases} 0, & \psi_c \leq 0, \\ \lambda_c, & \psi_c \leq 0, \end{cases} \end{aligned} \quad (10.5)$$

where \bar{C}_c and λ_c are experimentally determined functions of temperature T .

The evolutionary equation for the change of the coordinates of the creep surface center is assumed to be of the form [16]:

$$\dot{\rho}_{ij}^c = g_1^c \dot{e}_{ij}^c - g_2^c \rho_{ij}^c \dot{\lambda}_c, \quad (10.6)$$

where g_1^c and $g_2^c > 0$ are experimentally determined material parameters.

Concretizing relation (10.3), the law of orthogonality can be written in the following form:

$$\dot{e}_{ij}^c = \lambda_c(\psi_c, T) S_{ij}^c = \lambda_c \psi_c S_{ij}^c = \lambda_c \left(\frac{\sqrt{S_{ij}^c S_{ij}^c} - \bar{C}_c}{C_c} \right) S_{ij}^c, \quad (10.7)$$

whence the expression for the length of the creep deformation trajectory can be written as follows [17]:

$$\dot{\lambda}_c = \sqrt{\frac{2}{3}} \dot{e}_u^c = \sqrt{\frac{2}{3}} \lambda_c \left(\sqrt{S_{ij}^c S_{ij}^c} - \bar{C}_c \right). \quad (10.8)$$

From (10.8), for the three parts of the creep curve [14], the expression for λ_c will assume the following form [16]:

$$\lambda_c = \begin{cases} 0, & \psi_c \leq 0 \vee \chi_c = 0, \\ \lambda_c^I, & \psi_c > 0 \wedge 0 < \chi_c \leq \chi_c^{(1)}, \\ \lambda_c^{II}, & \psi_c > 0 \wedge \chi_c^{(1)} < \chi_c \leq \chi_c^{(2)}, \\ \lambda_c^{III}, & \psi_c > 0 \wedge \chi_c^{(2)} < \chi_c \leq \chi_c^{(3)}, \end{cases} \quad (10.9)$$

where

$$\lambda_c^I = \lambda_c^{(0)} \left(1 - \frac{e_{11}^c}{e_{11}^{c(1)}} \right) + \lambda_c^{(1)} \frac{e_{11}^c}{e_{11}^{c(1)}}$$

,

$$\lambda_c^{II} = \frac{3}{2} \frac{\dot{e}_{11}^{\text{fat}}}{\left(\sigma'_{11} - \frac{3}{2} \rho_{11}^c - \bar{\sigma}_c \right)}$$

,

$$\lambda_c^{III} = \lambda_c^{II}(\omega)$$

are obtained experimentally with a laboratory specimen in a uniaxial stressed state [16].

In formula (10.9): $\lambda_c^{(0)}$ and $\lambda_c^{(1)}$ are values of λ_c in the initial and final points of the first part of the creep curve of the material; $e_{11}^{c(1)}$, $e_{11}^{c(2)}$, and $e_{11}^{c(3)}$ are limits of the parts of the creep curve for a uniaxial stressed state; $\dot{e}_{11}^{c(\text{init})}$ is creep strain rate at an initial time, $\dot{e}_{11}^{c(\text{fat})}$ is creep strain rate along the part of the steady-state creep (the second part of the creep curve); ω is damage degree of the damaged material; $\bar{\sigma}_c = \sqrt{\frac{2}{3}} \bar{C}_c$ is creep limit in a uniaxial stressed state [14, 16].

Equations (10.1)–(10.9) describe the transient and steady-state parts of the creep curve in multiaxial stressed states, as well as the main effects of the creep process under alternating loading.

At the stage of the development of defects scattered over the volume, the effect of damage degree on the physical–mechanical characteristics of the material is observed. In the first approximation, this effect can be accounted for, using the concept of degrading continuum and introducing effective stresses [2, 9, 11]:

$$\tilde{\sigma}'_{ij} = F_1(\omega) \sigma'_{ij} = \frac{G}{\tilde{G}} \sigma'_{ij}, \quad \tilde{\sigma} = F_2(\omega) \sigma = \frac{\kappa}{\tilde{\kappa}} \sigma \quad (10.10)$$

where \tilde{G} , $\tilde{\kappa}$ are effective moduli of elasticity defined by McKenzie's formulas [11]:

$$\tilde{G} = G(1 - \omega) \left[1 - \frac{(6K + 12G)}{(9K + 8G)} \omega \right], \quad (10.11)$$

$$\tilde{K} = 4GK(1 - \omega)/(4G + 3K\omega). \quad (10.12)$$

Effective internal variable $\tilde{\rho}_{ij}^c$ is defined in a similar way:

$$\tilde{\rho}_{ij}^c = F_1(\omega) \rho_{ij}^c = \frac{G}{\tilde{G}} \rho_{ij}^c. \quad (10.13)$$

(b) *Evolutionary equations of damage accumulation*

It is postulated that creep damage accumulation rate is defined by the following evolutionary equation [5, 7, 8, 17]:

$$\dot{\omega} = f_1(\beta) f_2(\omega) f_3(W_c) f_4(\dot{W}_c), \quad (10.14)$$

where functions f_i , $i = 1 \dots 4$ account for: voluminosity of stressed state ($f_1(\beta)$), accumulated damage level ($f_2(\omega)$), accumulated relative energy of damage spent on the nucleation of defects ($f_3(W_c)$), and rate of change of damage energy ($f_4(\dot{W}_c)$).

In (10.14):

$$f_1(\beta) = \exp(\beta),$$

$$f_2(\omega) = \begin{cases} 0, & W_c \leq W_c^a, \\ \omega^{1/3}(1 - \omega)^{2/3}, & W_c > W_c^a \wedge \omega \leq 1/3, \\ \frac{\sqrt[3]{16}}{9} \omega^{-1/3}(1 - \omega)^{-2/3}, & W_c > W_c^a \wedge \omega > 1/3, \end{cases} \quad (10.15)$$

$$f_3(W_c) = \frac{W_c - W_c^a}{W_c^f}, \quad f_4(\dot{W}_c) = \dot{W}_c / W_c^f, \quad \dot{W}_c = \rho_{ij}^c \dot{\epsilon}_{ij}^c, \quad W_c = \int_0^t \dot{W}_c dt, \quad (10.16)$$

where β is the parameter of voluminosity of stressed state ($\beta = \sigma/\sigma_u$), W_c^a is the value of damage energy W_c at the end of the stage of nucleation of scattered creep defects (at the beginning of the second part of the creep curve), and W_c^f is the value of energy corresponding to the nucleation of a macroscopic crack (the end of the third part of the creep curve).

The duration of the microdefect nucleation phase will be related to the value of parameter W_c^a .

When the dimensions of microdefects become comparable with the average distance between them, the process of merging starts (breakage of the remaining continuous gaps between the defects). No detailed model of the merging of cavities was constructed in the present paper; to account for this process, the kinetic equation (due to its term $f_2(\omega)$) was formulated so that, when damage degree reaches its value

$\omega = 1/3$, relation $\dot{\omega} = f_1(\omega)$ takes into account the avalanche-like increase of the damage degree value.

(c) ***Strength criterion of the damaged material***

The condition when damage degree ω reaches its critical value

$$\omega = \omega_f \leq 1 \quad (10.17)$$

is taken as the criterion of the end of the phase of growth of scattered microdefects (the stage of formation of a macrocrack)

Integrating evolutionary equation of damage accumulation (10.14)–(10.16) simultaneously with defining relations of thermal viscoplasticity (10.1)–(10.13) and failure criterion (10.17) for a known history of thermal–mechanical loading in a particular elementary volume of the material, one can predict the moment of nucleation of a macrocrack when the material degrades according to the long-term strength mechanism.

(d) ***A methodology for determining parameters of the defining relations of MDM***

Material parameters of equations of MDM are determined from the basic experiments. The main type of the basic experiments is isothermal, at constant basic temperatures T_j , using cylindrical tubular and cylindrical solid specimens. The chosen type of specimens has to provide a homogeneous distribution of stress, strain, and temperature fields within the working part, preventing loss of stability and change of form of the specimens under alternating loading, maximally excluding any effect of concentrators on the stressed–strained state in the region of transition from the working part of the specimen to its thick parts.

To determine the main material parameters of relations of thermal creep (10.1)–(10.9), basic temperatures T_j are determined, at which creep processes are observed in the given material. For each basic temperature, a specimen is tested by alternating loading according to the “soft” loading scheme, with intermediate holding periods, during which the parameters of the creep curve $e_{11}^c(t)$ at $\sigma_{11} = \text{const}$ are measured. Then, using the defining relations of transient creep, material parameters of thermal plasticity are determined [16].

To determine the parameters of evolutionary Eq. (10.14) for creep, the third part of creep curves $e_{11}^c(\sigma_{11}, T_j)$ at different constant stresses and temperatures is used. It can be done much more simply if the creep curves are similar [2]. In this case, the relative curve for $T = T_j$ is assumed as a basic curve.

(e) ***Integrating the defining relations of MDM***

Defining the main characteristics of the process of viscoplastic deformation of damaged materials (state parameters) is reduced to writing the defining relations of MDM in increments, which depend on the chosen time step, Δt . Time step Δt can be

corrected along complex parts of the deformation trajectory during the entire computational time on condition of the stability of the computations. Such an approach [18] is most appropriate when analyzing boundary-value problems of mechanics of damaged media, and it is used in the present paper.

In a general case, stresses, plastic strains and creep strains are determined by integrating equations of thermal creep (10.1)–(10.9), using the four-point Runge–Kutta method with correcting the stress deviator, followed by determining stresses, using equations of thermal plasticity [12–14], accounting for the average creep strain rate at time $t^{n+1} = t^n + \Delta t$.

10.3 Investigation Results

Work [19] presents the results of experimentally studying processes of short-term high-temperature creep of the VZh-159 heat-resistant alloy, as obtained in the Laboratory for Testing Physical-Mechanical Properties of Structural Materials, Research Institute for Mechanics, Nizhny Novgorod Lobachevski State University, under the general leadership of D. A. Kazakov. The experiments were conducted on the ZWICKZ030 general-purpose test machine (Germany), with the MAYTEC-HT080/1 heating system. Measuring was done using a force gauge of class 1 according to ISO 7500-1 (deviation from the assigned force during one test is within 15 N) and a high-temperature longitudinal strain gauge (type – PMA – 12/V7-1). To control the temperature inside the high-temperature oven, three type-K thermocouples in the three zones and on the specimen were used. The preset temperature (deviation within 2 °C) was maintained using an HTO-08/1 electronic control block.

The tests were conducted using solid cross-sectional cylindrical specimens with the length of the working part $l = 50$ mm and diameter $d = 8$ mm in the conditions of uniaxial tension for different levels of normal stresses σ_{11} and temperatures T .

The short-term creep process up to macrocracking according to the long-term strength mechanism was analyzed using the «EXPMODEL» program designed for numerically modeling non-isothermal viscoplastic deformation and damage accumulation in structural materials (metals and their alloys) under non-regular nonstationary thermal–mechanical loading. The physical–mechanical characteristics of the VZh-159 heat-resistant alloy and the material parameters of the MDM model are listed in Table 10.1 [16].

Figures 10.1, 10.2, 10.3 and 10.4 depict the creep curves for the following:

- temperature $T = 750$ °C and stresses $\sigma_{11} = 350$ MPa and 450 MPa, respectively (Fig. 10.1);
- temperature $T = 850$ °C and stresses $\sigma_{11} = 120$ MPa and 150 MPa, respectively (Fig. 10.2);
- temperature $T = 750$ °C and transfer from stress level $\sigma_{11} = 350$ MPa to stress level— $\sigma_{11} = 450$ MPa (Fig. 10.3);

Table 10.1 Physical–mechanical characteristics and material parameters of the MDM model of the VZh-159 heat-resistant alloy

$T, \text{ }^\circ\text{C}$	$K, \text{ MPa}$	$G, \text{ MPa}$	$\bar{C}_c, \text{ MPa}$	$\lambda_c^{(0)}, \text{ 1/MPa.hr}$	$\lambda_c^{(1)}, \text{ 1/MPa.hr}$	$g_1^c, \text{ MPa}$	g_2^c
750	137000	64000	265	0.0005	0.0005	1100	150
850	113000	52000	85	0.00068	0.00068	1000	150
$W_c^f, \text{ MJ/m}^3$	$W_c^a, \text{ MJ/m}^3$	α_c	r_c	k_c	$\chi_c^{(1)}$	$\chi_c^{(2)}$	ω_f
57.5	14.3	1	0.1	1	0	0.025	0.83
14	5	1	0.1	1	0	0.06	0.83

Fig. 10.1 The creep curves for temperature $T = 750 \text{ }^\circ\text{C}$ and stresses $\sigma_{11} = 350 \text{ MPa}$ and 450 MPa

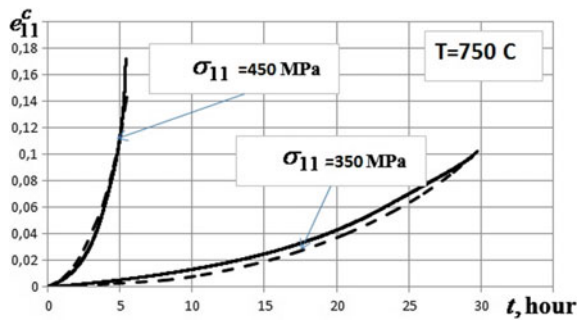


Fig. 10.2 The creep curves for temperature $T = 850 \text{ }^\circ\text{C}$ and stresses $\sigma_{11} = 120 \text{ MPa}$ and 150 MPa

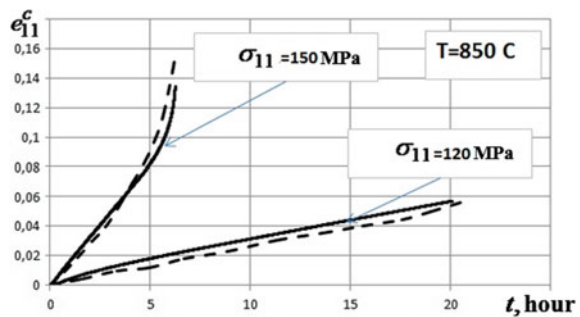


Fig. 10.3 The creep curves for temperature $T = 750 \text{ }^\circ\text{C}$ and transfer from stress level $\sigma_{11} = 350 \text{ MPa}$ to stress level— $\sigma_{11} = 450 \text{ MPa}$

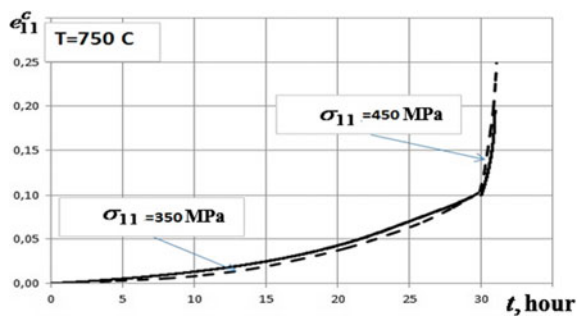
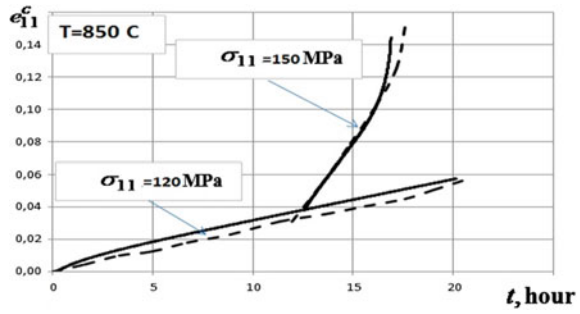


Fig. 10.4 The creep curves for temperature $T = 850^\circ\text{C}$ and transfer from stress level $\sigma_{11} = 120\text{ MPa}$ to stress level— $\sigma_{11} = 150\text{ MPa}$



- temperature $T = 850^\circ\text{C}$ and transfer from stress level $\sigma_{11} = 120\text{ MPa}$ to stress level— $\sigma_{11} = 150\text{ MPa}$ (Fig. 10.4).

In the figures, the solid lines show the results of numerical modeling, using defining relations of MDM (10.1)–(10.17), the dashed lines correspond to the experimental results. It can be seen that the experimental and the numerical data agree both qualitatively and quantitatively.

Figures 10.5–10.9, for the experiment shown in Fig. 10.4, give the relations for the following:

- effective stresses $\tilde{\sigma}_{11}$ and $\tilde{\rho}_{11}^c$ as a function of process time t (Figs. 10.5 and 10.6,

Fig. 10.5 The relations for effective stresses $\tilde{\sigma}_{11}$ which as a function of process time t for the experiment shown in Fig. 10.4

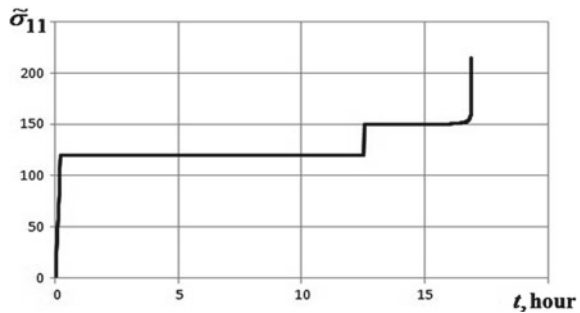
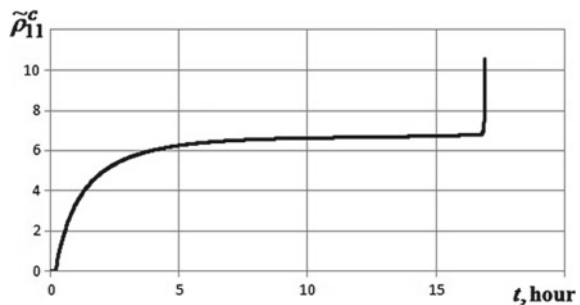


Fig. 10.6 The relations for effective $\tilde{\rho}_{11}^c$ as a function of process time t for the experiment shown in Fig. 10.4



respectively);

- effective radius of the zero-level creep surface \tilde{C}_c as a function of process time t (Fig. 10.7);
- creep failure energy W_c as a function of process time t (Fig. 10.8); damage values ω as a function of process time t (Fig. 10.9).

In general, after analyzing the obtained numerical results, it can be noted that the proposed model of damage media qualitatively and quantitatively describes the main effects observed for transient creep of structural materials (metals and their

Fig. 10.7 The relations for effective radius of the zero-level creep surface \tilde{C}_c as a function of process time t for the experiment shown in Fig. 10.4

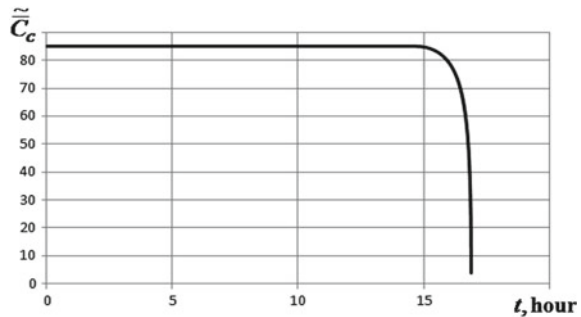


Fig. 10.8 The relations for the effective radius of the zero-level creep surface \tilde{C}_c as a function of process time t for the experiment shown in Fig. 10.4

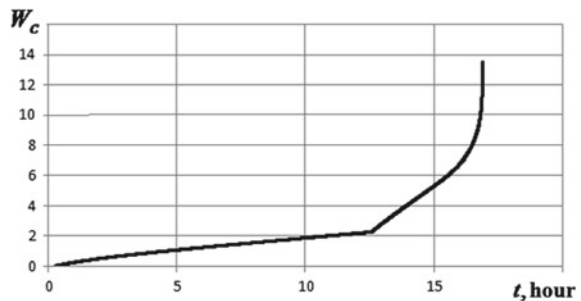
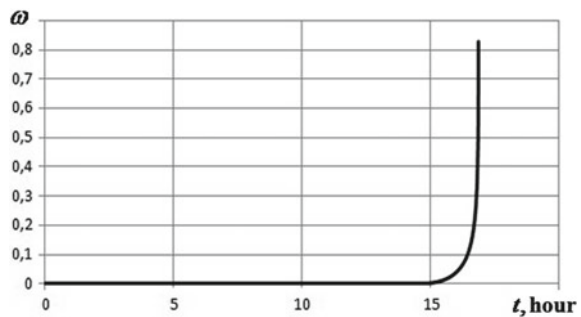


Fig. 10.9 The relations for damage values ω as a function of process time t for the experiment shown in Fig. 10.4



alloys) and the degradation of initial strength properties of materials according to the long-term strength degradation mechanism.

The next example presents the results of numerically studying the carrying capacity of an NPP reactor vessel in the conditions of a hypothetical emergency according to the long-term strength mechanism. The material of the reactor vessel is steel 15H2NMFA.

An axisymmetric reactor vessel consisting of a cylindrical sidewall with an elliptical bottom was used as an analytical model. The emergency situation was modeled by an effect of internal hydrostatic pressure p_1 , changing from zero at a height of $h = 1.5$ m from the lowest point of the bottom and modeling a force effect from the meltdown, internal pressure p_2 , and temperature T varying within the analyzed part of the reactor vessel from 184°C to 1510°C.

Two values of temperature T on the region in the apex of the outer surface of the elliptical bottom were used in the analysis:

- $T = 594^\circ\text{C}$ (the first version of the analysis—Fig. 10.10a), taken from [10];
- $T = 800^\circ\text{C}$ (the second version of the analysis—Fig. 10.10b), taken from [20].

The geometrical dimensions and the temperature distribution over the reactor vessel surface (the temperature on the internal and external surfaces of the vessel) were used as boundary conditions when analyzing the temperature fields in the reactor vessel cross section.

In Fig. 10.10, temperature distributions are shown in yellow, and the reactor vessel in blue.

Temperature field distribution in the reactor vessel in the condition of a serious accident, obtained based on the corresponding thermal–physical analyses (numerically analyzing the problem of heat-conduction) with increasing the temperature up

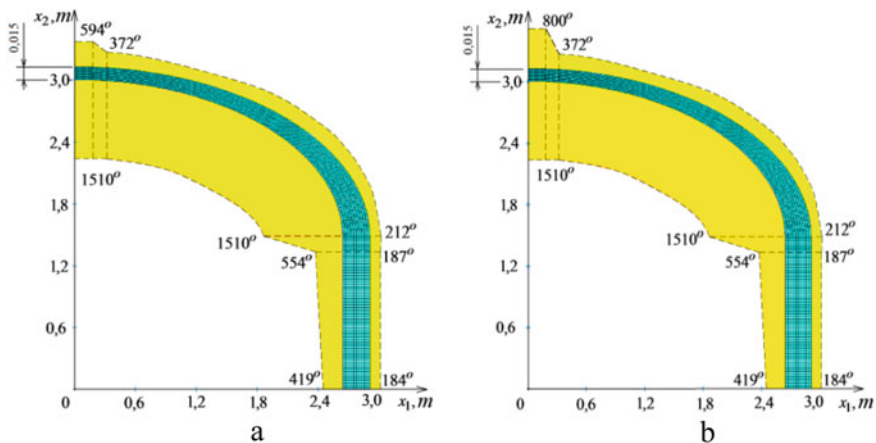


Fig. 10.10 **a** $T = 594^\circ\text{C}$, taken from [10], **b** $T = 800^\circ\text{C}$, taken from [20]

to maximal values (the duration of the heating stage was 1 min) for the two above-mentioned versions of analysis, is depicted in Fig. 10.11 (close views of the most “critical” zones are given at the bottom of the pictures).

Before directly modeling the emergency, the reliability of the developed MDM model was analyzed, and the material parameters of steel 15H2NMFA were determined in the temperature range from 20 °C to 1200 °C. To this end, the experimental data published in [21, 22] was used.

Papers [21, 22] present the results of experimentally studying the processes of short-range transient creep of steel 15H2NMFA in the temperature range up to 1200 °C. The creep process up to macrocracking was analyzed, using the physical–mechanical characteristics and material parameters of the MDM model for steel 15H2NMFA listed in Table 10.2.

Figures 10.12 and 10.13 show creep curves for the following:

- temperature $T = 900\text{ °C}$ and stresses $\sigma_{11} = 20; 22$ and 26.5 MPa, respectively (Fig. 10.12);
- temperature $T = 1200\text{ °C}$ and stresses $\sigma_{11} = 4.5; 5.4$ and 6.3 MPa, respectively (Fig. 10.13).

In the pictures, the solid lines correspond to the results of numerical modeling, using defining relations of MDM (10.1)–(10.17), whereas the markers show the corresponding experimental data. Qualitative and quantitative agreement of the experimental and numerical data is observed, both in the values and in the character of the change of strains along all the three parts of the creep curve and in the time of macrocracking, which makes it possible to conclude that the modeling process is adequate and that the material parameters contained in the developed defining relations of MDM are determined accurately.

The problem of evaluating the long-term strength of the NPP reactor vessel under thermal–mechanical loading was numerically analyzed in two stages.

At the first stage, the stage of increasing the pressure and temperature up to maximal values during a short interval (the duration of the heating stage was 1 min) was analyzed.

At the second stage, the pressure and temperature remained constant.

A number of analyses were done that differed in the value of internal pressure p_2 .

Four values of pressure p_2 were used in the analyses:

- $p_2 = 1.25; 1.35; 1.5,$ and 2 MPa for the version of the temperature field depicted in Fig. 10.10a;
- $p_2 = 0.6; 0.7; 0.8,$ and 1 MPa for the version of the temperature field shown in Fig. 10.10b.

At all stages, the load acting on the bottom of the reactor vessel from the hydrostatic effect of the meltdown was modeled.

It is to be noted that, in constructing the analytical model, the effect of the zone of the elliptical bottom was taken into account, in which the material, due to heavy meltdown, practically does not resist deformation. For this reason, the thickness of

Fig. 10.11 Temperature field distribution in the reactor vessel in the condition of a serious accident

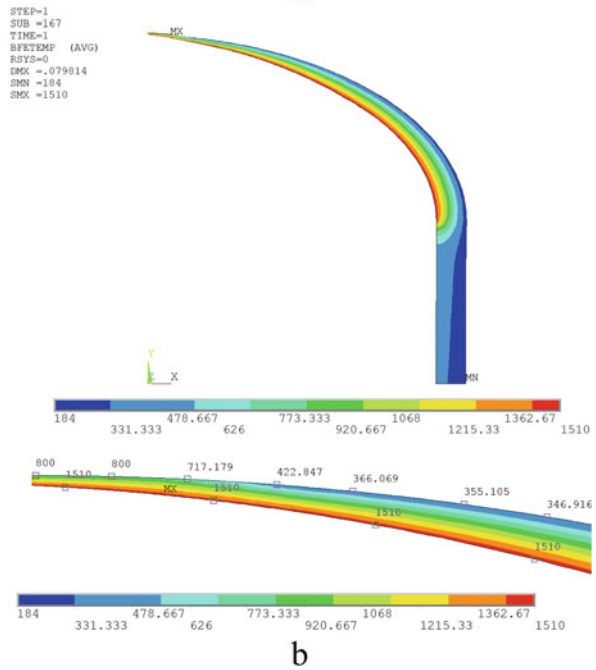
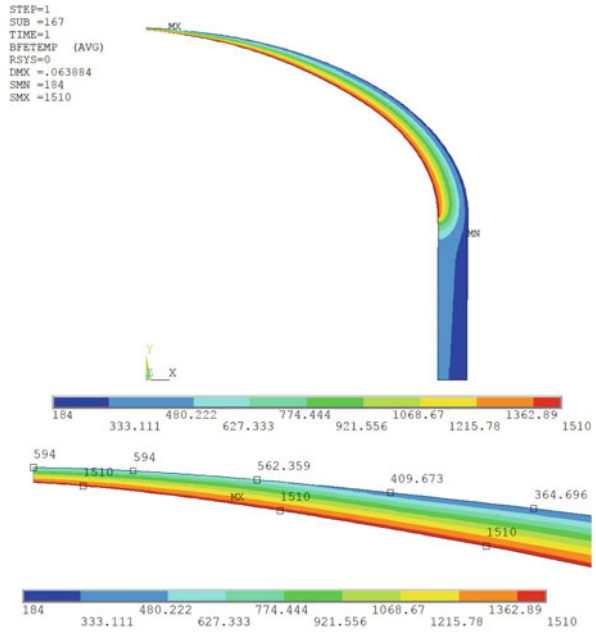


Table 10.2 Physical–mechanical characteristics and material parameters of the MDM model of steel 15H2NMFA

$T, ^\circ\text{C}$	K_t, MPa	G, MPa	\bar{C}_c, MPa	$\lambda_c^{(0)}, 1/\text{MPa}\cdot\text{hr}$	$\lambda_c^{(1)}, 1/\text{MPa}\cdot\text{hr}$	g_1^c, MPa	g_2^c	$W_c^f, \text{MJ}/\text{m}^3$	$W_c^a, \text{MJ}/\text{m}^3$	ω_f
600	138000	63500	110	0.000045	0.00009	30000	1000	26	11.2	0.8
800	34700	16000	29	0.00026	0.00052	3500	350	7	3.7	0.8
900	66700	30800	9	0.0002	0.000053	1000	300	2.6	1.24	0.8
1200	9170	4230	1.5	0.00027	0.00027	100	100	0.65	0.21	0.8

Fig. 10.12 Creep curves for temperature $T = 900^\circ\text{C}$ and stresses $\sigma_{11} = 20$; 22 and 26.5 MPa

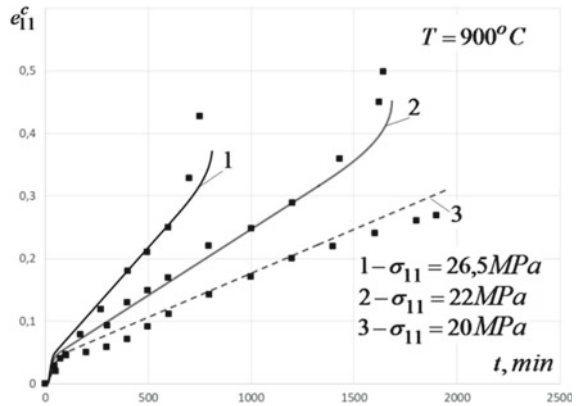
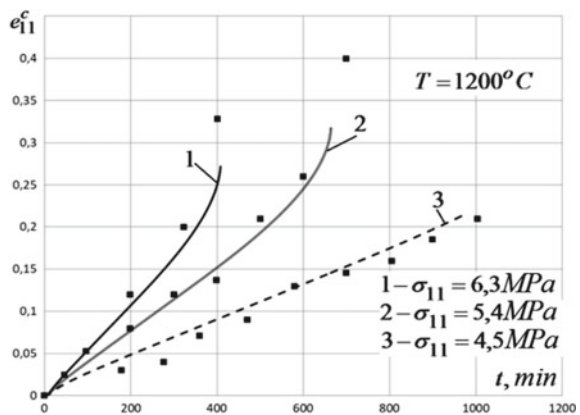


Fig. 10.13 Creep curves for temperature $T = 1200^\circ\text{C}$ and stresses $\sigma_{11} = 4.5$; 5.4 and 6.3 MPa



the elliptical bottom in the analytical model was reduced by the depth of the meltdown zone ($T > 1200^\circ\text{C}$).

As a result of the numerical analysis it was found that, in all the versions of the analyses conducted, the second stage (holding), accompanied by intensively developing creep strains and growing defects, proved to be the most important one from the viewpoint of long-term strength.

In particular, it was found that, for $p_2 \leq 1.3\text{ MPa}$ (in the version of the temperature field shown in Fig. 10.10a) and $p_2 \leq 0.6\text{ MPa}$ in the version of the temperature field (Fig. 10.10b), at time $t > 5$ hour in the first version of the analyses and $t > 57$ hour for the second one, the creep strain rate in the zone of maximal loading of the reactor vessel, located in the zone of the apex of the elliptical bottom, proved to be close to zero.

For pressures $p_2 \geq 1.3\text{ MPa}$ in the first version of the analyses and $p_2 = 0.6\text{ MPa}$ in the second one, deformation of the reactor vessel under a loading effect was

accompanied by an intensive change of form due to progressive creep of the material in the central part of the elliptical bottom.

Figure 10.14 depicts stress intensity distribution over the cross-section of the reactor vessel for $p_2 = 1.5$ Mpa at different times for the temperature field version (Fig. 10.10a), whereas Fig. 10.15 shows the same for $p_2 = 1$ Mpa for the temperature field version presented in Fig. 10.10b. Numerical analysis of the stress field of the facility reveals the fact that the zone of maximal loading, from the viewpoint of stress intensity values, displaces with time, and at $T = 111.5$ min (for the first version of the analysis) and at $T = 126.4$ min (for the second one), when the growth of creep strains in the central part of the elliptical bottom leads to the loss of carrying capacity of the vessel (nucleation of a macrocrack), it is localized on the external surface in the vicinity of the region where the cylindrical sidewall transfers to the elliptical bottom of the reactor vessel.

Figure 10.16 presents the inelastic strain intensity distribution over the cross section of the vessel at different times for $p_2 = 1.5$ Mpa and the temperature field (Fig. 10.10a), and Fig. 10.17 illustrates the same for $p_2 = 1$ Mpa and temperature field (Fig. 10.10b). It is evident that, in contrast to the results presented in Figs. 10.14 and 10.15, the most “critical” zone (that with the highest level of creep strain intensity) is located in the central part of the elliptical bottom of the reactor vessel, where damage accumulation processes are the most intensive.

The damage degree distribution over the reactor vessel cross section at the time of nucleation of a macrocrack for the first version of the analysis is shown in Fig. 10.18, and for the second one in Fig. 10.19. It can be seen that a macroscopic crack for both versions of the analysis nucleates in the central part of the elliptical bottom in the vicinity of the median surface of the structural element (in Figs. 10.18 and 10.19, the part of the zone where a macrocrack nucleates is shown separately).

Figure 10.20 presents damage degree ω as a function of process time t in the most critical zone (point A in Fig. 10.18) for the version of the temperature field shown in Fig. 10.10a and different values of pressure p_2 , whereas in Fig. 10.21, the analogous relations are given for the version of the temperature field shown in Fig. 10.10b.

The deformed configuration of the reactor vessel by the time preceding the exhaustion of its carrying capacity is depicted in Fig. 10.22 for both of the above versions of analyses, respectively (the displacement in Fig. 10.22, is scaled up by 2).

Figure 10.23 shows time to failure as a function of active pressure p_2 for the version of the temperature field shown in Fig. 10.10a, and for that shown in Fig. 10.10b.

Analysis of the obtained numerical results reveals the following characteristic laws of the deformation process of the NPP reactor vessel:

- for the version of the temperature field depicted in Fig. 10.10a, the limiting value of pressure p_2 , not resulting in the nucleation of a macrocrack according to the long-term strength mechanism must not exceed $p_2 = 1.3$ Mpa, whereas for the temperature field in Fig. 10.10b this value is $p_2 = 0.6$ Mpa;
- the numerical results of determining limiting values of pressure, obtained in the present work, agree with those published in [23].

Fig. 10.14 Stress intensity distribution over the cross section of the reactor vessel for $p_2 = 1.5$ Mpa at different times for the temperature field version (Fig. 10.10a)

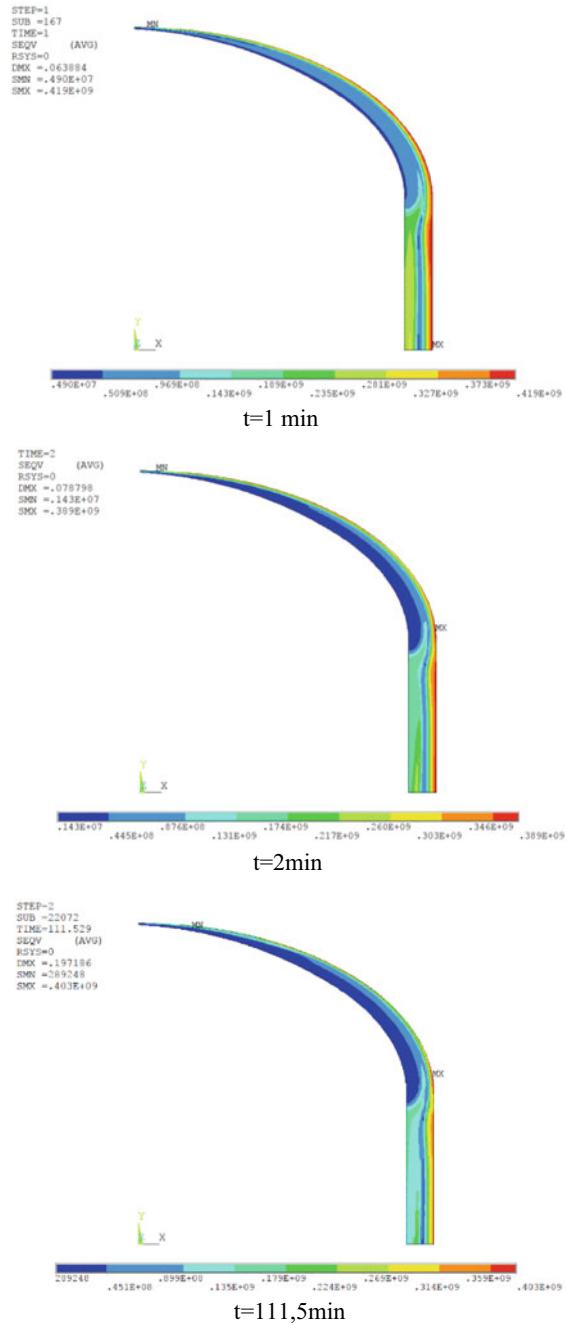


Fig. 10.15 Stress intensity distribution over the cross section of the reactor vessel for $p_2 = 1$ Mpa at different times for the temperature field version (Fig. 10.10b)

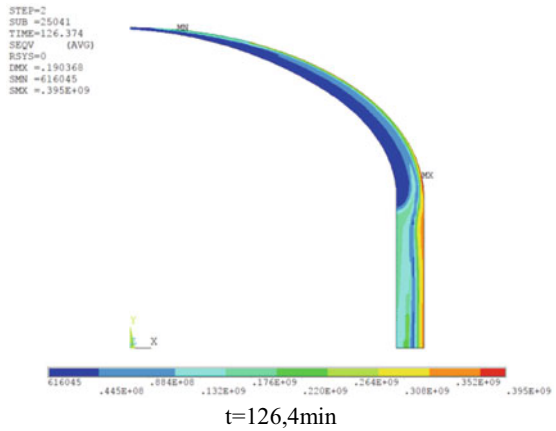
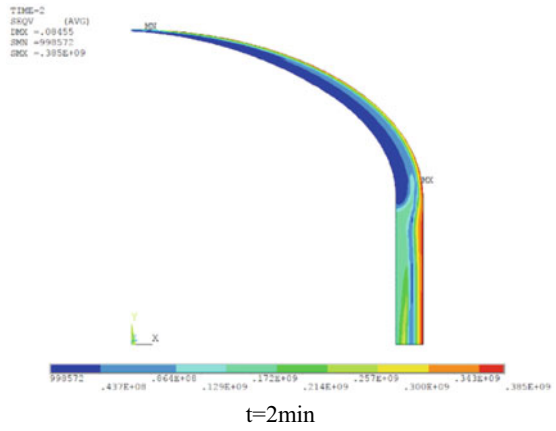
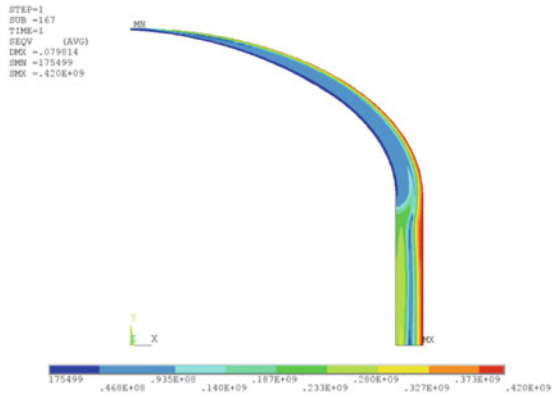


Fig. 10.16 Inelastic strain intensity distribution over the cross section of the vessel at different times for $p_2 = 1.5 \text{ Mpa}$ and the temperature field (Fig. 10.10a)

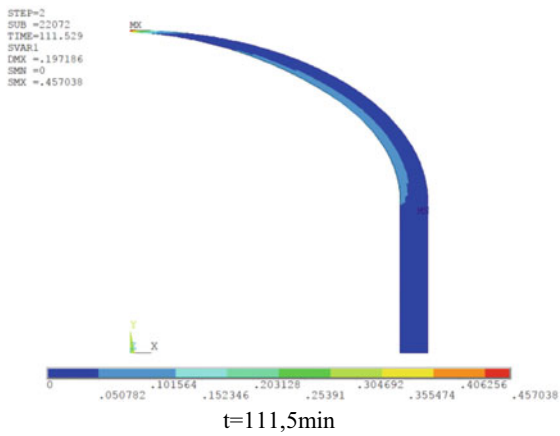
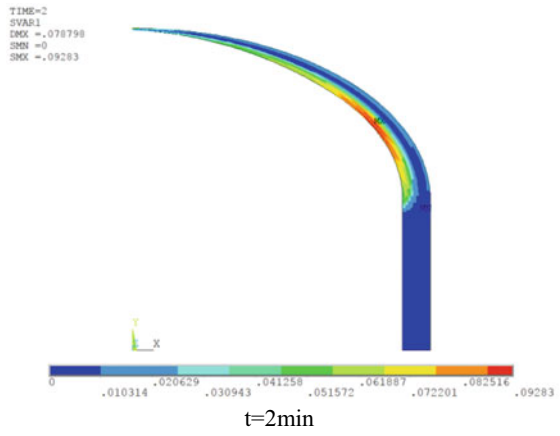
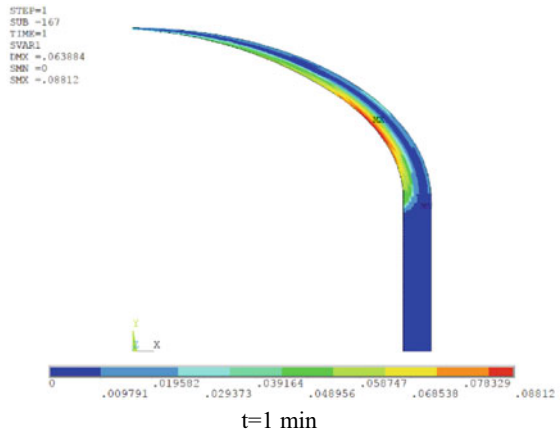
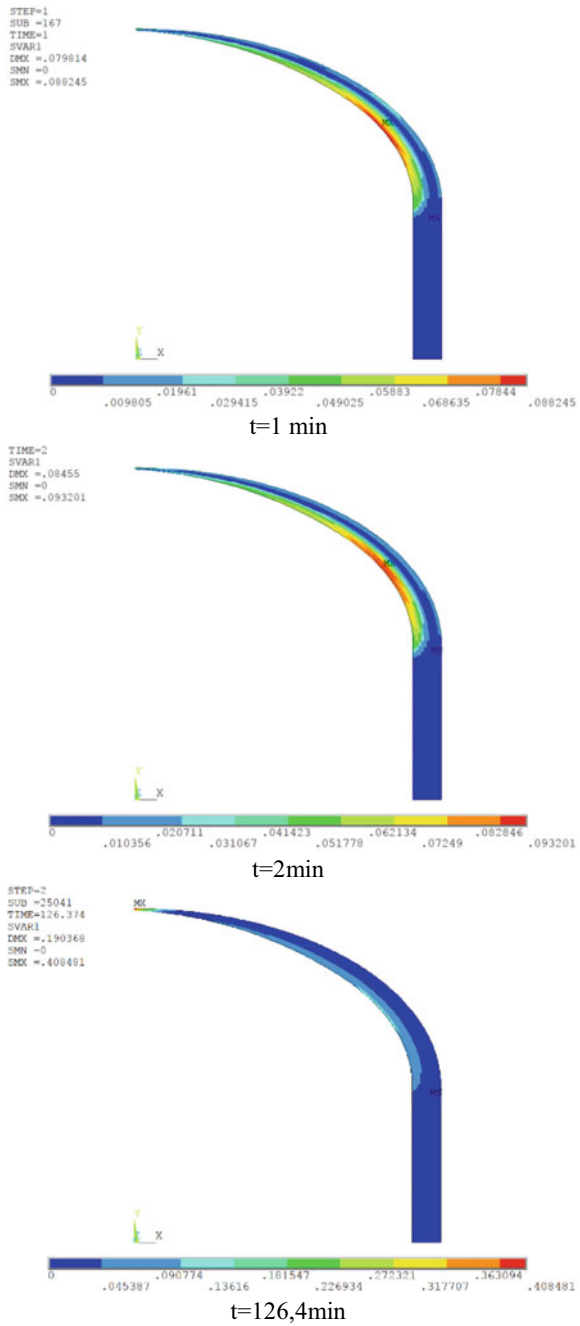


Fig. 10.17 inelastic strain intensity distribution over the cross section of the vessel at different times for $p_2 = 1$ Mpa and the temperature field (Fig. 10.10b)



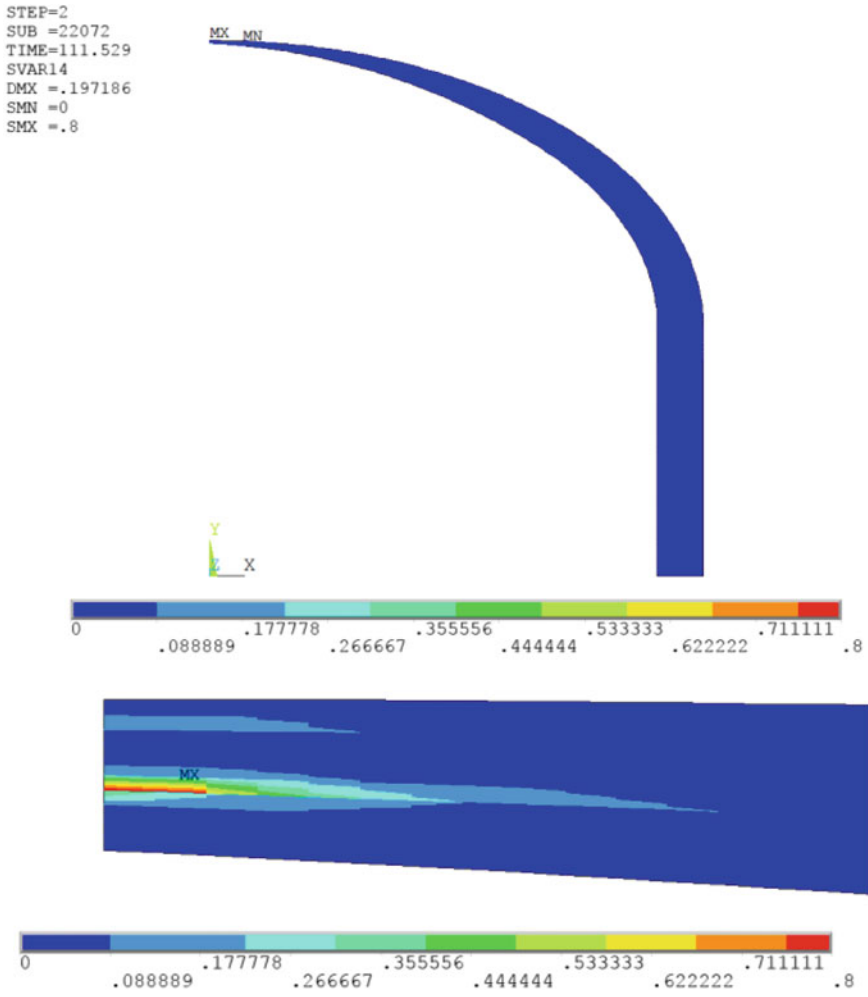


Fig. 10.18 The damage degree distribution over the reactor vessel cross section at the time of nucleation of a macrocrack for the first version of the analysis

Thus, the present numerical analyses and their comparison with the available experimental data make it possible to conclude that the developed defining relations of MDM adequately accounts for the degradation of structural materials according to the long-term strength mechanism and can be effectively used for evaluating long-term strength of materials and structures.

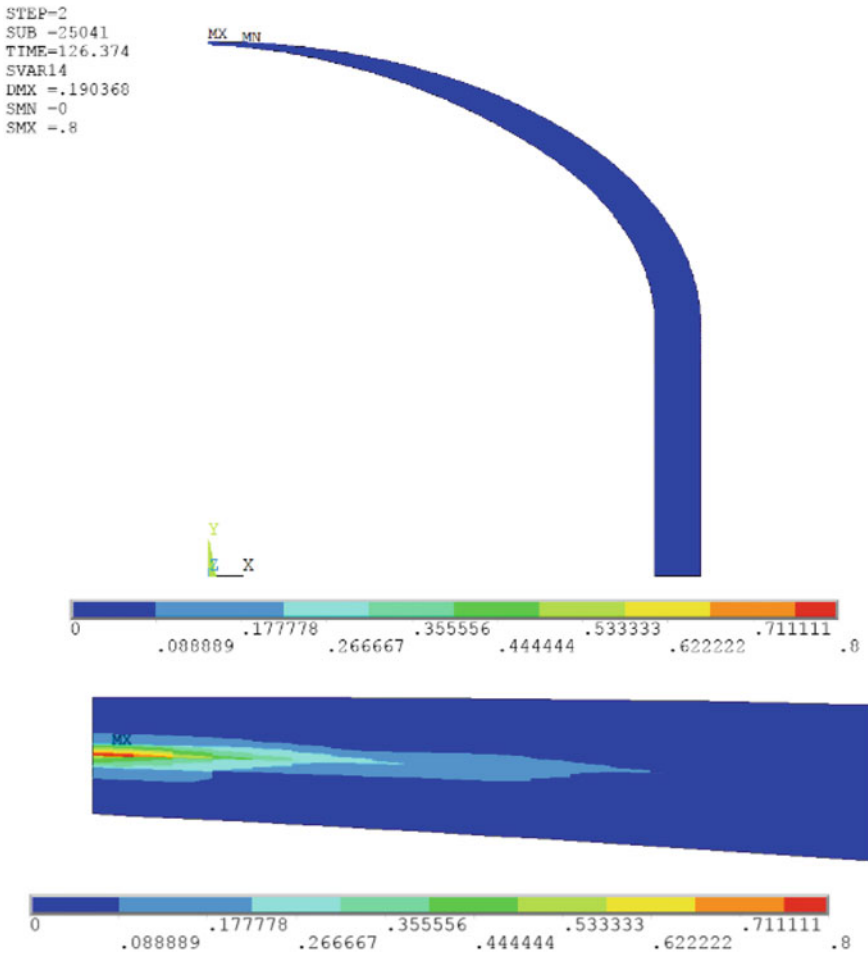


Fig. 10.19 The damage degree distribution over the reactor vessel cross section at the time of nucleation of a macrocrack for the second version of the analysis

10.4 Conclusions

A mathematical model of mechanics of damaged media has been developed, which describes processes of inelastic deformation and damage accumulation in structural materials (metals and their alloys) in the presence of degradation of their initial strength properties according to the long-term strength mechanism.

Using numerical modeling and comparing the obtained results with test data, the reliability of the defining relations of MDM in the presence of creep has been assessed, which made it possible to come to a conclusion about the reliability of the

Fig. 10.20 Damage degree ω as a function of process time t in the most critical zone (point A in Fig. 10.18) for the version of the temperature field shown in Fig. 10.10a and different values of pressure p_2

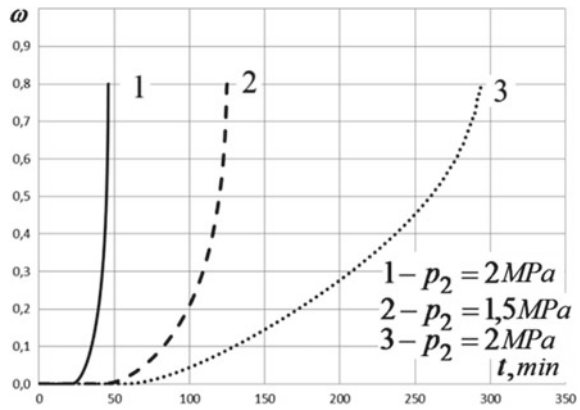
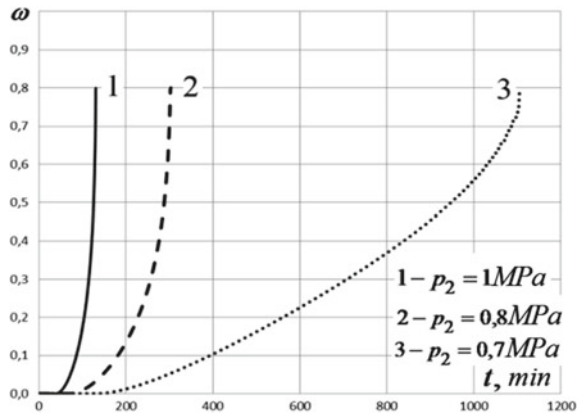


Fig. 10.21 Damage degree ω as a function of process time t in the most critical zone (point A in Fig. 10.18) for the version of the temperature field shown in Fig. 10.10b and different values of pressure p_2



developed modeling representations and the accuracy of the developed methodology of determining material parameters entering the above relations.

The results of numerically analyzing the carrying capacity of an NPP reactor vessel in the conditions of a hypothetical accident are presented, which corroborates the prediction of the loss of carrying capacity of such facilities.

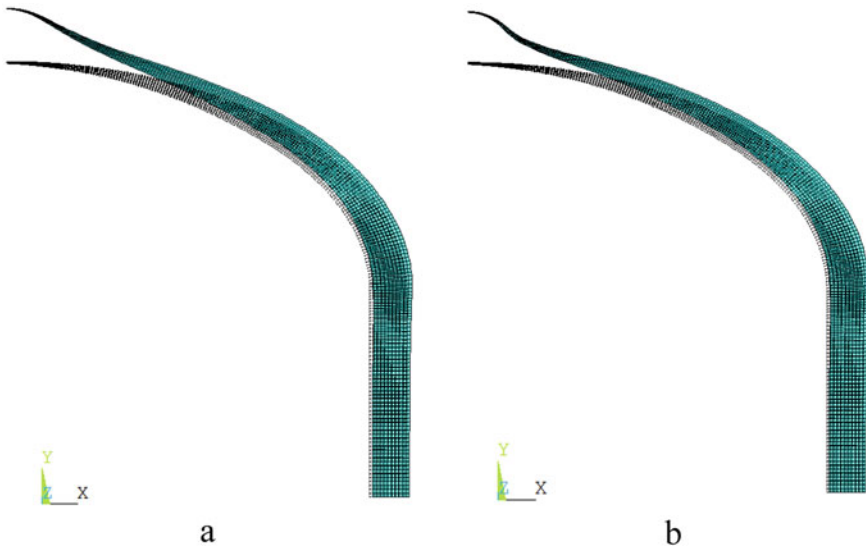
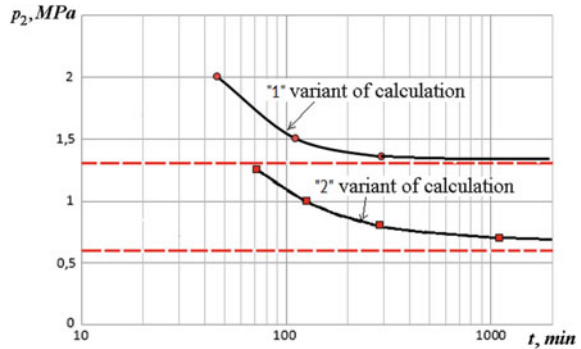


Fig. 10.22 The deformed configuration of the reactor vessel by the time preceding the exhaustion of its carrying capacity

Fig. 10.23 Time to failure as a function of active pressure p_2 for the version of the temperature field shown in Fig. 10.10a, and for that shown in Fig. 10.10b



Acknowledgements The work is financially supported by the Federal Targeted Program for Research and Development in Priority Areas of Development of the Russian Scientific and Technological Complex for 2014–2020 under the contract № 075-15-2019-1702 (unique identifier RFMEFI60519X0183).

References

1. Mitenkov, F.M., Kaydalov, V.F., Korotkikh, Y.G.: *Metody obosnovaniya resursa yadernyh energeticheskikh ustanovok.* (in Rus.) M.: Mashinostroyeniye, (2007)
2. Volkov, I.A., Korotkikh, Y.G.: *Uraveniya sostoyaniya vyazkoupругoplasticheskikh sred s povrezhdeniyami.* (in Rus.) M.: Fizmatlit, (2008)

3. Lokoshenko, A.M.: Polzuchest i dlitel'naya prochnost metallov. (in Rus.) M.: Fizmatlit, (2016)
4. Woodford, D.A.: Povrezhdeniye pri polzuchesti I kontsepsiya ostatochnoy dolgovechnosti (in Rus.) Teoreticheskiye osnovy inzhenernykh raschetov. **101**(4), 1–8 (1979)
5. Lemaitre, J.: Damage modelling for prediction of plastic or creep fatigue failure in structures. Transaction 5th International Conference SMRiT, North Holland, 1979, paper No. L5/1b
6. Murakami, S., Imaizumi, T.: Mechanical description of creep damage and its experimental verification. *J. Mec. Theor. Appl.* **1**, 743–761 (1982)
7. Lemaitre, J.: A continuous damage mechanics model for ductile fracture. *J Eng Mater Technol* **107**(1), 83–89 (1985)
8. Chaboche, J.L.: Constitutive equation for cyclic plasticity and cyclic viscoplasticity. *Int. J. Plasticity* **5**(3), 247–302 (1989)
9. Volkov, I.A., Igumnov, L.A., Kazakov, D.A., Mironov, A.A., Tarasov, I.S., Shishulin, D.N., Smetanin, I.V.: Model povrezhdennoy sredy dlya opisaniya dlitel'noy prochnosti konstruktsionnykh materialov (metallov i ih splavov) (in Rus.) *Problemy prochnosti i plastichnosti.* **79**(3), 285–300 (2017)
10. Kazakov, D. A., Kapustin, S. A., Korotkikh, Y.G.: Modelirovaniye protsessov deformirovaniya I razrusheniya materialov i konstruktsiy. (in Rus.) N.Novgorod: Izd-vo Nizhegorodskogo un-ta. (1994)
11. Volkov, I.A., Igumnov, L.A.: Vvedeniye v kontinual'nuyu mehaniku povrezhdennoy sredy. (in Rus.) M.: FIZMATLIT, (2017)
12. Nikitenko, A.F.: Experimental verification of the hypothesis of the existence of surface creep under complex loading conditions. Report No. 1. *Strength Mater* **16**(8), 1063–1068 (1984a)
13. Nikitenko, A.F.: Experimental verification of the hypothesis of the existence of surface creep under complex loading conditions. Report No. 2. *Strength Mater* **16**(8), 1069–1071 (1984b)
14. Volkov, I.A., Igumnov, L.A., Korotkikh, Y.G.: Prikladnaya teoriya vyazkoplastichnosti. (in Rus.) N. Novgorod, -vo NNGU, (2015)
15. Volkov, I.A., Igumnov, L.A., Kazakov, D.A., Shishulin, D.N., Smetanin, I.V.: Opredeleniye sootnosheniya nestatsionarnoy polzuchesti pri slozhnom napryazhenom sostoyanii (in Rus.) *Problemy prochnosti i plastichnosti. Vyp.* **78**(4), 436–451 (2016)
16. Volkov, I.A., Igumnov, L.A., Kazakov, D.A., Emelyanov, A.A., Tarasov, I.S., Guseva, M.A.: Programm'naya realizatsiya protsessov vyazkoplasticheskogo deformirovaniya i nakopleniya povrezhdeniy v konstruktsionnykh splavah pri termomehanicheskom nagruzhenii (in Rus.) *Problemy prochnosti i plastichnosti.* **78**(2), 188–207 (2016)
17. Bodner, S. R., Lindholm, U. S.: An incremental criterion for time-dependent failure of materials. *ASME J Eng Mater Technol* **98**(2), 140–145 (1976)
18. Banthia, V., Mukherjee, S.: On an improved time integration scheme for stiff constitutive models of inelastic deformation. *ASME J Eng Mater Technol* **107**(4), 282–285 (1985)
19. Kapustin, S.A., Kazakov, D.A., Churilov, Yu.A., Galushenko, A.I.: i dr. Eksperimentalno-teoreticheskoye izucheniye povedeniya izdeliy iz zharoprochnogo splava v usloviyah vysokotemperaturnoy polzuchesti (in Rus.) *Problemy prochnosti i plastichnosti: Mezhdunarodnyy sbornik. N.Novgorod, issue.* **70**, 100–111 (2008)
20. Frizen, E.A., Semishkin, V.P., Pantyushin, S.I.: Termomehanicheskiy analiz povedeniya korpusa reaktora sredney moshnosti v usloviyah tyazholoy zaproektnoy avarii (in Rus.) (Gidropress, 2014)
21. Drobyshevskiy, N.I., Kiselev, A.E., Strizhov, V.F., Filippov, A.S.: HEFESTM: programmnoye sredstvo dlya rascheta vysokotemperaturnogo nelineynogo deformirovaniya (in Rus.) *Matem. modelirovaniye,* **22**(2), 45–63 (2010)
22. Loktionov, V.D., Sosnin, O.V., Lyubashevskaya, I.V.: Prochnostnyye svoystva i osobennosti deformatsionnogo povedeniya stali 15H2NMFA–A v temperaturnom diapazone 20–1100 °C (in Rus.) *Atomnaya energiya* **99**(3), 229–232 (2005)
23. Semishkin, V.P., Pazhetnov, V.V., Frtizen, E.A., Loktionov, V.D.: Tertermomehanicheskoe povedenie korpusa VVER v tyazheloy avarii (in Rus.) *Pyataya mezhdunarodnaya nauchno-tehnicheskaya konferentsiya “Obespecheniye bezopasnosti AES s VVER », Podilsk,* **29**(5), 1–6 (2007)

Chapter 11

Nonlinear Deformations of an Elastic Sphere with Couple Stresses and Distributed Dislocations



Leonid M. Zubov

Abstract The problem of nonlinear moment theory of elasticity about the equilibrium of a hollow sphere with distributed dislocations is considered. For an arbitrary isotropic micropolar elastic material and a spherically symmetric distribution of screw and edge dislocations, the problem is reduced to a system of nonlinear ordinary differential equations. In the case of a physically linear micropolar body model, exact solutions are found for the eigenstresses in the sphere due to the spherically symmetric distribution of edge dislocations.

Keywords Micropolar medium · Nonlinear elasticity · Spherical symmetry · Dislocation density · Eigenstresses · Exact solution

11.1 Introduction

In the present paper, we consider the spherically symmetric problems of the nonlinear theory of dislocations taking into account couple stresses, i.e., in the framework of the micropolar theory of elasticity. This model is also called the Cosserat continuum. The model of a micropolar medium is used to describe granular polycrystalline bodies, polymer composites, suspensions, liquid crystals, geophysical structures, biological tissues, metamaterials, nanostructured materials, etc. [1–5]. The basics of the nonlinearly theory of the Cosserat elastic continuum had been given in [6–10].

An important point of the microstructure of solids is the defects of the crystal lattice such as dislocations and disclinations [11–13]. The linear theory of continuously distributed dislocations and disclinations in micropolar media is developed in [14–16], and the nonlinear theory in [17, 18]. At present, only a very limited number of exact solutions in nonlinear theory of dislocations and disclinations for micropolar elastic media are known in the literature. Several solutions for isolated dislocations and disclinations in the nonlinear elastic Cosserat continuum are found in [8]. The

L. M. Zubov (✉)

Southern Federal University, ul. Milchakova 8a, Rostov-on-Don 344090, Russian Federation
e-mail: zubovl@yandex.ru

© Springer Nature Switzerland AG 2020

S. M. Aizikovich et al. (eds.), *Modeling, Synthesis and Fracture of Advanced Materials for Industrial and Medical Applications*, Advanced Structured Materials 136,
https://doi.org/10.1007/978-3-030-48161-2_11

175

planar axisymmetric problem of large deformations of a micropolar medium with distributed wedge disclinations is solved in [18].

Below in the paper, spherically symmetric solutions for large deformations of a micropolar medium with distributed dislocations were found. Spherically symmetric solutions of the nonlinear theory of dislocations without taking into account couple stresses were found earlier [19, 20]. In the framework of the linear micropolar theory of elasticity, spherically symmetric deformations of a hollow sphere with distributed dislocations and disclinations were studied in [21].

11.2 Basic Relations of Nonlinear Micropolar Continuum

Deformation of an elastic medium is described by mapping from a reference configuration to an actual one. In the case of micropolar continua, it is defined by two kinematically independent fields of translations and rotations

$$\mathbf{r} = \mathbf{r}(\mathbf{R}) = \mathbf{R} + \mathbf{u}(\mathbf{R}), \quad \mathbf{H} = \mathbf{H}(\mathbf{R}),$$

where $\mathbf{R} = X_k \mathbf{i}_k$ and X_k , $\mathbf{r} = x_s \mathbf{i}_s$ and x_s are the position vectors and Cartesian coordinates in the reference and actual configurations, respectively, \mathbf{i}_k are corresponding constant base vectors ($k = 1, 2, 3$), \mathbf{u} is the translation vector, and \mathbf{H} is the proper orthogonal tensor describing the rotational degrees of freedom of micropolar continua cold often microrotation tensor [6–8].

In what follows we use the following definitions of operators of gradient, divergence, and rotor (curl) in the coordinates of the reference configuration:

$$\begin{aligned} \text{Grad } \Psi &= \mathbf{R}^N \otimes \frac{\partial \Psi}{\partial Q^N}, & \text{Div } \Psi &= \mathbf{R}^N \cdot \frac{\partial \Psi}{\partial Q^N}, \\ \text{Rot } \Psi &= \mathbf{R}^N \times \frac{\partial \Psi}{\partial Q^N}, & \mathbf{R}^N &= \mathbf{i}_k \frac{\partial Q^N}{\partial X_k}, \end{aligned} \quad (11.1)$$

where Ψ is an arbitrary differentiable tensor field of any order, $Q^N = Q^N(X_1, X_2, X_3)$, $N = 1, 2, 3$, are Lagrangian curvilinear coordinates, \otimes denotes the tensor product, and cross and dot stand for vector and scalar products, respectively.

The governing equations of a micropolar elastic continuum are given by the following equations, see [6–10]:

Equilibrium equations:

$$\text{Div } \mathbf{D} + \rho \mathbf{f} = 0, \quad \text{Div } \mathbf{G} + (\mathbf{F}^T \cdot \mathbf{D})_{\times} + \rho \mathbf{l} = 0. \quad (11.2)$$

Constitutive relations:

$$\begin{aligned} \mathbf{D} &= \mathbf{P} \cdot \mathbf{H}, \quad \mathbf{G} = \mathbf{K} \cdot \mathbf{H}, \\ \mathbf{P} &= \frac{\partial W}{\partial \mathbf{E}}, \quad \mathbf{K} = \frac{\partial W}{\partial \mathbf{L}}, \quad W = W(\mathbf{E}, \mathbf{L}). \end{aligned} \quad (11.3)$$

Geometric relations:

$$\begin{aligned} \mathbf{E} &= \mathbf{F} \cdot \mathbf{H}^T, \\ \mathbf{L} &= \frac{1}{2} \mathbf{R}^N \otimes \left(\frac{\partial \mathbf{H}}{\partial Q^N} \cdot \mathbf{H}^T \right)_{\times} = \frac{1}{2} \mathbf{I} \operatorname{tr}[\mathbf{H} \cdot (\operatorname{Rot} \mathbf{H})^T] - \mathbf{H} \cdot (\operatorname{Rot} \mathbf{H})^T, \\ \mathbf{F} &= \operatorname{Grad} \mathbf{r}. \end{aligned} \quad (11.4)$$

Here \mathbf{D} and \mathbf{G} are the stress and couples stress tensors of the first Piola–Kirchhoff type, respectively, while \mathbf{P} and \mathbf{K} are these of the second Piola–Kirchhoff type, \mathbf{F} is deformation gradient, \mathbf{E} and \mathbf{L} are the strain tensors in the nonlinear micropolar continuum called stretch and wryness tensors, respectively (see [6–10]), \mathbf{I} is unit tensor, ρ is material density in the reference configuration, \mathbf{f} is the external distributed mass load, \mathbf{l} is the external distributed mass couple load, W is the strain energy density, and Φ_{\times} denotes the vector invariant of the second-order tensor Φ

$$\Phi_{\times} = (\Phi_{MN} \mathbf{R}^M \otimes \mathbf{R}^N)_{\times} \stackrel{\Delta}{=} \Phi_{MN} \mathbf{R}^M \times \mathbf{R}^N.$$

For isotropic micropolar continua strain energy W , stress and couples stressed tensors \mathbf{P} and \mathbf{K} are isotropic functions of strain tensors \mathbf{E} and \mathbf{L} [9]. This implies of the following relations:

$$\begin{aligned} W(\mathbf{Q}^T \cdot \mathbf{E} \cdot \mathbf{Q}, (\det \mathbf{Q}) \mathbf{Q}^T \cdot \mathbf{L} \cdot \mathbf{Q}) &= W(\mathbf{E}, \mathbf{L}) \\ \mathbf{P}(\mathbf{Q}^T \cdot \mathbf{E} \cdot \mathbf{Q}, (\det \mathbf{Q}) \mathbf{Q}^T \cdot \mathbf{L} \cdot \mathbf{Q}) &= \mathbf{Q}^T \cdot \mathbf{P}(\mathbf{E}, \mathbf{L}) \cdot \mathbf{Q} \\ \mathbf{K}(\mathbf{Q}^T \cdot \mathbf{E} \cdot \mathbf{Q}, (\det \mathbf{Q}) \mathbf{Q}^T \cdot \mathbf{L} \cdot \mathbf{Q}) &= (\det \mathbf{Q}) \mathbf{Q}^T \cdot \mathbf{K}(\mathbf{E}, \mathbf{L}) \cdot \mathbf{Q} \end{aligned} \quad (11.5)$$

for any arbitrary orthogonal tensor \mathbf{Q} . In Eqs. (11.5) we take into account that \mathbf{E} and \mathbf{P} are the true second-order tensors, while \mathbf{L} and \mathbf{K} are the second-order pseudotensors.

11.3 Continuously Distributed Dislocations

Let V be the area occupied by the elastic medium in the reference configuration. In order to introduce the dislocation density in a micropolar medium, we consider the problem of determining the displacement field $\mathbf{u}(\mathbf{R})$ of the medium from the tensor fields \mathbf{E} and \mathbf{H} specified in the multiply connected area V . These tensor fields are assumed to be differentiable and unambiguous in V . Considering that according to (11.4)

$$\text{Grad } \mathbf{u} = \mathbf{F} - \mathbf{I} = \mathbf{E} \cdot \mathbf{H} - \mathbf{I} \quad (11.6)$$

we see that in the case of a multiply connected area, the vector field $\mathbf{u}(\mathbf{R})$, and therefore the vector field $\mathbf{r}(\mathbf{R})$, are not uniquely defined, in general. This means the presence of isolated translational dislocations in the body [8], each of which is characterized by Burgers vector \mathbf{b}_n , by virtue of (11.6)

$$\mathbf{b}_n = \oint_{\Gamma_n} d\mathbf{R} \cdot (\mathbf{E} \cdot \mathbf{H} - \mathbf{I}) = \oint_{\Gamma_n} d\mathbf{R} \cdot \mathbf{F}, \quad n = 1, 2, \dots, n_0 \quad (11.7)$$

Here Γ_n is a simple closed contour enclosing the line of the n th dislocation only. The total Burgers vector of a discrete set of n_0 dislocations according to (11.7) is defined by the formula

$$\mathbf{B} = \sum_{n=1}^{n_0} \mathbf{b}_n = \sum_{n=1}^{n_0} \oint_{\Gamma_n} d\mathbf{R} \cdot \mathbf{F}. \quad (11.8)$$

Due to known properties of curvilinear integrals, the sum of integrals in (11.8) can be replaced by one integral along the closed contour Γ_0 enclosing the lines of all n_0 dislocations

$$\mathbf{B} = \oint_{\Gamma_0} d\mathbf{R} \cdot \mathbf{F}. \quad (11.9)$$

According to [17, 18], we passed from a discrete set of dislocations to their continuous distribution, transforming the curvilinear integral (11.9) to a surface integral using Stokes' formula

$$\mathbf{B} = \iint_{\Sigma_0} \mathbf{N} \cdot \text{Rot } \mathbf{F} d\Sigma. \quad (11.10)$$

Here Σ_0 is the surface drawn over the contour Γ_0 , \mathbf{N} is the unit normal to Σ_0 . The expression (11.10) allows to introduce the density of continuously distributed dislocations as a second-order tensor $\boldsymbol{\alpha} \triangleq \text{Rot } \mathbf{F}$. The flux of $\boldsymbol{\alpha}$ through any surface is equal to the total Burgers vector of dislocations crossing this surface. Hereinafter, the dislocation density tensor is considered a given function of Lagrangian coordinates Q^N , which must satisfy the solenoidity condition

$$\text{Div } \boldsymbol{\alpha} = 0. \quad (11.11)$$

If dislocations with a given tensor density are distributed in the body, then the displacement field and the vector field \mathbf{r} do not exist. In this case, the third equation (11.4) is replaced by the incompatibility equation

$$\text{Rot } \mathbf{F} = \boldsymbol{\alpha} \quad (11.12)$$

and the tensor \mathbf{F} is called the distortion tensor.

The complete system of equilibrium equations for a micropolar elastic body with distributed dislocations contains tensor fields of distortion \mathbf{F} and microrotation \mathbf{H} as unknown functions and consists of the equilibrium equation (11.2), the incompatibility equation (11.12), the constitutive equations (11.3), and the geometric relations (11.4)₁, (11.4)₂.

11.4 Spherically Symmetric State

We consider an elastic body in the form of a hollow sphere with an outer radius of R_0 and an inner radius of R_1 . We introduce the spherical coordinates $Q^1 = R$, $Q^2 = \Phi$ (longitude), $Q^3 = \Theta$ (latitude) using the formulas

$$X_1 = R \cos \Phi \cos \Theta, \quad X_2 = R \sin \Phi \cos \Theta, \quad X_3 = R \sin \Theta.$$

In what follows, we will use an orthonormal vector basis $\mathbf{e}_R, \mathbf{e}_\Phi, \mathbf{e}_\Theta$ consisting of unit vectors tangent to coordinate lines

$$\begin{aligned} \mathbf{e}_R &= (\mathbf{i}_1 \cos \Phi + \mathbf{i}_2 \sin \Phi) \cos \Theta + \mathbf{i}_3 \sin \Theta, \\ \mathbf{e}_\Phi &= -\mathbf{i}_1 \sin \Phi + \mathbf{i}_2 \cos \Phi, \\ \mathbf{e}_\Theta &= -(\mathbf{i}_1 \cos \Phi + \mathbf{i}_2 \sin \Phi) \sin \Theta + \mathbf{i}_3 \cos \Theta. \end{aligned} \quad (11.13)$$

According to [19] a second-order tensor field \mathbf{S} will be called spherically symmetric, if its components in the basis $\mathbf{e}_R, \mathbf{e}_\Phi, \mathbf{e}_\Theta$ on each spherical surface $R = \text{const}$ are identical in all points of the surface and the tensor \mathbf{S} is invariant with respect to rotations around the radial axis, i.e., around the vector \mathbf{e}_R . A general representation of the spherically symmetric second-order tensor field has the form [19]

$$\begin{aligned} \mathbf{S} &= S_1(R)\mathbf{g} + S_2(R)\mathbf{d} + S_3(R)\mathbf{e}_R \otimes \mathbf{e}_R \\ \mathbf{g} &= \mathbf{e}_\Phi \otimes \mathbf{e}_\Phi + \mathbf{e}_\Theta \otimes \mathbf{e}_\Theta, \quad \mathbf{d} = \mathbf{e}_\Phi \otimes \mathbf{e}_\Theta - \mathbf{e}_\Theta \otimes \mathbf{e}_\Phi. \end{aligned} \quad (11.14)$$

Using Eqs. (11.13)–(11.14), the following relations are proved:

$$\begin{aligned} \text{Rot } \mathbf{S} &= \frac{1}{R} \frac{d}{dR} (RS_2) \mathbf{g} + \left(\frac{S_3 - S_1}{R} - \frac{dS_1}{dR} \right) \mathbf{d} + \frac{2}{R} S_2 \mathbf{e}_R \otimes \mathbf{e}_R \\ \text{Div } \mathbf{S} &= \left[\frac{dS_3}{dR} + \frac{2}{R} (S_3 - S_1) \right] \mathbf{e}_R. \end{aligned} \quad (11.15)$$

We assume that there are distributed dislocations in the sphere and their tensor density is

$$\boldsymbol{\alpha} = \alpha_1(R) \mathbf{g} + \alpha_2(R) \mathbf{d} + \alpha_3(R) \mathbf{e}_R \otimes \mathbf{e}_R. \quad (11.16)$$

The first summand in Eq. (11.16) describes the distribution of screw dislocations whose lines coincide with meridians and parallels. The second summand corresponds to a spherically symmetric distribution of edge dislocations. And the third one describes the distribution of screw dislocations with a radial axis.

Considering the equilibrium problem of an elastic sphere with distributed dislocations, unknown functions \mathbf{F} and \mathbf{H} will be sought in the form of spherically symmetric tensor fields

$$\mathbf{F} = F_1(R) \mathbf{g} + F_2(R) \mathbf{d} + F_3(R) \mathbf{e}_R \otimes \mathbf{e}_R \quad (11.17)$$

$$\mathbf{H} = H_1(R) \mathbf{g} + H_2(R) \mathbf{d} + H_3(R) \mathbf{e}_R \otimes \mathbf{e}_R \quad (11.18)$$

The requirements $\mathbf{H} \cdot \mathbf{H}^T = \mathbf{I}$, $\det \mathbf{H} = 1$, meaning that the rotation tensor is proper orthogonal, lead to the equalities $H_1^2 + H_2^2 = 1$, $H_3 = 1$. The expression (11.18) takes the form

$$\mathbf{H} = \cos \chi(R) \mathbf{g} + \sin \chi(R) \mathbf{d} + \mathbf{e}_R \otimes \mathbf{e}_R. \quad (11.19)$$

The geometrical meaning of Eq. (11.19) is that each elementary volume of the elastic sphere rotates around a radial axis by an angle $\chi(R)$.

Using Eqs. (11.4), (11.17), (11.19), we find the strain and wryness tensors

$$\begin{aligned} \mathbf{E} &= (F_1 \cos \chi + F_2 \sin \chi) \mathbf{g} + (F_2 \cos \chi - F_1 \sin \chi) \mathbf{d} + F_3 \mathbf{e}_R \otimes \mathbf{e}_R \\ \mathbf{L} &= \frac{\sin \chi}{R} \mathbf{g} + \frac{\cos \chi - 1}{R} \mathbf{d} + \frac{d\chi}{dR} \mathbf{e}_R \otimes \mathbf{e}_R. \end{aligned} \quad (11.20)$$

Considering a micropolar medium to be isotropic, let $\mathbf{Q} = \mathbf{Q}_1 = 2\mathbf{e}_R \otimes \mathbf{e}_R - \mathbf{I}$, $\det \mathbf{Q}_1 = 1$ in relations (11.5). In accordance with (11.20) we obtain

$$\mathbf{Q}_1^T \cdot \mathbf{E} \cdot \mathbf{Q}_1 = \mathbf{E}, \quad \mathbf{Q}_1^T \cdot \mathbf{L} \cdot \mathbf{Q}_1 = \mathbf{L} \quad (11.21)$$

From Eqs. (11.5) and (11.21) follow the equalities

$$\mathbf{Q}_1 \cdot \mathbf{P} = \mathbf{P} \cdot \mathbf{Q}_1, \quad \mathbf{Q}_1 \cdot \mathbf{K} = \mathbf{K} \cdot \mathbf{Q}_1 \quad (11.22)$$

whence follows

$$\begin{aligned}
 \mathbf{P} &= P_{RR} \mathbf{e}_R \otimes \mathbf{e}_R + P_{\Phi\Phi} \mathbf{e}_\Phi \otimes \mathbf{e}_\Phi \\
 &\quad + P_{\Phi\Theta} \mathbf{e}_\Phi \otimes \mathbf{e}_\Theta + P_{\Theta\Phi} \mathbf{e}_\Theta \otimes \mathbf{e}_\Phi + P_{\Theta\Theta} \mathbf{e}_\Theta \otimes \mathbf{e}_\Theta \\
 \mathbf{K} &= K_{RR} \mathbf{e}_R \otimes \mathbf{e}_R + K_{\Phi\Phi} \mathbf{e}_\Phi \otimes \mathbf{e}_\Phi \\
 &\quad + K_{\Phi\Theta} \mathbf{e}_\Phi \otimes \mathbf{e}_\Theta + K_{\Theta\Phi} \mathbf{e}_\Theta \otimes \mathbf{e}_\Phi + K_{\Theta\Theta} \mathbf{e}_\Theta \otimes \mathbf{e}_\Theta.
 \end{aligned} \tag{11.23}$$

Relations similar to Eqs. (11.21), (11.22) are also satisfied for the tensor $\mathbf{Q} = \mathbf{Q}_2 = \mathbf{e}_R \otimes \mathbf{e}_R + \mathbf{d}$, $\det \mathbf{Q}_2 = 1$, whence we have

$$P_{\Phi\Phi} = P_{\Theta\Theta}, \quad P_{\Phi\Theta} = -P_{\Theta\Phi}, \quad K_{\Phi\Phi} = K_{\Theta\Theta}, \quad K_{\Phi\Theta} = -K_{\Theta\Phi} \tag{11.24}$$

Equations (11.23), (11.24) mean that upon deformation in the form of (11.17) and (11.18) the stress and couple stress tensors for any isotropic homogeneous material are spherically symmetrical

$$\begin{aligned}
 \mathbf{P} &= P_1(R)\mathbf{g} + P_2(R)\mathbf{d} + P_3(R)\mathbf{e}_R \otimes \mathbf{e}_R \\
 \mathbf{K} &= K_1(R)\mathbf{g} + K_2(R)\mathbf{d} + K_3(R)\mathbf{e}_R \otimes \mathbf{e}_R.
 \end{aligned} \tag{11.25}$$

In accordance with Eqs. (11.3), (11.17), (11.19) the stress and couple stress tensors of the first Piola–Kirchhoff type \mathbf{D} and \mathbf{G} , respectively, are also spherically symmetric and take the form

$$\begin{aligned}
 \mathbf{D} &= D_1(R)\mathbf{g} + D_2(R)\mathbf{d} + D_3(R)\mathbf{e}_R \otimes \mathbf{e}_R \\
 \mathbf{G} &= G_1(R)\mathbf{g} + G_2(R)\mathbf{d} + G_3(R)\mathbf{e}_R \otimes \mathbf{e}_R \\
 D_1 &= P_1 \cos \chi - P_2 \sin \chi, \quad D_2 = P_1 \sin \chi + P_2 \cos \chi, \quad D_3 = P_3 \\
 G_1 &= K_1 \cos \chi - K_2 \sin \chi, \quad G_2 = K_1 \sin \chi + K_2 \cos \chi, \quad G_3 = K_3
 \end{aligned} \tag{11.26}$$

We suppose that mass loads are defined by spherically symmetric vector fields

$$\mathbf{f} = f(R)\mathbf{e}_R, \quad \mathbf{l} = l(R)\mathbf{e}_R \tag{11.27}$$

According to Eqs. (11.15), (11.17), (11.26) and (11.27), vector equilibrium equations (11.2) are reduced to two scalar equations

$$\frac{dD_3}{dR} + \frac{2(D_3 - D_1)}{R} + \rho f(R) = 0 \tag{11.28}$$

$$\frac{dG_3}{dR} + \frac{2(G_3 - G_1)}{R} + 2F_1 D_2 + \rho l(R) = 0 \tag{11.29}$$

Tensor incompatibility equation (11.12) in the case of a spherically symmetric deformation, by virtue of Eqs. (11.15)–(11.17), is equivalent to three scalar equations

$$2F_2 = R\alpha_3, \quad \frac{d}{dR}(RF_2) = R\alpha_1, \quad F_3 = \frac{d}{dR}(RF_1) + R\alpha_2 \quad (11.30)$$

The solenoidity condition (11.11) of the dislocation density tensor according to Eq. (11.15) leads to the following restriction on components of the tensor α

$$\alpha_1 = \alpha_3 + \frac{1}{2}R \frac{d\alpha_3}{dR}. \quad (11.31)$$

Note that the density of edge dislocations α_2 is not included in Eq. (11.31). This means that $\alpha_2(R)$ can be an arbitrary function, including the Dirac delta function. Since the dislocation densities $\alpha_m(R)$, $m = 1, 2, 3$ are considered to be given functions, the first Eq. (11.30) defines the function $F_2(R)$; the second Eq. (11.30) is the result of the first one and Eq. (11.31). The third Eq. (11.30) expresses the function $F_3(R)$ through the function $F_1(R)$. The latter remains an unknown function. The values D_m , G_n , ($m, n = 1, 2, 3$) are expressed through this function as well as through another unknown function $\chi(R)$ using the constitutive equations for isotropic material. Hence the equilibrium equations (11.28), (11.29) form a system of nonlinear ordinary differential equations with respect to $F_1(R)$, $\chi(R)$. Mass loads $f(R)$, $l(R)$ are considered to be given functions.

We assume that an elastic sphere is loaded with uniformly distributed pressure: p_0 on the outer surface $R = R_0$ and p_1 on the inner surface $R = R_1$. In addition, the surfaces of the sphere is loaded with uniformly distributed torque with intensities m_0 and m_1 per unit surface area of the deformed body. Therefore the boundary conditions for the specified system of equations are as follows:

$$\begin{aligned} D_3 &= -p_0 F_1^2, & G_3 &= m_0 F_1^2 & \text{at } R &= R_0 \\ D_3 &= -p_1 F_1^2, & G_3 &= m_1 F_1^2 & \text{at } R &= R_1. \end{aligned} \quad (11.32)$$

Thus, the problem of large deformations of an elastic sphere with a spherically symmetric dislocation distribution is reduced to a nonlinear boundary value problem for a system of ordinary differential equations in the case of an arbitrary isotropic micropolar material.

11.5 Physically Linear Material

As a specific model of an isotropic micropolar body, we consider a physically linear material [2, 7, 8] for which the specific strain energy is the quadratic form of tensors $\mathbf{E} - \mathbf{I}$ and \mathbf{L} , while tensors \mathbf{P} and \mathbf{K} are linear functions of these tensors.

$$\begin{aligned}
2W &= \lambda \operatorname{tr}^2 (\mathbf{E} - \mathbf{I}) + (\mu + \varkappa) \operatorname{tr} [(\mathbf{E} - \mathbf{I}) \cdot (\mathbf{E}^T - \mathbf{I})] \\
&\quad + (\mu - \varkappa) \operatorname{tr} (\mathbf{E} - \mathbf{I})^2 + \gamma_1 \operatorname{tr}^2 \mathbf{L} + \gamma_2 \operatorname{tr} (\mathbf{L} \cdot \mathbf{L}^T) + \gamma_3 \operatorname{tr} \mathbf{L}^2. \\
\mathbf{P} &= \lambda \mathbf{I} \operatorname{tr} (\mathbf{E} - \mathbf{I}) + (\mu + \varkappa) (\mathbf{E} - \mathbf{I}) + (\mu - \varkappa) (\mathbf{E}^T - \mathbf{I}), \\
\mathbf{K} &= \gamma_1 \mathbf{I} \operatorname{tr} \mathbf{L} + \gamma_2 \mathbf{L} + \gamma_3 \mathbf{L}^T.
\end{aligned} \tag{11.33}$$

Here $\lambda, \mu, \varkappa, \gamma_1, \gamma_2, \gamma_3$ are material constants. For a spherically symmetric state based on Eqs. (11.3), (11.17)–(11.20), (11.26), (11.33) we get

$$\begin{aligned}
D_1 &= \lambda(F_3 + 2F_1 \cos \chi - 3) \cos \chi + 2\mu (F_1 \cos \chi - 1) \cos \chi \\
&\quad + 2\varkappa F_1 \sin^2 \chi + (\lambda + \mu - \varkappa) F_2 \sin 2\chi \\
D_2 &= \lambda(F_3 + 2F_1 \cos \chi - 3) \sin \chi + 2\mu (F_1 \cos \chi - 1) \sin \chi \\
&\quad - \varkappa F_1 \sin 2\chi + 2\lambda F_2 \sin^2 \chi + (\mu + \varkappa) F_2 - (\mu - \varkappa) F_2 \cos 2\chi \\
D_3 &= \lambda(F_3 + 2F_1 \cos \chi - 3) + 2\mu (F_3 - 1) + 2\lambda F_2 \sin \chi \\
G_1 &= \frac{1}{R} \left[\gamma_1 \left(R \cos \chi \frac{d\chi}{dR} + \sin 2\chi \right) + \gamma_2 \sin \chi + \gamma_3 (\sin 2\chi - \sin \chi) \right] \\
G_2 &= \frac{1}{R} \left[\gamma_1 \sin \chi \left(R \frac{d\chi}{dR} + 2 \sin \chi \right) + \gamma_2 (1 - \cos \chi) + \gamma_3 (\cos \chi - \cos 2\chi) \right] \\
G_3 &= (\gamma_1 + \gamma_2 + \gamma_3) \frac{d\chi}{dR} + \frac{2\gamma}{R} \sin \chi
\end{aligned} \tag{11.34}$$

Relations (11.28)–(11.32), (11.34) form a nonlinear boundary value problem of the equilibrium of a sphere with distributed dislocations in the case of a physically linear micropolar material.

11.6 Exact Solution of the Eigenstress Problem

Eigenstresses in the theory of dislocations are called stresses in an elastic body that are caused only by dislocations but with no any of external loads. Assuming $f = 0$, $l = 0$, $p_0 = 0$, $p_1 = 0$, $m_0 = 0$, $m_1 = 0$ in Eqs. (11.28), (11.29), (11.32), (11.34), we obtain the formulation of the boundary spherically symmetric eigenstress problem for physically linear micropolar material.

We consider a special case about the distribution of dislocations when $\alpha_1(R) = 0$, $\alpha_3(R) = 0$, and $\alpha_2(R)$ is an arbitrary function. Then, by virtue of (11.30), we obtain $F_2(R) = 0$. The couple equilibrium equation (11.29) is satisfied if $\chi(R) = 0$. Indeed, then according to Eq. (11.34) we get $D_2 = 0$, $G_1 = G_2 = G_3 = 0$, and stress is expressed as follows:

$$\begin{aligned}
 D_1 &= \frac{2\mu}{1-2\nu}(F_1 + \nu F_3 - 1 - \nu), \\
 D_3 &= \frac{2\mu}{1-2\nu}[2\nu F_1 + (\nu - 1)F_3 - 1 - \nu] \\
 \nu &= \frac{\lambda}{2(\lambda + \mu)}
 \end{aligned}
 \tag{11.35}$$

Inverting Eq. (11.35) we get

$$F_1 = \frac{(1-\nu)D_1 - \nu D_3}{2\mu(1+\nu)} + 1, \quad F_3 = \frac{D_3 - 2\nu D_1}{2\mu(1+\nu)} + 1.
 \tag{11.36}$$

The equilibrium equation (11.28), the incompatibility equation (11.30)₃, and expressions (11.36) give the differential equation for the function $D_3(R)$

$$\frac{d^2 D_3}{dR^2} + \frac{4}{R} \frac{dD_3}{dR} = \beta(R), \quad \beta(R) \triangleq \frac{4\mu(1+\nu)\alpha_2(R)}{(\nu-1)R}.
 \tag{11.37}$$

Equation (11.37) has the following general solution

$$D_3(R) = -\frac{1}{3R^3} \int_{R_1}^R r^4 \beta(r) dr + \frac{1}{3} \int_{R_1}^R r \beta(r) dr + C_1 + C_2 R^{-3}.
 \tag{11.38}$$

Constants C_1 and C_2 are determined from the boundary conditions $D_3(R_0) = 0$, $D_3(R_1) = 0$ and have the form

$$C_1 = -\frac{C_2}{R_1^3}, \quad C_2 = \frac{R_0^3 R_1^3}{3(R_0^3 - R_1^3)} \left[\int_{R_1}^{R_0} r \beta(r) dr - \frac{1}{R_0^3} \int_{R_1}^{R_0} r^4 \beta(r) dr \right]
 \tag{11.39}$$

The stress $D_1(R)$ is expressed via solution (11.38), (11.39) using Eq. (11.28), and then the distortion components are found on the basis of Eq. (11.36).

The obtained exact solution of the nonlinear eigenstress problem is characterized by the absence of couple stresses. It turns out that there is another exact solution of this eigenstress problem in which the couple stresses are not identically equal to zero. In this solution, the microrotation field is a half-turn (i.e., a 180-degree rotation) around the radial axis. This field of microrotations corresponds to the equality $\chi(R) = \pm\pi$. As it follows from Eq. (11.34), with $\cos \chi = -1$ we obtain $G_1 = 0$, $G_2 \neq 0$, $G_3 = 0$, $D_2 = 0$ and the couple equilibrium equation (11.29) for $l = 0$ is satisfied, as well as the couple boundary conditions (11.32) for $m_0 = m_1 = 0$. The stress D_1 and D_3 at $\cos \chi = -1$ on the basis of Eq. (11.34) are written as follows:

$$\begin{aligned} D_1 &= \frac{2\mu\nu}{1-2\nu}(F_1 - \nu F_3 + 1 + \nu), \\ D_3 &= \frac{2\mu\nu}{1-2\nu}[(1-\nu)F_3 - 2\nu F_1 - 1 - \nu] \end{aligned} \quad (11.40)$$

From Eq. (11.40) we get

$$F_1 = \frac{(1-\nu)D_1 + \nu D_3}{2\mu(1+\nu)} - 1, \quad F_3 = \frac{2\nu D_1 + D_3}{2\mu(1+\nu)} + 1. \quad (11.41)$$

The equation for $D_3(R)$ arising from Eq. (11.28), the third of Eq. (11.30), and Eq. (11.41) will take the form

$$\begin{aligned} \frac{d^2 D_3}{dR^2} + \frac{4}{R} \frac{dD_3}{dR} - \frac{4\nu D_3}{(1-\nu)R^2} &= \gamma(R), \\ \gamma(R) &\triangleq \frac{4\mu(1+\nu)}{(1-\nu)R^2} [2 - R\alpha_2(R)] \end{aligned} \quad (11.42)$$

Equation (11.42) has the following solution

$$\begin{aligned} D_3(R) &= \sqrt{\frac{1-\nu}{9+7\nu}} \left[R^{\lambda_1} \int_{R_1}^R r^{\lambda_2+4} \gamma(r) dr \right. \\ &\quad \left. - R^{\lambda_2} \int_{R_1}^R r^{\lambda_1+4} \gamma(r) dr + B_1 R^{\lambda_1} + B_2 R^{\lambda_2} \right] \\ \lambda_1 &= -\frac{3}{2} + \frac{1}{2} \sqrt{\frac{9+7\nu}{1-\nu}}, \quad \lambda_2 = -\frac{3}{2} - \frac{1}{2} \sqrt{\frac{9+7\nu}{1-\nu}} \end{aligned} \quad (11.43)$$

Constants B_1, B_2 are determined from the boundary conditions $D_3(R_1) = D_3(R_0) = 0$.

Thus, within the framework of a physically linear micropolar material model, two exact solutions are found for eigenstresses in a nonlinearly elastic sphere with boundary dislocations distributed with density $\boldsymbol{\alpha} = \alpha_2(R)(\mathbf{e}_\phi \otimes \mathbf{e}_\theta - \mathbf{e}_\theta \otimes \mathbf{e}_\phi)$ where $\alpha_2(R)$ is an arbitrary function. One of these solutions is characterized by the absence of couple stresses. In the other solution, couple stresses are non-zero and are described by the formula

$$\mathbf{G} = \frac{2(\gamma_2 - \gamma_3)}{R} (\mathbf{e}_\phi \otimes \mathbf{e}_\theta - \mathbf{e}_\theta \otimes \mathbf{e}_\phi) \quad (11.44)$$

11.7 Conclusion

In this paper, the stress state at large spherically symmetric deformations of an elastic sphere made of a micropolar material is studied. A spherically symmetric distribution of screw and edge dislocations is specified in the sphere. Hydrostatic pressures and distributed couple loads are applied on the outer and inner surfaces of the sphere. Using the theory of spherically symmetric tensor fields and the properties of isotropic tensor functions, we reduce the original three-dimensional problem to a boundary value problem for a nonlinear system of ordinary differential equations. The problem is reduced to ordinary differential equations for an arbitrary isotropic micropolar elastic material. As a special case, the eigenstress problem is studied, that is, the problem of a self-balanced stress state that exists with no external force and couple loads. Within the framework of the physically linear micropolar medium model, exact analytical solutions to the eigenstresses problem in a sphere caused by a spherically symmetric distribution of edge dislocations are found. It is established that for the same dislocation density, there are two self-balanced spherical symmetric states of the sphere. In one of them, couple stresses are identical to zero, and in the other there is a non-trivial field of couple stresses.

Acknowledgments The research was supported by the Russian Science Foundation (18-11-00069).

References

1. Aero, J., Kuvshinskij, E.: Fundamental equations of the theory of elastic media with rotationally interacted particles. *Sov. Phys. Solid State* **2**(7), 1272–1281 (1961)
2. Pal'mov, V.: Fundamental equations of the theory of asymmetric elasticity. *J. Appl. Math. Mech.* **28**(6), 1341–1345 (1964)
3. Nowacki, W.: *Theory of Asymmetric Elasticity*. Pergamon Press, Oxford (1986)
4. Eringen, A.: *Microcontinuum Fields Theories. I. Foundations and Solids*. Springer, New York (1999)
5. Erofeev, V.: *Wave Process in Solids with Microstructure*. World Scientific, Singapore (2003)
6. Toupin, R.: Theories of elasticity with couple-stress. *Arch. Ration. Mech. Anal.* **17**(2), 85–112 (1964)
7. Shkutin, L.: *Mechanics of Deformations of Flexible Bodies (In Russian)*. Nauka, Novosibirsk (1988)
8. Zubov, L.: *Nonlinear Theory of Dislocations and Disclinations in Elastic Bodies*. Springer, Berlin (1997)
9. Nikitin, E., Zubov, L.: Conservation laws and conjugate solutions in the elasticity of simple materials and materials with couple stress. *J. Elast.* **51**(1), 1–22 (1998)
10. Pietraszkiewicz, W., Eremeyev, V.: On natural strain measures of the non-linear micropolar continuum. *Int. J. Solids Struct.* **46**(3–4), 774–787 (2009)
11. Gutkin, M., Ovid'ko, L.: *Plastic Deformation in Nanocrystalline Materials*. Springer, Berlin (2004)
12. Clayton, J.: *Nonlinear Mechanics of Crystals*. Springer, Dordrecht (2011)
13. Maugin, G.: Defects, dislocations and the general theory of material inhomogeneity. In: *Generalized Continua and Dislocation Theory. CISM Courses and Lectures*, vol. 537, pp. 1–83. Springer, Vienna (2012)

14. De Wit, R.: Continual Theory of Disclinations (in Russ.). Mir, Moscow (1977)
15. Zelenina, A., Zubov, L.: Quasi-solid states of micropolar elastic bodies. Dokl. Phys. **62**(1), 30–33 (2017)
16. Zubov, L.: Static-geometric analogy in the micropolar theory of elasticity. Dokl. Phys. **62**(9), 434–437 (2017)
17. Zubov, L.: Continuously distributed dislocations and disclinations in nonlinearly elastic micropolar media. Dokl. Phys. **49**(5), 308–310 (2004)
18. Zubov, L.: The continuum theory of dislocations and disclinations in nonlinearly elastic micropolar media. Mech. Solids **46**(3), 348–356 (2011)
19. Zubov, L.: Spherically symmetric solutions in the nonlinear theory of dislocations. Dokl. Phys. **59**(9), 419–422 (2014)
20. Goloveshkina, E., Zubov, L.: Universal spherically symmetric solution of nonlinear dislocation theory for incompressible isotropic elastic medium. Arch. Appl. Mech. **89**(3), 409–424 (2019)
21. Zelenina, A., Zubov, L.: Spherically symmetric deformations of micropolar elastic medium with distributed dislocations and disclinations. Adv. Struct. Mater. **87**, 357–369 (2018)